

**ESTIMATING METHANE EMISSIONS IN CANADA USING
ATMOSPHERIC OBSERVATIONS FROM EARTH TO SPACE**

SABOUR BARAY

A DISSERTATION SUBMITTED TO THE FACULTY OF
GRADUATE STUDIES IN PARTIAL FUFILLMENT OF THE
REQUIREMENTS FOR THE DEGREE OF

DOCTOR OF PHILOSOPHY

GRADUATE PROGRAM IN CHEMISTRY

YORK UNIVERSITY

TORONTO, ONTARIO

OCTOBER 2021

© SABOUR BARAY, 2021

ABSTRACT

Methane is a significant greenhouse gas with 25–32 times the global warming potential of carbon dioxide. Global sources and sinks of methane are understood to be $550 \pm 60 \text{ Tg a}^{-1}$. The possible causes of changing decadal trends in atmospheric methane concentrations since the 1990's is not well understood, since this requires a precision in global emissions quantification better than 20 Tg a^{-1} . Atmospheric observations at the local, regional, or national scale can provide “top-down” constraints on emissions to verify “bottom-up” emissions that may not be well characterized. Cavity ring down spectroscopy (CRDS) instruments deliver highly precise in-situ measurements of methane, with 1 Hz precision better than 2 ppb. A comprehensive aircraft campaign in the Athabasca Oil Sands Region of Alberta (AOSR) in summer 2013, led by Environment and Climate Change Canada (ECCC), deployed a CRDS alongside a suite of instrumentation to measure atmospheric pollutants and meteorological parameters. These observations allowed for the comprehensive identification and quantification of methane emissions from unconventional oil extraction. Emissions estimates were 48% higher than those reported in the national greenhouse gas inventory. A series of lower cost follow up campaigns in 2014 and 2017 using a CRDS instrument mobilized with a vehicle allowed for cold season monitoring of emissions and select quantification where atmospheric parameters were favorable, showing continued discrepancies with inventory reporting. To estimate emissions across Canada at the national scale, methane measurements from ECCC long-term monitoring stations over 2010-2015 were utilized in conjunction with satellite remote sensing observations from the Greenhouse Gas Observing Satellite (GOSAT) operated by the Japanese Aerospace Agency (JAXA). These atmospheric observations were assimilated in the GEOS-Chem chemical transport model to constrain emissions using a Bayesian inverse modelling methodology. Results showed 42% higher emissions from anthropogenic sources and 21% lower emissions from natural sources, which are mostly wetlands, when compared to the prior estimate. Through the combinations of all studies presented herein, approximately $2\text{--}4 \text{ Tg a}^{-1}$ of methane emissions in Canada were reallocated for the year of 2013, where $1\text{--}3 \text{ Tg a}^{-1}$ was added to anthropogenic sources and $2\text{--}4 \text{ Tg a}^{-1}$ was deducted from natural sources, which is substantial relative to the anthropogenic

inventory in Canada which is 4–5 Tg a⁻¹. This reallocation is 0.4–0.8% of the entire global budget of 550 Tg a⁻¹, where only a ~3% change in the source-sink balance can cause the observed trends in atmospheric methane. These results show that atmospheric observations from surface, aircraft and satellites are critical for constraining the methane budget in Canada, and improvements are necessary to these types of atmospheric observations over the world to constrain the methane cycle within the precision needed to understand decadal trends.

ACKNOWLEDGEMENTS

This work was made possible through support from a community of scientists and teachers. First and foremost, I thank my supervisor, Robert McLaren. Every opportunity that I was given for my development as a scientist began with his support. He shared with me an enthusiasm for atmospheric chemistry, taught me the fundamentals of scientific research, and gave me freedom in my studies to pursue my interests. I could not have asked for a better advisor. I thank my committee members, Mark Gordon, Cora Young, John Liggio, and former committee members Shao-Meng Li and Jochen Rudolph for their valuable discussions on this work.

I am grateful to members of the Environment and Climate Change Canada Air Quality and Climate Chemistry Research Divisions for providing the data used in this work. Thank you to the JOSM team members for accomplishing the Oil Sands campaigns, especially Katherine Hayden and Ralf Staebler.

I am grateful to Daniel Jacob for welcoming me into his Atmospheric Chemistry Modeling Group at Harvard University for 5 months of my PhD, which developed my keen interest in modelling, data assimilation and satellite observations. I thank Dylan Jones for being my teacher in inverse methods, welcoming me as a pseudo-member of his group at the University of Toronto, and giving me a valuable local hub of the data assimilation and modelling community.

I am grateful to the members of the Centre for Atmospheric Chemistry at York University. Thank you to Carol Weldon for the years of administrative support she provided to us graduate students. Thank you to the fellow students I've had the pleasure of working with, especially Csilla Csukat and Zoe Davis.

Finally, I thank my parents for raising me to be a lifelong student of knowledge. I thank my siblings and the rest of my family who have always made science and math great fun. For me, that is all it has been.

TABLE OF CONTENTS

ABSTRACT	ii
ACKNOWLEDGEMENTS	iv
TABLE OF CONTENTS	v
LIST OF TABLES	ix
LIST OF FIGURES	xi
LIST OF SYMBOLS AND ABBREVIATIONS	xx
Chapter 1 Introduction to atmospheric measurements of methane	1
1.1 The Earth’s methane cycle	1
1.2 Atmospheric measurements of methane.....	9
1.2.1 Theoretical background of spectroscopy and methane.....	9
1.2.2 In-situ measurements	11
1.2.3 Satellite observations	13
1.3 Estimating emissions using atmospheric measurements	14
1.3.1 Comparison of bottom-up and top-down methods	14
1.3.2 Experimental methods	15
1.3.3 Modelling methods	19
1.4 Scientific objectives and structure of the dissertation	23
References	26
Chapter 2 Quantification of methane sources in the Athabasca Oil Sands Region of Alberta by aircraft mass-balance	32
Author Contributions.....	32
Abstract.....	33
2.1 Introduction	34
2.2 Experimental.....	37
2.2.1 Instrumentation	37

2.2.2 Aircraft flights.....	38
2.2.3 Mass balance approaches for determining CH ₄ emissions	40
2.3 Results and discussion.....	44
2.3.1 Identification of sources of CH ₄	44
2.3.2 Quantification of CH ₄ emission rates from sources.....	51
2.3.3 Emission rates of CH ₄ from AOSR facilities.....	59
2.3.4 Comparison to emission inventories.....	62
2.4 Conclusions	65
Acknowledgements	66
References	68
Chapter 3 Cold season methane emissions estimated in the Athabasca Oil Sands Region of Alberta using mobile surface measurements.....	74
Author Contributions.....	74
Abstract.....	75
3.1 Introduction	76
3.2 Data and methods	81
3.2.1 Description of measurements.....	81
3.2.2 Mobile Surface Mass Balance Approach (MSMB).....	82
3.3 Results and discussion.....	84
3.3.1 CH ₄ measurements downwind of tailings ponds during cold seasons.....	84
3.3.2 Measurements of transient CH ₄ leaks.....	88
3.3.3 Emissions estimates using MSMB	91
3.3.4 Comparison between top-down and bottom-up estimates.....	103
3.4 Conclusions	107
Acknowledgements	108
Conflict of interest.....	108
References	109

Chapter 4 Estimating 2010-2015 anthropogenic and natural methane emissions in Canada using ECCC surface and GOSAT satellite observations.....	112
Author Contributions.....	112
Abstract.....	113
4.1 Introduction	114
4.2 Data and methods	116
4.2.1 Observations	117
4.2.2 Forward Model	120
4.2.3 Inverse Model Methodology.....	124
4.3 Results and discussion.....	128
4.3.1 Evaluation of WetCHARTS extended ensemble for wetland emissions in Canada	128
4.3.2 Comparative Analysis of Inversions using ECCC in situ and GOSAT Satellite Data	134
4.3.3 Joint inversions combining ECCC in situ and GOSAT satellite data.....	140
4.3.4 Comparison to independent aircraft and in situ data	145
4.4 Conclusions	148
Competing Interests.....	151
Data Availability	151
Acknowledgements	151
References	152
Chapter 5 Surveying urban methane emissions in the Greater Toronto Area using mobile surface measurements	157
Abstract.....	158
5.1 Introduction	159
5.2 Data and Methods.....	161
5.2.1 Description of Measurements	161
5.2.2 Determination of Vehicle Emissions Factors	163
5.3 Results and Discussion.....	163

5.3.1 Measurements of On-Road Vehicle Methane.....	163
5.3.2 Mobile Survey of GTA Methane	169
5.4 Conclusions	173
References	175
Chapter 6 Conclusions.....	178
Appendices.....	183
Appendix A: Supplement to Quantification of methane sources in the Athabasca Oil Sands Region of Alberta by aircraft mass balance	183
A.1 Assessment of Uncertainties	183
A.2 Meteorological Conditions.....	184
Appendix B: Supplement to Cold season methane emissions estimated in the Athabasca Oil Sands Region of Alberta using mobile surface measurements	195
B.1 Analysis of winds.....	195
B.2 Sensitivity analysis of mass balance emissions rate calculations	210
Supplement references	211
Appendix C: Supplement to Estimating 2010-2015 anthropogenic and natural methane emissions in Canada using ECCC surface and GOSAT satellite observations	212
C.1 Monthly GOSAT Data in the Canadian Domain	212
C.2 Sensitivity of Seasonal Emissions to Climatological Data	213
C.3 Evaluation of bias in the global model.....	215
C.4 Diagnostics of Sectoral and Provincial Inversions.....	229
C.5 Combined ECCC+GOSAT Monthly Inversion	238
Supplement References.....	240

LIST OF TABLES

Table 1.1: Global methane budget from 2003-2012 adapted from Saunio et al. (2016). Emissions are in Tg a^{-1} , the mean value is reported with the range in square brackets. The top-down column values are emissions that are constrained by atmospheric measurements, and the bottom-up column values are from process-based inventory estimates. 4

Table 2.1: Enhancements of $\Delta\text{C}_2\text{H}_6$ from canister measurements overlapping with CH_4 plumes across three flights (Aug 14, Aug 16 and Sep 02). Mean enhanced ΔCH_4 is shown over the course of ~20s canister sampling times with ethane-to-methane ratios (EMRs) computed..... 51

Table 2.2: Comparison of emissions rates (in tonnes $\text{CH}_4 \text{ hr}^{-1}$) determined from the screen approach (n estimates per facility), the box-approach (n estimates per facility), and the uncertainty weighted average for each method and facility. The 5-facility AOSR total is show in the final column and row. 61

Table 3.1 Estimated atmospheric conditions and transport time for plume transects. 93

Table 3.2 Meteorological data used for the calculation of $3t^*$ and PG atmospheric stability class for each transect. 94

Table 4.1: Descriptive list of ECCC in situ observation sites used in the analysis. 118

Table 4.2: Mean 2010–2015 prior estimates of Canadian methane emissions used in GEOS-Chem arranged according to categories in the National Inventory (Environment and Climate Change Canada, 2017). 122

Table 5.1: Fuel-based emissions factors for mobile combustion sources in Canada (Environment and Climate Change Canada, 2017)..... 160

Table 5.2: List of on-road measurement locations for the October 2014 field study..... 162

Table 5.3: Tailpipe emissions factors from individual vehicle experiments..... 169

Table 5.4: Comparison of natural gas leaks as a function of road driven in different North American urban centers..... 173

Table A.1-6: Top: Sensitivity analysis displaying uncertainty contributions shown in percent change from the best-estimate emissions rate, added in quadrature for totals. Uncertainties in individual plumes are noted with superscripts for tailings ponds (t), mines (m) and facility/other (f). Screen estimates using an overlapping subset of downwind measurements from a box flight of the same day are shown with an asterisk (*). Middle: List of emissions rates for source categories and facility totals in tonnes CH_4 per hour (tonnes hr^{-1}). Bottom: Various aircraft flight details and meteorological parameters..... 185

Table B.1: Locations, elevation, and altitudes of measurements of the wind measurement stations from WBEA. *NA = instrument type is not known.	197
Table B.2 Transect average of wind-speed within the PBL for Mar 28 and Mar 31 2017 plumes. Instrumental uncertainty is the manufacturer reported uncertainty of the WindRass instrument (Table B.1). Interpolation uncertainty is the root-mean square error of the power-law fit to the vertical profile of wind-speed from 0–310 m (Fig. B.5).	201
Table B.3 Transect average of wind-direction from measurements 0–310 m above surface level for Mar 28 and Mar 31 2017 plumes. Instrumental uncertainty is the manufacturer reported uncertainty of the WindRass instrument (Table B.1).	201
Table B.4 Linear Regression Statistics for correlation between Mannix and WindRass wind-speeds at comparable altitudes above the local surface and above sea-level for March 2017. Note that N=2800, the 5-minute Mannix data was vector averaged into the 15-minute time intervals of the WindRass data, the Mannix data was the y-data and that the y-intercept was set to zero.	202
Table B.5 Circular regression statistics for correlation between Mannix and WindRass Wind-Directions at comparable altitudes above the local surface and above sea-level for March 2017. Note that N=2800, the 5-minute Mannix data was vector averaged into the 15-minute time intervals of the WindRass data, and the Mannix data was the y-data. The statistics were calculated using the Circular Statistics Toolbox in MATLAB (Berens, 2009).	203
Table B.6 Power-Law Exponents (PLI) for Urban and Rural Wind Profiles (EPA, 2000).....	208
Table B.7 Sensitivity analysis for the four experimental transects on Mar 28 2017 and Mar 31 2017	210
Table C.1 Climatological sites used for air temperature and total precipitation measurements for the seasonality comparison.	214
Table C.2 Mean annual model-measurement differences at background sites ESP and ALT.	218
Table C.3 Sensitivity test against independent observations.....	236
Table C.4 Sensitivity analysis of the Sectoral (5 state vector) inversion. The error estimates from the posterior error covariance matrix are compared to the yearly variance and the change in emissions using alternative observation vectors.	237
Table C.5 Sensitivity analysis of the Provincial (16 state vector) inversion. As per S4 error estimates from the posterior error covariance matrix are compared to the yearly variance and the change in emissions using alternative observation vectors.	238

LIST OF FIGURES

Figure 1.1: 800,000-year history of methane in the Earth’s atmosphere. The blue line shows data from ice core samples taken at EPICA Dome C, Antarctica (Loulergue et al., 2008), the green line shows data from ice core samples taken at Law Dome, Antarctica (Etheridge et al., 1998), and the red line shows data from flask samples taken at Mauna Loa, Hawaii (Dlugokencky et al., 1995)..... 2

Figure 1.2: Time series of flask methane measurements at Mauna Loa, Hawaii from 1983–2020 (c/o Ed Dlugokencky, NOAA/GML (gml.noaa.gov/ccgg/trends_ch4/)). The red line shows the monthly mean measurements from hourly flask samples, and the black line shows the de-seasonalized annual mean. 8

Figure 1.3: Optical depths of CH₄, CO₂, H₂O, N₂O and CO in the 1500–2500 nm SWIR spectral region from Jacob et al. (2016). The calculations are based on the US Standard Atmosphere with surface concentrations of 399 ppm CO₂, 1.9 ppm CH₄, 330 ppb N₂O, and 80 ppb CO..... 10

Figure 1.4: Schematic of a typical CRDS instrument from Maithani and Pradhan (2020). A tunable diode laser transmits light into an optical cavity with high reflectivity mirrors such that a large kilometer-scale path length is created in the instrument. The intensity of the reflected light is measured using a detector and the resulting difference in the ring-down time depends on the concentration of gas in the sample..... 12

Figure 1.5: Comparison of one year of satellite retrievals of dry-air column averaged methane (XCH₄) over the globe from three instruments in order of generation: SCIAMACHY, GOSAT, and TROPOMI. Note the color scales are shifted from 2003 to 2019 due to the change in the methane background. There are 2,127,713 observations of XCH₄ in 2003 from SCIAMACHY, 233,407 observations in 2013 from GOSAT, and 64,021,218 observations in 2019 from TROPOMI. SCIAMACHY data is shown averaged on a 0.5 × 0.5° grid for visibility, GOSAT data is left as circular pixels, and TROPOMI data is averaged on a 0.25 × 0.25° grid..... 14

Figure 2.1: Flight tracks from flights capturing emissions from SML (Aug 14, Aug 16), SUN (Aug 16, Aug 29), CNRL (Aug 20, Sep 02), SAJ (Aug 21, Sep 06 not shown), and SAU (Aug 29, Sep 06 not shown). SML and SAU are shown in blue, SUN in pink, CNRL in yellow and SAJ in dark orange..... 40

Figure 2.2: Top: Aircraft measurements of CH₄ (red), BTEX (blue) and rBC (black) from a single transect at 150 m agl downwind of SML and SUN on Aug 16. Four plumes are labelled A (SML Mine), B (SML Tailings), C (SUN Tailings), D (SUN Mine). Bottom: CH₄ mixing ratios along the 150 m agl transect for the above time

series. Each data point is color coded for CH₄ mixing ratio as well as instantaneous wind vector measured on the aircraft at that location. Red arrows indicate air parcel back-trajectories based on linear back extrapolation of the aircraft measured wind vectors at plume centres, with end points at 100 min (A), and 20 min (B-D). 46

Figure 2.3: Top: Aircraft measurements of CH₄ (red), BTEX (blue) and rBC (black) from single transect ~150 m agl downwind of CNRL. Plume A (CNRL Tailings Pond), Plume B (CNRL Mine) Plume C CNRL Facility. Bottom: CH₄ mixing ratios along 150 m agl transect for above time series. Each data point is color coded for CH₄ mixing ratio as well as instantaneous wind vector measured on the aircraft at that location. Red arrows show back-trajectories based on linear extrapolation of measured wind speed and direction. 49

Figure 2.4: Interpolated CH₄ mixing ratios for the Aug 14 box flight surrounding SML..... 53

Figure 2.5: Curtain plots showing interpolated CH₄, BTEX, NO_y, rBC and SO₂ mixing ratios for the Aug 14 box flight around SML. Red-dashed box indicates the primary plume on the North screen, yellow-dashed box indicates the secondary plume on the West screen, and black-dashed box indicates the tertiary incoming plume on the East screen. Orange dashed-circle shows the upgrader plume on the North screen. 54

Figure 2.6: Source-apportioned emissions rates of CH₄ determined by the screen mass-balance method (Eq. 2.1) for the SML, SUN, CNRL, SAJ and SAU facilities. Emissions rates are the average of three mass-balance flights for SML over two days, two flights each for SUN, SAJ and SAU on separate days, and one flight for CNRL. 56

Figure 2.7: Map image showing interpolated CH₄ mixing ratios for the Aug 16 Total Oil Sands screen. 61

Figure 2.8: Comparison of emissions rates determined for the five major facilities (SML, SAU, SUN, CNRL, SAJ) with the Total OS Screen Flight (see Fig. 2.7 for the flight track). Also shown is the CH₄ emissions taken from the Canadian GHGRP Emissions Inventory for the year 2013, scaled down from annual to hourly emissions assuming constant temporal emissions. Note that in the inventory, SML and SAU emissions are reported as a single facility, while our estimates are derived separately. 64

Figure 3.1: Map of facilities and methane emission sources in the AOSR. Facility boundaries and land disturbance shapefiles are from the Alberta Environment and Parks Oil Sands Information Portal (<http://osip.alberta.ca/>). Shaded boxes show the five main facilities: Open pit mining is shown with the orange line, the plant site locations are shown in pink, and tailings ponds are shown in white (minor) and teal (major). The two major ponds that account for >90% of methane emissions (Baray et al., 2018) are emphasized: Mildred Lake Settling Basin (MLSB) in Syncrude Mildred Lake and Pond 2/3 in Suncor..... 80

Figure 3.2: Map of CH ₄ measurements from the Fall/Winter 2014 and Winter/Spring 2017 field studies. Gray lines show the facility boundaries corresponding to Figure 3.1. Data is averaged on a 0.005° × 0.005° grid; the colour scale shows the maximum CH ₄ mixing ratio at each grid cell.	82
Figure 3.3: Mobile CH ₄ measurements from Nov 21 2014 (top panels A and B) and Mar 30 2017 (bottom panels C and D) downwind of Suncor Pond 2/3 (teal highlight). Measurements were conducted along Highway 63. The right panels show the time series corresponding to the plumes nearest P23 where maximum mixing ratios of 3.039 ppm in 2014 and 2.775 ppm in 2017 were observed.....	86
Figure 3.4: Mobile CH ₄ measurements from Nov 19 2014 (top panels A and B) and Mar 31 2017 (bottom panels C and D) downwind of Syncrude Mildred Lake Settling Basin (teal highlight). Measurements were conducted further north than Figure 3.3 along the same Highway 63. The right panels show the time series corresponding to the plumes nearest MLSB where maximum mixing ratios of 2.994 ppm in 2014 and 2.738 ppm in 2017 were observed.....	87
Figure 3.5: Mobile CH ₄ measurements from Nov 21 2014 (top panels A and B) and Mar 30 2017 (bottom panels C and D). Mixing ratios scale with the height of the yellow bars to emphasize high measurements. Time series plots are shown in log scale with base 2. Measurements show CH ₄ enhancements up to 23 ppm in 2014 near CNRL and up to 87 ppm in 2017 near SML and SUN. Note that the spikes in Panel D are due to repeat measurements of the same incident, which was observed between 13:10 MDT to 14:20 MDT as the vehicle circled the area.....	90
Figure 3.6: Mobile measurements from Mar 31 2017 showing the west-east transect 5A (Panel A) that identified a CH ₄ plume from the SUN facility downwind from open-pit mining. Panel B shows the corresponding time series of CH ₄ mixing ratios for the two repeat transects of the same plume; West-East (Transect 5A) and East-West (Transect 5B).....	95
Figure 3.7: Mar 31 2017 LIDAR profile from AMS1. Aerosol backscatter is shown in the color bar on a relative scale. The pink line shows the best estimate for the PBL height. Transects 5A/B occurred between 11:00 to 12:00 MDT.....	96
Figure 3.8: HYSPLIT backward trajectory modelling of plume origins for the Mar 31 2017 transect 5A north of SUN. Panel A shows back trajectories modelled at three plume locations: west boundary (red), maximum (blue) and east boundary (green) using two different archived meteorology products (GDAS; left two lines and NARR; right line) at two different measurement times 17:00 and 18:00 UTC. GDAS shows a small difference in the wind speed at the two times (resulting in two lines), while NARR is the same. The bottom panel shows forward dispersion modelling using	

GDAS meteorology 1 hour prior with plume origins at (a) the North Steepbank Mine and (b) Pond 2/3.	98
Figure 3.9: Emissions rates for the four repeat transects of Suncor open-pit mining emissions. Error bars are from the sensitivity analysis (Supplement B.1.4) which incorporates uncertainties in the CH ₄ measurements and background, the wind speed and direction, and the PBL height retrieval.	100
Figure 3.10: Mobile measurements from Mar 30 2017 showing the west-east transect 3 that identified a CH ₄ plume from the CNRL facility downwind from open-pit mining. Panel B shows the corresponding time series of CH ₄ mixing ratios.	102
Figure 3.11: Comparison of top-down emission rates (brown and blue bars) to GHGRP (green line and squares) for the Suncor facility. The 2013 tailings ponds and mining emissions rates are from the summer 2013 aircraft campaign (Baray et al., 2018). The 2017 tailings ponds emissions are from the summer 2017 TAPOS eddy covariance measurements (You et al., 2021), and the 2017 open-pit mining emissions are from this study using measurements from March 2017, both upscaled for the year.	106
Figure 4.1: ECCC surface (left) and GOSAT satellite (right) observations used in the inverse analysis. A descriptive list of the ECCC sites is shown in Table 4.1. GOSAT data shown is from a single year in 2013 and is filtered to the Canadian domain within 45°N–60°N latitude and 50°W–150°W longitude. There are ~600 GOSAT observations per month in this domain with a minimum Nov–Jan (112–248) and maximum Jul–Sep (872–1098), individual months are shown in the Supplement (Fig. C.1).	120
Figure 4.2: Prior estimates of anthropogenic and natural methane emissions. Colour bars are in log scale in units of kg CH ₄ km ⁻² a ⁻¹ . Most anthropogenic emissions fall under the energy category (A) which are oil and gas in the ICF inventory (Sheng et al., 2017) plus minor emissions from coal in EDGAR 4.3.2. Livestock (B) and waste (C) are from EDGAR. Natural emissions are primarily wetlands from the WetCHARTS inventory (D; Bloom et al., 2017).	123
Figure 4.3: Ensemble members from the WetCHARTS v1.0 inventory (Bloom et al., 2017) with totals for wetland methane emissions within Canada for each configuration shown in Tg CH ₄ a ⁻¹ . Ensemble members vary according to the use of three CH ₄ :C q ₁₀ temperature dependencies and two inundation extent scenarios (GLWD vs. GLOBCOVER) for 3×2=6 scenarios.	132
Figure 4.4: Time series of 2013–2015 modelled and observed methane concentrations. Monthly-mean methane from ECCC in situ observations (black) are shown and compared to six GEOS-Chem simulations differing in the use of WetCHARTS ensemble members for wetland emissions, with other emissions corresponding to	

Table 4.2. The six configurations are labelled GCXY where first digit (X=1,2,3) corresponds to the CH₄:C q₁₀ temperature dependency, which decreases the sensitivity of emissions to temperature with increasing value. The second digit (Y=3,4) corresponds to the model used for inundation extent (3 = GLWD, 4 = GLOBCOVER) where GLOBCOVER produces lower emissions in Canada. Emissions configurations are those shown in Fig. 4.3 in order of magnitude from red to purple lines, with the shaded red showing the range of concentrations. Sites are LLB, Alberta (A), ETL, Saskatchewan (B), FRA, Northern Ontario (C) and EGB, Southern Ontario (D). 133

Figure 4.5: Comparative analysis of inversion results optimizing annual total Canadian anthropogenic emissions (top) and monthly total natural emissions (bottom) in an $n = 78$ state-vector element setup. The posterior emissions determined using ECCC in situ (blue) and GOSAT satellite (green) data are compared to the prior (gray). Error bars are from the diagonal elements of the posterior error covariance matrix. 136

Figure 4.6: Mean 2010–2015 seasonal pattern of natural methane emissions in Tg month⁻¹. The annual total emissions are 14.8 Tg a⁻¹ (prior, gray), 11.6 ± 1.2 Tg a⁻¹ (posterior ECCC, blue) and 11.7 ± 1.2 Tg a⁻¹ (posterior GOSAT, green). The posterior results are within the uncertainty range provided by the WetCHARTS extended ensemble (3.9–32.4 Tg a⁻¹ for Canada). 140

Figure 4.7: Joint-inversions combining 2010–2015 ECCC in situ and GOSAT satellite data showing how the combined observing system remains limited towards resolving all Canadian sources. Inversions are done for each year and we present the six-year average with error bars showing the 1σ standard deviation of the yearly results. Hatched bars indicate sources that are not well-constrained, these are defined as state vector elements with averaging kernel sensitivities less than 0.8 which are affected by aliasing with other sources (See Supplemental Fig. C.9 and C.10). The top panel shows the sectoral inversion according to the categories in the National Inventory (Energy, Agriculture, Waste) and two natural categories (Wetlands and Other Natural). As an example, the diagnostics in Figure C.9 shows Agriculture emissions are beneath the noise and cannot be distinguished from Energy. The bottom panel shows the subnational regional inversion according to provinces (BC British Columbia, AB Alberta, SK, Saskatchewan, MB Manitoba, ON Ontario, QC Quebec) and aggregated regions (ATL Atlantic Canada, NOR Northern Territories) further subdivided according to total anthropogenic and total natural emissions. The diagnostics in Fig. C.10 show more than half of the regions are at or below the noise. For anthropogenic emissions, the best constraints are on provinces AB and ON. For natural emissions, the best constraints are on AB, SK, MB and ON. 144

Figure 4.8: Evaluation of inversion results with reduced-major axis (RMA) regressions using independent data. The top four panels show the comparison to ECCC

surface observations at Chapais and Chibougamau in Quebec, Canada and the bottom four panels show the comparison to NOAA aircraft profiles at East Trout Lake, Saskatchewan. The agreement of observations with prior simulated methane concentrations (blue) are compared to posterior concentrations using optimized emissions from the monthly inversion (green), the sectoral inversion (magenta), and the provincial inversion (orange). The coefficient of determination (R^2), slope and mean bias are shown as metrics of agreement..... 147

Figure 5.1: Time series plots of CH₄ (red), CO₂ (green) and CO (blue) measurements from three locations in the 2014 study: Highway 401/Allen road on Oct 21 (panel A), Highway 400/7 on Oct 23 (panel B), and the YorkU commuter parking garage on Oct 29 (panel C). 165

Figure 5.2: Correlation plot of CH₄ vs CO₂ for Oct 21 2014 measurements shown in Figure 5.1A..... 167

Figure 5.3: Tailpipe emissions from a cold start vehicle observed on Oct 27. Time series of CO, CO₂ and CH₄ for the small 1-minute period of enhancement (right). Correlation plots of CH₄ vs. CO₂ (top left) and CO vs. CO₂ (bottom left). 168

Figure 5.4: Mobile survey of GTA methane leaks conducted on May 18 2017. Approximately 90 kilometers of road was driven between 10:30 am to 4:30 pm local time (EDT)..... 171

Figure 5.5: Timeseries of methane measurements May 18 2017 from 10:30 am to 4:30 pm local time (EDT) corresponding to Figure 5.4. The EDF leak threshold (blue line) is defined as 10% higher than the background, and the black circles show the four measured leaks above this requirement. Measurements of the wastewater facility are highlighted in purple and not included in the leak calculations. 172

Figure A.1: Background profiles, [CH₄]_B(z), were selected from regions of the interpolated screens away from plume sources, corresponding to 2-20km spatial lengths depending on the flight paths. Error bars are the 1 σ variability within the 2-20km spatial regions of background air. Background CH₄ for the vertical regions 150-200m above ground to the surface are estimated based on extrapolations (constant or linear) from the lowest transects to the surface and included in the uncertainty analysis. The lowest 5 aircraft transects usually converged to a constant value (Box 3,5,6,7,9 left to right) or showed a small linear enhancement (Box 2,4,8) which provided best fits to the surface. 192

Figure A.2: Correlation Plots for Plumes A-D corresponding to Figure 2.2 (SML Mine, SML Tailings Pond, SUN Tailings Pond, SUN Mine). CH₄ is well correlated with tracer species NO_y, BC and BTEX for the various sources. Linear coefficients of determination (r^2) are in the range of 0.44-0.83. The lowest r^2 values are from the CH₄ vs BTEX plot for Plume C and the CH₄ vs NO_y and CH₄ vs BC plots for Plume D.

These two sources correspond to lower emissions and mixing ratios of both CH₄ and the 5 associated species. In the context of our results, this analysis confirms the correlation of CH₄ with various species as shown in Figure 2.2 which are used to spatially define plume boundaries. 193

Figure A.3: Time series plots of methane (red line) and discrete canisters samples analyzed for ethane (blue lines) corresponding to the same plumes used in Table 2.1 for the ethane/methane ratio calculations. These are a small subset of the canisters that were sampled over the aircraft campaign. These example plumes attempt to isolate known sources from the three facilities and support the conclusion that there were not any significant sources of ethane in the AOSR, in agreement with Simpson et al., 2010. 194

Figure B.1: Locations of meteorological measurement instruments and example of transect 1 from March 31st 198

Figure B.2: Vertical profiles of wind-speed (top) and wind-direction (bottom) for the transects on March 28th 199

Figure B.3: Vertical profiles of wind-speed (top) and -direction (bottom) for transects on March 31st 200

Figure B.4: Comparison of March 28th wind-speeds from different measurement locations. The altitudes in the plot legends for each location refer to altitude above surface level at the measurement location. 204

Figure B.5: Comparison of March 28th wind-directions from different measurement locations. The altitudes in the plot legends for each location refer to altitude above surface level at the measurement location. 205

Figure B.6: Comparison of March 31st wind-speeds from different measurement locations. The altitudes in the plot legends for each location refer to altitude above surface level at the measurement location. 206

Figure B.7: Comparison of March 31st wind-directions from different measurement locations. The altitudes in the plot legends for each location refer to altitude above surface level at the measurement location. 207

Figure B.8: Power law fits of average vertical profiles of wind-speed from 0-310 m above local surface level and predicted profiles using the 10 m wind-speed and the PLI for rural conditions and slightly unstable conditions in Table B.4 for March 28th (top) and March 31st (bottom). 209

Figure C.1: GOSAT observations per month in the year 2013 corresponding to Fig. 4.1 in the main text ($n=7656$ observations for the entire year). Observations are filtered to land data that is within 50°W to 150° W longitude and 45°N to 60° N latitude. 213

Figure C.2: Mean seasonal pattern of 2010-2015 methane emissions from the prior (gray), posterior constrained with ECCC data (blue), posterior constrained with

GOSAT data (green). This is compared to the seasonal pattern of monthly mean air temperature (orange, right axis) and precipitation (pink, left axis) from station measurements listed in Table C.1. Both air temperature and precipitation show an asymmetry about the July peak, with higher temperature and precipitation in the fall months than the spring..... 215

Figure C.3: Time-series comparison (left) from 2009–2015 of surface GEOS-Chem simulated methane (red) and measured in situ methane (black) at site ESP off the west coast of British Columbia. Comparison to NOAA aircraft profiles (right) from 2009–2015 at the same site using a reduced major axis (RMA) regression along with the 1:1 line (black)..... 217

Figure C.4: Sensitivity analysis of inversion results depending on the use of model background correction for surface pixels. Referred to as the monthly inversion, this approach optimizes annual total Canadian anthropogenic emissions (top) and monthly total natural emissions (bottom) in an $n = 78$ state-vector element setup. The prior emissions (gray) are compared to the posterior results using GOSAT (green), and the posterior using ECCC data with an unadjusted background (blue), ECCC data using a background adjusted according to the yearly difference at ESP (teal) and ALT (purple) from Table C.2..... 219

Figure C.5: Sensitivity analysis of inversion results depending on the inclusion of sites EGB and SBL which are sensitive to cross-border transport from the United States. Similar to Fig. C.4, the monthly inversion optimizes annual total Canadian anthropogenic emissions (top) and monthly total natural emissions (bottom) in an $n = 78$ state-vector element setup. The prior emissions (gray) are compared to the posterior results using GOSAT (green), and the posterior using ECCC data including all sites (blue) and ECCC data excluding EGB and SBL (yellow). 221

Figure C.6: Time series (left) from 2010–2015 of the difference between GEOS-Chem simulated total column methane and GOSAT observations after applying bias corrections, showing a consistent global background for methane. Data used in the inversion for Canada is from 45° N to 60° N (purple line) and shows acceptable differences within 5 ppb over the entire global latitude band. To produce the left figure, the latitude-dependent bias (right) is shown with the polynomial correction that is applied (gray dash) that is within a magnitude of 0.3 to 2.9 ppb for the same latitude. ... 224

Figure C.7: Sensitivity of 2013 posterior GOSAT constrained methane emissions to bias corrections used in the GEOS-Chem simulated total column of methane. For comparison, the prior in 2013 (gray) and the posterior in 2013 constrained by ECCC data (unadjusted, blue) are shown. The digits in the GOSAT label represent the binary use of bias corrections (1 = applied, 0 = not applied). The first digit corresponds to the use of the latitude bias correction, the second digit corresponds to the use of the

monthly bias correction, hence GOSAT11 is the base case that applies both bias corrections and GOSAT00 is the case with no bias corrections applied..... 226

Figure C.8: Model comparison to independent NOAA observations globally from 2010–2015. The top panel shows data used in the global model comparison. Red diamonds indicate NOAA surface flasks, purple circles indicate NOAA ship data, and blue lines indicate HIPPO III, IV and V aircraft data. Comparison of the prior and posterior emissions in GEOS-Chem is shown using a reduced-major axis regression against NOAA Surface flasks (bottom-left), HIPPO III, IV and V aircraft data (bottom-middle), and NOAA Ship data (bottom-right). 228

Figure C.9: Diagnostics of the sectoral inversion used to evaluate the independence and information content of the 5 state vector elements. The error-normalized posterior correlation matrix (top left) shows the correlations between elements. The averaging kernel matrix (top right) shows where the independent pieces of information are (DOFS = 3.3). The singular vector decomposition of the pre-whitened jacobian (bottom) quantifies the signal-to-noise ratio of the significant elements – these are the singular values listed above one (4 in total). The singular vector below noise (agriculture) is shown as a dashed line..... 232

Figure C.10: Similar to Fig. C.9 for the 16 state vector provincial inversion. The DOFS from the averaging kernel matrix are 7.9, which are consistent with the number of singular values greater than unity in the pre-whitened jacobian matrix (8 in total). In the bottom panel, the singular vectors below the noise (corresponding to singular values less than one) are shown as light-dashed lines, these show which emissions are not constrained by observations. 233

Figure C.11: Sensitivity analysis of the results from the monthly inversion including a comparison to the combined ECCC+GOSAT inversion. Following Fig. 4.4 in the main text, the monthly inversion optimizes annual total Canadian anthropogenic emissions (top) and monthly total natural emissions (bottom) in an $n = 78$ state-vector element setup. The prior emissions (gray) are compared to the posterior results using GOSAT (green), and the posterior combining both ECCC and GOSAT data (purple). ... 239

LIST OF SYMBOLS AND ABBREVIATIONS

agl	Above ground level
AOSR	Athabasca Oil Sands Region
ASL	Above sea level
CH₄	Methane
CNRL	Canadian National Resources Limited Horizon
CO	Carbon monoxide
CO₂	Carbon dioxide
CRDS	Cavity ring-down spectroscopy
CTM	Chemical transport model
DOFS	Degrees of freedom for signal
ECCE	Environment and Climate Change Canada
EDGAR	Emission Database for Global Atmospheric Research
ESRL	Earth System Research Laboratory
GEOS	Geostationary Operational Environmental Satellites
GHG	Greenhouse gas
GHGRP	Greenhouse gas reporting program
GOSAT	Greenhouse Gases Observing Satellite
GTA	Greater Toronto Area
H₂O	Water
HCHO	Formaldehyde
HIPPO	HIAPER pole-to-pole observations
HITRAN	High-resolution transmission molecular absorption database
HYSPLIT	Hybrid single-particle Lagrangian integrated trajectory model
IKL	Imperial Kears Lake
IPCC	Intergovernmental Panel on Climate Change

JOSM	Joint Oil Sands Monitoring
LIDAR	Light detection and ranging
MLSB	Mildred Lake Settling Basin
MSMB	Mobile-surface mass balance
NASA	National Aeronautics and Space Administration
NCEP	National Centers for Environmental Prediction
NIR	Near-infrared
NIST	National Institute and Standards Technology
NOAA	National Oceanic and Atmospheric Administration
NO_x	Nitrogen oxides (NO ₂ + NO)
OCO-2	Orbiting Carbon Observatory 2
OH	Hydroxyl radical
OI	Optimal interpolation
OSSE	Observing System Simulation Experiment
PBL	Planetary boundary layer
PDF	Probability density function
ppbv	Parts per billion volume
ppmv	Parts per million volume
rBC	Refractory black carbon
RF	Radiative forcing
RT	Radiative transfer
SAJ	Shell Albian Muskeg River and Jackpine
SAU	Syncrude Aurora
SCIAMACHY	Scanning Imaging Absorption Spectrometer for Atmospheric Cartography
SML	Syncrude Mildred Lake
SO₂	Sulfur dioxide
SRON	Netherlands Institute for Space Research
STILT	Stochastic time-inverted Lagrangian transport model

SUN	Suncor Energy OSG
SWIR	Shortwave infrared
SYN	Syncrude Canada Limited
TANSO-FTS	Thermal and near-infrared sensor for carbon observation Fourier transport spectrometer
TCCON	Total carbon column observing network
TERRA	Top-down emissions rate retrieval algorithm
TES	Tropospheric Emission Spectrometer
TIR	Thermal infrared
TROPOMI	TROPOspheric Monitoring Instrument
UNFCCC	United Nations Framework Convention on Climate Change
UoL	University of Leicester
UV	Ultraviolet
VOC	Volatile organic compound
WBEA	Wood Buffalo Environmental Association
XCH₄	Column-averaged methane

I was born not knowing and have had only a little time to change that here and there.

~Richard Feynman

Chapter 1 Introduction to atmospheric measurements of methane

1.1 The Earth's methane cycle

Methane (CH_4) is the simplest organic molecule in the universe. It originates through chemical processing of solar nebulae and is present on several planets and their moons in the solar system, including Mars, Jupiter, Saturn (especially on its moon Titan; Tobie et al., 2006), Uranus and Neptune. On Earth, methane is cycled through the atmosphere, primarily produced through biological activity, and removed through oxidation chemistry (Prather et al., 2012). For this reason, suspicious observations of methane cycles on Mars (Webster et al., 2018) have caused a stir of curiosity about extraplanetary life, although this could be due to an abiotic geological mechanism. While methane does not necessarily indicate the presence of biological life, on Earth it is certainly true that biological life necessitates the presence of methane.

The history of methane on Earth can be investigated through laboratory measurements of trapped bubbles in ice core samples from Antarctica. Figure 1.1 shows an 800,000-year history of methane in the Earth's atmosphere adapted from Etheridge et al. (1998) and Loulergue et al. (2008). In this method, trapped bubbles are samples of the historical atmosphere and the depth of the drilled ice is related to the age of the sample. The relationship between the depth of ice and the age is determined using snow accumulation and mechanical flow models or using other independent markers which include radionuclide measurements (Parrenin et al., 2007). The historical average mixing ratio from 800,000 BCE to 1800 CE is 520 ppb. From 1800 CE to 2021 CE, the mixing ratio has abruptly increased to nearly 1900 ppb today, coinciding with the transition into the industrial age, the extensive use of fossil fuel combustion to power the modern world, and large-scale agricultural domestication.

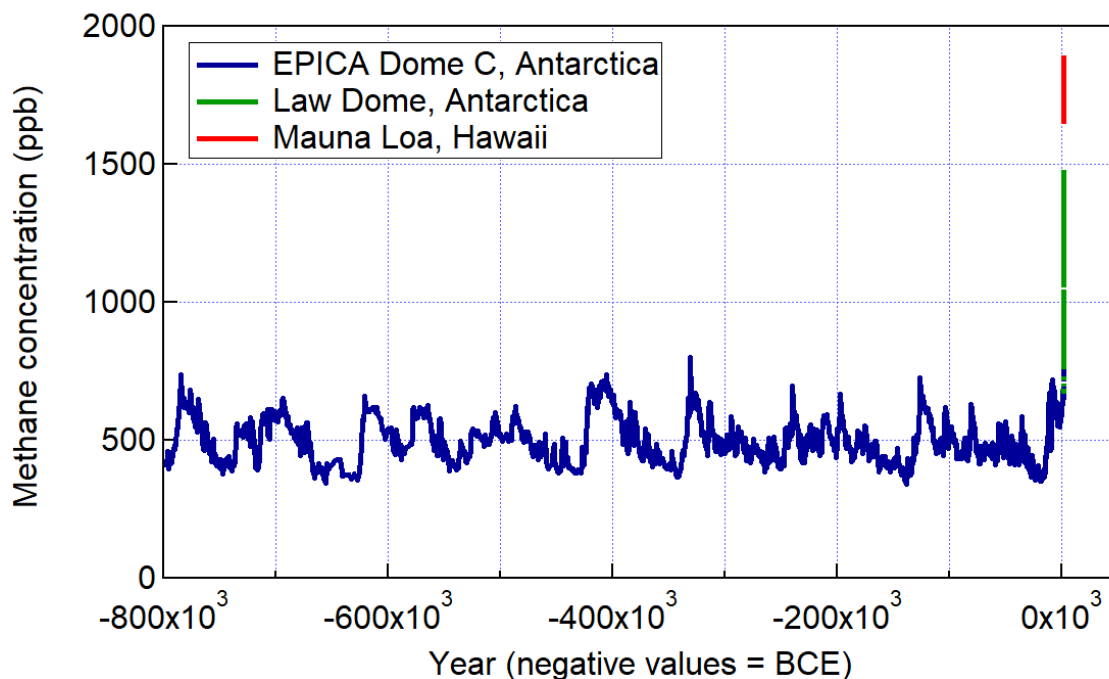


Figure 1.1: 800,000-year history of methane in the Earth’s atmosphere. The blue line shows data from ice core samples taken at EPICA Dome C, Antarctica (Loulergue et al., 2008), the green line shows data from ice core samples taken at Law Dome, Antarctica (Etheridge et al., 1998), and the red line shows data from flask samples taken at Mauna Loa, Hawaii (Dlugokencky et al., 1995).

Anthropogenic activities continue to influence the change in atmospheric methane. Table 1.1 shows the global methane budget adapted from Saunio et al. (2016). Global methane emissions are 540–568 Tg a⁻¹ in the “top-down” column, which are emissions constrained by atmospheric measurements. Anthropogenic emissions are from fossil fuels (105 Tg a⁻¹), biomass burning (34 Tg a⁻¹), and agriculture and waste (195 Tg a⁻¹) which includes enteric fermentation and manure, rice cultivation, landfills and wastewater treatment, and other minor sources. Natural emissions are dominated by wetlands (167 Tg a⁻¹), in addition to natural sources (64 Tg a⁻¹) from geological seeps, freshwater lakes, termites, wildfires and other minor sources. The primary sink of methane is oxidation by the hydroxyl radical OH throughout the entire atmosphere (Jacob, 1999) which results in a lifetime of 9.1 ± 0.9 years (Prather et al., 2012). The total chemical loss of methane (515 Tg a⁻¹) includes a minor sink from oxidation by the chlorine radical Cl, which is

in addition to a terrestrial sink from soil absorption (33 Tg a^{-1}). This results in a source-sink imbalance of $+10 \text{ Tg a}^{-1}$ and an atmospheric growth rate of 10.0 ppb a^{-1} . From this summary we see that present-day anthropogenic activities are $\sim 60\%$ of the global methane budget, which explains the abrupt change shown in Figure 1.1 from the 800,000-year pattern.

Table 1.1: Global methane budget from 2003-2012 adapted from Saunio et al. (2016).

Emissions are in Tg a⁻¹, the mean value is reported with the range in square brackets. The top-down column values are emissions that are constrained by atmospheric measurements, and the bottom-up column values are from process-based inventory estimates.

	Top-down	Bottom-up
Natural sources	231 [194–296]	384 [257–524]
Wetlands	167 [127–202]	185 [153–227]
Other natural sources	64 [21–132]	199 [104–297]
Fresh waters		122 [60–180]
Geological seeps (onshore)		40 [30–56]
Geological seeps (offshore)		12 [5–20]
Wild animals		10 [5–15]
Termites		9 [3–15]
Wildfires		3 [1–5]
Permafrost soils		1 [0–1]
Other (incl. hydrates)		2 [0–5]
Anthropogenic sources	328 [259–370]	352 [340–360]
Agriculture and waste	195 [178–206]	188 [115–243]
Enteric fermentation & manure		106 [97–111]
Landfills & waste		59 [52–63]
Rice cultivation		30 [24–36]
Fossil fuels	105 [77–133]	121 [114–133]
Coal mining		41 [26–50]
Oil, gas & industry		79 [69–88]
Biomass & biofuel burning	34 [15–53]	30 [27–35]
Sinks		
Total chemical loss	515 ^a	
Soil uptake	33 [28–38]	
Sum of sources	558 [540–568]	736 [596–884]
Sum of sinks	548 ^b	
Imbalance	10 ^b	
Atmospheric growth rate	10.0 [9.4–10.6]	

^a Defined as the different between the total sink and soil uptake.

^b Not directly computed; the total sink is inferred from global mass balance.

Methane is removed from the atmosphere according to a multistep chemical oxidation to produce carbon dioxide (CO₂), with carbon monoxide (CO) and formaldehyde (HCHO) as important intermediates that have other climate and air quality consequences. The reaction with OH is initiated



where M is any molecule in the third body reaction, such as O₂ or N₂, that dissipates the energy released. The methylperoxy radical (CH₃O₂) reacts with peroxy radicals (HO₂) to produce the methylhydroperoxide (CH₃OOH) radical



CH₃OOH is oxidized to produce HCHO



HCHO is an important air quality gas and can be an abundant source of free radicals. HCHO further photodissociates or is oxidized to produce carbon monoxide (CO)



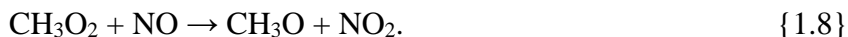
CO is relevant for air quality as it is hazardous to human health, concentrations of CO have been steadily reduced through public policy interventions (Raub et al., 2000). CO is finally oxidized to produce CO₂



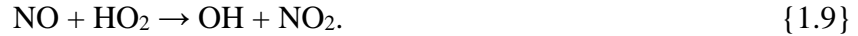
Alternatively, the minor methane sink with stratospheric Cl produces hydrochloric acid (HCl)



In addition to the reactions above, CH₄ is an important precursor of tropospheric ozone (O₃), a hazardous air pollutant, in an environment rich in nitrogen oxides (NO_x):



NO₂ is also produced with the reaction of NO and the peroxy radical HO₂



NO₂ is photolyzed to produce O₃



The reactions above show that methane is important for both air quality and climate. Methane is a major sink of tropospheric OH and influences the oxidative capacity of the atmosphere. In addition, methane is a precursor for air pollutants such as CO, HCHO, and tropospheric O₃ as well as a precursor for climate-forcing gases like CO₂ and stratospheric H₂O.

Methane's increasing mixing ratio in the atmosphere has consequences on the Earth's climate. The majority of radiation from the Sun comes in the form of visible light (380 to 700 nm), which is partially reflected by clouds and other high albedo surfaces like snow, desert sand, and ice. The rest of incoming visible radiation is absorbed by the Earth's surface which is re-emitted as blackbody radiation in the infrared spectrum. Greenhouse gases (GHGs) are molecules in the atmosphere that absorb infrared radiation and hence insulate the energy of the atmosphere by preventing the complete transmission of outgoing infrared radiation into space. The greenhouse effect on Earth is primarily due to water vapor (H₂O), followed by carbon dioxide (CO₂) and third methane. Radiative forcing is defined by the IPCC as the change in the energy budget of the Earth's atmosphere due to anthropogenic and/or natural factors of climate change, which excludes the baseline effect from water vapor unless it is changed due to a secondary mechanism (Myhre et al., 2013). Hence, methane (0.61 W m⁻²) is the second most important GHG for radiative forcing next to carbon dioxide (1.82 W m⁻²). The lower lifetime of methane compared to carbon dioxide makes methane an attractive target for climate mitigation policy, since reductions (or increases) in methane emissions will provide more immediate climate impacts. If reductions in CO₂ emissions occur too slowly to deter the more damaging impacts of climate change, near-term reductions in methane are an alternative to complex climate geoengineering strategies (Vaughan and Lenton, 2011).

On the centennial-scale, methane has been unambiguously increasing since the pre-industrial era due to increasing anthropogenic emissions. However, the causality of recent decadal trends, which are sensitive to small changes in the global budget, are more uncertain. Figure 1.2 shows

measurements of background methane at Mauna Loa, Hawaii (19.536° N, 155.576° W) from 1983 to 2020 adapted from NOAA (Dlugokencky et al., 1995). The growth rate of atmospheric methane levelled off from the 1990's to early 2000's. This hiatus continued until 2007 when methane concentrations began a renewed growth continuing to present time (Dlugokencky et al., 2009). Differing hypotheses have attempted to constrain the possible causes of these decadal trends. Associated increases with ethane have attributed recent growth to oil and gas (Hausmann et al., 2016). An increasing trend of isotopically lighter methane has been associated with increasing biogenic emissions from wetlands and agriculture (Nisbet et al., 2016), however decreasing biomass burning emissions may be masking increasing oil and gas emissions in the global isotopic ratios (Worden et al., 2017). Observations of methyl chloroform (CH_3CCl_3) suggest decreasing OH may have resulted in the renewed growth (Rigby et al., 2017; Turner et al., 2017). Causal attribution of the methane growth rate has continued to be challenging partly because a 3% source-sink imbalance, or 15–20 Tg a^{-1} , can result in the observed rate of increase.

The present-day global methane emission of $560 \pm 60 \text{ Tg a}^{-1}$ is inferred by mass balance with the global sinks (Prather et al., 2012). This ~10% uncertainty range is reasonable as an initial input for earth-system modelling; however, it is insufficient for understanding the 3% source-sink imbalance that characterizes the present-day methane growth rate (Turner et al., 2017). Furthermore, the contributions from different source sectors and countries or regions are also highly uncertain (Dlugokencky et al., 2011; Kirschke et al., 2013).

Improving constraints on national methane emissions is a requirement of successful mitigation policy (Nisbet et al., 2020). In 2021 Canada renewed its commitment to substantial methane reductions through the Global Methane Pledge alongside the United States and the European Union. The pledge commits to reducing global methane emissions by 30% below 2020 levels by 2030, which would successfully invert the methane growth rate if implemented. Canada is developing a plan to reduce oil and gas methane emissions by at least 75% below 2021 levels by 2030, which is beyond a previous 2016 pledge to reduce oil and gas emissions by 40–45% by 2025 from 2021 levels (Government of Canada, 2021). However, uncertainties regarding national methane emissions confound the ability to verify baseline emissions and monitor reductions. Numerous studies in Canada have shown divergence between emissions reported in

the inventory and emissions derived by atmospheric measurements, especially from oil and gas emissions in Western Canada (Atherton et al., 2017; Johnson et al., 2017; Maasackers et al., 2019; Chan et al., 2020), but may include waste emissions from urban cores such as the Greater Toronto Area (Ars et al., 2020). These uncertainties in anthropogenic sources are further complicated by much larger overlapping natural emissions from wetlands that are also highly uncertain (Miller et al., 2016). The following sections illustrate how atmospheric measurements and their applications in emissions rate retrieval methods address the need to better characterize methane emissions.

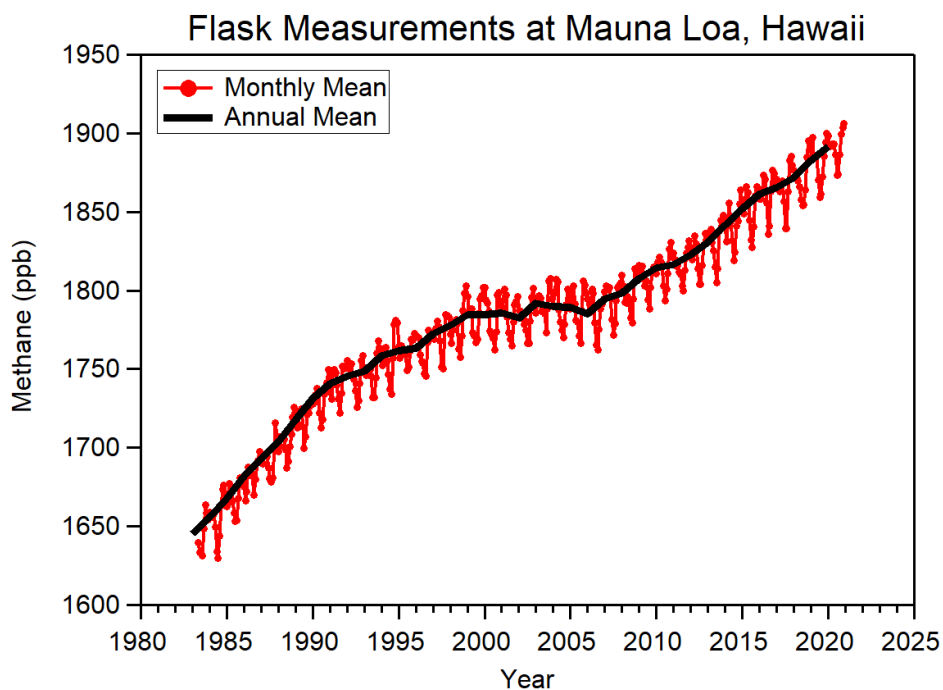


Figure 1.2: Time series of flask methane measurements at Mauna Loa, Hawaii from 1983–2020 (c/o Ed Dlugokencky, NOAA/GML (gml.noaa.gov/ccgg/trends_ch4/)). The red line shows the monthly mean measurements from hourly flask samples, and the black line shows the de-seasonalized annual mean.

1.2 Atmospheric measurements of methane

1.2.1 Theoretical background of spectroscopy and methane

Atmospheric measurements provide information on the distribution and change in concentrations of chemical species; this knowledge provides constraints on the processes responsible for the observed spatial and temporal patterns. Spectroscopy is the study of how molecules interact in specificity with wavelengths of light. Molecules absorb energy according to transitions in their translational, rotational, and vibrational motion or their electronic energy state. These molecular transitions produce spectral lines that can be the targets of instrument design. The difference in observed intensity at spectral lines after light has travelled through a path containing the substance is related to the concentration according to Beer-Lambert's Law. The path travelled by light can be contained within an in-situ instrument that actively produces artificial light using a laser source, or the path can include the entire atmosphere with an instrument that passively collects solar backscatter radiation. In the case of instruments with large path lengths, interference due to Rayleigh scattering by air molecules and Mie scattering by aerosols affects the measured radiances, so retrieval algorithms are designed to account for these effects.

Methane is a tetrahedral molecule of the form XY_4 and is readily observed using a variety of techniques due to its absorption properties in the infrared spectral range. Its vibrational transitions are the most relevant for the infrared region and are always coupled with rotational transitions. GHGs tend to be polar molecules because the absorption and emission of an infrared photon corresponds to a transition in the energy state of the molecular dipole. While methane is a symmetric molecule and does not have a permanent dipole, vibrational transitions create changes in the dipole moments which give rise to vibration-rotational transitions. In addition to the fundamental vibrational bands, methane has several lower intensity overtone and combination bands which account for spectral peaks outside of the normal modes.

Figure 1.3 shows the optical depth of CH_4 in the 1500–2500 nm short wave infrared (SWIR) spectral region, and is compared to CO_2 , CO , H_2O and N_2O (adapted from Jacob et al., 2016). The line-by-line absorption spectra are from the High-resolution TRANsmission molecular

absorption (HITRAN 2016) database (Gordon et al., 2017), which is smoothed to a spectral resolution of 0.1 nm. Commercially available in-situ instruments that deploy telecom-industry lasers typically target the 1.65 μm band for simultaneous CH_4 , CO_2 and H_2O measurement or the 2.3 μm band to include CO measurements, although other spectral regions are feasible. In the case of satellites, all solar backscatter instruments have exclusively operated in either the 1.65 μm or 2.3 μm region. For space-based observations, while the 2.3 μm band is stronger and allows for simultaneous retrieval of CO, solar radiation is 3 times weaker at 2.3 μm than at 1.65 μm , and the 1.65 μm band has the advantage of simultaneous CO_2 retrieval which is used in proxy algorithms that use CO_2 (Parquet et al., 2011). Hence the strategy of the spectroscopic approach can be customized for the objectives of the observations and their viewing placement from Earth to space.

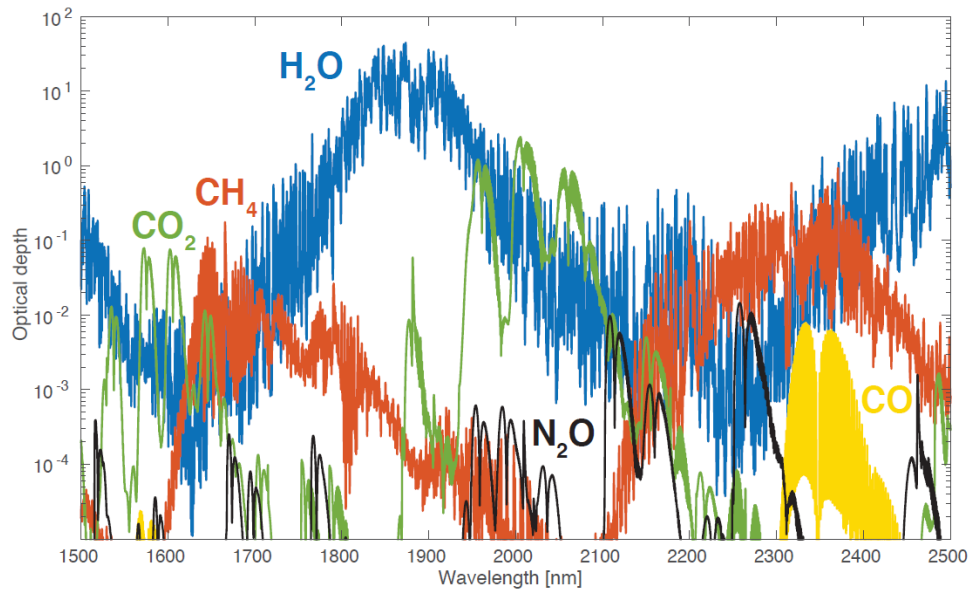


Figure 1.3: Optical depths of CH_4 , CO_2 , H_2O , N_2O and CO in the 1500–2500 nm SWIR spectral region from Jacob et al. (2016). The calculations are based on the US Standard Atmosphere with surface concentrations of 399 ppm CO_2 , 1.9 ppm CH_4 , 330 ppb N_2O , and 80 ppb CO.

1.2.2 In-situ measurements

Historically, methane has been measured using flame-ionization gas chromatography (Dlugokencky et al., 1995). When automated with an in-situ sampling approach, this method produced quasi-continuous data at 60 samples per day. An alternative sampling strategy is discrete sampling of the atmosphere into pre-flushed flasks. This method requires a record of the time and location of the sample, such as the programmable flask sampling used by NOAA (Turnbull et al., 2012), which are later brought for laboratory analysis. While flask sampling is much lower frequency it has been useful for long term, weekly sampling of the atmosphere and for mobile measurements (such as by aircraft) where delicate instruments could not be readily mobilized. In Canada, both quasi-continuous and discrete methods have been used in long-term monitoring at a network of stations, such as the northernmost station, Alert, Nunavut (82.45°N, 62.51°W). This site is managed by Environment and Climate Change Canada (ECCC) and has been collecting data from 1985 to present time as part of the global sampling network.

In the last decade, in-situ measurements for methane have rapidly advanced due to improvements in the precision and mobility of commercially available spectroscopic instrumentation. The improvement of spectroscopic techniques, and in particular cavity ring-down spectroscopy (CRDS), have allowed for high-frequency (0.5–1.0 Hz), high-precision (<5 ppb) instrumentation to be deployed in field studies (Maithani and Pradhan, 2020). The use of CRDS instruments have expanded the spatial coverage that long-term monitoring stations have provided (Ishizawa et al., 2019), and these measurements have allowed for the deployment of surface-vehicle, ship, or aircraft measurements in novel regional studies. Figure 1.4 shows the schematic for a typical CRDS instrument. A tunable telecom-industry laser in the SWIR is used and the beam is reflected against very high reflectivity (>99.99%) mirrors to create a large path length of several kilometers within the instrument before reaching a detector. The CRDS method experimentally measures the rate of decay of light in time which differs from traditional absorption spectroscopy that measures small changes in intensities due to the presence of a sample. The ‘ring-down’ time is the time it takes for the signal to drop with and without a sample, to calculate the concentration of methane in the cavity (Wheeler et al., 1998)

$$I(t) = I_0 \exp\left\{-\frac{t}{\tau} - \alpha ct\right\} \quad \{1.11\}$$

where $I(t)$ is the time dependent t decay of initial light intensity I_0 , and c is the speed of light. The molecular absorption coefficient α is in dimensions of length^{-1} such that $\alpha = \sigma C$, which is the product of the sample absorption cross-section σ and concentration C . The term $-\frac{t}{\tau}$ describes the decay of light due to cavity losses such as mirror transmission, and the term $-\alpha ct$ is the added loss of light from the presence of a sample due to molecular absorption at a specific wavelength. Here, τ is the empty cavity ring-down time, which is the time for the intensity to decay to $1/e$ of its original value. The empty ring-down time is determined from the baseline level between absorption features where $\alpha = 0$, and the sample decay rate can be determined by least-squares fitting of the decay of light intensity with time, giving concentration. This algorithm occurs in less than a second. Although the stability of the instrument is very sensitive to laser temperature, mirror alignment, and the cavity pressure and temperature conditions, CRDS instruments have been designed that are highly secure and specialized for aircraft or other turbulent measurement platforms (Karion et al., 2013; Peischl et al., 2013). Due to these high frequency and high precision measurements, CRDS instrumentation have established a standard for in-situ measurements in regional methane studies.

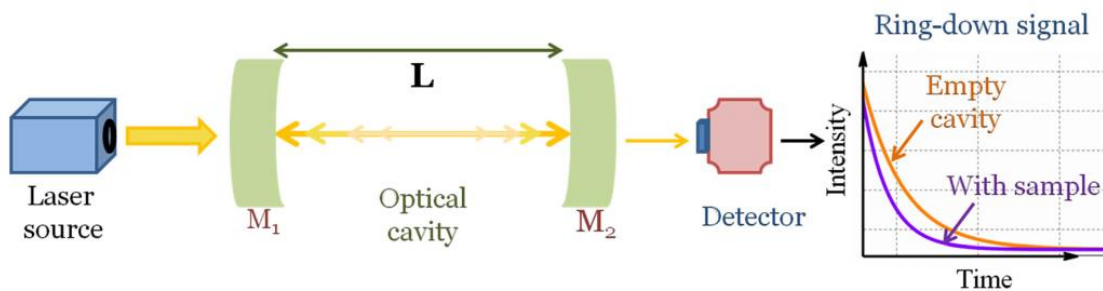


Figure 1.4: Schematic of a typical CRDS instrument from Maithani and Pradhan (2020). A tunable diode laser transmits light into an optical cavity with high reflectivity mirrors such that a large kilometer-scale path length is created in the instrument. The intensity of the reflected light is measured using a detector and the resulting difference in the ring-down time depends on the concentration of gas in the sample.

1.2.3 Satellite observations

The first satellite observations of methane from space were accomplished with the Interferometric Monitor for Greenhouse gases (IMG) thermal infrared instrument in 1996–1997 (Clerbaux et al., 2003), and measurements of total methane columns by solar backscatter began with the Scanning Imaging Absorption Spectrometer for Atmospheric Cartography (SCIAMACHY) in 2003–2012 (Frankenberg et al., 2006), although SCIAMACHY began to degrade after 2005. Thermal infrared instruments operate in the $8\mu\text{m}$ spectral range and are more sensitive to the upper troposphere than the surface, this is less ideal for constraining terrestrial emissions. Solar backscatter instruments accomplish uniform column sensitivity because they operate in the $1.65\ \mu\text{m}$ or $2.3\ \mu\text{m}$ region, this is nearly transparent to the atmosphere unless clouds interfere in the retrieval. The Greenhouse Gas Observing Satellite (GOSAT) launched in 2009 by the Japanese Aerospace Exploration Agency (JAXA) substantially improved on the precision of SCIAMACHY (from 1.5% to 0.6%) and has been highly valuable for constraining methane emissions (Parker et al., 2020). The TROPospheric MONitoring instrument (TROPOMI) launched in 2017 further improved upon GOSAT by shrinking the pixel size to $7 \times 7\ \text{km}^2$, providing full daily coverage, and matching the individual observation precision that made GOSAT useful (Hu et al., 2018). These rapid advancements in satellite instrumentation within the last two decades has inspired the phrase of a golden age for satellite observation of atmospheric gases. Figure 1.5 shows the spatial coverage of one year of SCIAMACHY, GOSAT and TROPOMI dry-air column averaged methane (XCH_4) observations. SCIAMACHY provided global coverage every 6 days with a pixel size of $30 \times 60\ \text{km}^2$. GOSAT provides repeat coverage every 3 days at cross-track pixels about 260 km apart, with a pixel size of $10 \times 10\ \text{km}^2$. The latest generation instrument TROPOMI provides full daily global coverage with a pixel size of $7 \times 7\ \text{km}^2$.

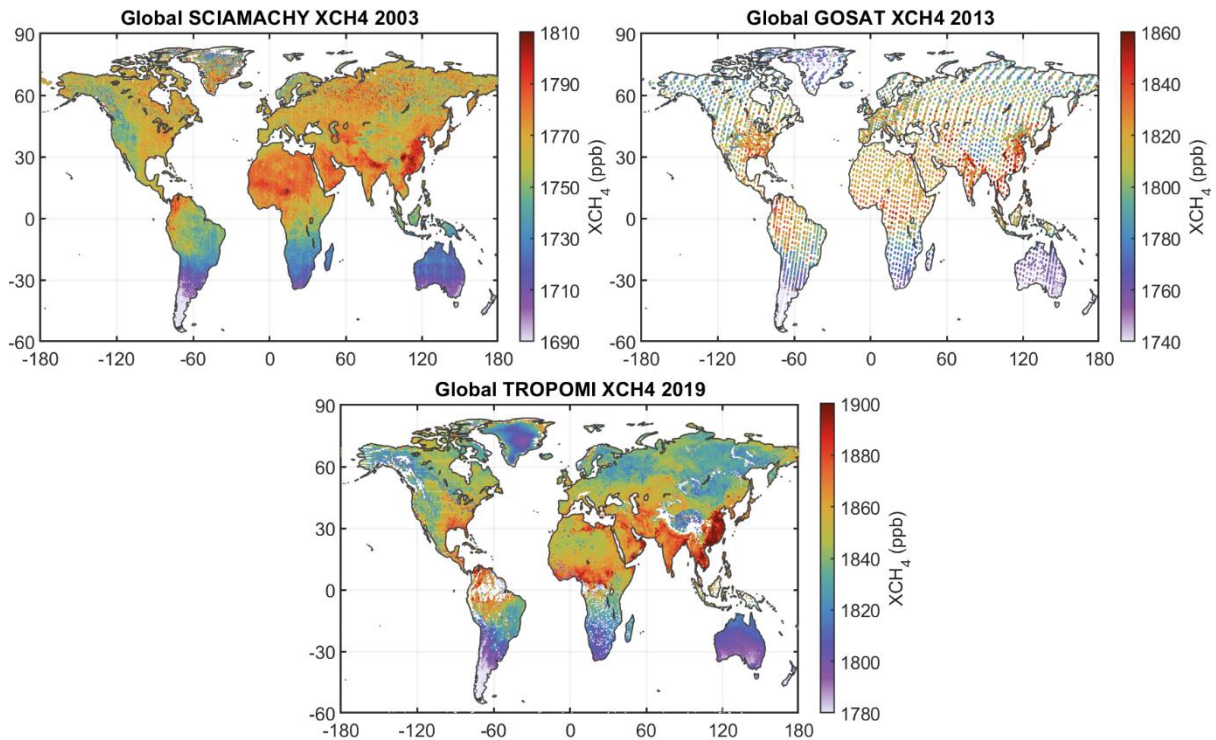


Figure 1.5: Comparison of one year of satellite retrievals of dry-air column averaged methane (XCH_4) over the globe from three instruments in order of generation: SCIAMACHY, GOSAT, and TROPOMI. Note the color scales are shifted from 2003 to 2019 due to the change in the methane background. There are 2,127,713 observations of XCH_4 in 2003 from SCIAMACHY, 233,407 observations in 2013 from GOSAT, and 64,021,218 observations in 2019 from TROPOMI. SCIAMACHY data is shown averaged on a $0.5 \times 0.5^\circ$ grid for visibility, GOSAT data is left as circular pixels, and TROPOMI data is averaged on a $0.25 \times 0.25^\circ$ grid.

1.3 Estimating emissions using atmospheric measurements

1.3.1 Comparison of bottom-up and top-down methods

Methane emissions that are used for climate policy normally rely on “bottom-up” emission inventories that depend on activity rates and emissions factors for individual source processes. For example, total emissions from enteric fermentation can be estimated by determining the emissions factor per unit of livestock. This can be scaled with activity factors by multiplying by the total number of livestock per farm for a facility total, and the number of farms in a region for

national reporting. Due to this process-based approach, bottom-up estimates that use advanced Tier 2/3 methods from the Intergovernmental Panel on Climate Change (IPCC, 2006) can provide detailed accounting for national inventories. “Top-down” methods use atmospheric observations to constrain emissions. These require an algorithm to attribute measured concentrations to emissions. Emissions can be determined based purely on the measurements themselves, which are referred to here as experimental methods, or can be determined based on a comparison to predicted concentrations from a prior model, referred to as modelling methods.

Top-down emissions are often at odds with bottom-up estimates which has generated discussion on reconciliation pathways. Disagreement between top-down and bottom-up estimates can be reflective of a flaw in the reporting practices within inventories due to: (i) emissions that are missing, (ii) under (or over) accounted for, (iii) problematic super-emitters that are not accounted for by activity factors, or (iv) errors due to the limited temporal coverage of top-down field studies (Zavala-Araiza et al., 2015). Some emissions by their nature – such as wetlands – are extraordinarily variable even at the microtopographic scale, and the linear scaling of activity factors result in large order-of-magnitude errors in Canada (Bloom et al., 2017). While IPCC Tier 2/3 methods require detailed accounting of processes, these practices do not require inventories to be published on a spatially disaggregated grid, which are needed as emissions inputs for atmospheric models. Hence many top-down studies have had to rely on the Emissions Database for Global Atmospheric Research (EDGAR) inventory (European Commission, 2011), which provide emissions spatially attributed on a global grid but is based on cruder IPCC Tier 1 methods. Studies that “remake” inventories using improved accounting are highly valuable as datasets for modelling studies (Maasakkers et al., 2016; Bloom et al., 2017; Sheng et al., 2017; Scarpelli et al., 2020).

1.3.2 Experimental methods

Experimentalist approaches to emissions rate estimations are broadly defined as those that do not rely on comparisons to atmospheric models. In these methods, measurements are used entirely on their own to derive emissions estimates. This can be accomplished based on the

design of field studies, the careful placement of measurements, and the application of retrieval algorithms.

In general, experimentalist methods are based on mass balance formulations that solve the continuity equation (Jacob, 1999). Experimental methods can also include co-released tracer studies (McLaren et al., 1996) and controlled release experiments which derive general relationships between concentrations and emissions (Maazallahi et al. 2020) which are not discussed in detail here. For mass balance methods, measurements that are placed both upwind and downwind of a specific source, or a collection of sources, can infer the emissions based on the change in methane concentrations. Since plumes have dynamic transport which changes with meteorological conditions, measurements are mobilized to scan large upwind and downwind regions to optimally characterize the plume structure. Mass balance methods can be deployed for many types of measurements provided they successfully characterize plumes; these can include mobilized-surface measurements (Atherton et al., 2017; Ars et al., 2020), aircraft measurements (Karion et al., 2013; Peischl et al., 2013; Cambaliza et al., 2014; Gordon et al., 2015) and satellite observations (Nassar et al., 2017; Varon et al., 2020). In many cases, the methane measurements are best complemented with detailed meteorological measurements to characterize surface and elevated winds and boundary layer conditions. Methane measurements can also be complimented with measurements of other chemical species that can provide confirmation of plume source origins. When mobile methane measurements provide a downwind plume cross-section, the relationship between emissions and methane measurements is described as

$$E_{adv} = \iint_{x_i, z_s}^{x_n, z_b} ([CH_4] - [CH_4]_B) \times U_{\perp} dx dz \quad \{1.12\}$$

where E_{adv} is the advective horizontal flux of methane emissions through the plane created by the measurements, $[CH_4]$ are the downwind methane measurements affected by the plume, subtracted by the upwind background measurements $[CH_4]_B$, U_{\perp} is the wind speed component through the plane, which is perpendicular to the direction of travel of the mobilized measurements. The flux (enhancement \times perpendicular wind speed) is in units of mass per area

per time, which is integrated over the entire horizontal distance x_i to x_n , from the surface z_s up to the vertical boundary layer height z_b , to retrieve emissions per unit time.

The integral in equation {1.12} assumes that the methane measurements have vertical resolution in the atmosphere. This is accomplished by aircrafts that fly transects through plumes at multiple altitudes from a low height that can be safely flown above the surface to the top of the planetary boundary layer (PBL). In the example of a surface methane plume with measurements that are sufficiently downwind for full vertical mixing to take place, then equation {1.12} can be simplified by replacing the vertical integral with a multiplication by the boundary layer height z_b

$$E_{CH} = \int_{x_i}^{x_n} ([CH_4] - [CH_4]_B) \times U_{\perp} \times z_b dx \quad \{1.13\}$$

This simplification is applied to cases where vertically resolved measurements are not available. Some algorithms have used equation {1.13} despite having full vertically resolved measurements; the purpose being to test the assumption of a well-mixed boundary layer by estimating emissions at differing-altitude transects independently, and then using the variance in the emissions estimates to derive an uncertainty of the mass balance method, which was 30–50% (Cambaliza et al., 2014). To improve the uncertainties of aircraft mass balance, Gordon et al. (2015) derived a more sophisticated formulation of equation {1.12}, by adding estimates of vertical fluxes, turbulent fluxes, and a term for the change in mass due to meteorological factors. Equation {1.12} is sometimes referred to as a simple ‘box approach’ in the literature due to the estimation of input and output fluxes – regardless of the flight formation of the aircraft measurements. However, the full formulation of the box approach that uses aircraft measurements encircling a source follows Gordon et al. (2015) as

$$E_{Box} = E_{CH} + E_{CHT} + E_{CV} + E_{CVT} + E_{CM} \quad \{1.14\}$$

where E_{Box} is the net emission rate from the sources within the box, E_{CH} is the horizontal advective flux shown in {1.12}, E_{CHT} is the horizontal turbulent flux, E_{CV} and E_{CVT} are the vertical advective and turbulent fluxes respectively, and E_{CM} is the change in CH₄ mass within the box volume due to changes in pressure and temperature. Because the box includes screens that are downwind, upwind and lateral to sources, incoming (background) and outgoing (background + source) fluxes are determined as a part of the horizontal flux terms (E_{CH} and E_{CHT}). Vertical fluxes through the box top are estimated according to the conservation of air mass within the control volume and the mixing ratio at the top edge of the box. E_{CM} is estimated according to the time derivative of the ideal gas law, based on measured changes in pressure and temperature over the flight time.

The application of mass-balance approaches is also useful for satellite observations, which can successfully characterize upwind and downwind methane concentrations from a swath of pixels overpassing in the same day. Since methane has a high background, the source emissions rates, the satellite instrument precision, and spatial coverage specifications must be high to achieve optimal signal-to-noise. Since the quality of satellite observations has been rapidly improving in the last decade, the applications of this method have also been increasing. There are various methods to derive emissions estimates from satellite observations that are generally related to mass balance, these include fitting pixel enhancements to a Gaussian plume (Nassar et al., 2017), relating the pixel enhancement itself to a source rate (Jacob et al., 2016), and integrating the mass enhancement at all the downwind pixels (Varon et al., 2018). Jacob et al. (2016) shows a simple source-pixel method can be used to relate the enhancement of a pixel of dimension W [m] containing a source to the source rate:

$$Q = \frac{UWp}{g\Omega_a} \Delta\Omega \quad \{1.15\}$$

where Q [kg s⁻¹] is the emissions rate, U [m s⁻¹] is the wind speed, p is the surface pressure, g is the acceleration of gravity, Ω_a [kg m⁻²] is the column of dry air and $\Delta\Omega$ is the mean methane pixel enhancement [kg m⁻²]. Varon et al. (2018) shows that the source-pixel method neglects

information from pixels downwind of the source, and that an integrated mass enhancement (IME) method can better use downwind information from fine-scale ($50 \times 50 \text{ m}^2$) satellite pixels.

$$Q = \frac{1}{\tau} \text{IME} = \frac{U_{eff}}{L} \text{IME} = \frac{U_{eff}}{L} \sum_{j=1}^N \Delta\Omega_j A_j \quad \{1.16\}$$

Here the source rate Q is related to the IME and the residence time of methane in the pixel τ , where $1/\tau$ is the effective wind speed U_{eff} divided by the plume size L . The IME is the sum of N downwind pixels of area A_j containing the enhancement $\Delta\Omega_j$. This approach was able to verify coal mine vents in the United States, Australia, and China ranging from 2000 to 6000 kg h^{-1} at a precision of 40–45% (Varon et al., 2020).

1.3.3 Modelling methods

Atmospheric modelling is a valuable tool used to make predictions on chemical distributions. Models are based on the state-of-the-science understanding of sources, sinks, chemistry, and transport. Measurements are a natural complement to models since simulated concentrations can be validated. The validation process can be used to revise simulation inputs and improve the predictability of the atmosphere. Models and observations are connected in this way and develop in tandem with technology over time. Observations improve with novel instrument design resulting in upgraded precision and spatial coverage. Models improve with the availability of advanced computational resources and with software engineering to better capitalize on higher processing and memory capacity. These improvements are mutually beneficial; as the quality of observations improve, the quality of models can improve with better constraints from observations, providing an improved understanding of processes and resulting in more accurate predictions of the atmosphere.

The simulation of methane in the atmosphere is relatively linear due to its long lifetime and a lack of feedback mechanisms with OH, resulting in a direct relationship with emissions that can

be constrained with observations. This contrasts with more complicated modelling of very short-lived chemical species with complex chemistry and sinks. The model can be summarized as

$$\mathbf{F}(\mathbf{x}) = \mathbf{K}\mathbf{x} + \mathbf{b} \quad \{1.17\}$$

where $\mathbf{F}(\mathbf{x})$ is the simulated concentration of methane based on the input distribution of emissions \mathbf{x} . The Jacobian matrix \mathbf{K} describes the linear, transport-based relationship between the sources and the observed concentrations, and the background \mathbf{b} is the distribution of methane existing in the atmosphere from the initial conditions. $\mathbf{F}(\mathbf{x})$ is often referred to as the *forward model*. Forward models can be used in more qualitative studies with comparisons to observations that are used to diagnose biases in the model.

The differences between modelled and observed methane concentrations can be used to derive optimized emissions according to Bayesian inference. This procedure is referred to as *inverse* modelling. Bayes' theorem gives

$$P(\mathbf{x}|\mathbf{y}) = \frac{P(\mathbf{x})P(\mathbf{y}|\mathbf{x})}{P(\mathbf{y})} \quad \{1.18\}$$

Where $P(\mathbf{x})$ and $P(\mathbf{y})$ are the probability density functions (PDFs) of the prior \mathbf{x} and the observations \mathbf{y} , $P(\mathbf{y}|\mathbf{x})$ is the observation PDF of \mathbf{y} given the true value of \mathbf{x} , and $P(\mathbf{x}|\mathbf{y})$ is the posterior PDF of \mathbf{x} given \mathbf{y} . Assuming Gaussian PDFs, the optimal estimate of emissions is the maximum of $P(\mathbf{x}|\mathbf{y})$, which is obtained by solving $\nabla_{\mathbf{x}}P(\mathbf{x}|\mathbf{y}) = 0$. This optimization problem is solved by minimizing the Bayesian cost function $J(\mathbf{x})$ (Rodgers, 2000):

$$J(\mathbf{x}) = \frac{1}{2}(\mathbf{x} - \mathbf{x}_a)^T \mathbf{S}_a^{-1}(\mathbf{x} - \mathbf{x}_a) + \frac{1}{2}(\mathbf{y} - \mathbf{F}(\mathbf{x}))^T \mathbf{S}_o^{-1}(\mathbf{y} - \mathbf{F}(\mathbf{x})) \quad \{1.19\}$$

Where \mathbf{x} (of size n) is the vector of emissions being optimized and \mathbf{x}_a is the vector of prior emissions, \mathbf{y} (of size m) is the vector of observations that is compared to the simulated concentrations $\mathbf{F}(\mathbf{x})$. \mathbf{S}_a is the prior error covariance matrix which is the uncertainty in the prior state of emissions, and \mathbf{S}_o is the observational error covariance matrix which includes both instrument and model error. The inverse problem can be solved using different data assimilation techniques (Jacob et al., 2016). The analytical solution of the cost function $dJ(\mathbf{x})/d\mathbf{x} = 0$ yields the optimal posterior solution $\hat{\mathbf{x}}$:

$$\hat{\mathbf{x}} = \mathbf{x}_a + \mathbf{S}_a \mathbf{K}^T (\mathbf{K} \mathbf{S}_a \mathbf{K}^T + \mathbf{S}_o)^{-1} (\mathbf{y} - \mathbf{K} \mathbf{x}_a) \quad \{1.20\}$$

The analytical solution provides closed-form error characterization, such that the posterior error covariance $\hat{\mathbf{S}}$ of the posterior solution $\hat{\mathbf{x}}$ is given by:

$$\hat{\mathbf{S}} = (\mathbf{K}^T \mathbf{S}_o^{-1} \mathbf{K} + \mathbf{S}_a^{-1})^{-1} \quad \{1.21\}$$

The averaging kernel matrix \mathbf{A} is used to evaluate the capability of the observations to constrain the emissions and is given by:

$$\mathbf{A} = \mathbf{I}_n - \hat{\mathbf{S}} \mathbf{S}_a^{-1} \quad \{1.22\}$$

where \mathbf{I}_n is the identity matrix of length n corresponding to the number of state vector elements. The averaging kernel matrix \mathbf{A} describes the sensitivity of the posterior solution $\hat{\mathbf{x}}$ to the true state \mathbf{x} ($\mathbf{A} = d\hat{\mathbf{x}}/d\mathbf{x}$). The trace of \mathbf{A} provides the degrees of freedom for signal (DOFS), which is the number of pieces of information of the state vector that is gained from the inversion ($\text{DOFS} \leq n$). The diagonal values of \mathbf{A} provide information on which state vector elements can be

constrained by observations above the noise, and higher DOFS closer to n correspond to better constrained sources in total.

Inverse modelling is a powerful approach to provide constraints on emissions at the local (McKain et al., 2015), regional (Wecht et al., 2014), continental (Turner et al., 2015), and global (Maasakkers et al., 2019) scales. A useful test of the posterior emissions from the inverse model is to leave some observations out of the vector \mathbf{y} , which can be used as independent validation of the optimized results. For example, suborbital surface and aircraft observations can be used to verify the results of continental inversions using GOSAT satellite data and demonstrate improved agreement (Turner et al., 2015). The challenges inherent to inverse modelling are related to the traditional assumptions of Gaussian error distributions (Maasakkers et al., 2019), assumptions related to the state vector being optimized (Heald et al., 2004) which include how transport errors are treated (Stanevich et al., 2020) and whether some sources or the OH sink is held constant (Rigby et al., 2017; Turner et al., 2017), and assumptions related to the structure of errors and correlations within the assimilated observations (Connor et al., 2016). Studies that evaluate these technical issues with synthetic data and controlled experiments where the prior \mathbf{x}_a is intentionally biased from known ‘true’ emissions $\hat{\mathbf{x}}$ (such as pre-defining $\mathbf{x}_a = 0.5\hat{\mathbf{x}}$) are known as observing system simulation experiments (OSSE). OSSE’s can determine which assumptions are optimal for retrieving these ‘true’ emissions and are highly valuable to ascertain best practices and observing network capabilities.

1.4 Scientific objectives and structure of the dissertation

The central question of this thesis is how atmospheric observations can better inform methane emissions in Canada. The chapters of this thesis employ surface, aircraft and spaceborne measurements that probe different regions of the atmosphere. These observations are used in experimental and modelling approaches to constrain emissions at the local, regional, and national scale which include urban, rural, and industrial environments as well as emissions from both anthropogenic and natural sources.

The following are key research questions in the thesis chapters:

Chapter 2: How can aircraft in-situ measurements from an extensive field-campaign inform methane emissions in the Athabasca Oil Sands Region (AOSR) of Alberta using an experimental approach? How can measurements from a library of chemical species support source-attribution of these methane emissions?

Chapter 3: How can mobile-surface in-situ measurements complement the information provided by full aircraft studies in the AOSR using an experimental approach? How can these less resource-intensive measurements support the limitations of temporal coverage inherent to field studies?

Chapter 4: How can long-term measurements from in-situ surface stations and satellites disentangle and quantify anthropogenic and natural sources in Canada using an inverse modelling approach? What are the limitations of the inverse modelling approach towards subnational-level source attribution in Canada, and how can these limitations be attributed to the observations or model?

Chapter 5: How can in-situ surface-measurements in the Greater Toronto Area (GTA) inform methane emissions from natural gas infrastructure and mobile combustion in an urban environment?

Thesis chapters have been published (**Chapter 2**), are in press (**Chapter 3**), or in the process of submission (**Chapter 4**) in the journal *Atmospheric Chemistry and Physics* with the following references:

Chapter 2: Quantification of methane sources in the Athabasca Oil Sands Region of Alberta by aircraft mass balance

Baray, S., Darlington, A., Gordon, M., Hayden, K. L., Leithead, A., Li, S.-M., Liu, P. S. K., Mittermeier, R. L., Moussa, S. G., O'Brien, J., Staebler, R., Wolde, M., Worthy, D., and McLaren, R.: Quantification of methane sources in the Athabasca Oil Sands Region of Alberta by aircraft mass balance, *Atmos. Chem. Phys.*, 18, 7361–7378, <https://doi.org/10.5194/acp-18-7361-2018>, 2018.

Chapter 3: Cold-Season methane emissions estimated in the Athabasca Oil Sands Region of Alberta using mobile surface measurements

Baray, S., Hayden, K. L., Sheppard, A., Davis, Z., Strawbridge, K., Staebler, R., McLaren, R.: Cold-Season methane emissions estimated in the Athabasca Oil Sands Region of Alberta using mobile surface measurements, in prep.

Chapter 4: Estimating 2010–2015 anthropogenic and natural methane emissions in Canada using ECCC surface and GOSAT satellite observations

Baray, S., Jacob, D. J., Massakkars, J. D., Sheng, J.-X., Sulprizio, M. P., Jones, D. B. A., Bloom, A. A., and McLaren, R.: Estimating 2010–2015 Anthropogenic and Natural Methane Emissions in Canada using ECCC Surface and GOSAT Satellite Observations, *Atmos. Chem. Phys. Discuss.* [preprint], <https://doi.org/10.5194/acp-2020-1195>, in review, 2021.

The measurements used in **Chapter 2** are from the Joint Canada-Alberta Oil Sands (JOSM) Summer-Intensive 2013 aircraft campaign led by Environment and Climate Change Canada (ECCC) which are available in a public repository. The measurements in **Chapter 3** are from follow-up Fall 2014 and Spring 2017 campaigns also led by York U and ECCC. The

measurements used in **Chapter 4** are from publicly available datasets, these are: (1) the ECCC greenhouse gas monitoring program and (2) the GOSAT University of Leicester proxy XCO₂ retrievals. For these three chapters, the study design, analysis, and interpretation has been performed by the author for the purpose of this thesis. The studies were completed using observation datasets or modelling inputs constructed by other researchers; their contribution of data and/or scientific input is either credited by co-authorship or acknowledgements. The measurements and field-study design in **Chapter 5** were performed by the author and Robert McLaren, as well as the analysis and interpretation of results. All chapters were written by the author with input from co-investigators.

References

- Ars, S., Vogel, F., Arrowsmith, C., Heerah, S., Knuckey, E., Lavoie, J., Lee, C., Pak, N. M., Phillips, J. L., and Wunch, D.: Investigation of the Spatial Distribution of Methane Sources in the Greater Toronto Area Using Mobile Gas Monitoring Systems, *Environ. Sci. Technol.*, 54, 15671–15679, <https://doi.org/10.1021/acs.est.0c05386>, 2020.
- Atherton, E., Risk, D., Fougère, C., Lavoie, M., Marshall, A., Werring, J., Williams, J. P. and Minions, C.: Mobile measurement of methane emissions from natural gas developments in northeastern British Columbia, Canada, *Atmos. Chem. Phys.*, 17(20), 12405–12420, doi:10.5194/acp-17-12405-2017, 2017.
- Cambaliza, M. O. L., Shepson, P. B., Caulton, D. R., Stirm, B., Samarov, D., Gurney, K. R., Turnbull, J., Davis, K. J., Possolo, A., Karion, A., Sweeney, C., Moser, B., Hendricks, A., Lauvaux, T., Mays, K., Whetstone, J., Huang, J., Razlivanov, I., Miles, N. L., and Richardson, S. J.: Assessment of uncertainties of an aircraft-based mass balance approach for quantifying urban greenhouse gas emissions, *Atmos. Chem. Phys.*, 14, 9029–9050, <https://doi.org/10.5194/acp-14-9029-2014>, 2014.
- Chan, E., Worthy, D. E. J., Chan, D., Ishizawa, M., Moran, M. D., Delcloo, A., and Vogel, F.: Eight-Year Estimates of Methane Emissions from Oil and Gas Operations in Western Canada Are Nearly Twice Those Reported in Inventories, *Environ. Sci. Technol.*, 54, 14899–14909, <https://doi.org/10.1021/acs.est.0c04117>, 2020.
- Clerbaux, C., Hadji-Lazaro, J., Turquety, S., Mégie, G., and Coheur, P.-F.: Trace gas measurements from infrared satellite for chemistry and climate applications, *Atmos. Chem. Phys.*, 3, 1495–1508, <https://doi.org/10.5194/acp-3-1495-2003>, 2003.
- Connor, B., Bösch, H., McDuffie, J., Taylor, T., Fu, D., Frankenberg, C., O'Dell, C., Payne, V. H., Gunson, M., Pollock, R., Hobbs, J., Oyafuso, F., and Jiang, Y.: Quantification of uncertainties in OCO-2 measurements of XCO₂: simulations and linear error analysis, *Atmos. Meas. Tech.*, 9, 5227–5238, <https://doi.org/10.5194/amt-9-5227-2016>, 2016.
- Crosson, E. R.: A cavity ring-down analyzer for measuring atmospheric levels of methane, carbon dioxide, and water vapor, *Appl. Phys. B*, 92, 403–408, <https://doi.org/10.1007/s00340-008-3135-y>, 2008.
- Dlugokencky, E. J., Steele, L. P., Lang, P. M., and Masarie, K. A.: Atmospheric methane at Mauna Loa and Barrow observatories: Presentation and analysis of in situ measurements, *J. Geophys. Res.*, 100, 23103, <https://doi.org/10.1029/95JD02460>, 1995.
- Dlugokencky, E. J., Bruhwiler, L., White, J. W. C., Emmons, L. K., Novelli, P. C., Montzka, S. A., Masarie, K. A., Lang, P. M., Crotwell, A. M., Miller, J. B., and Gatti, L. V.: Observational constraints on recent increases in the atmospheric CH₄ burden, *Geophys. Res. Lett.*, 36, L18803, <https://doi.org/10.1029/2009GL039780>, 2009.
- Dlugokencky, E. J., Nisbet, E. G., Fisher, R., and Lowry, D.: Global atmospheric methane: budget, changes and dangers, *Phil. Trans. R. Soc. A.*, 369, 2058–2072, <https://doi.org/10.1098/rsta.2010.0341>, 2011.
- Etheridge, D. M., Steele, L. P., Francey, R. J., and Langenfelds, R. L.: Atmospheric methane between 1000 A.D. and present: Evidence of anthropogenic emissions and climatic variability, *J. Geophys. Res.*, 103, 15979–15993, <https://doi.org/10.1029/98JD00923>, 1998.

European Commission: Joint Research Centre, and Netherlands Environmental Assessment Agency, Emission database for global atmospheric research (EDGAR), available at: <http://edgar.jrc.ec.europa.eu>, Release version 4.2, 2011.

Frankenberg, C., Meirink, J. F., Bergamaschi, P., Goede, A. P. H., Heimann, M., Körner, S., Platt, U., van Weele, M., and Wagner, T.: Satellite cartography of atmospheric methane from SCIAMACHY on board ENVISAT: Analysis of the years 2003 and 2004, *J. Geophys. Res.*, 111, D07303, <https://doi.org/10.1029/2005JD006235>, 2006.

Gordon, I. E., Rothman, L. S., Hill, C., Kochanov, R. V., Tan, Y., Bernath, P. F., Birk, M., Boudon, V., Campargue, A., Chance, K. V., Drouin, B. J., Flaud, J.-M., Gamache, R. R., Hodges, J. T., Jacquemart, D., Perevalov, V. I., Perrin, A., Shine, K. P., Smith, M.-A. H., Tennyson, J., Toon, G. C., Tran, H., Tyuterev, V. G., Barbe, A., Császár, A. G., Devi, V. M., Furtenbacher, T., Harrison, J. J., Hartmann, J.-M., Jolly, A., Johnson, T. J., Karman, T., Kleiner, I., Kyuberis, A. A., Loos, J., Lyulin, O. M., Massie, S. T., Mikhailenko, S. N., Moazzen-Ahmadi, N., Müller, H. S. P., Naumenko, O. V., Nikitin, A. V., Polyansky, O. L., Rey, M., Rotger, M., Sharpe, S. W., Sung, K., Starikova, E., Tashkun, S. A., Auwera, J. V., Wagner, G., Wilzewski, J., Wcisło, P., Yu, S., and Zak, E. J.: The HITRAN2016 molecular spectroscopic database, *Journal of Quantitative Spectroscopy and Radiative Transfer*, 203, 3–69, <https://doi.org/10.1016/j.jqsrt.2017.06.038>, 2017.

Gordon, M., Li, S.-M., Staebler, R., Darlington, A., Hayden, K., O'Brien, J., and Wolde, M.: Determining air pollutant emission rates based on mass balance using airborne measurement data over the Alberta oil sands operations, *Atmos. Meas. Tech.*, 8, 3745–3765, <https://doi.org/10.5194/amt-8-3745-2015>, 2015.

Government of Canada, Canada confirms its support for the Global Methane Pledge and announces ambitious domestic actions to slash methane emissions [Press release], Oct 11 2021, available at: <https://www.canada.ca/en/environment-climate-change/news/2021/10/canada-confirms-its-support-for-the-global-methane-pledge-and-announces-ambitious-domestic-actions-to-slash-methane-emissions.html> (Last access: Nov 21, 2021).

Hausmann, P., Sussmann, R., and Smale, D.: Contribution of oil and natural gas production to renewed increase in atmospheric methane (2007–2014): top-down estimate from ethane and methane column observations, *Atmos. Chem. Phys.*, 16, 3227–3244, <https://doi.org/10.5194/acp-16-3227-2016>, 2016.

Heald, C. L., Jacob, D. J., Jones, D. B. A., Palmer, P. I., Logan, J. A., Streets, D. G., Sachse, G. W., Gille, J. C., Hoffman, R. N., and Nehrkorn, T.: Comparative inverse analysis of satellite (MOPITT) and aircraft (TRACE-P) observations to estimate Asian sources of carbon monoxide: COMPARATIVE INVERSE ANALYSIS, *J. Geophys. Res.*, 109, <https://doi.org/10.1029/2004JD005185>, 2004.

Hu, H., Landgraf, J., Detmers, R., Borsdorff, T., Aan de Brugh, J., Aben, I., Butz, A., and Hasekamp, O.: Toward Global Mapping of Methane With TROPOMI: First Results and Intersatellite Comparison to GOSAT, *Geophys. Res. Lett.*, 45, 3682–3689, <https://doi.org/10.1002/2018GL077259>, 2018.

IPCC: 2006 IPCC Guidelines for National Greenhouse Gas Inventories, Prepared by the National Greenhouse Gas Inventories Programme, edited by: Eggleston, H. S., Buendia, L., Miwa, K., Ngara, T., and Tanabe, K., IGES, Japan, 2006.

Ishizawa, M., Chan, D., Worthy, D., Chan, E., Vogel, F. and Maksyutov, S.: Analysis of atmospheric CH₄ in Canadian Arctic and estimation of the regional CH₄ fluxes, *Atmos. Chem. Phys.*, 19(7), 4637–4658, doi:10.5194/acp-19-4637-2019, 2019.

Jacob, D. J.: Introduction to Atmospheric Chemistry, Princeton University Press, <https://doi.org/10.1515/9781400841547>, 1999.

Jacob, D. J., Turner, A. J., Maasackers, J. D., Sheng, J., Sun, K., Liu, X., Chance, K., Aben, I., McKeever, J., and Frankenberg, C.: Satellite observations of atmospheric methane and their value for quantifying methane emissions, *Atmos. Chem. Phys.*, 16, 14371–14396, <https://doi.org/10.5194/acp-16-14371-2016>, 2016.

Johnson, M. R., Tyner, D. R., Conley, S., Schwietzke, S. and Zavala-Araiza, D.: Comparisons of Airborne Measurements and Inventory Estimates of Methane Emissions in the Alberta Upstream Oil and Gas Sector, *Environ. Sci. Technol.*, 51(21), 13008–13017, doi:10.1021/acs.est.7b03525, 2017.

Karion, A., Sweeney, C., Pétron, G., Frost, G., Michael Hardesty, R., Kofler, J., Miller, B. R., Newberger, T., Wolter, S., Banta, R., Brewer, A., Dlugokencky, E., Lang, P., Montzka, S. A., Schnell, R., Tans, P., Trainer, M., Zamora, R., and Conley, S.: Methane emissions estimate from airborne measurements over a western United States natural gas field: CH₄ EMISSIONS OVER A NATURAL GAS FIELD, *Geophys. Res. Lett.*, 40, 4393–4397, <https://doi.org/10.1002/grl.50811>, 2013.

Kirschke, S., Bousquet, P., Ciais, P., Saunois, M., Canadell, J. G., Dlugokencky, E. J., Bergamaschi, P., Bergmann, D., Blake, D. R., Bruhwiler, L., Cameron-Smith, P., Castaldi, S., Chevallier, F., Feng, L., Fraser, A., Heimann, M., Hodson, E. L., Houweling, S., Josse, B., Fraser, P. J., Krummel, P. B., Lamarque, J.-F., Langenfelds, R. L., Le Quéré, C., Naik, V., O’Doherty, S., Palmer, P. I., Pison, I., Plummer, D., Poulter, B., Prinn, R. G., Rigby, M., Ringeval, B., Santini, M., Schmidt, M., Shindell, D. T., Simpson, I. J., Spahni, R., Steele, L. P., Strode, S. A., Sudo, K., Szopa, S., van der Werf, G. R., Voulgarakis, A., van Weele, M., Weiss, R. F., Williams, J. E., and Zeng, G.: Three decades of global methane sources and sinks, *Nature Geosci*, 6, 813–823, <https://doi.org/10.1038/ngeo1955>, 2013.

Loulergue, L., Schilt, A., Spahni, R., Masson-Delmotte, V., Blunier, T., Lemieux, B., Barnola, J.-M., Raynaud, D., Stocker, T. F., and Chappellaz, J.: Orbital and millennial-scale features of atmospheric CH₄ over the past 800,000 years, *Nature*, 453, 383–386, <https://doi.org/10.1038/nature06950>, 2008.

Maasackers, J. D., Jacob, D. J., Sulprizio, M. P., Scarpelli, T. R., Nesser, H., Sheng, J.-X., Zhang, Y., Hersher, M., Bloom, A. A., Bowman, K. W., Worden, J. R., Janssens-Maenhout, G., and Parker, R. J.: Global distribution of methane emissions, emission trends, and OH concentrations and trends inferred from an inversion of GOSAT satellite data for 2010–2015, *Atmos. Chem. Phys.*, 19, 7859–7881, <https://doi.org/10.5194/acp-19-7859-2019>, 2019.

Maazallahi, H., Fernandez, J. M., Menoud, M., Zavala-Araiza, D., Weller, Z. D., Schwietzke, S., von Fischer, J. C., Denier van der Gon, H., and Röckmann, T.: Methane mapping, emission quantification, and attribution in two European cities: Utrecht (NL) and Hamburg (DE), *Atmos. Chem. Phys.*, 20, 14717–14740, <https://doi.org/10.5194/acp-20-14717-2020>, 2020.

Maithani, S. and Pradhan, M.: Cavity ring-down spectroscopy and its applications to environmental, chemical and biomedical systems, *J Chem Sci*, 132, 114, <https://doi.org/10.1007/s12039-020-01817-x>, 2020.

Martinez, B., Miller, T. W., and Yalin, A. P.: Cavity Ring-Down Methane Sensor for Small Unmanned Aerial Systems, *Sensors*, 20, 454, <https://doi.org/10.3390/s20020454>, 2020.

McKain, K., Down, A., Raciti, S. M., Budney, J., Hutyra, L. R., Floerchinger, C., Herndon, S. C., Nehrkorn, T., Zahniser, M. S., Jackson, R. B., Phillips, N., and Wofsy, S. C.: Methane emissions from natural gas infrastructure and use in the urban region of Boston, Massachusetts, *Proc Natl Acad Sci USA*, 112, 1941–1946, <https://doi.org/10.1073/pnas.1416261112>, 2015.

- McLaren, R., Gertler, A. W., Wittorff, D. N., Belzer, W., Dann, T., and Singleton, D. L.: Real-World Measurements of Exhaust and Evaporative Emissions in the Cassiar Tunnel Predicted by Chemical Mass Balance Modeling, *Environmental Science & Technology*, 30, 3001-3009, 10.1021/es960036k, 1996.
- Miller, S. M., Commane, R., Melton, J. R., Andrews, A. E., Benmergui, J., Dlugokencky, E. J., Janssens-Maenhout, G., Michalak, A. M., Sweeney, C. and Worthy, D. E. J.: Evaluation of wetland methane emissions across North America using atmospheric data and inverse modeling, *Biogeosciences*, 13(4), 1329–1339, doi:10.5194/bg-13-1329-2016, 2016.
- Myhre, G., Shindell, D., Bréon, F.-M., Collins, W., Fuglestvedt, J., Huang, J., Koch, D., Lamarque, J.-F., Lee, D., Mendoza, B., Nakajima, T., Robock, A., Stephens, G., Takemura, T., and Zhang, H.: Anthropogenic and Natural Radiative Forcing, in: *Climate Change 2013: The Physical Science Basis. Contribution of Working Group I to the Fifth Assessment Report of the Intergovernmental Panel on Climate Change*, edited by: Stocker, T. F., Qin, D., Plattner, G.-K., Tignor, M., Allen, S. K., Boschung, J., Nauels, A., Xia, Y., Bex, V., and Midgley, P. M., Cambridge University Press, Cambridge, United Kingdom and New York, NY, USA, 2013.
- Nassar, R., Hill, T. G., McLinden, C. A., Wunch, D., Jones, D. B. A., and Crisp, D.: Quantifying CO₂ Emissions From Individual Power Plants From Space, *Geophys. Res. Lett.*, 44, <https://doi.org/10.1002/2017GL074702>, 2017.
- Nisbet, E. G., Dlugokencky, E. J., Manning, M. R., Lowry, D., Fisher, R. E., France, J. L., Michel, S. E., Miller, J. B., White, J. W. C., Vaughn, B., Bousquet, P., Pyle, J. A., Warwick, N. J., Cain, M., Brownlow, R., Zazzeri, G., Lanoisellé, M., Manning, A. C., Gloor, E., Worthy, D. E. J., Brunke, E.-G., Labuschagne, C., Wolff, E. W., and Ganesan, A. L.: Rising atmospheric methane: 2007-2014 growth and isotopic shift: RISING METHANE 2007-2014, *Global Biogeochem. Cycles*, 30, 1356–1370, <https://doi.org/10.1002/2016GB005406>, 2016.
- Nisbet, E. G., Fisher, R. E., Lowry, D., France, J. L., Allen, G., Bakkaloglu, S., Broderick, T. J., Cain, M., Coleman, M., Fernandez, J., Forster, G., Griffiths, P. T., Iverach, C. P., Kelly, B. F. J., Manning, M. R., Nisbet-Jones, P. B. R., Pyle, J. A., Townsend-Small, A., al-Shalaan, A., Warwick, N., and Zazzeri, G.: Methane Mitigation: Methods to Reduce Emissions, on the Path to the Paris Agreement, *Rev. Geophys.*, 58, <https://doi.org/10.1029/2019RG000675>, 2020.
- Parker, R., Boesch, H., Cogan, A., Fraser, A., Feng, L., Palmer, P. I., Messerschmidt, J., Deutscher, N., Griffith, D. W. T., Notholt, J., Wennberg, P. O., and Wunch, D.: Methane observations from the Greenhouse Gases Observing SATellite: Comparison to ground-based TCCON data and model calculations: GOSAT CH₄ OBSERVATIONS, *Geophys. Res. Lett.*, 38, <https://doi.org/10.1029/2011GL047871>, 2011.
- Parker, R. J., Webb, A., Boesch, H., Somkuti, P., Barrio Guillo, R., Di Noia, A., Kalaitzi, N., Anand, J., Bergamaschi, P., Chevallier, F., Palmer, P. I., Feng, L., Deutscher, N. M., Feist, D. G., Griffith, D. W. T., Hase, F., Kivi, R., Morino, I., Notholt, J., Oh, Y.-S., Ohyama, H., Petri, C., Pollard, D. F., Roehl, C., Sha, M. K., Shiomi, K., Strong, K., Sussmann, R., Te, Y., Velasco, V. A., Warneke, T., Wennberg, P. O., and Wunch, D.: A Decade of GOSAT Proxy Satellite CH₄ Observations, *Atmosphere – Atmospheric Chemistry and Physics*, <https://doi.org/10.5194/essd-2020-114>, 2020.
- Parrenin, F., Barnola, J.-M., Beer, J., Blunier, T., Castellano, E., Chappellaz, J., Dreyfus, G., Fischer, H., Fujita, S., Jouzel, J., Kawamura, K., Lemieux-Dudon, B., Loulergue, L., Masson-Delmotte, V., Narcisi, B., Petit, J.-R., Raisbeck, G., Raynaud, D., Ruth, U., Schwander, J., Severi, M., Spahni, R., Steffensen, J. P., Svensson, A., Udisti, R., Waelbroeck, C., and Wolff, E.: The EDC3 chronology for the EPICA Dome C ice core, *Clim. Past*, 3, 485–497, <https://doi.org/10.5194/cp-3-485-2007>, 2007.

- Peischl, J., Ryerson, T. B., Brioude, J., Aikin, K. C., Andrews, A. E., Atlas, E., Blake, D., Daube, B. C., de Gouw, J. A., Dlugokencky, E., Frost, G. J., Gentner, D. R., Gilman, J. B., Goldstein, A. H., Harley, R. A., Holloway, J. S., Kofler, J., Kuster, W. C., Lang, P. M., Novelli, P. C., Santoni, G. W., Trainer, M., Wofsy, S. C., and Parrish, D. D.: Quantifying sources of methane using light alkanes in the Los Angeles basin, California, *Journal of Geophysical Research: Atmospheres*, 118, 4974–4990, [10.1002/jgrd.50413](https://doi.org/10.1002/jgrd.50413), 2013.
- Prather, M. J., Holmes, C. D., and Hsu, J.: Reactive greenhouse gas scenarios: Systematic exploration of uncertainties and the role of atmospheric chemistry: *ATMOSPHERIC CHEMISTRY AND GREENHOUSE GASES*, *Geophys. Res. Lett.*, 39, n/a-n/a, <https://doi.org/10.1029/2012GL051440>, 2012.
- Raub, J. A., Mathieu-Nolf, M., Hampson, N. B., and Thom, S. R.: Carbon monoxide poisoning — a public health perspective, *Toxicology*, 145, 1–14, [https://doi.org/10.1016/S0300-483X\(99\)00217-6](https://doi.org/10.1016/S0300-483X(99)00217-6), 2000.
- Rigby, M., Montzka, S. A., Prinn, R. G., White, J. W. C., Young, D., O’Doherty, S., Lunt, M. F., Ganesan, A. L., Manning, A. J., Simmonds, P. G., Salameh, P. K., Harth, C. M., Mühle, J., Weiss, R. F., Fraser, P. J., Steele, L. P., Krummel, P. B., McCulloch, A., and Park, S.: Role of atmospheric oxidation in recent methane growth, *Proc Natl Acad Sci USA*, 114, 5373–5377, <https://doi.org/10.1073/pnas.1616426114>, 2017.
- Saunio, M., Stavert, A. R., Poulter, B., Bousquet, P., Canadell, J. G., Jackson, R. B., Raymond, P. A., Dlugokencky, E. J., Houweling, S., Patra, P. K., Ciais, P., Arora, V. K., Bastviken, D., Bergamaschi, P., Blake, D. R., Brailsford, G., Bruhwiler, L., Carlson, K. M., Carrol, M., Castaldi, S., Chandra, N., Crevoisier, C., Crill, P. M., Covey, K., Curry, C. L., Etiope, G., Frankenberg, C., Gedney, N., Hegglin, M. I., Höglund-Isaksson, L., Hugelius, G., Ishizawa, M., Ito, A., Janssens-Maenhout, G., Jensen, K. M., Joos, F., Kleinen, T., Krummel, P. B., Langenfelds, R. L., Laruelle, G. G., Liu, L., Machida, T., Maksyutov, S., McDonald, K. C., McNorton, J., Miller, P. A., Melton, J. R., Morino, I., Müller, J., Murguía-Flores, F., Naik, V., Niwa, Y., Noce, S., O’Doherty, S., Parker, R. J., Peng, C., Peng, S., Peters, G. P., Prigent, C., Prinn, R., Ramonet, M., Regnier, P., Riley, W. J., Rosentreter, J. A., Segers, A., Simpson, I. J., Shi, H., Smith, S. J., Steele, L. P., Thornton, B. F., Tian, H., Tohjima, Y., Tubiello, F. N., Tsuruta, A., Viovy, N., Voulgarakis, A., Weber, T. S., van Weele, M., van der Werf, G. R., Weiss, R. F., Worthy, D., Wunch, D., Yin, Y., Yoshida, Y., Zhang, W., Zhang, Z., Zhao, Y., Zheng, B., Zhu, Q., Zhu, Q., and Zhuang, Q.: The Global Methane Budget 2000–2017, *Earth Syst. Sci. Data*, 12, 1561–1623, <https://doi.org/10.5194/essd-12-1561-2020>, 2020.
- Stanevich, I., Jones, D. B. A., Strong, K., Parker, R. J., Boesch, H., Wunch, D., Notholt, J., Petri, C., Warneke, T., Sussmann, R., Schneider, M., Hase, F., Kivi, R., Deutscher, N. M., Velazco, V. A., Walker, K. A., and Deng, F.: Characterizing model errors in chemical transport modeling of methane: impact of model resolution in versions v9-02 of GEOS-Chem and v35j of its adjoint model, *Geosci. Model Dev.*, 13, 3839–3862, <https://doi.org/10.5194/gmd-13-3839-2020>, 2020.
- Tobie, G., Lunine, J. I., and Sotin, C.: Episodic outgassing as the origin of atmospheric methane on Titan, *Nature*, 440, 61–64, <https://doi.org/10.1038/nature04497>, 2006.
- Turner, A. J., Jacob, D. J., Wecht, K. J., Maasackers, J. D., Lundgren, E., Andrews, A. E., Biraud, S. C., Boesch, H., Bowman, K. W., Deutscher, N. M., Dubey, M. K., Griffith, D. W. T., Hase, F., Kuze, A., Notholt, J., Ohyama, H., Parker, R., Payne, V. H., Sussmann, R., Sweeney, C., Velazco, V. A., Warneke, T., Wennberg, P. O., and Wunch, D.: Estimating global and North American methane emissions with high spatial resolution using GOSAT satellite data, *Atmos. Chem. Phys.*, 15, 7049–7069, <https://doi.org/10.5194/acp-15-7049-2015>, 2015.

- Turner, A. J., Frankenberg, C., Wennberg, P. O., and Jacob, D. J.: Ambiguity in the causes for decadal trends in atmospheric methane and hydroxyl, *Proc Natl Acad Sci USA*, 114, 5367–5372, <https://doi.org/10.1073/pnas.1616020114>, 2017.
- Varon, D. J., Jacob, D. J., McKeever, J., Jervis, D., Durak, B. O. A., Xia, Y., and Huang, Y.: Quantifying methane point sources from fine-scale satellite observations of atmospheric methane plumes, *Atmos. Meas. Tech.*, 11, 5673–5686, <https://doi.org/10.5194/amt-11-5673-2018>, 2018.
- Varon, D. J., Jacob, D. J., Jervis, D., and McKeever, J.: Quantifying Time-Averaged Methane Emissions from Individual Coal Mine Vents with GHGSat-D Satellite Observations, *Environ. Sci. Technol.*, 54, 10246–10253, <https://doi.org/10.1021/acs.est.0c01213>, 2020.
- Vaughan, N. E. and Lenton, T. M.: A review of climate geoengineering proposals, *Climatic Change*, 109, 745–790, <https://doi.org/10.1007/s10584-011-0027-7>, 2011.
- Webster, C. R., Mahaffy, P. R., Atreya, S. K., Moores, J. E., Flesch, G. J., Malespin, C., McKay, C. P., Martinez, G., Smith, C. L., Martin-Torres, J., Gomez-Elvira, J., Zorzano, M.-P., Wong, M. H., Trainer, M. G., Steele, A., Archer, D., Sutter, B., Coll, P. J., Freissinet, C., Meslin, P.-Y., Gough, R. V., House, C. H., Pavlov, A., Eigenbrode, J. L., Glavin, D. P., Pearson, J. C., Keymeulen, D., Christensen, L. E., Schwenzer, S. P., Navarro-Gonzalez, R., Pla-García, J., Rafkin, S. C. R., Vicente-Retortillo, Á., Kahanpää, H., Viudez-Moreiras, D., Smith, M. D., Harri, A.-M., Genzer, M., Hassler, D. M., Lemmon, M., Crisp, J., Sander, S. P., Zurek, R. W., and Vasavada, A. R.: Background levels of methane in Mars' atmosphere show strong seasonal variations, *Science*, 360, 1093–1096, <https://doi.org/10.1126/science.aag0131>, 2018.
- Wecht, K. J., Jacob, D. J., Sulprizio, M. P., Santoni, G. W., Wofsy, S. C., Parker, R., Bösch, H., and Worden, J.: Spatially resolving methane emissions in California: constraints from the CalNex aircraft campaign and from present (GOSAT, TES) and future (TROPOMI, geostationary) satellite observations, *Atmos. Chem. Phys.*, 14, 8173–8184, <https://doi.org/10.5194/acp-14-8173-2014>, 2014.
- Wheeler, M. D., Newman, S. M., Orr-Ewing, A. J., and Ashfold, M. N. R.: Cavity ring-down spectroscopy, *Faraday Trans.*, 94, 337–351, <https://doi.org/10.1039/a707686j>, 1998.
- Worden, J. R., Bloom, A. A., Pandey, S., Jiang, Z., Worden, H. M., Walker, T. W., Houweling, S., and Röckmann, T.: Reduced biomass burning emissions reconcile conflicting estimates of the post-2006 atmospheric methane budget, *Nat Commun*, 8, 2227, <https://doi.org/10.1038/s41467-017-02246-0>, 2017.

Chapter 2 Quantification of methane sources in the Athabasca Oil Sands Region of Alberta by aircraft mass-balance

Author Contributions

Sabour Baray¹, Andrea Darlington², Mark Gordon³, Katherine L. Hayden², Amy Leithead², Shao-Meng Li², Peter S.K. Liu², Richard L. Mittermeier², Samar G. Moussa², Jason O'Brien², Ralph Staebler², Mengistu Wolde⁴, Doug Worthy⁵, Robert McLaren¹

1. Centre for Atmospheric Chemistry, York University, Toronto
2. Air Quality Research Division, Environment and Climate Change Canada, Toronto
3. Earth and Space Science and Engineering, York University, Toronto
4. National Research Council of Canada, Ottawa
5. Climate Research Division, Environment and Climate Change Canada, Toronto, Canada

SB and RM designed the study. SB conducted the analysis with contributions from MG, SML and RM. AD and MG were the lead developers of the TERRA algorithm with contributions from SB. AD, MG, KLH, AL, SML, PSKL, RLM, SGM, JOB, RS, MW, DW, and RM conducted measurements during the JOSM field campaign.

Abstract

Aircraft-based measurements of methane (CH_4) and other air pollutants in the Athabasca Oil Sands Region (AOSR) were made during a summer intensive field campaign between August 13 and September 7 2013, in support of the Joint Canada–Alberta Implementation Plan for Oil Sands Monitoring. Chemical signatures were used to identify CH_4 sources from tailings ponds (BTEX VOC's), open-pit surface mines (NO_y and rBC) and elevated plumes from bitumen upgrading facilities (SO_2 and NO_y). Emission rates of CH_4 were determined for the five primary surface mining facilities in the region using two mass balance methods. Emission rates from source categories within each facility were estimated when plumes from the sources were spatially separable. Tailings ponds accounted for 45% of total CH_4 emissions measured from the major surface mining facilities in the region while emissions from operations in the open pit mines accounted for ~50%. The average open pit surface mining emission rates ranged from 1.2 to 2.8 tonnes of $\text{CH}_4 \text{ hr}^{-1}$ for different facilities in the AOSR. Amongst the 19 tailings ponds, Mildred Lake Settling Basin, the oldest pond in the region, was found to be responsible for the majority of tailings ponds emissions of CH_4 (>70%). The sum of measured emission rates of CH_4 from the five major facilities, 19.2 ± 1.1 tonnes $\text{CH}_4 \text{ hr}^{-1}$, was similar to a single mass balance determination of CH_4 from all major sources in the AOSR determined from a single flight downwind of the facilities, 23.7 ± 3.7 tonnes $\text{CH}_4 \text{ hr}^{-1}$. The measured hourly CH_4 emission rate from all facilities in the AOSR is $48 \pm 8\%$ higher than that extracted for 2013 from the Canadian Green House Gas Reporting Program, a legislated facility-reported Emissions Inventory, converted to hourly units. The measured emissions correspond to an emissions rate of $0.17 \pm 0.01 \text{ Tg } \text{CH}_4 \text{ yr}^{-1}$, if the emissions are assumed temporally constant, an uncertain assumption. The emission rates reported here are relevant for the summer season. In future, effort should be devoted to measurements in different seasons to further our understanding of seasonal parameters impacting fugitive emissions of CH_4 and to allow better estimates of annual emissions and year to year variability.

2.1 Introduction

Methane (CH₄) is a significant greenhouse gas (GHG), second in rank to carbon dioxide (CO₂) in terms of its direct radiative forcing (Montzka et al., 2011; IPCC, 2013). Controlling emissions of CH₄ is an attractive climate control strategy because of its shorter atmospheric lifetime ($\tau \sim 9$ years) and larger global warming potential (GWP) compared to CO₂ (IPCC, 2013). Emissions of CH₄ include biogenic (animal husbandry, landfills, wetlands, agriculture), pyrogenic (biomass burning) and thermogenic sources (fossil fuel reservoirs). The most important sink of CH₄ is reaction with the hydroxyl radical (OH) in the troposphere (Vaghjiani and Ravishankara, 1991), which produces formaldehyde (HCHO) that is subsequently photolyzed or oxidized to yield CO and eventually CO₂. In addition to climate implications, CH₄ also has air quality implications through its role in NO_x catalysed ozone formation in the troposphere, especially in areas with large sources of CH₄. Of recent interest are wintertime rapid ozone formation events (OFEs) seen in regions of intense oil and gas extraction (Pinto, 2009; Schnell et al., 2009) that are associated with snow coverage (Edwards et al., 2013), shallow boundary layers (Schnell et al., 2016), high levels of ozone precursors and enhanced photolysis of HCHO and other carbonyls under radical limited conditions (Edwards et al., 2014).

The growth of the atmospheric burden of CH₄ increased in the post industrial revolution, slowed in the 1980's and 90's (Worthy et al., 2009), paused between 1990-2007 but has increased again starting in 2007, with an atmospheric growth rate of $\sim 0.4\%$ yr⁻¹ from 2007-2014 in the northern hemisphere (Hausmann et al., 2016). Satellite observations have suggested a 30% increase in CH₄ emissions in the USA during 2002-2014 (Turner et al., 2016). The 2009-2014 trend in CH₄ mixing ratios and tropospheric columns of ethane was attributed to oil/gas production in the USA (Helmig et al., 2016) and recent increases in tropospheric columns of ethane and methane have suggested the global oil and gas sector to be partially responsible (Hausmann et al., 2016). Contrasting this, a recent study suggests that North American CH₄ emissions have been flat from 2000-2012 (Bruhwiler et al., 2017) and there is still ambiguity in the source versus sink role for the recent increase in atmospheric CH₄ (Turner et al., 2017). The above uncertainties underline a need for better quantification of anthropogenic emissions of CH₄ to the atmosphere and motivate the current study.

Emission inventories can quantify the contributions of specific sources to the atmosphere. However, bottom-up inventories benefit from top-down measurements and validation (Fujita et al., 1992), due to the difficulty in identifying all possible points of emission and quantifying all emissions in a large complex source (e.g., a city or a facility). Top-down measurements of various types have long been used in the validation of emission inventories and emission models including comparison of surface based pollutant profiles and ratios (Fujita et al., 1992; Jiang et al., 1997; Fujita et al., 1995), source-receptor methods (Scheff and Wadden, 1993; Fujita et al., 1995; McLaren et al., 1996), aircraft based flux measurements (Mays et al., 2009), measurement/modelling hybrid methods (Allen et al., 2004; Shephard et al., 2015) and satellite measurements (McLinden et al., 2012; McLinden et al., 2014; Turner et al., 2016; Kort et al., 2014; Jacob et al., 2016). Multiple studies have suggested underestimation of CH₄ emissions from natural gas infrastructure (Brandt et al., 2014; Hendrick et al., 2016). Several recent aircraft studies using mass balance approaches have quantified CH₄ emissions in oil and gas regions and compared these to inventory emission rates and/or leakage rates (Karion et al., 2013; Peischl et al., 2013; Karion et al., 2015; Peischl et al., 2015; Peischl et al., 2016; Lavoie et al., 2015). Other studies have used top-down satellite measurements to quantify emission of CH₄ in oil and gas regions (Schneising et al., 2014; Kort et al., 2014). As such, top-down measurement of methane emissions and comparison with bottom-up inventories can make a significant contribution to our understanding of the sources of CH₄.

In this study we quantify total emission rates of CH₄ from facilities in the Athabasca Oil Sands Region (AOSR) of Alberta in the summer of 2013. Alberta has large deposits of oil sands, an unconventional viscous mixture of bitumen, sand, silt, clay, water and trapped gases (Stringham, 2012). Canada has proven reserves of 1.69×10^{11} barrels of oil (2.7×10^{13} litres), third largest in the world, 97% of which are located in the oil sands [Orbach, 2012]. Approximately 82% of the oil sands are located in the AOSR north of Fort McMurray with 20% located in near surface deposits (depth < 100m) that can be mined using open pit techniques and the remainder located in deeper deposits requiring underground in-situ extraction. In both cases the oil must be separated from sand requiring the use of hot water or steam froth treatment, and organic solvent diluents (naphtha or paraffin) are used to help separate water and solids and/or to decrease the

bitumen viscosity. For surface mining processes, once the bitumen is separated, process water containing unrecovered organic diluents is recycled but some is discharged in large tailings ponds open to the atmosphere for further remediation. Oil extraction in the AOSR is unique in that unlike other oil and gas regions, CH₄ is not the primary economic commodity being extracted, but is an unintended by-product. In particular, a significant fraction of the CH₄ is not associated with fossil fuel reserves, but is emitted from the tailings ponds (Small et al., 2015). The factors giving rise to the release of CH₄ from these ponds are complex but include the organic and inorganic chemical composition of the ponds, the diversity and types of microbial communities, especially methanogens, as well as the age of the ponds. It is reported that it took 20 years and 15 years for the largest ponds at Syncrude and Suncor respectively, to show evidence of methane bubbling from the surface (Small et al., 2015). Additional fugitive CH₄ is associated with the gaseous component of the oil sand along with other gases (Strausz, 2003; Johnson et al., 2016) that are released during overburden removal, open pit mining and/or subsequent processing.

In the summer of 2013, an intensive ambient air measurement campaign took place in the AOSR with both ground and airborne components in support of the Joint Oil Sands Monitoring (JOSM) Plan (JOSM, 2012). The airborne measurements were conducted to address four objectives: i) to measure and quantify air emissions from the oil sands mining facilities, ii) to study the downwind physical and chemical transformation of pollutants emitted, iii) to provide spatio-temporal measurement of pollutants suitable for intercomparison with simultaneous satellite nadir overpasses in the region, and iv) to support air quality model prediction capabilities. In this paper, we report CH₄ emissions from industrial facilities in the AOSR based on the airborne campaign. We applied the Top-down Emissions Rate Retrieval Algorithm (TERRA) mass-balance approach (Gordon et al., 2015) to determine total CH₄ emissions rates from each of the major industrial facilities, as well as a second mass-balance approach using downwind flight tracks to spatially separate CH₄ emissions from different sources in each facility. Emissions rates of CH₄ are determined for the five major facilities in the region: Syncrude Mildred Lake (SML), Suncor Energy OSG (SUN), Canadian Natural Resources Limited Horizon (CNRL), Shell Albian Muskeg River and Jackpine (SAJ) and Syncrude Aurora

(SAU). These results are the first source-attributed emissions estimates for the facilities in the AOSR, obtained by identifying and characterizing plume origins according to signatures of chemical tracer species.

2.2 Experimental

2.2.1 Instrumentation

An array of instruments for the measurement of trace gases, aerosols, meteorological and aircraft state parameters were installed aboard the National Research Council of Canada Convair 580 research aircraft. Measurements of CH₄, CO₂, CO and H₂O were made using a cavity ring-down spectrometer (Picarro G2401-m) at an interpolated rate of approximately 0.5 Hz with a flow rate of ~435 sccm min⁻¹. The precision of the CH₄ measurement was 2 ppb, and the uncertainty of the measurement at background (~ 1.9 ppm) was 3.3 ppb (@2 sec). The instrument was calibrated six times before, during and after the project using two standard reference gases traceable to NOAA GMD standards. Methane mixing ratios are reported throughout as dry mole fractions in the paper. Necessary parameters for emissions estimation included Temperature (T), measured using Rosemount probe, Dewpoint temperature (T_d), measured with an Edgetech hygrometer, and pressure (P), measured with a DigiQuartz sensor. The three-component wind speed (U_x, U_y, U_z) was derived from a Rosemount 858 probe, GPS and Honeywell HG1700 inertial measurement unit. The uncertainty of horizontal and vertical winds on the aircraft are 0.6 and 0.4 m/s respectively (Williams and Marcotte, 2000). Geospatial information (latitude, longitude, ellipsoid height altitude) was measured by GPS.

Nitrogen oxides (NO, NO₂ and NO_y) were measured with a modified trace level chemiluminescent analyser (Thermo Scientific Model 42i-TL). A molybdenum converter (325 °C) was used to convert NO_y species to NO and an NO₂ specific converter (Droplet Measurement Technologies) was used to convert NO₂ to NO. Detection limits for NO, NO₂, and NO_y were determined to be 0.08 ppb (1 sec), 0.20 ppb (2 sec), 0.09 ppb (1 sec) respectively. Sulfur dioxide (SO₂) was measured with a pulsed UV fluorescence analyser (Thermo Scientific: Model 43i-TLE) with a detection limit of 0.7 ppb (1 sec). Ambient air was drawn in through filtered 6.35 mm (1/4") diameter PFA tubing taken from a rear-facing inlet located on the roof

toward the rear of the aircraft. Measurements of NO, NO₂, NO_y and SO₂ were made downstream of a constant pressure inlet system maintained at 770 mmHg with a total flow rate of 5 Lpm. In-flight zero and background determinations were made several times throughout each flight and the analysers were calibrated multiple times during the study against National Institute and Standards Technology (NIST) certified reference gases.

Refractory black carbon mass (rBC), was measured with a Droplet Measurement Technologies (DMT) Single Particle Soot Photometer (SP2). Ambient air was subsampled from the main aerosol flow that was brought into the main cabin with a forward-facing shrouded diffuser isokinetic aerosol inlet (Cheng et al., 2017). Benzene, toluene, ethylbenzene and xylenes (BTEX) were measured by a Proton Transfer Reaction time-of-flight Mass Spectrometer (PTRMS) from the main gas inlet. Further technical details are provided elsewhere (Li et al., 2017). The delay time of each instrument was determined experimentally and through calculations based on sample flow rates and inlet volumes. Total delays are contributed to by the response time of the instruments (1–3 sec) as well as the volume of sampling tubing. Data were adjusted to account for the total delay times of 2-6 sec to spatially and temporally synchronize the different measurements (Picarro delay time = 6 sec). The average speed of the aircraft was 90 m s⁻¹ during the research flights, thus providing a spatial resolution of 90-270 m based upon the internal response time of each measurement.

2.2.2 Aircraft flights

In total, there were 22 flights with 84 hours of measurements in the AOSR between August 13 and September 7, 2013. The flights were designed for three purposes; measurement of pollutant emissions from facilities (Gordon et al., 2015; Li et al., 2017), measurement of pollutant transformation downwind of the AOSR (Liggio et al., 2016) and comparison with satellite overpasses (Shephard et al., 2015). Thirteen flights were dedicated to quantifying facility emissions with a minimum of two flights for each of the SML, SUN, CNRL, SAJ and SAU facilities. CH₄ above background was not detected during the 2013 flights targeting the Imperial Kearsal Lake (IKL) facility, which was not in full production mode at the time (but has since expanded significantly), nor from the Suncor Firebag in-situ operation. We did detect CH₄ above

background suspected to originate from the Suncor MacKay River operation (west of SML). We were not able to quantify this source separately, however emissions from this source are included in one measurement of the total emissions from all mining facilities in the AOSR using a wide downwind screen (see section 2.3.4 and Fig. 2.7). Several other flights are not included in the analysis due to unfavourable meteorological conditions including wind shear problems or insufficient numbers of transects. In total, seven flights were found to be suitable for identifying and quantifying emissions of CH₄ from the facilities. Figure 2.1 displays several of the flight tracks over and downwind of the target facilities north of the Fort McMurray airport.

The flight patterns designed for the quantification of emissions rates were of two types: i) screen flights, wherein the aircraft flew transects perpendicular to the plume downwind of one or more facilities, and ii) box flights, wherein the aircraft flew transects at multiple heights around a single target facility in a box-type pattern (Gordon et al., 2015; Li et al., 2017). The transects were performed at heights from 150 to 1370 m above ground level (agl), complemented by vertical profiles designed to determine the height of the planetary boundary layer (PBL) and to compare with ground based measurements.

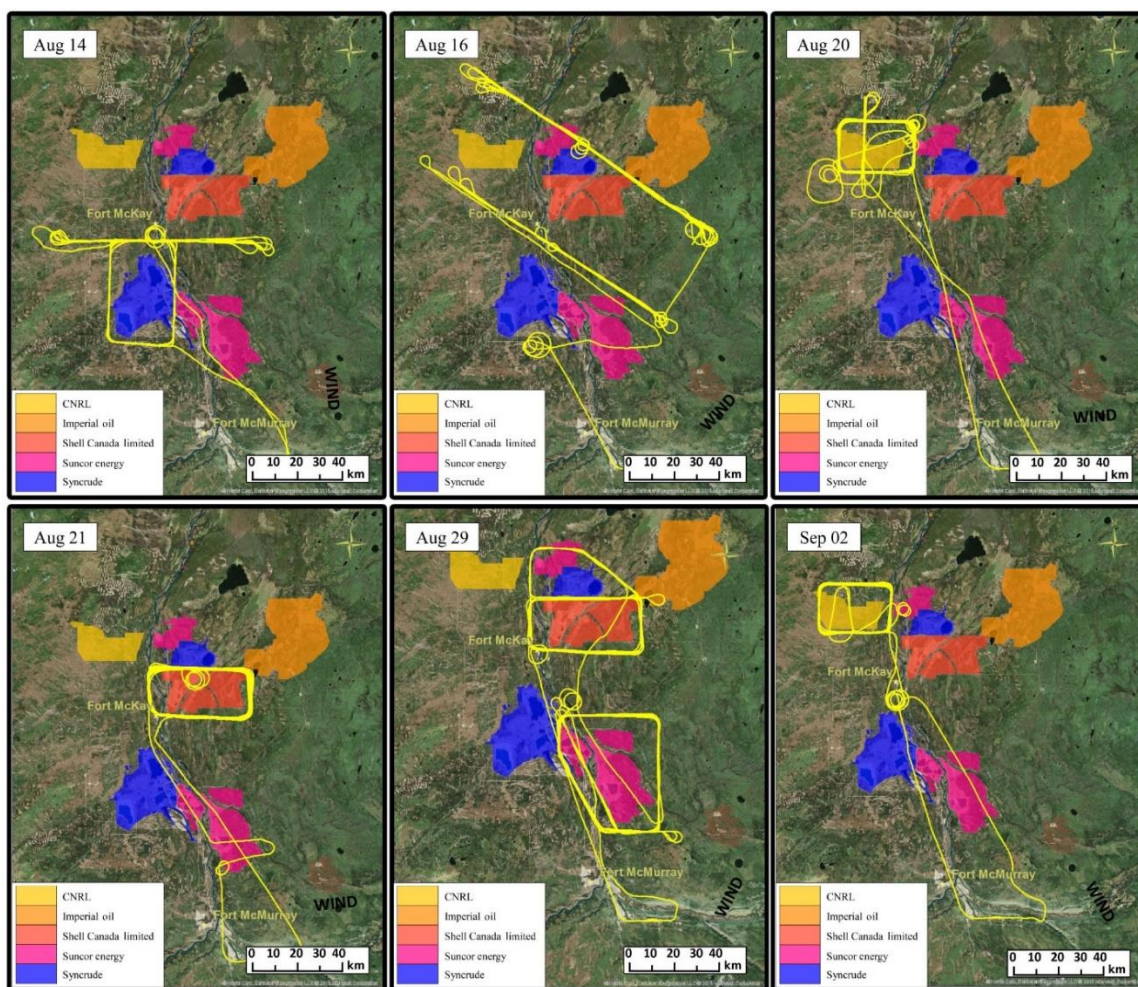


Figure 2.1: Flight tracks from flights capturing emissions from SML (Aug 14, Aug 16), SUN (Aug 16, Aug 29), CNRL (Aug 20, Sep 02), SAJ (Aug 21, Sep 06 not shown), and SAU (Aug 29, Sep 06 not shown). SML and SAU are shown in blue, SUN in pink, CNRL in yellow and SAJ in dark orange.

2.2.3 Mass balance approaches for determining CH₄ emissions

Following the TERRA methodology (Gordon et al., 2015), the time resolved measurements were interpolated using covariance kriging to produce a 40 m (horizontal, s) by 20 m (vertical, z) contiguous screen of CH₄ mixing ratios. Within TERRA, the CH₄ mixing ratios are extrapolated from the lowest transect (~150 m agl) to the surface using a constant, linear or half-gaussian extrapolation, depending on the type of source and the boundary layer conditions at the time.

Uncertainty estimates (see section A.1 in Supplemental) are included according to the various types of surface extrapolation applied. Interpolated matrices were constructed for measurements of air pressure (P_{air}) and temperature (T_{air}) in order to determine the air mass balance within the box and to convert mixing ratios to mass densities. Spatially equivalent interpolations of wind velocity perpendicular to aircraft motion (U_{\perp}) were created from the vector components of wind speed and direction measurements.

Emissions rates were determined according to the two different mass-balance approaches for screen and/or box flight patterns. Horizontal tracks at multiple altitudes flown perpendicular to the general wind direction produce a virtual screen downwind of the target that is intercepted by emission plumes from the facilities. Fluxes of CH_4 moving through each 40×20 m pixel (corresponding to size $s \times z$) can be determined from the interpolated matrices and integrated for a dimensional s by z target area according to Equation 2.1,

$$E_{\text{Screen}} = \iint_{s_1, z_b}^{s_n, z_t} ([\text{CH}_4] - [\text{CH}_4]_B) \times U_{\perp} ds dz \quad \{2.1\}$$

where $([\text{CH}_4] - [\text{CH}_4]_B)$ is the enhanced mixing ratio of CH_4 above background, U_{\perp} is the horizontal wind velocity perpendicular to the screen (e.g. $U \times \sin \theta$, θ = angle between wind vector and airplane vector), s_1 and s_n are the horizontal integration limits along the screen transect, z_b and z_t are the bottom and top vertical integration limits. Background mixing ratios of CH_4 were determined from the outside edges of the screens away from plume sources. Because $[\text{CH}_4]_B$ varies with height, a vertically variant background profile was subtracted from each vertical measurement column, an approach used in other mass balance determinations (Cambaliza et al., 2014; Karion et al., 2013). Example vertical profiles of $[\text{CH}_4]_B(z)$ for each day are included in Figure A.1 (Supplemental Information). The simple mass balance approach represented by Eq.2.1 can be applied to individual downwind screens from other flight paths (i.e. box flights) to determine CH_4 emissions from specific sources within a facility.

The second mass balance method used in this paper is to apply the full box-model TERRA algorithm (Gordon et al., 2015), to compute total emissions from all sources within a box, where the box is made up of multiple (4-6) screens forming a polygon encompassing a facility. This more rigorous mass balance approach used for calculating total emissions from a facility is represented by Equation 2.2

$$E_{Box} = E_{CH} + E_{CHT} + E_{CV} + E_{CVT} + E_{CM} \quad \{2.2\}$$

where E_{Box} , the total emissions rate from all sources within a box, is the sum of the horizontal advective and turbulent fluxes (E_{CH} and E_{CHT}), vertical advective and turbulent fluxes (E_{CV} and E_{CVT}), and the change in CH_4 mass within the box volume (E_{CM}). Because the box includes screens that are downwind, upwind and lateral to sources, incoming (background) and outgoing (background + source) fluxes are determined as a part of the horizontal flux terms (E_{CH} and E_{CHT}). Vertical fluxes through the box top, normally ignored in the conventional mass balance approaches (Eq. 2.1), are estimated according to the conservation of air mass within the box volume and the mixing ratio at the top edge of the box. E_{CM} is estimated according to the time derivative of the ideal gas law, based on measured changes in pressure and temperature over the flight time (see Gordon et al., 2015 for a full discussion).

The advantage of the box approach (Eq. 2.2) over the screen approach is a more precise estimate of total emissions by accounting for incoming and outgoing fluxes and meteorological effects within a volume. However, this flight pattern takes more time to completely surround a target facility. The advantage of the screen approach (Eq. 2.1) is the computation of CH_4 fluxes per pixel, which can thus be used to spatially integrate individual emission plumes of arbitrary shapes when the sources can be spatially resolved. Studies applying aircraft mass-balance methods have used each of single-height transect (Karion et al., 2013; Peischl et al., 2016), single screens (Cambaliza et al., 2014; Walter et al., 2012), spiral (Wratt et al., 2001; Gatti et al., 2014), and full box flight paths (Gordon et al., 2015) for the purpose of determining emissions rates and characterizing meteorological conditions. The aircraft flights presented contained various segments of tracks that allowed applications of all the above methods. In this work we apply a systematic approach deriving information from each of these techniques for a comprehensive

top-down characterization of CH₄ sources and emissions in the region. Single-height transects are used to determine source chemical signatures by identifying CH₄ enhancements and their associations with other trace-gas species. Vertical profiles are used to determine the PBL height throughout flights. Single screens are used to determine CH₄ emissions rates (Eq. 2.1) for facilities and their individual sources when plumes are spatially resolved. Box flights are used to determine total CH₄ emissions from facilities at a lower uncertainty (Eq. 2.2) and source-specific emissions are determined where possible (Eq. 2.1).

The summertime emission rates measured in this study are reported in units of metric tonnes CH₄ per hour, an appropriate unit given the duration of the flights (i.e., a few hours). We do not attempt to derive annual emissions as the assumptions needed to do so are highly uncertain without measurements in other seasons for a volatile species such as CH₄. However, we do make a first order comparison to emission inventories and other studies that report emissions on an annual basis by downscaling the annual emissions to hourly emission rates using an assumption of a constant temporal factor throughout the entire year. This is appropriate for emission inventories that are based upon measurement of emissions or emission factors in summer, that then upscale their emission rates of CH₄ to annual emissions using a constant temporal factor assumption (e.g., GOA, 2014). However, the assumption of a constant temporal factor is far from being validated and further measurements in different months are needed to understand the potential for seasonal variability of fugitive emissions of CH₄.

Previous work shows the box approach has a demonstrated uncertainty of 25-27% for total emissions of CH₄ from a facility in the AOSR (Gordon et al., 2015). Uncertainty due to extrapolation of CH₄ mixing ratios from the lowest height measurements to the surface was estimated to be 15% and 26% in that study. In contrast, screen approaches used in other studies have estimated uncertainty in the range of 30-50% (Cambaliza et al., 2014) with the main sources of error attributed to the reliability of plume characterization and the stability of meteorological conditions. In this study, uncertainties in both the box and screen estimates are reduced through i) a high number of transects over a wide vertical range to accurately characterize vertical structure in the PBL, ii) reliable measurements of background CH₄ (or incoming fluxes for boxes), iii) measurements of the PBL height to account for meteorological

variance, and iv) measurements within time periods of minimal PBL change. In addition, the enhancement of CH₄ in the plumes downwind of the facilities and high precision of the Picarro instrument minimize uncertainties in plume characterization and background CH₄. The overall uncertainty for computed CH₄ emission rates for an individual determination was estimated to be less than 30% (see Supplemental for a complete evaluation and discussion of uncertainties).

2.3 Results and discussion

2.3.1 Identification of sources of CH₄

Two example flights from three different facilities (SML, SUN and CNRL) are presented to demonstrate CH₄ emissions in the AOSR are mainly from three source types: open pit mining, tailings ponds, and facility activities. Emissions from the remaining two facilities (SAJ and SAU) were shown to be primarily open pit mining. Source categories were identified by measurements of CH₄, NO_y, BTEX, and rBC. Figure 2.2 shows measurements from one low-level transect of a screen flight on Aug 16, 2013 (9 transects in total). This transect was flown at a height of approximately 150 m agl downwind of the SML and SUN facilities, showing clear separation of emission sources from the two facilities. Four distinct plumes are visible, labelled A-D, with linear air parcel back-trajectories indicated in red arrows. Back trajectories were determined using the wind speeds and wind directions measured on the aircraft at flight level from the positions of maximum CH₄, back extrapolated as a general indicator of plume origin. This methodology creates a western bias in our plume origins. A more careful analysis of surface winds at several meteorological stations in the local vicinity at the time of the aircraft transect shows that surface wind directions were from ~ 140-180° (SE) compared to the flight level winds, ~220° (SW). The low level surface winds are likely channelled by the river valley, which runs in a SE to NW direction. Thus the trajectories of air masses originating at the surface and mixing upwards have a clockwise rotation, a very local effect, placing the actual plume sources further east than the linear tracks show in Figure 2.2. Plume A shows a maximum mixing ratio of 2.68 ppm CH₄, an enhancement of ~ 0.58 ppm above a background of ~2.1 ppm on this day in this region. This enhanced CH₄ is associated with values of 2.3 µg/m³ rBC and 47 ppb NO_y. The simple linear wind back-trajectory places the origin of the air mass near the western edge of open

pit surface mining activity ~100-min earlier, although as mentioned the actual source is likely slightly east of that location due to the clockwise rotation of the plumes. The combination of rBC and NO_y is indicative of exhaust of heavy hauler diesel trucks that operate in open pit mines. However, significant CH₄ emissions are not expected from the truck exhaust, as emissions factors of CH₄ from off-road gasoline and diesel combustion indicate that the CH₄/CO₂ emission ratio would be 1 to 2 orders of magnitude lower (Environment Canada, 2015) than the $\Delta\text{CH}_4/\Delta\text{CO}_2$ observed in this plume (0.58 ppm CH₄ / 16.1 ppm CO₂). Disturbance of the oil sands at the mine faces by the trucks is a well-known source of CH₄ with minor emissions of CO₂ and other VOC's (Strausz, 2003) as well as intermediate volatility organic compounds (Tokarek, 2017). Thus, Plume A is interpreted to be a combination of heavy truck exhaust, indicated by the presence of rBC and NO_y, that spatially overlaps with the mine face source of CH₄. Plume D shows a similar chemical profile with a maximum CH₄ of 2.40 ppm, ~ 0.30 ppm above background, associated with elevated levels of NO_y (40ppb) and rBC (1.5 µg/m³). The back-trajectory for Plume D is in agreement with an origin at one of two locations of open pit mining activity at SUN. The two plumes show a similar $\Delta\text{NO}_y/\Delta\text{rBC}$ ratio within the range of 15-30 ppb per ug/m³. We consistently measure this profile of NO_y and rBC enhancements from active mines across all five facilities.

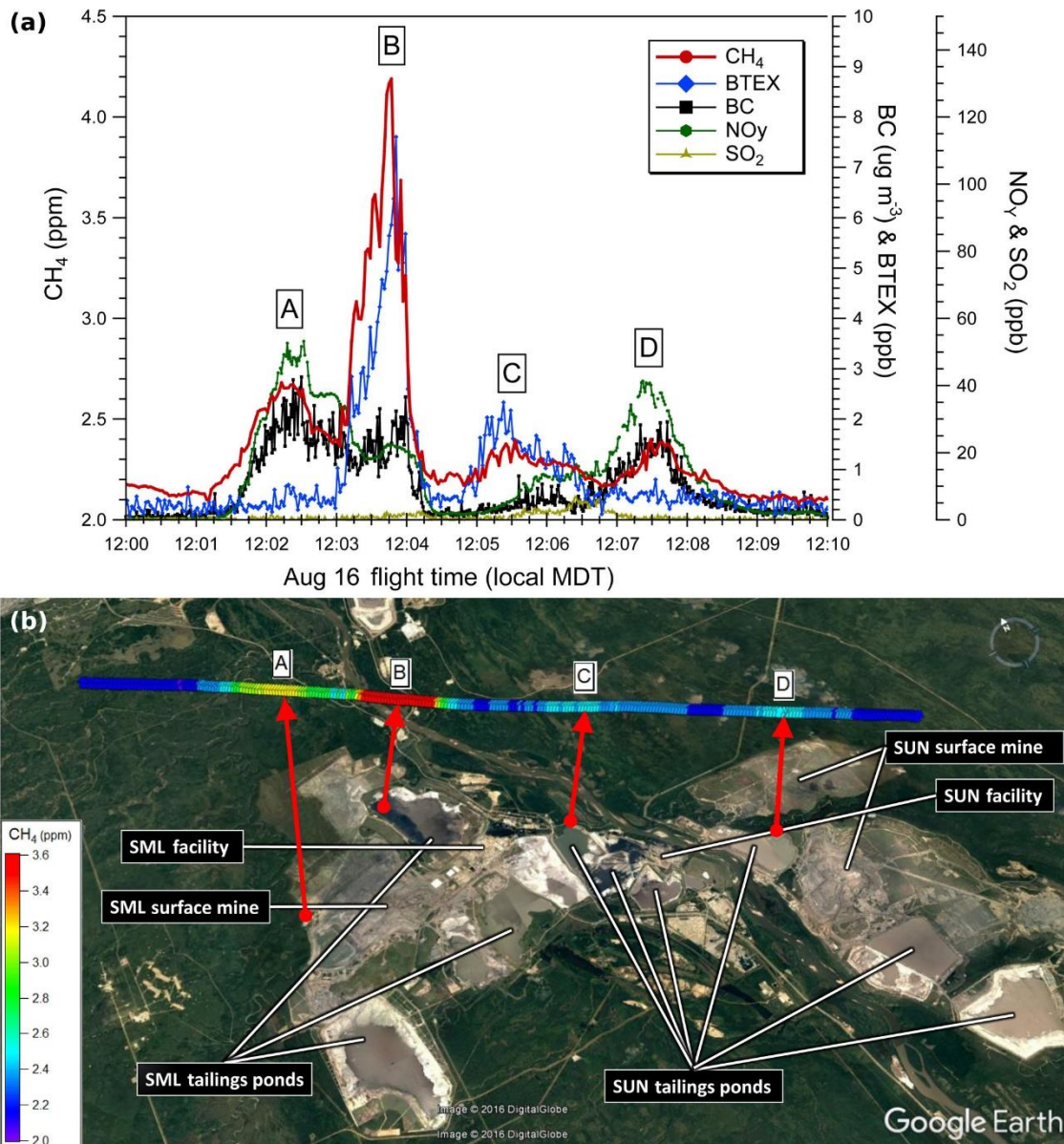


Figure 2.2: Top: Aircraft measurements of CH₄ (red), BTEX (blue) and rBC (black) from a single transect at 150 m agl downwind of SML and SUN on Aug 16. Four plumes are labelled A (SML Mine), B (SML Tailings), C (SUN Tailings), D (SUN Mine). Bottom: CH₄ mixing ratios along the 150 m agl transect for the above time series. Each data point is color coded for CH₄ mixing ratio as well as instantaneous wind vector measured on the aircraft at that location. Red arrows indicate air parcel back-trajectories based on linear back extrapolation of the aircraft measured wind vectors at plume centres, with end points at 100 min (A), and 20 min (B-D).

Plume B (Fig. 2.2) shows the highest CH₄ mixing ratio at 4.19 ppm, an enhancement of ~2.09 ppm above background. The back-trajectory from the position of the maximum CH₄ places the air mass over the western edge of Mildred Lake Settling Basin (MLSB) tailings pond ~ 20 minutes earlier. The CH₄ enhancement occurs simultaneously with a decrease in NO_y and rBC and an enhancement of total BTEX from ~0 ppb to a maximum of 7.6 ppb. Tailings ponds are known to contain significant quantities of BTEX compounds due to waste streams of mature fine tailings containing naphtha diluent flowing into the pond (Small et al., 2015). This is similar to the chemical profile observed in Plume C, with a back-trajectory placing the air mass over one of several possible SUN facility tailings ponds shown in Figure 2.2 (Ponds 6, Pond 5 and Pond 2/3 in figure Small et al, 2015). This indicates the presence of CH₄ emissions from multiple tailings ponds. Anaerobic digestion of organic matter in the tailings pond is the primary mechanism for the production of this biogenic CH₄ (Siddique et al., 2012). For Plume C the measured mixing ratio enhancements are 0.25 ppm CH₄ and 2.3 ppb of BTEX. The lower CH₄ enhancement compared to Plume B suggests less CH₄ is emitted from this pond, in agreement with Small et al (2015). The peak-to-peak CH₄/BTEX ratios from Plume B and Plume C are ~300 ppb ppb⁻¹, and ~100 ppb ppb⁻¹ respectively. The difference in measured inter-facility CH₄/BTEX ratios could arise from a number of factors including different pond ages, history, depth, methanogenic behaviour, or use of different diluents in each facility. The in-plume correlations of CH₄ with the associated tracers (NO_y, rBC and BTEX) for each of the Plumes identified in Figure 2.2 are shown in Figure A.2 (Supplemental Information).

Our observations are qualitatively consistent with pond-specific industry reported CH₄ emission factors, which present SML and SUN Ponds 2/3 (Small et al., 2015) as the highest CH₄ emitting tailings ponds in the region. We consistently measured relative enhancements from plumes downwind of SML and SUN according to the pattern of Plumes B and C in Figure 2.2, demonstrating the feasibility of using BTEX compounds as tracers for CH₄ being emitted from tailings ponds. We expect that BTEX would be greatly reduced from the tailings ponds of those facilities using paraffinic froth treatment (e.g., SAJ) instead of naphtha. In such cases, light hydrocarbons could in principle be used as tracers for the tailings ponds emissions of CH₄. However, we did not detect methane plumes above detection limit that were distinct from the

open pit mining plumes of CH₄ associated with rBC and NO_x for any facilities other than SML and SUN.

Elevated plumes from facility stacks are the primary sources of SO₂ in the AOSR due to the bitumen upgrading process. Hence, a significant enhancement of SO₂ can be used as a tracer for plant or stack CH₄ sources. However, this is not measured at the height shown in Figure 2.2, which shows a maximum SO₂ of only 5 ppb for this transect between Plumes C and D at 150 m agl. For the same flight (Figure 2.2), maximum SO₂ was 131 ppb for a transect ~350 m above ground, with an associated narrow peak of CH₄ with maximum mixing ratio of 2.11 ppm. While higher-altitude SO₂ plumes were frequently measured downwind of various facilities over the course of the aircraft campaign, in most cases no significant CH₄ enhancements were observed in these plumes. A similar case is discussed in Section 2.3.2 where we show the full range of vertical measurements and a lack of enhanced CH₄ in the SO₂ plume. Ground-level CH₄ from tailings ponds and open pit mine faces therefore dominate the CH₄ emissions in the region, with minor contributions from industrial plants.

We next compare the profiles from SML and SUN to a third facility, CNRL Horizon. Figure 2.3 shows a similar transect at ~150 m agl from the Sep 02 flight in the vicinity of CNRL. The bottom panel of Figure 2.3 shows that there was considerable wind divergence at this time (see back trajectory arrows for A, B, C). This wind divergence was also present in the next pass of the aircraft on the south side of CNRL at a height of 300m (not shown). While this divergence aids in the visualization of source separation, they invoke uncertainty in the mass balance determinations. The emission rates on Sep 02 were determined using ten transects from a flight much earlier in time than that shown in Fig 2.3., when the winds were more consistent in direction (NNW).

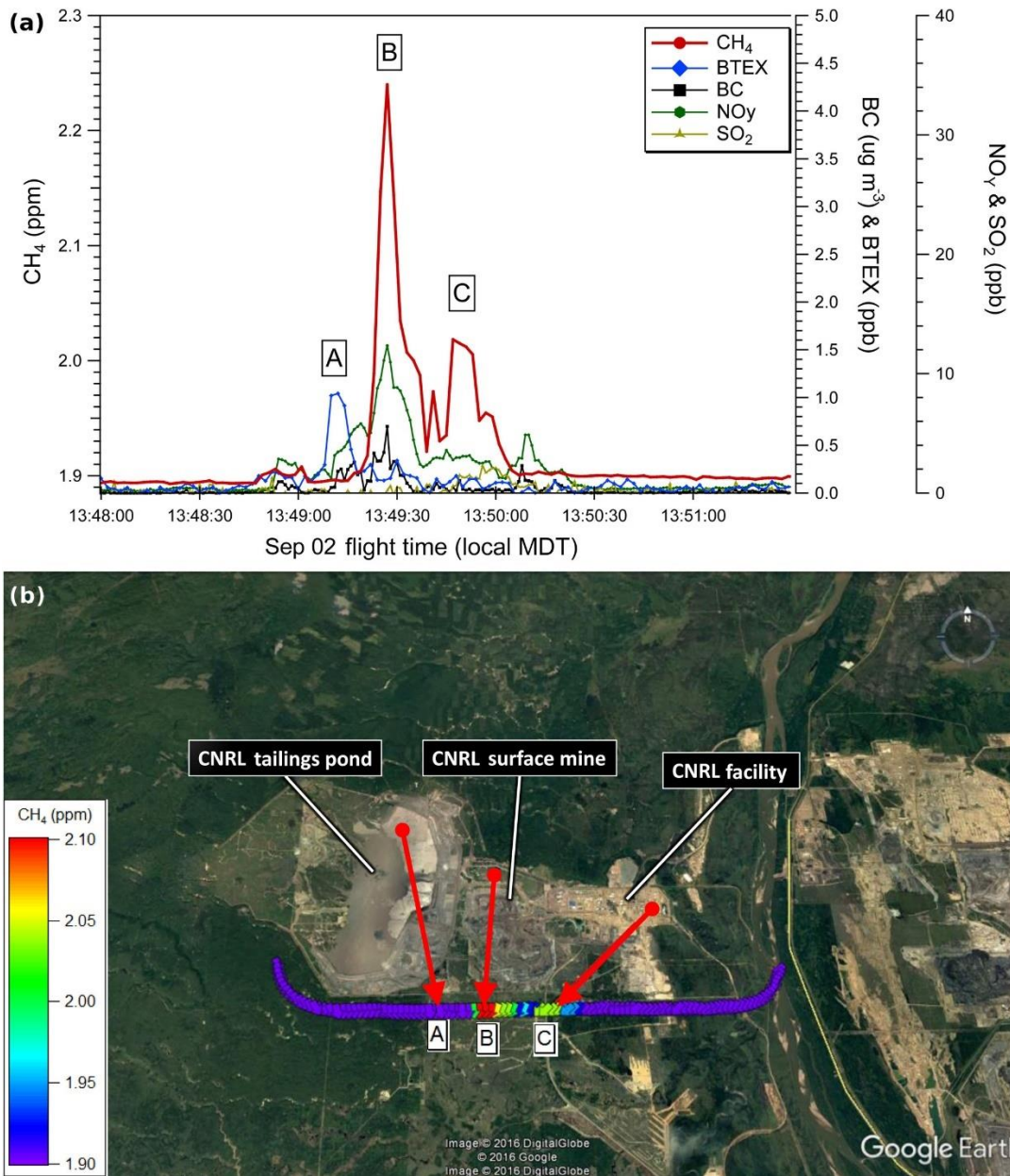


Figure 2.3: Top: Aircraft measurements of CH₄ (red), BTEX (blue) and rBC (black) from single transect ~150 m agl downwind of CNRL. Plume A (CNRL Tailings Pond), Plume B (CNRL Mine) Plume C CNRL Facility. Bottom: CH₄ mixing ratios along 150 m agl transect for above time series. Each data point is color coded for CH₄ mixing ratio as well as instantaneous wind vector measured on the aircraft at that location. Red arrows show back-trajectories based on linear extrapolation of measured wind speed and direction.

While Plume A shows a small enhancement of ~1 ppb BTEX downwind of the tailings pond, in contrast to SML and SUN no significant CH₄ was associated with it. This is consistent with the pond-specific emission factors presented in Small et al. (2015) that do not list the CNRL tailings pond as a significant source of CH₄. The primary Plume B included a CH₄ mixing ratio up to 2.24 ppm (enhancement of ~0.34 ppm above background) associated with 12 ppb NO_y and 0.7 ug/m³ rBC downwind of the CNRL mine. Consistent with the previously described open pit profile and the back trajectory, we identify Plume B as an open pit mining source of CH₄. A secondary Plume C was measured with maximum CH₄ of 2.02 ppm (enhancement of ~0.12 ppm) east of the open pit mine. The lack of associated species does not relate the origin of Plume C to either a tailings pond nor an open pit mine source of CH₄. The plume is downwind of the main CNRL plant and closer in horizontal proximity to SO₂ plumes measured during higher altitude transects. This suggests a CH₄ source near the main plant that could originate from venting or flaring activity, electricity cogeneration using natural gas or natural gas leakage. Thus the primary source of CH₄ from the CNRL facility is open pit surface mining activity with a secondary undetermined source from the main plant.

Source profiles of CH₄ are further compared to measurements of ethane (C₂H₆). Source-attribution studies for CH₄ commonly use higher ethane-to-methane ratios (EMRs) as a signature for oil and gas emissions, on both a regional (Peischl et al., 2016) and global (Hausmann et al., 2016) scale, while low EMR ratios can be indicative of microbial sources of methane that do not emit ethane (agriculture, landfills, wetlands, etc.) (Smith et al., 2015). C₂H₆, along with other VOC's, was measured from 20-second grab samples collected in 3-L Summa canisters. The VOC's were analysed offline using GC-MS and GC-FID methods described elsewhere [Li et al., 2017]. Table 2.1 shows C₂H₆ measurements from three different flights (Aug 14, Aug 16 and Sep 02) when canister sampling overlapped with the plume descriptions listed previously. In all cases shown, enhancements of C₂H₆ above background (0.8 – 1.5ppb) were in the range of only 1-2 ppb, normally the highest enhancements for each flight (within 1 ppb of 95th percentile). The small emissions rates of ethane (EMRs <1.4%) across flights contrasts with the high EMRs (i.e. 40-50%) seen for conventional oil and gas fields in other regions of North America (Peischl et al., 2016;Smith et al., 2015) and is lower than all the possible EMR source scenarios tested in

Hausmann et al. (2016). The problems associated with determining EMR ratios from a combination of continuous CH₄ measurements and discrete canister sampling of ethane from aircraft have been highlighted recently, where it was shown that actual EMR ratios determined in this way can be off by up to a factor of two (Smith et al., 2015). Thus the limited EMR data shown in the Table 2.1 are not intended to be a comprehensive measure of EMR in the AOSR but simply to support the conclusion that the major sources of methane from the facilities in the AOSR are microbial in nature without a significant co-emission of ethane. The low EMRs are consistent with previous measurements in the region (Simpson et al., 2010) and are an indication of the unique character of unconventional bitumen sources. As such, global estimates of the relative contributions of oil and gas emissions to decadal increases in atmospheric CH₄ that are based on C₂H₆ and CH₄ measurements in the free troposphere (Hausmann et al., 2016) would not capture AOSR emissions due to the low C₂H₆ emissions in this region.

Table 2.1: Enhancements of $\Delta\text{C}_2\text{H}_6$ from canister measurements overlapping with CH₄ plumes across three flights (Aug 14, Aug 16 and Sep 02). Mean enhanced ΔCH_4 is shown over the course of ~20s canister sampling times with ethane-to-methane ratios (EMRs) computed.

Scenario	$\Delta\text{C}_2\text{H}_6$ (ppb)	ΔCH_4 (ppb)	EMR (%)
SML Ponds (Aug 14)	3.2	814	0.40
SML Mines (Aug 14)	2.6	365	0.72
SUN Ponds (Aug 16)	1.2	215	0.56
SUN Mines (Aug 16)	1.1	185	0.59
CNRL (Sep 02)	1.9	137	1.39

2.3.2 Quantification of CH₄ emission rates from sources

The source chemical profiles in section 2.3.1 can be used in combination with the screen mass-balance method (Eq. 2.1) to isolate and quantify categories of AOSR emissions. As an example, we show the Aug 14 flight surrounding the SML facility, which consisted of a box and screen path flown in rapid succession. Figure 2.4 shows an image of the interpolated aircraft

measurements from the box path creating a contiguous mesh superimposed on a map of the region. Winds were from the south at 186 ± 48 degrees over the course of the day. Three distinct ground-based plumes of CH₄ are visible, a primary plume (Plume N) on the northern screen (~6500 m wide) exiting the box, a secondary plume (Plume NW) at the northwest corner (~7000 m wide) exiting the box and a smaller plume (Plume E) on the eastern screen (~3000 m in width) entering the box from outside the SML facility boundary. The lowest aircraft transect was at a height of ~150 m agl, with maximum CH₄ mixing ratios of 3.00 ppm, 2.60 ppm and 2.63 ppm respectively for the three plumes. Mixing ratios of CH₄ below 150 m agl, are based on a linear extrapolation of interpolated pixels to the surface, corresponding to maximum surface mixing ratios of 3.48, 3.17 and 3.06 ppm for the primary (N), secondary (NW) and tertiary (E) plumes respectively. Extrapolation to the surface is the primary source of uncertainty for surface sources in this method, however the uncertainty can vary between flights depending on the meteorological conditions (Gordon et al., 2015). As a part of our uncertainty analysis in the Supplemental material, we have included an uncertainty associated with the differences in emission rates that arise from the use of linear, constant and half-Gaussian extrapolations in the calculations.

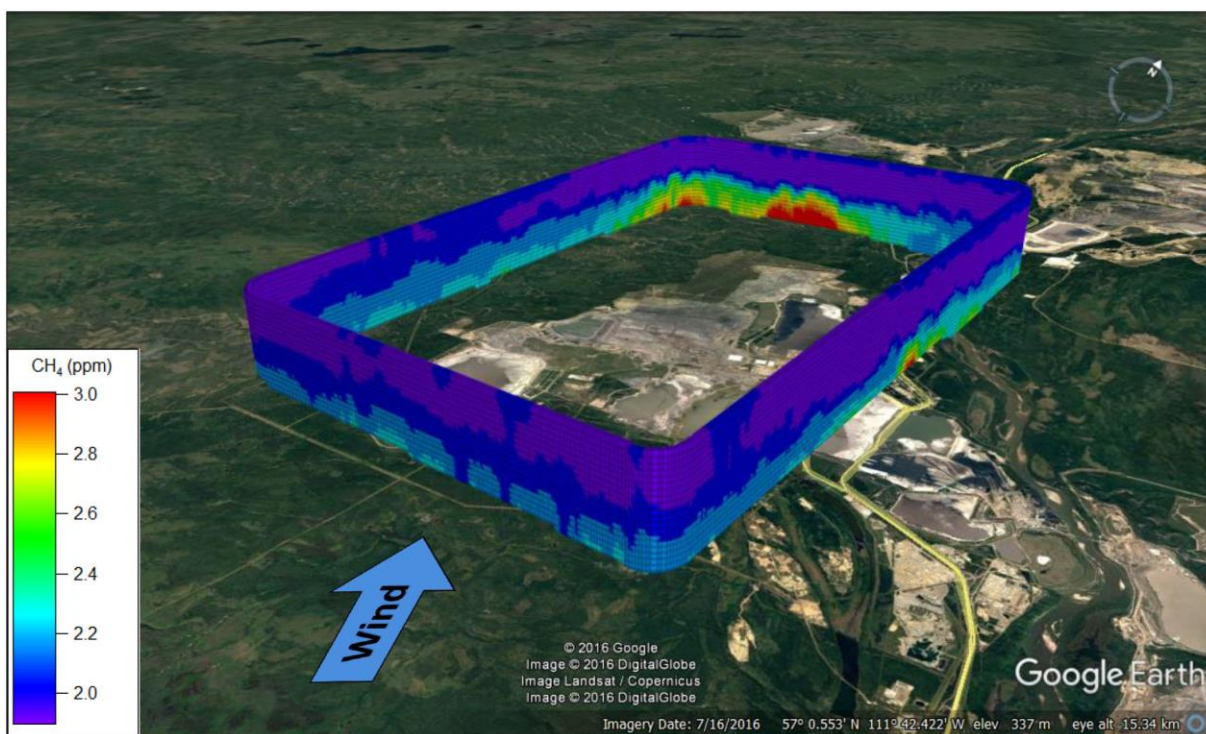


Figure 2.4: Interpolated CH₄ mixing ratios for the Aug 14 box flight surrounding SML.

Unwrapped curtain plots of CH₄, BTEX, NO_y, rBC and SO₂ from the Aug 14 box flight (Fig 2.4) are shown individually in Figure 2.5, projecting the 3-D virtual box onto a 2-D grid. The same three plumes from Fig 2.4 are highlighted by dotted boxes in red (N screen), yellow (NW corner), and black (E screen). The red and yellow boxes show sources originating from within the SML facility and the black boxes show a source originating outside of the SML boundaries and entering the box from the east. The largest SML CH₄ plume is associated with > 10 ppb BTEX and the absence of rBC and SO₂, with some NO_y (~20 ppb). This is consistent with the chemical signature associated with tailings pond emissions discussed previously. The NW plume is associated with >60 ppb of NO_y and up to 5 µg/m³ of rBC, with minimal BTEX and SO₂, consistent with the expected chemical signature from open pit surface mining. The smaller plume on the E screen is associated with elevated BTEX and CH₄ and is likely a plume from one of the SUN tailings ponds as the winds indicate the plume is entering the box. The elevated plume in Fig 2.5 (orange circles) with ~100 ppb SO₂ and ~30 ppb of NO_y is traced to the SML upgrader

activities, but with no enhancement of CH₄ above background on this day. A second NO_y plume is visible at the north-eastern corner of the box, not associated with any of the identified CH₄ source types. This NO_y plume likely originates from traffic on the main highway that passes between the SML and SUN facilities and/or trucks and other vehicles operating in and around the main SML facility.

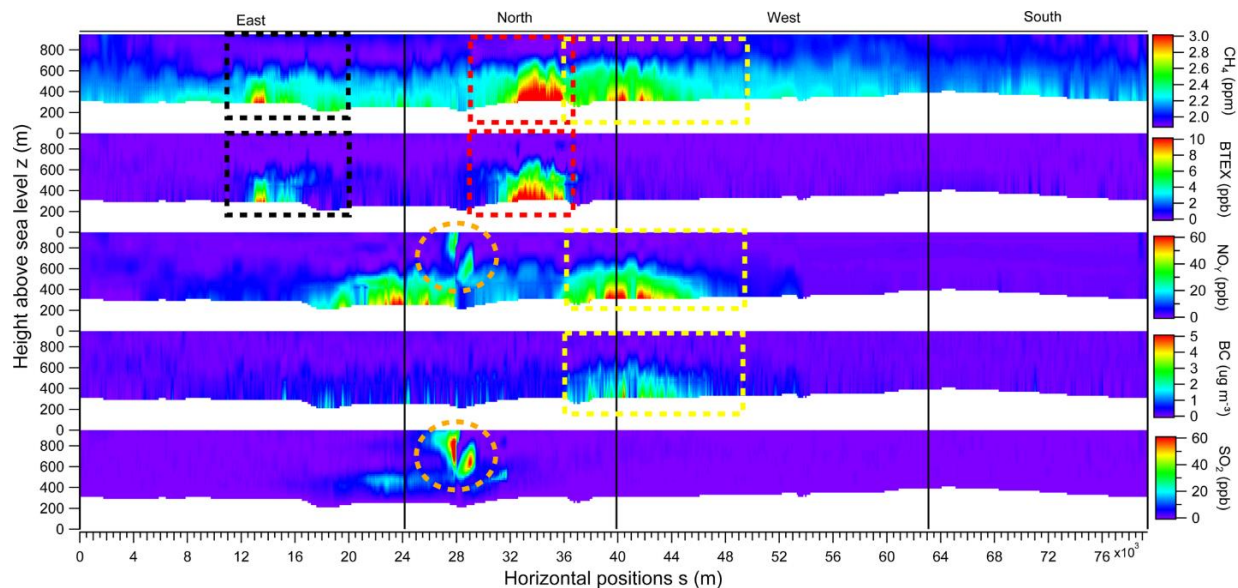


Figure 2.5: Curtain plots showing interpolated CH₄, BTEX, NO_y, rBC and SO₂ mixing ratios for the Aug 14 box flight around SML. Red-dashed box indicates the primary plume on the North screen, yellow-dashed box indicates the secondary plume on the West screen, and black-dashed box indicates the tertiary incoming plume on the East screen. Orange dashed-circle shows the upgrader plume on the North screen.

Boundaries of the plumes from separate sources are estimated using the tracer species listed in Fig. 2.5 by evaluating where the chemical signatures reached background levels. However, the SML tailings pond and open pit mine plumes were not completely resolved from one another, overlapping within a range of ~800 m. The uncertainties in the emission rates due to plume overlap were estimated by contracting and expanding the horizontal integration boundaries (s) by 800 m on each side (a total of ±1600 m) as part of the sensitivity analysis. A vertically varying

background profile ($[\text{CH}_4]_{\text{B}}(z)$) is determined using data from the upwind southern screen, as mentioned previously. Using a spatially identical screen of perpendicular wind $U_{\text{p}}(z)$, the fluxes are determined through each pixel and the total source emission is calculated by integrating the pixels within the plume boundaries (Eq. 2.1). CH_4 emission rates are computed to be 6.4 ± 1.2 metric tonnes per hour (tonnes hr^{-1}) for the SML main tailings pond and 2.7 ± 0.6 tonnes hr^{-1} for the SML open pit mine source. It is possible that the CH_4 plume from the SML tailings pond includes CH_4 emissions from the main SML plant facility (flaring, venting, natural gas leakage, etc.) that cannot be spatially separated from one another due to their proximity, however we anticipate the magnitude of these emissions are minor and captured within the error intervals listed.

This screen-based mass-balance approach for determining specific source emission rates (Eq. 2.1) is applied to flights with appropriate conditions for plume separation. Mean emissions rates of CH_4 from specific sources within the facilities SML, SUN, CNRL, SAU and SAJ are shown in Figure 2.6. SML emissions rates are the average of three mass-balance flights over two days (two on Aug 14 and one on Aug 16). Two flights on separate days were used for each of the SUN (Aug 16 and Aug 29), SAJ (Aug 21 and Sep 06) and SAU (Aug 29, Sep 06) facilities. One CNRL flight (Sep 02) had northerly wind conditions showing separation of sources on a southern screen. No significant daily variability is observed as the emissions rates for the same source agree within error. Duplicate and triplicate estimates for the same source are combined using an error-weighted uncertainty (Supplemental). SML and SUN had significant open-pit mining emissions of CH_4 , 2.8 ± 0.4 tonnes hr^{-1} and 1.8 ± 0.2 tonnes hr^{-1} respectively, and were the only facilities with tailings ponds emissions above detection limit, 6.4 ± 0.8 tonnes hr^{-1} and 2.4 ± 0.3 tonnes hr^{-1} . CNRL had open-pit mining emissions (2.6 ± 0.7 t/hr) and significant emissions originating from the main plant facility (1.0 ± 0.3 t/hr). Plumes of CH_4 from SAJ and SAU were only attributed to open-pit emissions, 1.2 ± 0.2 t/hr and 1.4 ± 0.2 t/hr respectively.

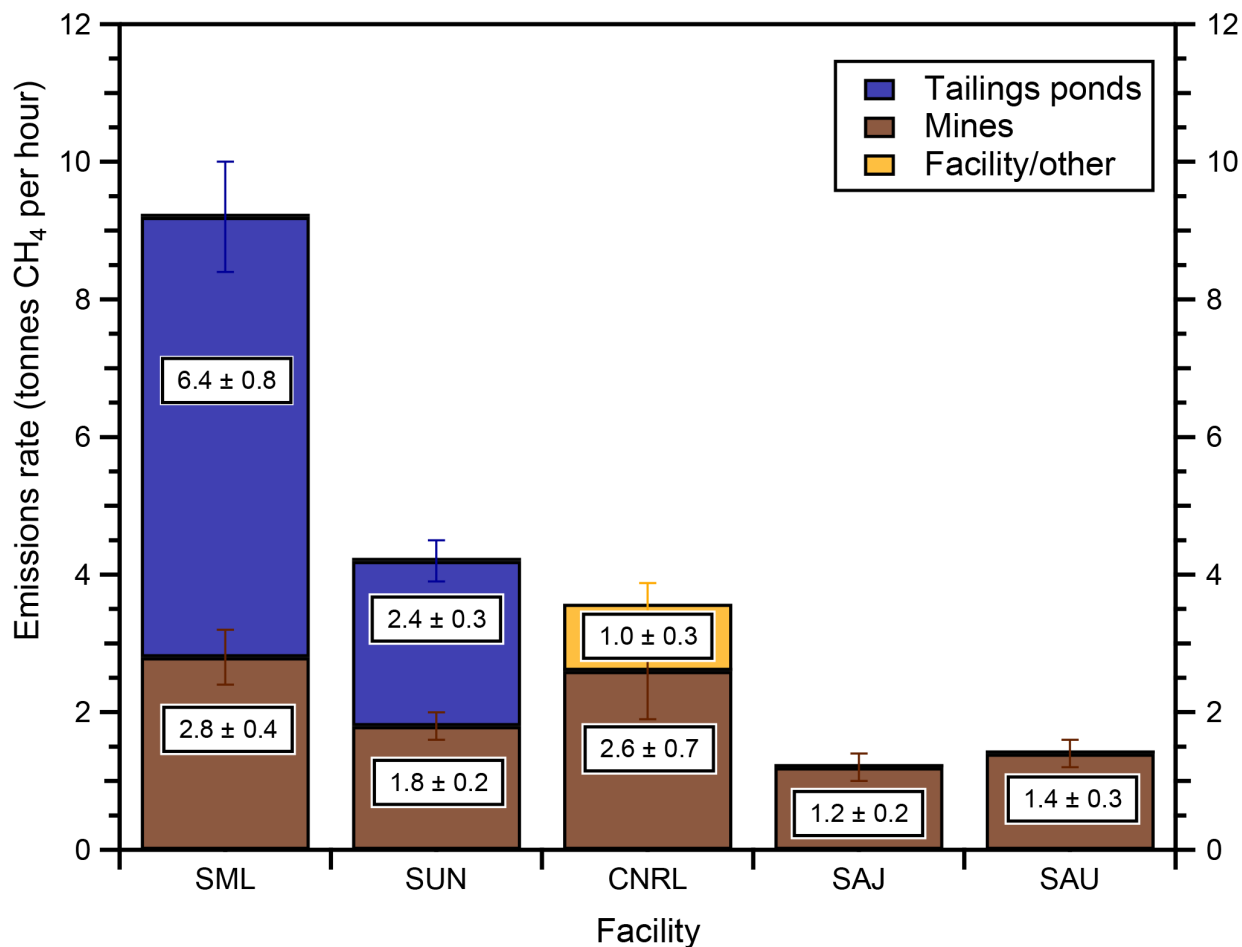


Figure 2.6: Source-apportioned emissions rates of CH₄ determined by the screen mass-balance method (Eq. 2.1) for the SML, SUN, CNRL, SAJ and SAU facilities. Emissions rates are the average of three mass-balance flights for SML over two days, two flights each for SUN, SAJ and SAU on separate days, and one flight for CNRL.

The plume-targeting screen mass balance method described here is unable to resolve emissions of CH₄ from multiple sources not characterized by the chemical profiles described in Section 2.3.1 if they cannot also be spatially separated. Because spatial s and z constraints are manually chosen by plume boundaries from chemical profiles, minor emissions may contribute to overestimation of the emissions from an individual source when highly coincidental in space such that the sources are not separable. For example, the emissions from the main plant were identifiable in the case of CNRL due to the separation and orientation of the plant, the open pit

and the tailings ponds with respect to the winds. This was not the case for the other major facilities in the AOSR where many of the sources were highly coincident in space. It is possible, and even likely, that other major facilities in this study also have CH₄ emissions from their main plants (venting, cogeneration, natural gas leakage, etc.) that are identified as tailings pond emissions or open pit emissions due to close proximity and our inability to deconvolute the sources spatially or chemically. However, we expect that the total emission rates of CH₄ from each facility are still accurate.

Emissions rates from each flight and individual sources (where possible) using the screen mass balance method are tabulated in the supplemental (Tables A.1-A.5). We did not measure a detectable tailings pond source of CH₄ from CNRL, SAJ and SAU. Associated enhancements of rBC and NO_y with CH₄ suggest that the CH₄ source from SAJ and SAU is also predominantly open pit mining. The results using the screen mass balance approach (Eq. 2.1) are further verified in Section 2.3.3 using emissions rates for each facility determined from the box approach (Eq. 2.2).

3.2.1 Comparison to Fugitive Emissions Literature

Average open pit surface mining emissions from the five facilities are within a range of 1.2-2.8 tonnes hr⁻¹ (Fig 2.6 and Table A.1-A.5). This shows some consistency in the nature of CH₄ release from open pit mining activity in the region, with differences that may possibly be attributed to the size of the surface disturbance taking place and the intensity of the mining activity. Methane emissions from open pit mines were recently estimated using a bottom-up emissions factor approach by analysing the gaseous composition in the overburden and oil sand component of drill core samples (Johnson et al., 2016). Emissions factors of CH₄ were then scaled up according to the total mass of material mined or the total bitumen produced. For 2013, Johnson et al. estimate total fugitive mining emissions in the region to be 21.4-46.0 ktonnes of CH₄ using total mined material, and 33.1-85.0 ktonnes of CH₄ using total mined bitumen. Our top-down approach estimates total fugitive emissions from open pit mining to be 9.7 ± 0.9 tonnes hr⁻¹, corresponding to 84.9 ± 7.9 ktonnes yr⁻¹ CH₄ if constant temporal emissions are assumed. Agreement with the upper estimates in Johnson (2016), despite the uncertainty associated with extrapolation to annual emissions, suggests that their bottom-up emissions factors from gases in

core samples may reliably predict real-world emissions provided there is accurate characterization of CH₄ in the core samples over the entire disturbed area. This is reasonable considering that it would be expected that degassing of an extremely volatile gas such as CH₄ from the oil sands material would be quantitative in a short period of time after the ore is exposed or crushed.

From our 2013 measurements, only two facilities, SML and SUN, had significant emissions of CH₄ from tailings ponds. Tailings ponds emissions accounted for ~70% and ~58% of total CH₄ from SML and SUN respectively. This accounted for ~45% of total emissions in the AOSR. Recently, bottom-up area-weighted emissions factors of CH₄ from 19 major tailings ponds in the AOSR were provided for the year 2012 (Small et al., 2015). The top three emitting ponds reported were ‘Mildred Lake Settling Basin’ (MLSB) and the ‘West In-Pit’ (WIP) pond within SML, and ‘Pond 2/3’ (P23) within SUN. These tailings ponds account for >96% of tailings ponds CH₄ in the region according to that study. This is qualitatively consistent with our measurements of CH₄ mainly from SML and SUN. Our method requires CH₄ plumes to be clearly enhanced above background, so trace amounts of CH₄ from ponds in the other three facilities were not detected. This could be related to differences in the chemical composition of the process streams being released into these ponds, or it could simply be due to these ponds being younger in age, with insufficient time for the anaerobic methanogenic communities to be established (Small et al., 2015). We are unable to differentiate emissions from ponds within the same facility due to overlapping chemical profiles from ponds within close proximity. However, using the ratios of relative pond emissions rates within the same facility presented in Small et al. (2015), (i.e. MLSB contributes 92% to SML emissions, Ponds 2/3 contribute 85% to SUN), we can infer individual pond emissions from our measurements assuming the relative contributions are accurate. The resulting emissions rates are 5.8 ± 0.8 tonnes hr⁻¹ for MLSB and 2.0 ± 0.3 for Ponds 2/3. This ranks the MLSB tailings pond as the highest area source of CH₄ in the AOSR, followed by the open-pit mines in SML and CNRL, and fourth Ponds 2/3 in SUN. Total CH₄ from tailings ponds in Small et al. (2015) are estimated to be 30.3 ktonnes of CH₄ per year, with 29.7 ktonnes of CH₄ from the SML and SUN facilities (~98%). Our total CH₄ emission rate determined for tailings ponds is 8.8 ± 0.9 tonnes hr⁻¹, which corresponds to 77.1 ± 7.9 ktonnes yr⁻¹.

¹ if a constant temporal factor is assumed. This is 2.3-2.9 times larger than the emissions inferred from the data in Small et al (2015), despite the uncertainty of extrapolation to an annual emissions rate. Our measurements suggest more work is needed to reconcile top-down and bottom-up CH₄ emissions.

2.3.3 Emission rates of CH₄ from AOSR facilities

Total emissions rates of CH₄ from each facility determined using the box mass balance method (TERRA) are tabulated in the supplemental (Tables A.1-A.5) along with the determinations using the screen approach. Where multiple screen estimates or multiple box estimates were available, uncertainty weighted ($1/\sigma^2$) averages were determined for each method for each facility and are summarized in Table 2.2. While the box method is in some cases based on the same downwind measurements as the screen approach, the two methods have several key differences (described in 2.3) and are treated as independent estimates. In particular, the box method does not resolve specifically targeted, individual plumes and instead determines the net outgoing flux from the closed volume surrounding the facility. Thus, consistency between the two estimates is evidence that the primary sources of CH₄ from facilities in the AOSR are tailings ponds, open pit mines and facility emissions captured by the source characterization in sections 2.3.1 and 2.3.2. In general, the total emissions from each facility using the screen and box methods are in agreement within uncertainty, which adds confidence to the measured emission rates reported here. In the final row of Table 2.2, we calculate a weighted average emission rate for each facility using all screen and box measurements. The CH₄ emission rates from the facilities are 8.6 ± 0.9 , 4.2 ± 0.4 , 3.6 ± 0.5 , 1.3 ± 0.2 , and 1.5 ± 0.2 tonnes CH₄ hr⁻¹ from the SML, SUN, CNRL, SAJ and SAU facilities, respectively.

3.4 Total emissions of CH₄ from the AOSR

The total CH₄ emissions from the five mining facilities in the AOSR, obtained by summing the best estimates (i.e., uncertainty weighted average of multiple measurements, bottom row, Table 2.2) of the individual facility emission rates is given in the final row and column of Table 2.2. The 5-facility total emission rate of CH₄ is 19.2 ± 1.1 tonnes CH₄ hr⁻¹. A final independent estimate of total AOSR emissions was obtained from a flight on Aug 16, utilizing an independent

transect screen ~75 km wide (Aug 16 Screen B) downwind of all major mining facilities in the AOSR (excluding Imperial Kears Lake and Suncor Firebag operations; but also inclusive of any emissions from Suncor MacKay River in-situ facility). The details of this flight are given in Supplemental Table A.6. The interpolated screen from the Aug 16 flight (Total OS) is shown in Figure 2.7. The screen was constructed from 10 aircraft horizontal transects from 250-900 m agl. Enhancements of CH₄ were measured over a wide horizontal subrange of ~60 km of the entire ~75 km screen. Winds were perpendicular to the plane from the southwest (225°), showing a large flux of CH₄ through the screen from upwind sources. The highest measured mixing ratios of CH₄ were 2.67 ppm at the ~250 m (agl) transect. Background CH₄ in the region was ~2.00 ppm taken as a vertical profile from the wings of the screen. Using the screen method (Eq. 2.1), the emissions rate was determined to be 23.0 ± 3.7 tonnes CH₄ hr⁻¹, which represents the emissions from all major facilities within the AOSR domain. This AOSR total is only slightly larger than the previous 5-facility total emission rate of 19.2 ± 1.1 tonnes hr⁻¹, but not statistically so, demonstrating the reproducibility of our measured estimates. It is entirely possible that there are other minor sources of CH₄ included in this larger number from smaller industrial operators in the region, trucks and vehicles on the main highway, and wetland emissions. In fact, the Canadian GHGRP inventory (see section 2.3.5) indicates that there is an additional 0.13 tonnes CH₄ hr⁻¹ emitted upwind and 0.17 tonnes CH₄ hr⁻¹ emitted downwind of the aircraft screen (Fig 2.7) from minor industrial facilities within the AOSR (both numbers downscaled from the facility reported annual emissions). The amount of CH₄ emitted from vehicles on the highway though is expected to be smaller. The fact that the two numbers are not statistically different supports the determination that the majority of the CH₄ in the AOSR is emitted from the 5 major industrial facilities in the region. The two values are combined here using an error-weighted uncertainty resulting in a final AOSR facility emissions estimate of 19.6 ± 1.1 tonnes CH₄ hr⁻¹, measured during a summertime period.

Table 2.2: Comparison of emissions rates (in tonnes CH₄ hr⁻¹) determined from the screen approach (n estimates per facility), the box-approach (n estimates per facility), and the uncertainty weighted average for each method and facility. The 5-facility AOSR total is show in the final column and row.

Method	SML (n)	SUN (n)	CNRL (n)	SAJ (n)	SAU (n)	Total AOSR
Screen	9.1±0.9 (3)	4.2±0.4 (2)	3.6±0.8 (2)	1.2±0.2 (2)	1.4±0.2 (2)	
Box	7.7±1.5 (1)	3.9±0.9 (1)	3.6±0.6 (2)	1.4±0.2 (2)	1.7±0.3 (1)	
Average	8.6±0.9 (4)	4.2±0.4 (3)	3.6±0.5 (4)	1.3±0.2 (4)	1.5±0.2 (3)	19.2 ± 1.1

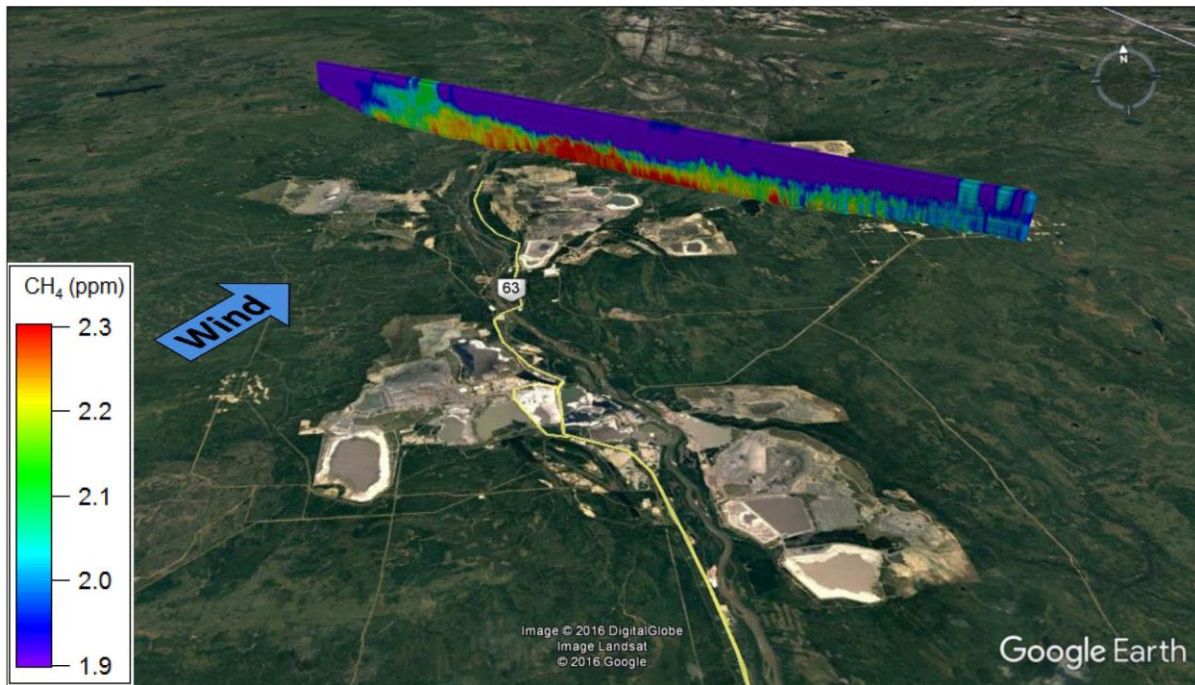


Figure 2.7: Map image showing interpolated CH₄ mixing ratios for the Aug 16 Total Oil Sands screen.

2.3.4 Comparison to emission inventories

Emissions of anthropogenic greenhouse gases are estimated by ECCC in Canada's GHG Inventory, which forms the basis for Canada's annual report to the United Nations Framework Convention on Climate Change, UNFCCC (ECCC, 2016). Currently, industrial facilities that emit more than 50 ktonnes CO₂eq yr⁻¹ are required to report their emissions annually to ECCC using the Greenhouse Gas Reporting Program (GHGRP), which is Canada's legislated, publicly accessible inventory of facility-reported greenhouse gas (GHG) data (ECCC, 2017b). Although the GHGRP inventory data is not necessarily used in Canada's GHG Inventory, changes are being proposed to expand monitoring requirements in the GHGRP, including lowering the reporting threshold to 10 ktonnes CO₂eq yr⁻¹ in order to enable direct use of the reported data in Canada's GHG Inventory (ECCC, 2017a). Emissions of CH₄ from all five major oil sands facilities discussed in this paper are present in the GHGRP Emissions Inventory on an annual basis. The annual emission rates of CH₄ extracted from the inventory were downscaled to hourly emissions rates for comparison with our measurements with an assumption of equal seasonal and diurnal profiles 365 days a year, 24 hours per day; for consistency with upscaling factors used to generate annual emissions (see Figure 2.8). While this may be questioned, it should be noted that fugitive emissions of CH₄ from mine faces and tailings ponds in the inventories are estimated based upon emission factors measured at oil sands facilities during summer months (June- Sept), which are then up scaled from hourly emissions to annual emissions using the same assumption that we used to downscale (365 x24), as per recommendation by the Government of Alberta (GOA, 2014). Specifically it is noted from the GOA report that emissions of gaseous species such as CH₄ (and CO₂) are not temperature dependent (unlike VOC's that have temperature dependent vapour pressures (Li et al., 2017)). The argument used to justify the use of a constant seasonal temporal factor in the GOA report is that temperatures at depth in a tailings pond are said to remain relatively constant throughout the year and thus, biogenic gas formation continues in the winter (GOA, 2014). For mine faces, the GHG component of the oil sand does not change with temperature and is likely released completely in a short period of time after being mined. Thus the government recommendation to oil sand facilities in preparing annual emission estimates of fugitive GHG's is that reduction factors should not to be used in extrapolating

summertime emissions over the rest of the year (GOA, 2014). Figure 2.8 shows a comparison of the total measured emission rates of CH₄ from the five industrial facilities (2013), the total measured CH₄ emission rate in the AOSR from the single downwind screen on Aug 16, 2013 and the sum of the facility emission rates from the Canadian GHGRP Emissions Inventory for 2013, expressed in hourly units. The combined facility emissions rate of 19.6 ± 1.1 tonnes hr⁻¹ is approximately 48 ± 8 % higher than the 5-facility total of 13.2 tonnes hr⁻¹ extracted from the inventory for 2013. Facility-to-facility comparisons show higher measured than reported emission rates for three out of the four facilities (SML and SAU facilities are combined as one in the inventory). In contrast, for CNRL our measured emission rate is 1.2 tonnes hr⁻¹ lower than the inventory. Since we have determined the composition of SML, SUN and SAJ emissions to be primarily from tailings ponds and open pit mining, there appears to be underestimation in the inventory of those particular area sources within these sites.

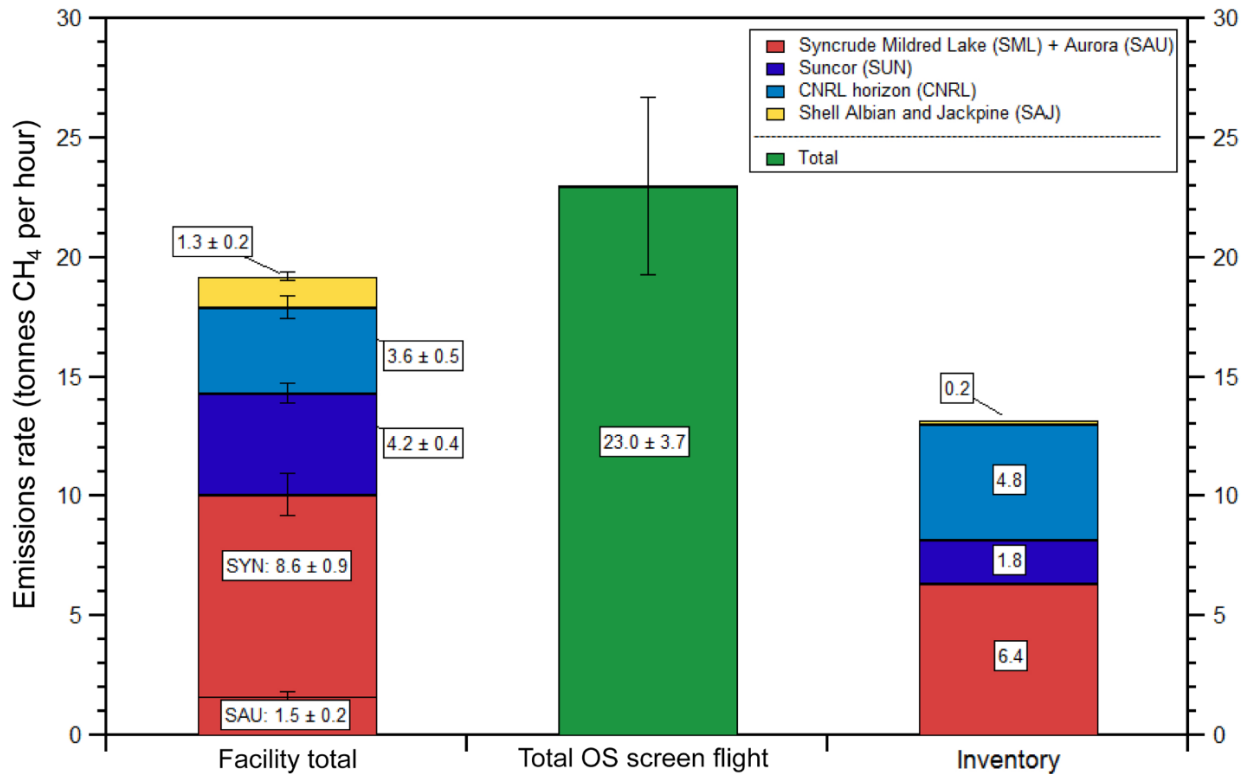


Figure 2.8: Comparison of emissions rates determined for the five major facilities (SML, SAU, SUN, CNRL, SAJ) with the Total OS Screen Flight (see Fig. 2.7 for the flight track). Also shown is the CH₄ emissions taken from the Canadian GHGRP Emissions Inventory for the year 2013, scaled down from annual to hourly emissions assuming constant temporal emissions. Note that in the inventory, SML and SAU emissions are reported as a single facility, while our estimates are derived separately.

These discrepancies indicate a need for inventory reconciliation between the bottom up and top-down estimates. It has been shown possible to reconcile divergent bottom-up and top-down CH₄ estimates for the Barnett Shale by using more comprehensive activity factors and better characterization of emissions from high emitter sites (Lyon et al., 2015) and continuous monitoring to identify these super emitters (Zavala-Araiza et al., 2015). Currently, bottom-up estimates in the AOSR are accomplished by systematic surface flux chamber measurements of area sources (surface mines, tailings ponds) to derive area-based emissions factors (GOA, 2014). While surface flux chamber measurements (Klenbusch, 1986; Conen and Smith, 1998) are

estimated to be 50-124% of the true emissions rate for a homogenous source (Klenbusch, 1986), it is unclear how the uncertainty propagates when the emissions factors are scaled to the full surface area of the heterogeneous AOSR emissions sources. The official survey protocol for open pit sources attempts to minimize the possibility of underestimating emissions by explicitly requiring fugitive surveys to include sampling at a range of locations within the open pit mine, where safe to do so, including high priority zones (disturbed in the last week), normal priority zones (disturbed from 1 week to 6 months ago) and low priority zones (disturbed > 6 months ago) (GOA, 2014). However, it seems that the recent core sampling methodology outlined by Johnson et al. (2016) has great promise and reduced uncertainty for estimating fugitive emissions from open pit mining.

2.4 Conclusions

We present a detailed approach to identifying and quantifying CH₄ emission sources from the surface mining facilities in the Athabasca Oil Sands Region of Alberta in the year 2013. Emissions of CH₄ are attributed to three major fugitive source types: tailings ponds, open pit mining activity, and emissions from plant facilities. Our method demonstrates the use of BTEX/VOCs as tracers for tailings ponds CH₄ plumes due to the use of diluent, and NO_y/rBC as tracers for surface mining due to heavy hauler diesel trucks operating co-spatially at mine faces in the open pit mines. The combination of SO₂/NO_y is used as a tracer for stack facility plumes which are observed to contain minor but detectable quantities of CH₄, although infrequently. We use the chemical signatures of sources and the screen mass-balance approach for 7 flights to determine total emissions rates of 8.8 ± 0.9 tonnes hr⁻¹ from tailings ponds, 45% of total CH₄ emissions in AOSR, 9.8 ± 0.9 tonnes hr⁻¹ from open pit surface mining (50%), and 1.0 ± 0.3 tonnes hr⁻¹ primary facility-associated and other sources (5%). Open pit mining emissions are measured from all five facilities in the range of 1.2-2.8 tonnes hr⁻¹. In contrast amongst the 19 tailings ponds in the region, CH₄ emissions above determinable levels were only measured from two facilities, SML and SUN. These emissions are likely due to two tailings ponds, MLSB (5.8 ± 0.8 tonnes hr⁻¹) and Ponds 2/3 (2.0 ± 0.3), which are ranked amongst the highest area sources of CH₄ in the region. These results demonstrate the large contributions (~45%) of a few tailings

ponds sources to total fugitive CH₄ emissions in the AOSR and highlight opportunities for strategic GHG mitigation. Our individual-plume sum is consistent with estimates derived using the TERRA box approach to determine total emissions within facility boundaries. The agreement between these two methods demonstrates that the three source types listed are representative of the major emissions of CH₄ in the AOSR. Further results from a ~75km flight screen that captured almost all AOSR emissions are able to reproduce total emissions derived from the sum of the five major facilities. Our final top-down estimate of the 2013 summertime emission rate in the region is 19.6 ± 1.1 tonnes CH₄ hr⁻¹ or 0.17 ± 0.1 Tg CH₄ yr⁻¹. We note that the annual emissions rate is only a first order approximation of what annual emissions might be if the temporal emissions are constant throughout the year; however, we consider this assumption to be highly uncertain as the seasonality of fugitive emissions rates of CH₄ in the Athabaska Oil Sands region is still a major uncertainty. Further effort should be devoted to measurements of these emission rates in different seasons, and to understand if ambient temperature and ice coverage on tailings ponds are important parameters or not. Our limited measurements of ethane and methane downwind of the AOSR facilities suggest that the EMR's are quite low, < 1.4%, likely because the fundamental source of the majority of the methane emissions are methanogenic, not thermogenic, in nature. Thus global estimates of the relative contributions of oil and gas emissions to increases in atmospheric CH₄ based on EMR measurements in the free troposphere would not capture AOSR emissions due to the low C₂H₆ emissions in the region.

Acknowledgements

Funding for the measurement campaign and the subsequent analysis was provided by the Climate Change and Air Pollution program of Environment and Climate Change Canada and from the Canada-Alberta Joint Oil Sands Monitoring Program. We thank the Convair-580 flight crew of the National Research Council of Canada, especially the pilots (Paul Kissmann, Rob Erdos and Tim Leslie), for conducting the aircraft flights. We thank the technical support staff, especially Andrew Sheppard, and the Data Management Team of the Air Quality Research Division for their hard work and support throughout the aircraft campaign. We thank Stewart Cober for his review of this manuscript, management in the field and skills as a flight director.

RM and SB acknowledge funding from NSERC Discovery and a grant from ECCC to support some of this work. SB & RM also acknowledge funding from the NSERC CREATE program, Integrating Atmospheric Chemistry and Physics from Earth to Space (IACPES).

References

- Allen, D., Pickering, K., and Fox-Rabinovitz, M.: Evaluation of pollutant outflow and CO sources during TRACE-P using model-calculated, aircraft-based, and Measurements of Pollution in the Troposphere (MOPITT)-derived CO concentrations, *Journal of Geophysical Research: Atmospheres*, 109, n/a-n/a, 10.1029/2003JD004250, 2004.
- Brandt, A. R., Heath, G. A., Kort, E. A., O'Sullivan, F., Pétron, G., Jordaan, S. M., Tans, P., Wilcox, J., Gopstein, A. M., Arent, D., Wofsy, S., Brown, N. J., Bradley, R., Stucky, G. D., Eardley, D., and Harriss, R.: Methane Leaks from North American Natural Gas Systems, *Science*, 343, 733-735, 10.1126/science.1247045, 2014.
- Bruhwyler, L. M., Basu, S., Bergamaschi, P., Bousquet, P., Dlugokencky, E., Houweling, S., Ishizawa, M., Kim, H. S., Locatelli, R., Maksyutov, S., Montzka, S., Pandey, S., Patra, P. K., Petron, G., Saunio, M., Sweeney, C., Schwietzke, S., Tans, P., and Weatherhead, E. C.: U.S. CH₄ emissions from oil and gas production: Have recent large increases been detected?, *Journal of Geophysical Research: Atmospheres*, 122, 4070-4083, 10.1002/2016JD026157, 2017.
- Cambaliza, M. O. L., Shepson, P. B., Caulton, D. R., Stirm, B., Samarov, D., Gurney, K. R., Turnbull, J., Davis, K. J., Possolo, A., Karion, A., Sweeney, C., Moser, B., Hendricks, A., Lauvaux, T., Mays, K., Whetstone, J., Huang, J., Razlivanov, I., Miles, N. L., and Richardson, S. J.: Assessment of uncertainties of an aircraft-based mass balance approach for quantifying urban greenhouse gas emissions, *Atmos. Chem. Phys.*, 14, 9029-9050, 10.5194/acp-14-9029-2014, 2014.
- Conen, F., and Smith, K. A.: A re-examination of closed flux chamber methods for the measurement of trace gas emissions from soils to the atmosphere, *European Journal of Soil Science*, 49, 701-707, 1998.
- ECCC: National Inventory Report 1990-2014: Greenhouse Gas Sources and Sinks in Canada, Executive Summary, Environment and Climate Change Canada, Gatineau, QC, 1-14, 2016.
- Greenhouse Gas Emissions Reporting Program: Expansion of the GHGRP
<https://www.ec.gc.ca/ges-ghg/default.asp?lang=En&n=F891687A-1>, access: July 27, 2017, 2017a.
- Facility Greenhouse Gas Reporting, Greenhouse Gas Emissions Reporting Program:
<https://www.ec.gc.ca/ges-ghg/default.asp?lang=En&n=040E378D-1>, access: July 27, 2017, 2017b.
- Edwards, P. M., Young, C. J., Aikin, K., deGouw, J., Dube, W. P., Geiger, F., Gilman, J., Helmig, D., Holloway, J. S., Kercher, J., Lerner, B., Martin, R., McLaren, R., Parrish, D. D., Peischl, J., Roberts, J. M., Ryerson, T. B., Thornton, J., Warneke, C., Williams, E. J., and Brown, S. S.: Ozone photochemistry in an oil and natural gas extraction region during winter: simulations of a snow-free season in the Uintah Basin, Utah, *Atmospheric Chemistry and Physics*, 13, 8955-8971, 10.5194/acp-13-8955-2013, 2013.
- Edwards, P. M., Brown, S. S., Roberts, J. M., Ahmadov, R., Banta, R. M., deGouw, J. A., Dube, W. P., Field, R. A., Flynn, J. H., Gilman, J. B., Graus, M., Helmig, D., Koss, A., Langford, A. O., Lefer, B. L., Lerner, B. M., Li, R., Li, S.-M., McKeen, S. A., Murphy, S. M., Parrish, D. D., Senff, C. J., Soltis, J., Stutz, J., Sweeney, C., Thompson, C. R., Trainer, M. K., Tsai, C., Veres, P. R., Washenfelder, R. A., Warneke, C., Wild, R. J., Young, C. J., Yuan, B., and Zamora, R.: High winter ozone pollution from carbonyl photolysis in an oil and gas basin, *Nature*, 514, 351-354, 10.1038/nature13767, 2014.
- Fujita, E. M., Croes, B. E., Bennett, C. L., Lawson, D. R., Lurmann, F. W., and Main, H. H.: Comparison of Emission Inventory and Ambient Concentration Ratios of CO, NMOG, and NO_x in California's South

Coast Air Basin, *Journal of the Air & Waste Management Association*, 42, 264-276, 10.1080/10473289.1992.10466989, 1992.

Fujita, E. M., Watson, J. G., Chow, J. C., and Magliano, K. L.: Receptor model and emissions inventory source apportionments of nonmethane organic gases in California's San Joaquin valley and San Francisco bay area, *Atmospheric Environment*, 29, 3019-3035, 1995.

Gatti, L. V., Gloor, M., Miller, J. B., Doughty, C. E., Malhi, Y., Domingues, L. G., Basso, L. S., Martinewski, A., Correia, C. S. C., Borges, V. F., Freitas, S., Braz, R., Anderson, L. O., Rocha, H., Grace, J., Phillips, O. L., and Lloyd, J.: Drought sensitivity of Amazonian carbon balance revealed by atmospheric measurements, *Nature*, 506, 76-80, 10.1038/nature12957, 2014.

GOA: Quantification of area fugitive emissions at oil sands mines, Government of Alberta, AlbertaESRD, *Climate Change*, 2014, No. 1, 1-15, 2014.

Gordon, M., Li, S. M., Staebler, R., Darlington, A., Hayden, K., O'Brien, J., and Wolde, M.: Determining air pollutant emission rates based on mass balance using airborne measurement data over the Alberta oil sands operations, *Atmos. Meas. Tech.*, 8, 3745-3765, 10.5194/amt-8-3745-2015, 2015.

Hausmann, P., Sussmann, R., and Smale, D.: Contribution of oil and natural gas production to renewed increase in atmospheric methane (2007–2014): top-down estimate from ethane and methane column observations, *Atmos. Chem. Phys.*, 16, 3227-3244, 10.5194/acp-16-3227-2016, 2016.

Helmig, D., Rossabi, S., Hueber, J., Tans, P., Montzka, S. A., Masarie, K., Thoning, K., Plass-Duelmer, C., Claude, A., Carpenter, L. J., Lewis, A. C., Punjabi, S., Reimann, S., Vollmer, M. K., Steinbrecher, R., Hannigan, J. W., Emmons, L. K., Mahieu, E., Franco, B., Smale, D., and Pozzer, A.: Reversal of global atmospheric ethane and propane trends largely due to US oil and natural gas production, *Nature Geosci*, 9, 490-495, 10.1038/ngeo2721, 2016.

Hendrick, M. F., Ackley, R., Sanaie-Movahed, B., Tang, X., and Phillips, N. G.: Fugitive methane emissions from leak-prone natural gas distribution infrastructure in urban environments, *Environmental Pollution*, 213, 710-716, 2016.

IPCC: *Climate Change 2013: The Physical Science Basis. Contribution of Working Group I to the Fifth Assessment Report of the Intergovernmental Panel on Climate Change*, Cambridge University Press, Cambridge, United Kingdom and New York, NY, USA, 1535 pp., 2013.

Jacob, D. J., Turner, A. J., Maasakkers, J. D., Sheng, J., Sun, K., Liu, X., Chance, K., Aben, I., McKeever, J., and Frankenberg, C.: Satellite observations of atmospheric methane and their value for quantifying methane emissions, *Atmos. Chem. Phys.*, 16, 14371-14396, 10.5194/acp-16-14371-2016, 2016.

Jiang, W., Singleton, D. L., Hedley, M., McLaren, R., Dann, T., and Wang, D.: Comparison of Organic Compound Compositions in the Emissions Inventory and Ambient Data for the Lower Fraser Valley, *Journal of the Air & Waste Management Association*, 47, 851-860, 10.1080/10473289.1997.10464457, 1997.

Johnson, M. R., Crosland, B. M., McEwen, J. D., Hager, D. B., Armitage, J. R., Karimi-Golpayegani, M., and Picard, D. J.: Estimating fugitive methane emissions from oil sands mining using extractive core samples, *Atmospheric Environment*, 144, 111-123, 2016.

JOSM: *Joint Canada/Alberta Implementation Plan for Oil Sands Monitoring* ISBN: 978-1-100-21630-0, 1-26, 2012.

Karion, A., Sweeney, C., Pétron, G., Frost, G., Michael Hardesty, R., Kofler, J., Miller, B. R., Newberger, T., Wolter, S., Banta, R., Brewer, A., Dlugokencky, E., Lang, P., Montzka, S. A., Schnell, R., Tans, P., Trainer, M., Zamora, R., and Conley, S.: Methane emissions estimate from airborne measurements over a western United States natural gas field, *Geophysical Research Letters*, 40, 4393-4397, 10.1002/grl.50811, 2013.

Karion, A., Sweeney, C., Kort, E. A., Shepson, P. B., Brewer, A., Cambaliza, M., Conley, S. A., Davis, K., Deng, A., Hardesty, M., Herndon, S. C., Lauvaux, T., Lavoie, T., Lyon, D., Newberger, T., Pétron, G., Rella, C., Smith, M., Wolter, S., Yacovitch, T. I., and Tans, P.: Aircraft-Based Estimate of Total Methane Emissions from the Barnett Shale Region, *Environmental Science & Technology*, 49, 8124-8131, 10.1021/acs.est.5b00217, 2015.

Klenbusch, M. R.: Measurement of gaseous emission rates from land surfaces using an emission isolation chamber, Radian Corporation EPA/600/8-86/008, 58 pages, 1986.

Kort, E. A., Frankenberg, C., Costigan, K. R., Lindenmaier, R., Dubey, M. K., and Wunch, D.: Four corners: The largest US methane anomaly viewed from space, *Geophysical Research Letters*, 41, 6898-6903, 10.1002/2014GL061503, 2014.

Lavoie, T. N., Shepson, P. B., Cambaliza, M. O. L., Stirm, B. H., Karion, A., Sweeney, C., Yacovitch, T. I., Herndon, S. C., Lan, X., and Lyon, D.: Aircraft-Based Measurements of Point Source Methane Emissions in the Barnett Shale Basin, *Environmental Science & Technology*, 49, 7904-7913, 10.1021/acs.est.5b00410, 2015.

Li, S.-M., Leithead, A., Moussa, S. G., Liggio, J., Moran, M. D., Wang, D., Hayden, K., Darlington, A., Gordon, M., Staebler, R., Makar, P. A., Stroud, C. A., McLaren, R., Liu, P. S. K., O'Brien, J., Mittermeier, R. L., Zhang, J., Marson, G., Cober, S. G., Wolde, M., and Wentzell, J. J. B.: Differences between measured and reported volatile organic compound emissions from oil sands facilities in Alberta, Canada, *Proceedings of the National Academy of Sciences*, 10.1073/pnas.1617862114, 2017.

Liggio, J., Li, S.-M., Hayden, K., Taha, Y. M., Stroud, C., Darlington, A., Drollette, B. D., Gordon, M., Lee, P., Liu, P., Leithead, A., Moussa, S. G., Wang, D., O'Brien, J., Mittermeier, R. L., Brook, J. R., Lu, G., Staebler, R. M., Han, Y., Tokarek, T. W., Osthoff, H. D., Makar, P. A., Zhang, J., L. Plata, D., and Gentner, D. R.: Oil sands operations as a large source of secondary organic aerosols, *Nature*, 534, 91-94, 10.1038/nature17646, 2016.

Lyon, D. R., Zavala-Araiza, D., Alvarez, R. A., Harriss, R., Palacios, V., Lan, X., Talbot, R., Lavoie, T., Shepson, P., Yacovitch, T. I., Herndon, S. C., Marchese, A. J., Zimmerle, D., Robinson, A. L., and Hamburg, S. P.: Constructing a Spatially Resolved Methane Emission Inventory for the Barnett Shale Region, *Environmental Science & Technology*, 49, 8147-8157, 10.1021/es506359c, 2015.

Mays, K. L., Shepson, P. B., Stirm, B. H., Karion, A., Sweeney, C., and Gurney, K. R.: Aircraft-Based Measurements of the Carbon Footprint of Indianapolis, *Environmental Science & Technology*, 43, 7816-7823, 10.1021/es901326b, 2009.

McLaren, R., Gertler, A. W., Wittorff, D. N., Belzer, W., Dann, T., and Singleton, D. L.: Real-World Measurements of Exhaust and Evaporative Emissions in the Cassiar Tunnel Predicted by Chemical Mass Balance Modeling, *Environmental Science & Technology*, 30, 3001-3009, 10.1021/es960036k, 1996.

McLinden, C. A., Fioletov, V., Boersma, K. F., Krotkov, N., Sioris, C. E., Veefkind, J. P., and Yang, K.: Air quality over the Canadian oil sands: A first assessment using satellite observations, *Geophysical Research Letters*, 39, n/a-n/a, 10.1029/2011GL050273, 2012.

- McLinden, C. A., Fioletov, V., Boersma, K. F., Kharol, S. K., Krotkov, N., Lamsal, L., Makar, P. A., Martin, R. V., Veefkind, J. P., and Yang, K.: Improved satellite retrievals of NO₂ and SO₂ over the Canadian oil sands and comparisons with surface measurements, *Atmos. Chem. Phys.*, 14, 3637-3656, 10.5194/acp-14-3637-2014, 2014.
- Montzka, S. A., Dlugokencky, E. J., and Butler, J. H.: Non-CO₂ greenhouse gases and climate change, *Nature*, 476, 43-50, 2011.
- Peischl, J., Ryerson, T. B., Brioude, J., Aikin, K. C., Andrews, A. E., Atlas, E., Blake, D., Daube, B. C., de Gouw, J. A., Dlugokencky, E., Frost, G. J., Gentner, D. R., Gilman, J. B., Goldstein, A. H., Harley, R. A., Holloway, J. S., Kofler, J., Kuster, W. C., Lang, P. M., Novelli, P. C., Santoni, G. W., Trainer, M., Wofsy, S. C., and Parrish, D. D.: Quantifying sources of methane using light alkanes in the Los Angeles basin, California, *Journal of Geophysical Research: Atmospheres*, 118, 4974-4990, 10.1002/jgrd.50413, 2013.
- Peischl, J., Ryerson, T. B., Aikin, K. C., de Gouw, J. A., Gilman, J. B., Holloway, J. S., Lerner, B. M., Nadkarni, R., Neuman, J. A., Nowak, J. B., Trainer, M., Warneke, C., and Parrish, D. D.: Quantifying atmospheric methane emissions from the Haynesville, Fayetteville, and northeastern Marcellus shale gas production regions, *Journal of Geophysical Research: Atmospheres*, 120, 2119-2139, 10.1002/2014JD022697, 2015.
- Peischl, J., Karion, A., Sweeney, C., Kort, E. A., Smith, M. L., Brandt, A. R., Yeskoo, T., Aikin, K. C., Conley, S. A., Gvakharia, A., Trainer, M., Wolter, S., and Ryerson, T. B.: Quantifying atmospheric methane emissions from oil and natural gas production in the Bakken shale region of North Dakota, *Journal of Geophysical Research: Atmospheres*, 121, 6101-6111, 10.1002/2015JD024631, 2016.
- Pinto, J.: Atmospheric Chemistry: Wyoming winter smog, *Nature Geosci*, 2, 88-89, 2009.
- Scheff, P. A., and Wadden, R. A.: Receptor modeling of volatile organic compounds. 1. Emission inventory and validation, *Environmental Science & Technology*, 27, 617-625, 10.1021/es00041a005, 1993.
- Schneising, O., Burrows, J. P., Dickerson, R. R., Buchwitz, M., Reuter, M., and Bovensmann, H.: Remote sensing of fugitive methane emissions from oil and gas production in North American tight geologic formations, *Earth's Future*, 2, 548-558, 10.1002/2014EF000265, 2014.
- Schnell, R. C., Oltmans, S. J., Neely, R. R., Endres, M. S., Molenaar, J. V., and White, A. B.: Rapid photochemical production of ozone at high concentrations in a rural site during winter, *Nature Geosci*, 2, 120-122, 2009.
- Schnell, R. C., Johnson, B. J., Oltmans, S. J., Cullis, P., Sterling, C., Hall, E., Jordan, A., Helmig, D., Petron, G., Ahmadov, R., Wendell, J., Albee, R., Boylan, P., Thompson, C. R., Evans, J., Hueber, J., Curtis, A. J., and Park, J.-H.: Quantifying wintertime boundary layer ozone production from frequent profile measurements in the Uinta Basin, UT, oil and gas region, *Journal of Geophysical Research: Atmospheres*, n/a-n/a, 10.1002/2016JD025130, 2016.
- Shephard, M. W., McLinden, C. A., Cady-Pereira, K. E., Luo, M., Moussa, S. G., Leithead, A., Liggio, J., Staebler, R. M., Akingunola, A., Makar, P., Lehr, P., Zhang, J., Henze, D. K., Millet, D. B., Bash, J. O., Zhu, L., Wells, K. C., Capps, S. L., Chaliyakunnel, S., Gordon, M., Hayden, K., Brook, J. R., Wolde, M., and Li, S. M.: Tropospheric Emission Spectrometer (TES) satellite observations of ammonia, methanol, formic acid, and carbon monoxide over the Canadian oil sands: validation and model evaluation, *Atmos. Meas. Tech.*, 8, 5189-5211, 10.5194/amt-8-5189-2015, 2015.

- Siddique, T., Penner, T., Klassen, J., Nesbø, C., and Foght, J. M.: Microbial Communities Involved in Methane Production from Hydrocarbons in Oil Sands Tailings, *Environmental Science & Technology*, 46, 9802-9810, 10.1021/es302202c, 2012.
- Simpson, I. J., Blake, N. J., Barletta, B., Diskin, G. S., Fuelberg, H. E., Gorham, K., Huey, L. G., Meinardi, S., Rowland, F. S., Vay, S. A., Weinheimer, A. J., Yang, M., and Blake, D. R.: Characterization of trace gases measured over Alberta oil sands mining operations: 76 speciated C₂-C₁₀ volatile organic compounds (VOCs), CO₂, CH₄, CO, NO, NO₂, NO_y, O₃ and SO₂, *Atmos. Chem. Phys.*, 10, 11931-11954, 10.5194/acp-10-11931-2010, 2010.
- Small, C. C., Cho, S., Hashisho, Z., and Ulrich, A. C.: Emissions from oil sands tailings ponds: Review of tailings pond parameters and emission estimates, *Journal of Petroleum Science and Engineering*, 127, 490-501, 2015.
- Smith, M. L., Kort, E. A., Karion, A., Sweeney, C., Herndon, S. C., and Yacovitch, T. I.: Airborne Ethane Observations in the Barnett Shale: Quantification of Ethane Flux and Attribution of Methane Emissions, *Environmental Science & Technology*, 49, 8158-8166, 10.1021/acs.est.5b00219, 2015.
- Strausz, O. P. L., Elizabeth M. : *The Chemistry of Alberta Oil Sands, Bitumens and Heavy Oils*, Alberta Energy Research Institute, 2003.
- Stringham, G.: Chapter 2 - Energy Developments in Canada's Oil Sands, in: *Developments in Environmental Science*, edited by: Kevin, E. P., Alberta Oil Sands Energy, Industry and the Environment, 11, Elsevier, Oxford, UK, 19-34, 2012.
- Tokarek, T. W. O.-A., C. A.; Huo, J. A.; McLaren, R.; Lee, A. K.; Gerrit, M.; Willis, M.D.; Abbatt, J.P.D.; Mihele, C.; Darlington, A.; Mittermeier, R. L.; Strawbridge, K.; Hayden, K. L.; Olfert, J. S.; Schnitzler, E.; Brownsey, D. K.; Assad, F. V.; Wentworth, G. R.; Tevlin, A.G.; Worthy, D. E. J.; Murphy, J. G.; Liggio, J.; Brook, J. R.; Osthoff, H. D.: Principal component analysis of ground site measurements in the Athabasca oil sands during summer 2013: Sources of IVOCs, *Atmospheric Chemistry and Physics*, in preparation, 2017.
- Turner, A. J., Jacob, D. J., Benmergui, J., Wofsy, S. C., Maasackers, J. D., Butz, A., Hasekamp, O., and Biraud, S. C.: A large increase in U.S. methane emissions over the past decade inferred from satellite data and surface observations, *Geophysical Research Letters*, 43, 2218-2224, 10.1002/2016GL067987, 2016.
- Turner, A. J., Frankenberg, C., Wennberg, P. O., and Jacob, D. J.: Ambiguity in the causes for decadal trends in atmospheric methane and hydroxyl, *Proceedings of the National Academy of Sciences*, 114, 5367-5372, 10.1073/pnas.1616020114, 2017.
- Vaghjiani, G. L., and Ravishankara, A.: New measurement of the rate coefficient for the reaction of OH with methane, *Nature*, 350, 406-409, 1991.
- Walter, D., Heue, K. P., Rauthe-Schöch, A., Brenninkmeijer, C. A. M., Lamsal, L. N., Krotkov, N. A., and Platt, U.: Flux calculation using CARIBIC DOAS aircraft measurements: SO₂ emission of Norilsk, *Journal of Geophysical Research: Atmospheres*, 117, n/a-n/a, 10.1029/2011JD017335, 2012.
- Williams, A., and Marcotte, D.: Wind Measurements on a Maneuvering Twin-Engine Turboprop Aircraft Accounting for Flow Distortion, *Journal of Atmospheric and Oceanic Technology*, 17, 795-810, 2000.
- Worthy, D. E. J., Chan, E., Ishizawa, M., Chan, D., Poss, C., Dlugokencky, E. J., Maksyutov, S., and Levin, I.: Decreasing anthropogenic methane emissions in Europe and Siberia inferred from continuous

carbon dioxide and methane observations at Alert, Canada, *Journal of Geophysical Research: Atmospheres*, 114, n/a-n/a, 10.1029/2008JD011239, 2009.

Wratt, D. S., Gimson, N. R., Brailsford, G. W., Lassey, K. R., Bromley, A. M., and Bell, M. J.: Estimating regional methane emissions from agriculture using aircraft measurements of concentration profiles, *Atmospheric Environment*, 35, 497-508, 2001.

Zavala-Araiza, D., Lyon, D., Alvarez, R. A., Palacios, V., Harriss, R., Lan, X., Talbot, R., and Hamburg, S. P.: Toward a Functional Definition of Methane Super-Emitters: Application to Natural Gas Production Sites, *Environmental Science & Technology*, 49, 8167-8174, 10.1021/acs.est.5b00133, 2015.

Chapter 3 Cold season methane emissions estimated in the Athabasca Oil Sands Region of Alberta using mobile surface measurements

Author Contributions

Sabour Baray¹, Katherine L. Hayden², Andrew Sheppard², Zoe Davis², Kevin Strawbridge, Ralf Staebler and Robert McLaren¹

1. Centre for Atmospheric Chemistry, York University, Toronto, Canada

2. Environment and Climate Change Canada, Toronto, Canada

SB, KLH and RM designed the study. SB conducted the analysis with contributions from KLH, ZD and RM. KLH, AS, KS and RM conducted the field studies. SB and RM wrote the paper with contributions from all authors.

Abstract

The Athabasca Oil Sands Region (AOSR) of Alberta, Canada is estimated to be responsible for ~10% of total methane (CH₄) emissions in the province of Alberta and ~4% nationally in Canada, with the majority of released CH₄ in this region being due to fugitive emissions that are an unintended by-product of operations. Our previous analysis of an aircraft campaign led by Environment and Climate Change Canada (ECCC) in summer 2013 showed that fugitive emissions of 19.6 ± 1.1 tonnes CH₄ hr⁻¹ are from surface mining activities (50%), tailings ponds (45%), and other facility-controlled releases of natural gas (5%). However, it is uncertain how these emissions vary by season and on an inter-annual basis. In this work we deployed surface measurements using a cost-effective mobile platform to survey cold season methane emissions in the AOSR. We use data from two mobile surface campaigns (Fall/Winter 2014 and Winter/Spring 2017) to provide insights into the behaviour of emissions under snow-covered conditions. Maximum enhancements from fugitive plumes (>1 km wide) up to 3.7 ppm were observed in 2014 and 4.3 ppm in 2017. Such enhancements were downwind of active tailings ponds showing the release of fugitive methane in these two cold seasons despite snow covered surfaces. Occasional geographically narrow enhancements of >15 ppm were observed in 2014, and as high as 87 ppm in 2017, from possible methane leaks and venting activity, however, the infrequency of these high enhancements indicate that over these field studies, these emissions are not comparable in magnitude to tailings ponds and open-pit mining. Emissions are estimated for select plumes using a mobile-surface mass-balance approach (MSMB). MSMB is an analogous method to aircraft mass-balance that assumes measured plumes are sufficiently distant from the source to be well-mixed in the planetary boundary layer (PBL). We show four repeat transects on two different days of a single source from the 2017 campaign with optimal conditions such that the measurement transect is more than triple the downwind distance needed for a well-mixed plume. We identify the source of this plume as Suncor open-pit mining using HYSPLIT modelling and estimate the source emission to be 1.0 ± 0.4 t hr⁻¹ with good reproducibility between the four transects. These observations show that significant fugitive emissions of methane from tailings ponds and surface mining persist in the cold season under snow-covered

conditions. We also show that there continues to be discrepancies between bottom-up and top-down emissions estimates that would require an improved observation network to resolve.

3.1 Introduction

Methane (CH₄) is a significant greenhouse gas with a global warming potential 28–34 times more than CO₂ on a 100-year timescale and is second next to CO₂ for direct radiative forcing (Myhre et al., 2013). Anthropogenic methane sources include oil and gas (extraction, transportation, combustion), in addition to agricultural activities (livestock, rice cultivation) and waste. Natural methane sources are primarily from wetlands but includes biomass burning and other minor sources such as seeps and termites (Saunio et al., 2016). The primary sink of atmospheric methane is oxidation by the hydroxyl radical (OH) resulting in a lifetime of 9.1 ± 0.9 years (Prather et al., 2012). Aggressive CH₄ emissions reductions are being pursued by parties signing the Paris Agreement. The comparatively short lifetime of CH₄ (compared to CO₂) is attractive for climate policy as effective emissions control brings near term benefits and anthropogenic emissions are often due to leaks or other preventable fugitive emissions.

The Athabasca Oil Sands Region (AOSR) in northern Alberta, Canada is estimated to be responsible for ~10% of total CH₄ emissions in the province of Alberta and ~4% nationally. While most of Alberta's methane emissions are due to the production and processing of natural gas and not oil (Sheng et al., 2017), Alberta contains very large deposits of oil sands, an unconventional viscous mixture of bitumen, silt, clay, water and trapped gases (Stringham, 2012), whose mining and upgrading produces emissions of methane as an unintended by-product. Of Canada's proven reserves of 1.69×10^{11} barrels of oil, 97% are in the oil sands, 82% of which are in the AOSR north of Fort McMurray. In the AOSR, 20% of these reserves are in the form of near-surface deposits within 100 m depth that are mined using the prevailing open pit mining technique, with the remainder located deeper underground requiring high energy in situ extraction (Simpson et al., 2010). For the surface mining method, heavy hauler trucks shovel oil sands from cleared mining areas which are transported to facilities where the bitumen is separated and upgraded. Extraction of the bitumen requires water, additives and naphtha or paraffin diluents. Process water containing organic diluents is recycled, but unrecovered diluent

is discharged in large tailings ponds, which are open to the atmosphere, along with additives and bitumen (Small et al., 2015). Surface mines release CH₄ and CO₂ because of thermogenic decomposition of the disturbed mined material and from leaking through fissures and the permeable surface. Tailings ponds release CH₄, CO₂, H₂S and other VOCs by complex mechanisms involving microbial communities that decompose the available hydrocarbons (Small et al., 2015; Baray et al., 2018; Zhang et al., 2019; You et al., 2021). Tailings ponds have vastly differing chemical composition, microbial diversity and emissions depending on the tailings type, use of additives and age of the pond (Small et al., 2015). Out of 19 tailings ponds in the region, the most methanogenic pond is Mildred Lake Settling Basin (MLSB) in the Syncrude Mildred Lake (SML) facility; methane bubbles were first observed 21 years after the establishment of the pond in 1978 (Yeh et al., 2010). Similarly, the second most methanogenic Pond 2/3 (P23) in the Suncor (SUN) facility began emitting methane 15 years after establishment 1968. The majority of the methane activity are from these two sites, MLSB and P23 are expected to be responsible for >90% of all tailings ponds methane emissions in the region (Small et al., 2015). An aircraft campaign in the summer of 2013 showed surface mines and tailings ponds together account for >95% of methane emissions, which are fugitive unintended by-products of oil sands extraction and processing (Baray et al., 2018). Figure 3.1 shows the spatial distribution of the largest emissions sources in the AOSR, which identifies select tailings ponds that account for most pond methane emissions, and methane sources from active surface mines.

There is a lack of measurements in the literature that demonstrate appropriate methods to estimate the seasonal pattern of fugitive emissions in the AOSR. Strausz (2003) showed that degassing of CH₄ and CO₂ from the mined oil sands is entropically and enthalpically favourable even at low temperatures with exposure to oxygen. Johnson et al. (2018) showed mining emissions can be predicted as a function of total mined material but was inconclusive towards determining if these emissions were the same emissions reported in the inventory or additional. For tailings ponds, ice and snow may cover most of their surfaces during the winter months and possibly trap emissions, however tailings outfalls at warmer discharge temperature can provide continuous disturbance, and an area of exposure to the atmosphere (Small et al., 2015). Five-week summertime eddy covariance flux measurements found no diurnal or day-to-day variability

in emissions at the major methane source P23 (You et al., 2020). However, long-term flux measurements at reclamation pond Base Mine Lake (BML; directly south of MLSB in Figure 3.1) found an order of magnitude differences in methane fluxes between multiple seasons and years (Clark et al., 2021). Although BML is a much smaller source of methane due to its water-capped fluid fine tailings composition. An improved observation network of consistent warm and cold season measurements across the unique ponds and facilities are necessary to address these continued uncertainties.

Aircraft campaigns provide comprehensive evaluation of emissions using a mass-balance approach, and a large array of simultaneous measurements inform the unique chemistry of the study area (Gordon et al., 2015; Li et al., 2017; Baray et al., 2018; Liggio et al., 2019). The limitation of aircraft campaigns is that they are resource-intensive and temporally limited to ‘snapshot’ emissions profiles, which leave uncertainties regarding the extrapolation of emissions rates across seasons to compare to yearly inventory totals. Satellite measurements can provide consistent observations year-round but are limited at Canadian latitudes due to uncertainties in the retrievals (Baray et al., 2021). Surface measurements can provide continuous temporal information but requires a dense and well-situated observation network of multiple instruments to provide useful spatial characterization. Mobile surface measurements are a novel and useful way to contribute additional information to the observation network. In other studies, vehicle-based measurements have been used to characterize industrial natural gas emissions in British Columbia (Atherton et al., 2017) and urban natural gas emissions in the Greater Toronto Area (Ars et al., 2020). The main limitation with mobile surface measurements is the lack of vertical information, which make the quantification of emissions by mass balance problematic. Some solutions to this problem take advantage of the linear relationship between emissions and measurements. These include using controlled release experiments or other known emissions scenarios to judge the linear relationship between methane ‘spikes’ and the required local emissions to produce the measurement levels (Maazallahi et al. 2020). Ars et al. 2020 combined mobile surface data with inverse modelling, which optimizes emissions by reducing the mismatch between predicted concentrations from a prior model and the measured concentrations. Mass-balance calculations using single-altitude data is common in the literature using aircraft

measurements (Cambaliza et al., 2014; Karion et al., 2015; Peischl et al., 2016) if it can be shown that measurements are sufficiently distant for plumes to be well-mixed in the PBL. Given the validity of this assumption and the availability of high-precision methane instruments, this approach can be readily applied to ground-level vehicle-based measurements.

In this study, we address temporal observation gaps using a cost effective mobile vehicle to measure surface methane levels and survey AOSR fugitive sources in two cold season field campaigns (Fall 2014 and Spring 2017). We demonstrate a mass balance approach by which mobile surface measurements can be used to estimate emissions. Mass balance methods can be used to determine emissions in numerous studies using either satellite (Varon et al., 2019), aircraft (Karion et al., 2015) and other surface-based remote sensing measurements (Davis et al., 2019). In the example of aircraft campaigns, measurements are conducted in either a downwind formation (line or screen) or in a box formation that surrounds a facility of interest (Baray et al., 2018). The box approach requires complete calculations of incoming and outgoing fluxes and determines emissions rates according to the net outflow of methane (Gordon et al., 2015). The downwind line or screen approaches require manually monitoring the methane background through upwind or lateral background measurements (Cambaliza et al., 2014). We estimate emissions for select plumes using a mobile-surface mass-balance approach (MSMB). MSMB relies on measurements being sufficiently distant from the sources for plumes to be well-mixed in the planetary boundary layer (PBL). We validate this assumption by parameterizing the PBL mixing using the dense network of meteorological measurements in the AOSR, as well as through LIDAR backscatter retrievals of the PBL. We show repeated CH₄ emissions estimates for the Suncor Mining facility (SUN) and demonstrate a discrepancy between top-down and bottom-up emissions estimates.

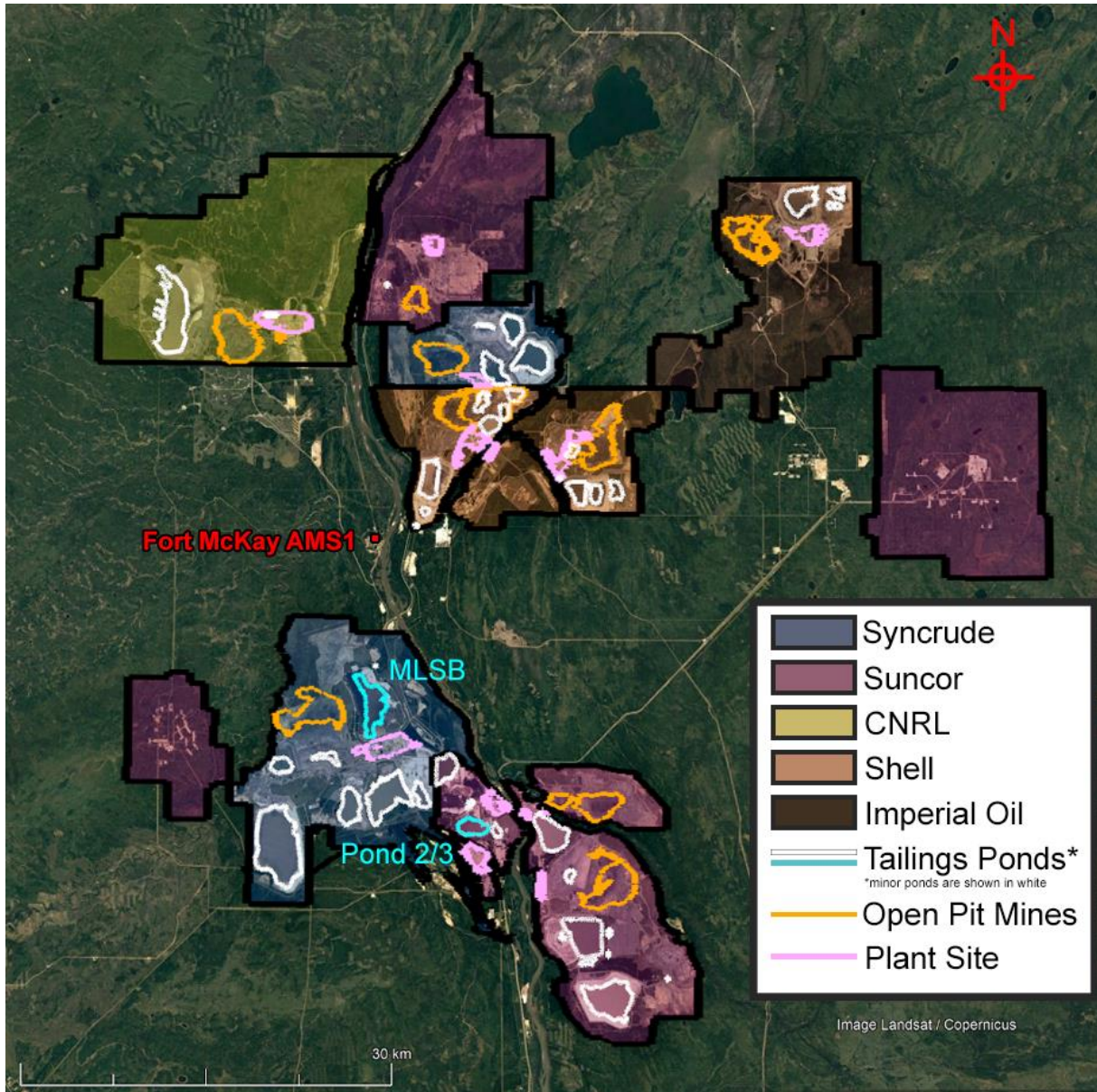


Figure 3.1: Map of facilities and methane emission sources in the AOSR. Facility boundaries and land disturbance shapefiles are from the Alberta Environment and Parks Oil Sands Information Portal (<http://osip.alberta.ca/>). Shaded boxes show the five main facilities: Open pit mining is shown with the orange line, the plant site locations are shown in pink, and tailings ponds are shown in white (minor) and teal (major). The two major ponds that account for >90% of methane emissions (Baray et al., 2018) are emphasized: Mildred Lake Settling Basin (MLSB) in Syncrude Mildred Lake and Pond 2/3 in Suncor.

3.2 Data and methods

3.2.1 Description of measurements

Measurements of dry mol fractions of CH₄, CO₂, CO and H₂O were made using a Picarro G2401-m cavity ring-down spectrometer (CRDS) (Picarro Inc.) at an interpolated rate of ~0.5Hz. The instrument was mounted inside a pickup truck, for both the Fall/Winter 2014 and the Winter/Spring 2017 study periods that was powered by auxiliary batteries. The inlet was a reverse-facing sample port with a 47 mm Teflon filter to remove particles that was regularly changed; a response time of 18 seconds was subtracted from the measurements due to the sample line length. The precision of the Picarro instrument is 2-3 ppb. The instrument was calibrated before and after the study periods using standard reference gases traceable to NOAA GMD standards. A GPS was used to measure position (latitude, longitude) and velocity (vehicle speed and course) at a rate of 1 Hz that was used to construct the map of CH₄ measurements and calculate the horizontal width of plumes for emissions calculations. Figure 3.2 shows the driving routes for the 2014 and 2017 field studies, with maximum CH₄ mixing ratios indicated on a colour scale. A large continuous observation network of chemical and meteorological tower measurements is operated by the Wood Buffalo Environmental Association (WBEA). A CLIMATRONIX instrument provided measurements of wind speed and direction which were used to validate winds from the WBEA network during times when the vehicle was stationary. Moving CLIMATRONIX measurements were not used directly in the mass balance calculations due to uncertainties in the vehicular approach. The WBEA network which includes vertical profiles from tower measurements was used to calculate the mean regional wind speed, this is the average wind speed from the approximate source to the measurements during the transect of interest and includes an uncertainty analysis for the vertical profile of winds (See Supplement 1.1–1.3). A WindRASS instrument which measures the vertical profile of temperature, wind speed, wind direction up to 250 m above ground level is run by Environment and Climate Change Canada and is included in the mean regional wind analysis. Boundary layer heights were derived using backscatter data from a LIDAR stationed at Fort Mackay (Strawbridge, 2013).

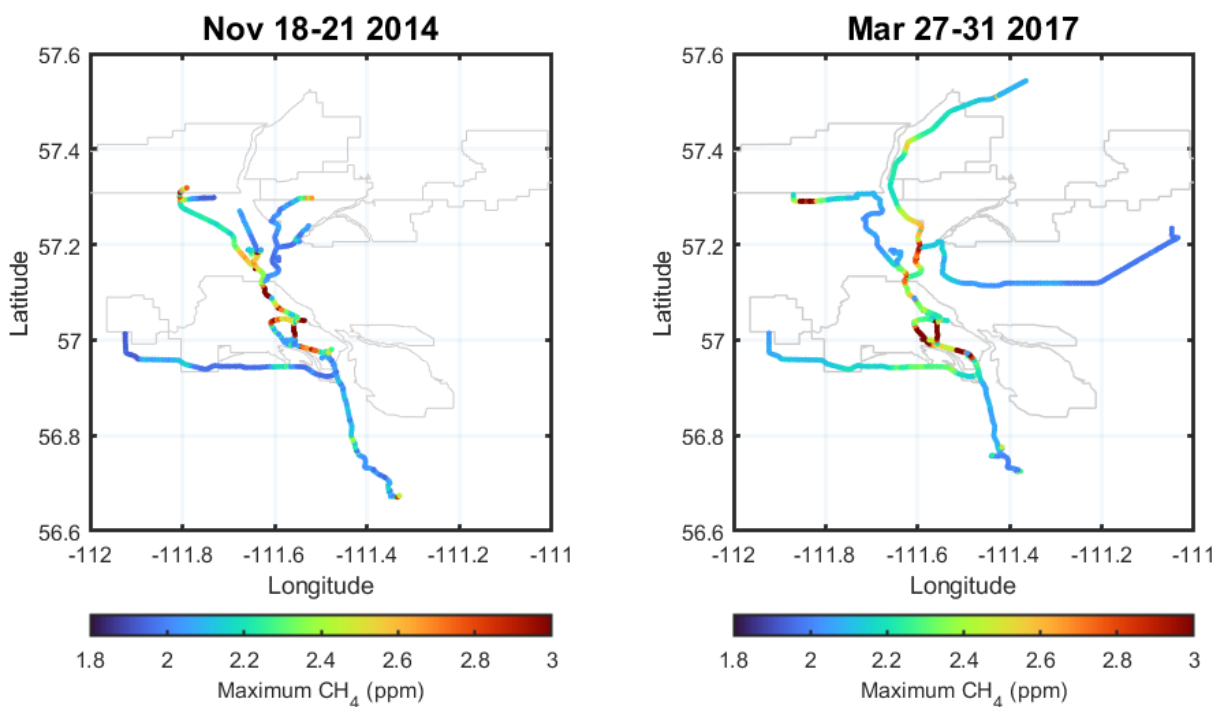


Figure 3.2: Map of CH₄ measurements from the Fall/Winter 2014 and Winter/Spring 2017 field studies. Gray lines show the facility boundaries corresponding to Figure 3.1. Data is averaged on a $0.005^\circ \times 0.005^\circ$ grid; the colour scale shows the maximum CH₄ mixing ratio at each grid cell.

3.2.2 Mobile Surface Mass Balance Approach (MSMB)

In this study we show a mobile-surface mass balance (MSMB) method to quantify CH₄ emissions. MSMB is similar in principle to the aircraft single transect method, whereby a single altitude of measurements can be used to estimate emissions. We use meteorological measurements from the regional WBEA network to validate the necessary atmospheric conditions for the mass balance method to be applicable. This method is valid if the measurements are sufficiently downwind of sources for the plume to be well mixed in the PBL, and the CH₄ mixing ratios exhibit a constant vertical profile. Under these conditions, the emissions rate of methane can be estimated using the integrated flux through a plane, which is

the product of background-enhanced CH₄ and the perpendicular wind speed over the entire plume width

$$Emission\ Rate = \int_{s_1}^{s_n} ([CH_4] - [CH_4]_B) \times U_{\perp} \times z_i \, ds \quad \{3.1\}$$

where $[CH_4] - [CH_4]_B$ is the background-enhanced CH₄, U_{\perp} is the mean regional wind speed perpendicular to the measurement transect, and z_i is the height of the PBL derived from the LIDAR measurements at Fort Mackay, integrated over the horizontal plume width. A response time of 18 ± 3 seconds was determined experimentally and subtracted from the data series to determine the vehicle position at the time of the measurements. The vehicle's speed was relatively constant (± 0.1 – 0.2 km/h) over the plume transects as measured by the GPS.

The validity of assuming surface emissions of methane were well mixed in the PBL was tested by calculating the mean time for a tracer to mix to the top of the PBL from the surface, t_* (Stull, 1988). A surface plume is expected to be fully mixed within $\sim 3t_*$ (Stull, 1988; Weil et al., 2004).

$$t_* = \frac{z_i}{w_*} \quad \{3.2\}$$

Where z_i is the PBL height and w_* is the convective velocity scale. During the daytime, w_* is an important factor controlling the diffusion in an unstable boundary layer.

$$w_* = (gQ_0z_i/T)^{1/3} \quad \{3.3\}$$

Where g is the acceleration due to gravity, Q_0 is the surface heat flux, z_i is the mixed layer height, T is temperature (Venkatram, 1978). The PBL height z_i was estimated from the LIDAR measurements at AMS1. T was obtained from WBEA meteorological measurements at AMS1 and verified by the vehicle CLIMATRONIX data. Q_0 was calculated using the approximation $Q_0 = AS$ (Briggs, 1982), where S is down-welling solar radiation and the constant A depends on ground cover, ranging from 0.55 for a dry surface to 0.25 for a crop canopy. Solar radiation S was obtained from the AMS1. The value of $3t_*$ was calculated conservatively assuming $A=0.25$

since it produces the smallest value of the surface heat flux (Q_o) and convective velocity, w^* and hence the corresponding largest value of $3t_*$ (see Supplement Table B.1 for the data used).

To evaluate the applicability of the $3t_*$ estimation, the Pasquill Gifford (PG) atmospheric stability class was determined for each plume transport time (U.S. EPA, 2000). The method uses the wind-speed at 10 m above the surface and the down-welling solar radiation, obtained from AMS1. We show in Section 3.3.1 how the data are filtered for conditions where the plume transport time is at least 30% higher than $3t_*$ under a PG class of C.

Aircraft mass-balance studies using single transects to determine emissions in a similar manner to Eq. {3.1} use higher altitude measurements that are extrapolated upward to the top of the PBL and downward to the surface. Alternatively, aircraft studies using multiple transects create a continuous screen and substitute the z_i term with an integral over the vertical dimension dz . These studies still rely on vertical extrapolation of measurements from the lowest aircraft transect to the ground which is usually ~ 150 m. The vertical profile of CH_4 from the surface to the top of the PBL for surface sources has been discussed in multiple studies (Cambaliza et al., 2014; Karion et al., 2015; Peischl et al., 2016) including in the AOSR area of interest (Baray et al. 2018) and has been shown to include scenarios where the profile is close to constant due to sufficient plume mixing.

3.3 Results and discussion

3.3.1 CH_4 measurements downwind of tailings ponds during cold seasons

Mobile measurements from the Fall 2014 and Spring 2017 field studies are used to survey the presence of tailings ponds methane emissions. While these measurements were conducted under snow-covered conditions, the tailings ponds may not entirely freeze in the cold-season due to sections with warmer tailings outfalls. To evaluate the presence of cold season CH_4 emissions, measurements were conducted downwind of the two major ponds MLSB and P23.

Figure 3.3 shows CH_4 mixing ratios downwind of P23 from the Suncor facility for both the Fall/Winter 2014 and Winter/Spring 2017 measurement campaigns. The driving route was along the primary Highway 63 that passes through the centre of the AOSR. Wind directions were from

the northeast on Nov 21 2014 and from the northwest on Mar 30 2017. Tailings P23 is highlighted in teal similar to Figure 3.1. The measurements in Nov 21 2014 show a maximum methane mixing ratio of 3.039 ppm on Highway 63 nearest to the pond, and a repeat maximum methane mixing ratio of 2.270 ppm at Aostra Road ~7 km away from the source. The measurements on Mar 30 2017 show a maximum methane mixing ratio of 2.775 ppm on Highway 63 nearest to the pond. Although on this day, there appeared to be some interference due to significant venting activity, this is visible in the red plume northwards along Highway 63 in Figure 3.3C and discussed in the Section 3.3.2. These results show P23 continues to release CH₄ in the cold season even under snow covered conditions.

Figure 3.4 shows measurements near MLSB from the Syncrude facility similar to Figure 3.3. The driving route is further north along Highway 63 than the P23 measurements with winds from the southwest on Nov 19 2014 and from the west on Mar 31 2017. Maximum methane mixing ratios are 2.994 ppm on Nov 19 2014 with a background of ~ 1.95 ppm and 2.738 ppm on Mar 31 2017 with a background of ~1.99 ppm. In both cases, the plume shows a major and a minor peak, and the width of the major peak is much less than the length of the entire MLSB pond. This is more noticeable on Mar 31 2017, where the maximum enhancement appears directly from the centre of MLSB. In this example, the plume width is ~2 km while the north-south length of MLSB is ~5.0 km. This suggests that MLSB may not be a homogenous area source of methane and can have regions of the pond where methane emissions are concentrated. This top-down result provides some guidance at constraining emissions using a high-resolution modelling approach (Nambiar et al. 2020) since it addresses whether tailings ponds should be modelled as uniform sources over the entire area (9.3 km² for MLSB) or as point sources for a specific region of the pond. This is a similar problem to modelling emissions from landfills and is better resolved with more detailed measurements of the source.

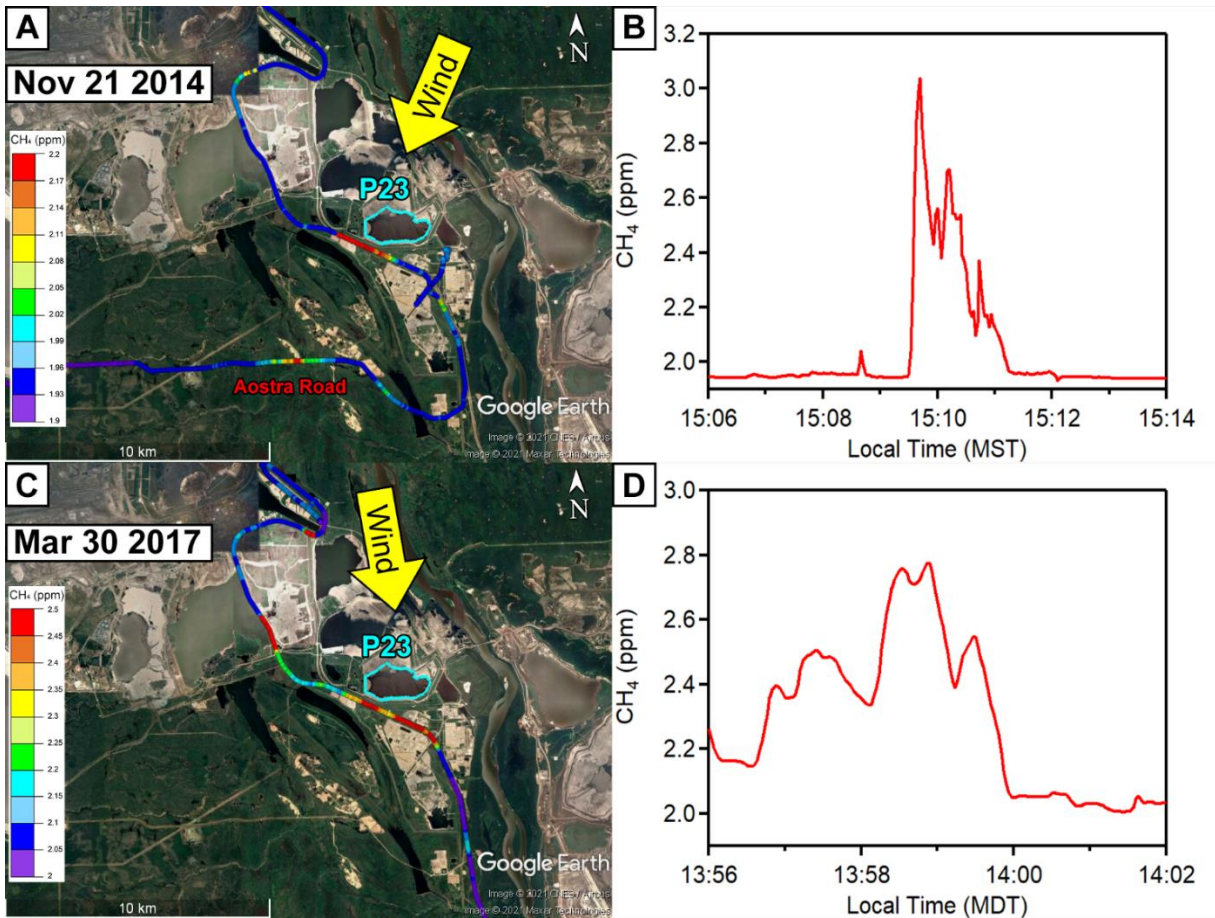


Figure 3.3: Mobile CH₄ measurements from Nov 21 2014 (top panels A and B) and Mar 30 2017 (bottom panels C and D) downwind of Suncor Pond 2/3 (teal highlight). Measurements were conducted along Highway 63. The right panels show the time series corresponding to the plumes nearest P23 where maximum mixing ratios of 3.039 ppm in 2014 and 2.775 ppm in 2017 were observed.

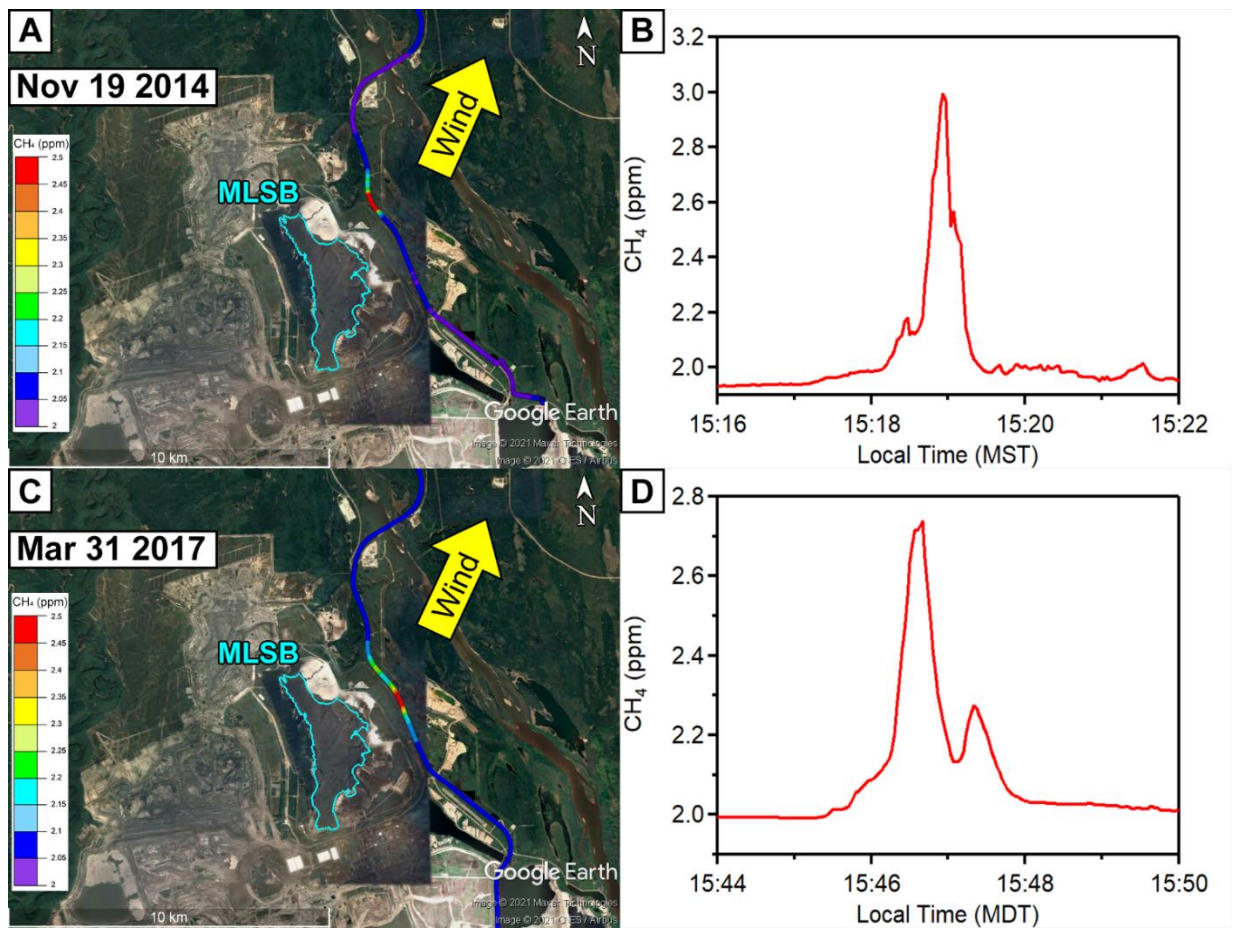


Figure 3.4: Mobile CH₄ measurements from Nov 19 2014 (top panels A and B) and Mar 31 2017 (bottom panels C and D) downwind of Syncrude Mildred Lake Settling Basin (teal highlight). Measurements were conducted further north than Figure 3.3 along the same Highway 63. The right panels show the time series corresponding to the plumes nearest MLSB where maximum mixing ratios of 2.994 ppm in 2014 and 2.738 ppm in 2017 were observed.

3.3.2 Measurements of transient CH₄ leaks

In the 2014 and 2017 studies we also make observations of transient, very high methane enhancements that are suggestive of methane leaks and in one case, visually confirmed venting activity without flaring. In the previous aircraft measurements from Baray et al. (2018), it was shown that emissions of methane from facility stacks were observed only from the CNRL facility in the northwest of the AOSR using sulphur dioxide (SO₂) measurements as a tracer species for this source. Methane enhancements were not observed from the main stacks of Syncrude and Suncor. Hence, Baray et al. (2018) attributed only 5% of methane emissions to facility stack emissions, which was limited to CNRL. The mobile surface measurements here show evidence of transient emissions that are particularly challenging to capture by aircraft and other top-down measurements.

Figure 3.5 shows measurements on Nov 21 2014 near the CNRL facility and Mar 30 2017 in the main Highway 63 between Syncrude and Suncor. A maximum enhancement of 23 ppm was measured in 2014 and 87 ppm was measured in 2017. The 2017 enhancement was associated with venting visually observed from a horizontal pipeline, with enough gas to produce a white plume. However, it is unclear as to the source of CH₄ enhancements. While these measured enhancements are high, the emissions rate as a function of the measured methane mixing ratio depends on the plume width or distance from the source, which is very small in these two cases.

There are substantial uncertainties in determining an emissions rate based on transient high concentrations. Weller et al. (2019) developed an open source algorithm for quantifying methane emissions rate from measured natural gas leaks based on mobile survey data, which was employed in the European cities in Maazallahi et al. (2020) and the Greater Toronto Area in Ars et al. (2020). The method uses a linear regression model that relates the methane emissions to the measured methane enhancement based on controlled release experiments and an average distance of 15.75 meters between the measurement and the leak. As shown in Maazallahi et al. (2020), a “medium” methane enhancement of 1.6–7.59 ppm at this spatial distance corresponds to an equivalent emissions rate of 0.3–1.7 kg hr⁻¹. This method may not be appropriate for the measurements shown in the AOSR since the linear model was calibrated for an urban

environment, while the AOSR is a mixed environment with forested and cleared industrial areas. Tailings ponds and open pit mining emissions are on the order of 10^3 kg hr^{-1} (Baray et al., 2018), hence for methane leaks or venting to be comparable they would have to accumulate substantially, which we did not observe during these field studies. Our measurements show that these incidents can occur, however their frequency and magnitude is not well understood. The existence of these emissions is especially challenging for top-down measurements to address; infrequent incidents of venting or accidental leaks resulting in large methane emissions could be missed by temporal gaps in field studies. These sources of methane may be better identified in the future by frequent, regional leak surveys (i.e., using drones, vehicles, or otherwise) that can detect CH_4 enhancements, or by next-generation satellite observations that can detect and quantify the emissions from space (Jacob et al., 2016). The current generation of global satellite observations is well-suited for capturing especially large incidents (Pandey et al., 2019), however the geographic position of the AOSR (57° N) poses an issue since satellite XCH_4 retrievals are more uncertain at higher latitudes (Baray et al., 2021). Future specialized instruments that are designed for fine-scale precision may better address facility-level needs.

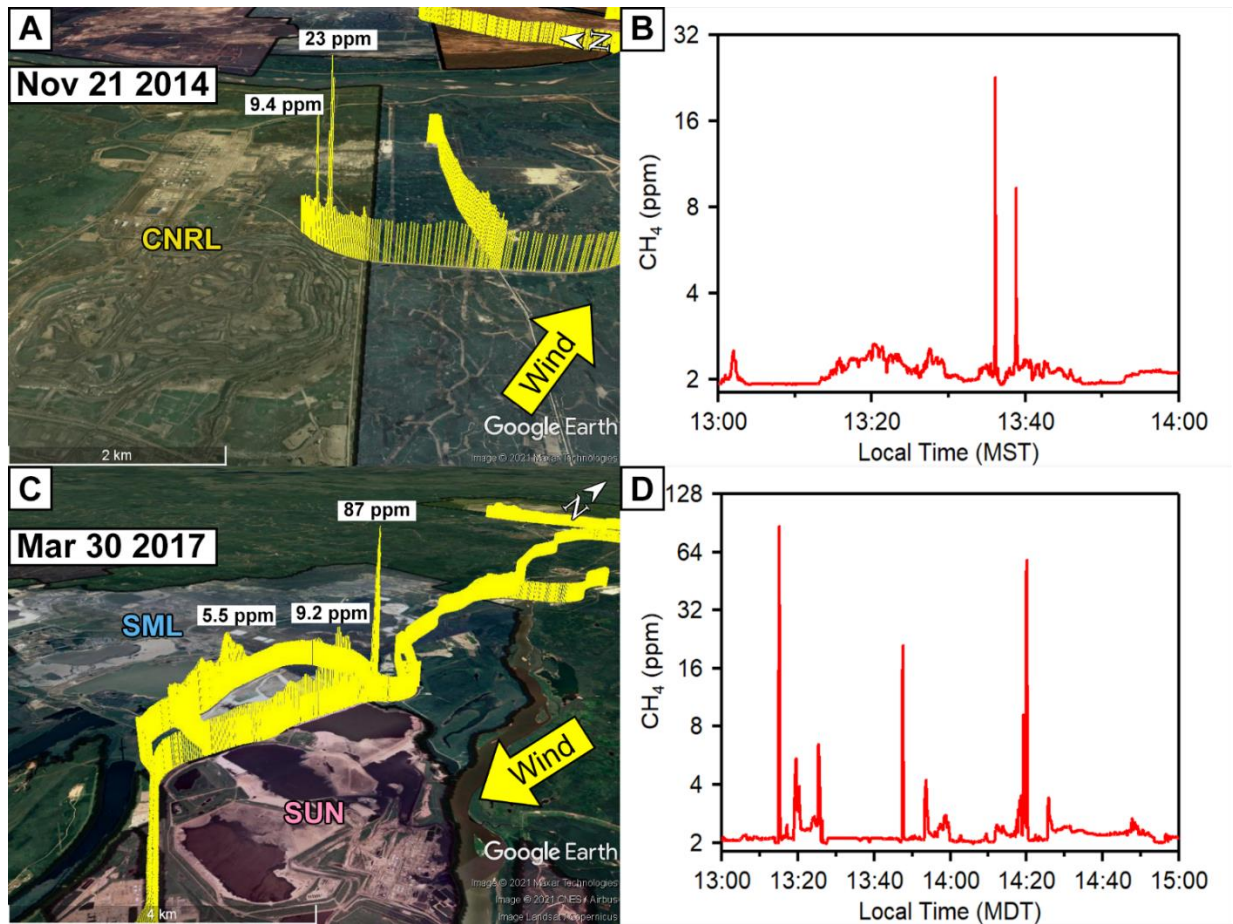


Figure 3.5: Mobile CH₄ measurements from Nov 21 2014 (top panels A and B) and Mar 30 2017 (bottom panels C and D). Mixing ratios scale with the height of the yellow bars to emphasize high measurements. Time series plots are shown in log scale with base 2. Measurements show CH₄ enhancements up to 23 ppm in 2014 near CNRL and up to 87 ppm in 2017 near SML and SUN. Note that the spikes in Panel D are due to repeat measurements of the same incident, which was observed between 13:10 MDT to 14:20 MDT as the vehicle circled the area.

3.3.3 Emissions estimates using MSMB

3.3.3.1 Filtering transects for optimal atmospheric conditions

Table 3.1 shows a list of transects that are used in mass balance emissions estimates and an analysis of the corresponding plume mixing conditions. These measurements are chosen for situations where the vehicle travelled in a path perpendicular to the downwind transport of CH₄ plumes from facilities. Transects that were immediately travelling in the opposite direction are indicated by the letters of the same number. For example, Figure 3.6 demonstrates the temporal evolution of the enhanced CH₄ measured in a Gaussian-shaped plume during the west to east transect 5A (11:20-11:25 MDT) immediately followed by an east to west transect 5B (11:45-11:50 MDT) just north of SUN on March 31, 2017.

Table 3.2 shows the meteorological data that is used to calculate the stability class and plume mixing time t^* . Figure 3.7 shows an example of the LIDAR data from AMS1 for Mar 31 2017 transects 5A/B, where the pink line shows the best estimate of the PBL height. For transect 5B corresponding to Figure 3.6, the PBL height is 310 ± 27 m a.g.l. and the estimated maximum time for a tracer to reach this height ($1t^*$) is 5 minutes. Hence the conservative estimate of $3t^*$ for complete mixing, from the larger of the estimates for the ground constant A, is 15 minutes. The plume travel time was estimated from the source distance and the boundary layer averaged wind-speed for the stability class C plumes and from the 10 m wind-speed at AMS1 for the stability class D plumes. Table 3.1 shows that based on a wind speed of 2.6 ± 0.3 m/s and a distance from the facility of 10–14 kilometres, the transport time from the source to the measurements is 57–101 minutes. Hence at this distance the plume is expected to be well mixed, with at least more than $11t^*$ which is the time it takes for a ground source to reach the top of the PBL where only $3t^*$ is required. Thus, the ground measurements under these conditions are expected to be representative of the entire PBL and eq. {3.1} to be applicable. Similarly, transects 5A, 2A and 2B follow the same reasoning. These four transects (two repeat pairs) are treated as the most optimal conditions to derive CH₄ emissions using the MSMB approach herein.

While other transects show a transport time greater than $3t^*$, this parameterization is best suited for the March 28st (plumes 2A and 2B) and March 31st (plumes 5A, 5B) measurements

since the atmospheric conditions were slightly unstable (C) while the other days had neutral (D) conditions. For transects 1A/B, the low solar irradiance (Table 3.2) and high PBL heights resulted in insufficient time for full mixing to occur, and these transects are rejected for use in MSMB. For the other transects 3, and 4A/B, the maximum $3t^*$ values are less than the minimum transport time, however the atmospheric conditions and neutral stability class were not optimal for a quantitative MSMB approach. Thus, in these cases, we cannot be confident that the transect is at a sufficient distance from the source to ensure methane is well mixed in the PBL. The MSMB analysis of the optimal transects is discussed in Section 3.3.3 and non-ideal transects in 3.3.4.

Table 3.1 Estimated atmospheric conditions and transport time for plume transects.

Transect Name ^a	Date	Time ^b (Local)	PG Stability Class ^c	Source Distance (km)	Max $3t_*$ (mins) ^d	Transport Time (mins) ^e	MSMB Status
1A	Nov 21 2014	15:36-15:41	D	6 - 8	60	45-111	Rejected
1B	Nov 21 2014	16:38-16:42	D	6 - 8	90	59-121	Rejected
2A	Mar 28 2017	13:18-13:25	C	10 - 14	32	56-97	Accepted
2B	Mar 28 2017	14:10-14:20	C	10 - 14	37	51-93	Accepted
3	Mar 30 2017	11:40-11:49	D	3 - 6	17	21-50	Uncertain
4A	Mar 30 2017	14:55-15:40	D	6 - 8	25	67-190	Uncertain
4B	Mar 30 2017	15:48-16:55	D	6 - 8	28	83-167	Uncertain
5A	Mar 31 2017	11:20-11:26	C	10 - 14	19	57-101	Accepted
5B	Mar 31 2017	11:45-11:51	C	10 - 14	15	57-101	Accepted

^a Letter naming of the same transect number identifies measurements that are immediate repeats of the same plume from the opposite direction.

^b Local time is MST and MDT in the 2014 and 2017 field studies, respectively.

^c Pasquill Gifford Stability class of C is slightly unstable, and D is neutral.

^d Corresponds to the maximum $3t_*$ parameterization from the lower estimate of w^* , a conservative estimate.

^e Transport time to the nearest possible source in the measured facility and not necessarily the actual source; plume origins are modelled using HYSPLIT and discussed in Section 3.3.2.

Table 3.2 Meteorological data used for the calculation of $3t^*$ and PG atmospheric stability class for each transect.

Transect	T (°C)	Wind Speed (m/s)	Solar Irradiance (W/m ²)	Z _{PBL} (m agl)	w* (m/s) ^a	t* (mins)
1A	8.0	1.7±0.5	37±6	745±57	0.6-0.9	15.3-20.1
1B	8.0	1.4±0.3	23±15	697±57	0.4-0.8	15.3-30.1
2A	4.6	2.7±0.3	179±16	631±22	1.0-1.4	8.0-10.6
2B	4.6	2.9±0.4	295±132	767±17	1.0-1.9	7.0-12.2
3	3.0	2.2±0.2	160±9	252±14	0.7-1.0	4.6-5.8
4A	4.0	1.1±0.4	121±12	356±13	0.7-1.0	6.2-8.3
4B	4.0	1.0±0.2	102±13	381±15	0.7-1.0	6.9-9.2
5A	3.5	2.6±0.3	380±162	369±33	0.9-1.6	4.1-6.5
5B	3.5	2.6±0.3	462±128	310±27	0.9-1.6	3.6-5.0

^a Range is based on the uncertainty in Z_{PBL} and A=0.25-0.55

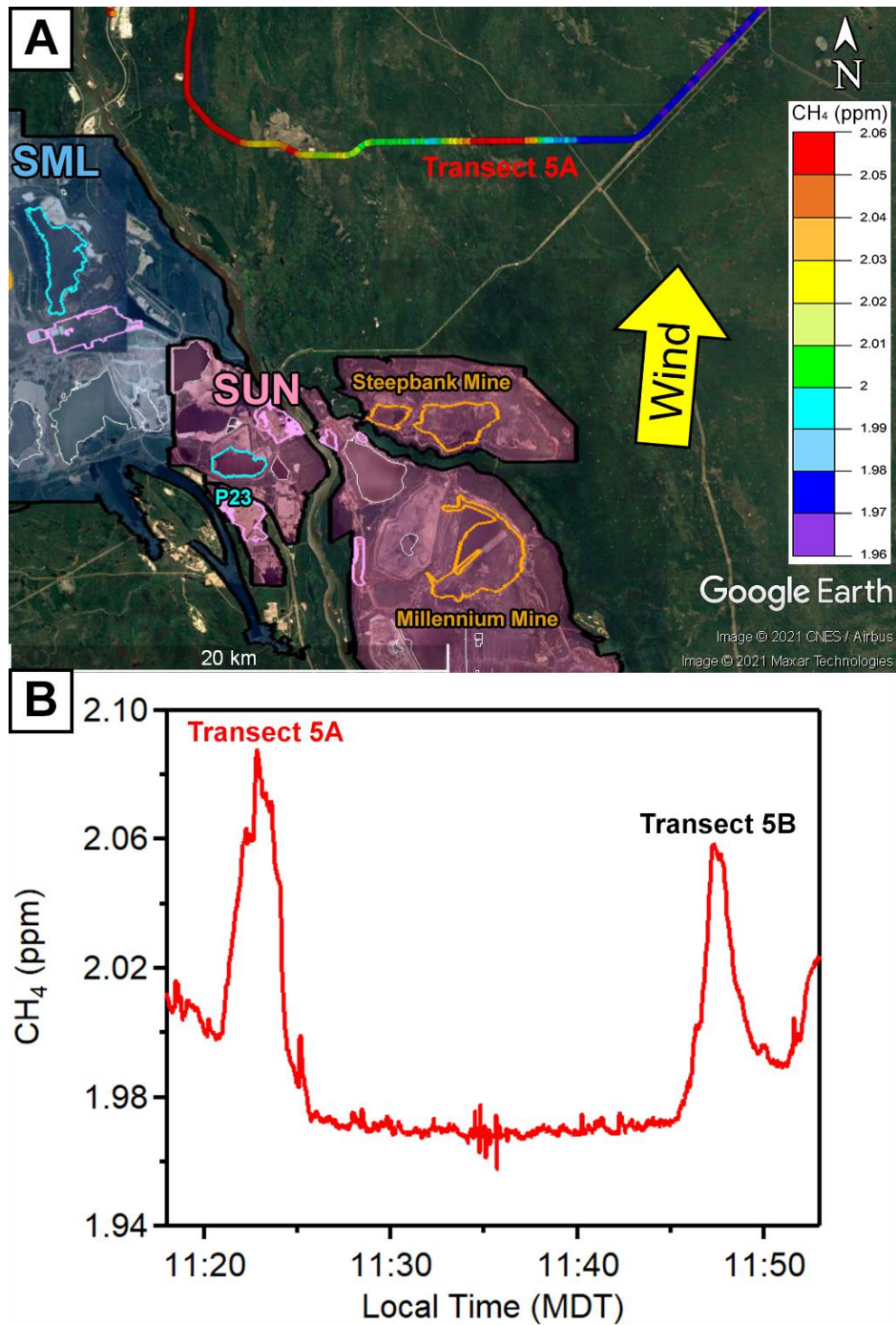


Figure 3.6: Mobile measurements from Mar 31 2017 showing the west-east transect 5A (Panel A) that identified a CH₄ plume from the SUN facility downwind from open-pit mining. Panel B shows the corresponding time series of CH₄ mixing ratios for the two repeat transects of the same plume; West-East (Transect 5A) and East-West (Transect 5B).

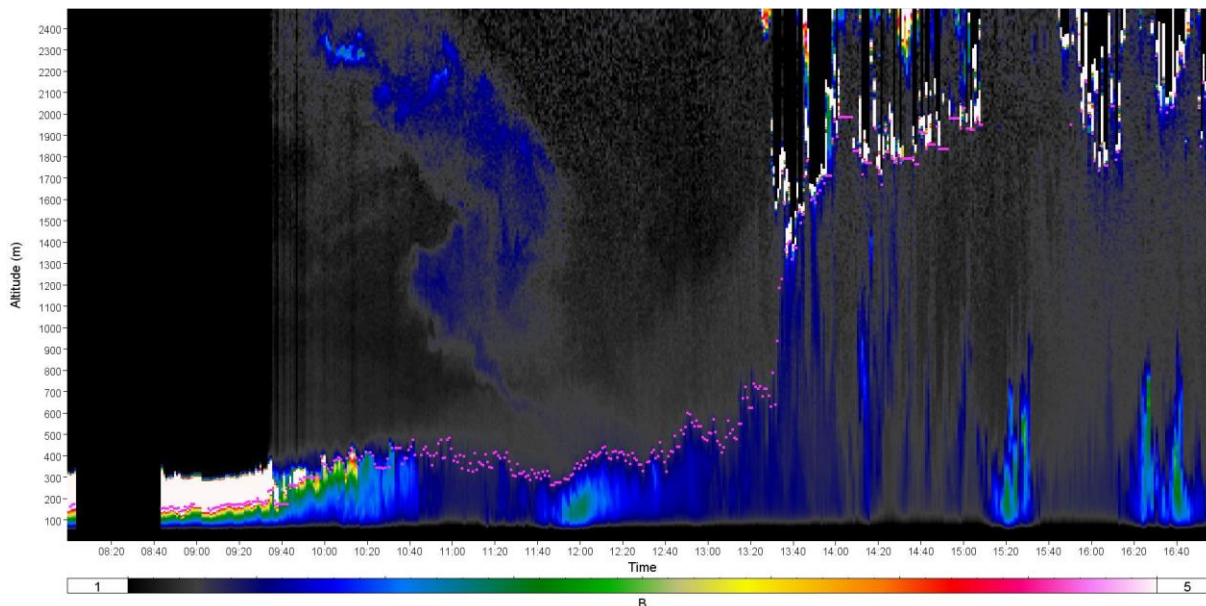


Figure 3.7: Mar 31 2017 LIDAR profile from AMS1. Aerosol backscatter is shown in the color bar on a relative scale. The pink line shows the best estimate for the PBL height. Transects 5A/B occurred between 11:00 to 12:00 MDT.

3.3.3.2 HYSPLIT modelling of plume origins

Plume origins are diagnosed for optimal transects 2A/B and 5A/B using the NOAA HYSPLIT back-trajectory and forward dispersion models (Stein et al., 2015). These four transects are repeat experiments on two separate days (March 28 and 31 2017) measuring a Gaussian CH₄ plume intersected north of the SUN facility under similar meteorological conditions with southerly winds. The web application of HYSPLIT (Rolph et al. 2017) is configured using two archived meteorological products for comparison: Global Data Assimilation (GDAS) at 0.5° resolution and North American Regional Reanalysis (NARR) at 32 km resolution. The back trajectories were run three times for each transect, using origins at the plume maxima and the east and west edges of the plume to produce a simple projection to known sources in the SUN facility (Baray et al. 2018), which were shown to release significant CH₄ in the previous section.

Figure 3.8A shows an example of the back trajectories for Mar 31 2017. The total number of back trajectories are 12 (3 plume boundaries x 2 met products x 2 measurement times), however only 9 are shown because the GDAS 17:00 and 18:00 UTC back trajectories are overlapping (i.e. no model change to wind speeds over the measurement time). The back trajectories project over the northern SUN mine and do not overlap with Pond 2/3 or with the primary SUN facility where upgrading occurs. In addition, Pond 2/3 is on the other side of the Athabasca River which runs through the Suncor facility boundaries between the three Millennium (east), Steepbank (north) and Voyageur (west) sites at this location. The topography and southerly winds makes it unlikely that the measurements made at this location would show a super positioning of surface mining and tailings ponds or facility emissions. To further examine these interpretations, we ran the HYSPLIT model in its forward dispersion mode at the expected plume origin locations at major sources in SUN, including Pond 2/3, beginning 1 hour prior to the measurements, and from the open pit mine (Figure 3.8B). The forward dispersion shows that simulating a source at the centre of the North Steepbank open-pit mine can result in the maxima of the measured plume, and Pond 2/3 is expected to be measured at the enhancements further west from the transect area. The forward dispersion results reproduce the measured enhancements and show the separation of sources for the transect used in mass balance calculations (SUN open pit mining) and the measurements further west (SUN ponds) which are not used. We note the forward dispersion analysis is not an independent validation of the back-trajectories, since the same model meteorology is used in both cases, however it provides more detail on the expected transport between known sources and the point of measurements. These modelling results show that it is unlikely that the tailings ponds emissions are overlapping with the main Gaussian plumes (Figure 3.6) and hence these plumes are attributed to emissions from the open pit mining. Increased confidence of plume origins would be through additional measurements of coincident species (tracers), such as VOCs for active tailings ponds and NO_x and black carbon for open pit mines (Baray et al., 2018).

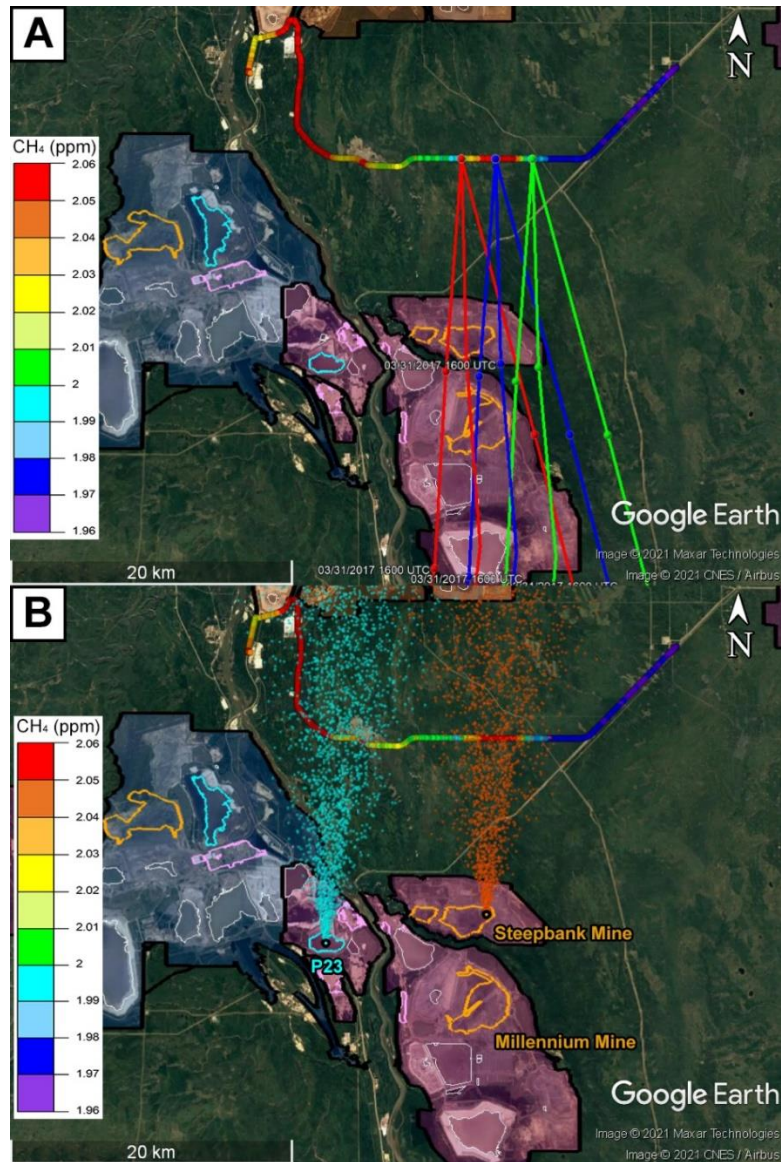


Figure 3.8: HYSPLIT backward trajectory modelling of plume origins for the Mar 31 2017 transect 5A north of SUN. Panel A shows back trajectories modelled at three plume locations: west boundary (red), maximum (blue) and east boundary (green) using two different archived meteorology products (GDAS; left two lines and NARR; right line) at two different measurement times 17:00 and 18:00 UTC. GDAS shows a small difference in the wind speed at the two times (resulting in two lines), while NARR is the same. The bottom panel shows forward dispersion modelling using GDAS meteorology 1 hour prior with plume origins at (a) the North Steepbank Mine and (b) Pond 2/3.

3.3.3.3 Emissions estimates for Suncor open pit mining

Figure 3.9 shows the emissions estimates for the SUN open-pit mining plume described in the previous section. In total there are four transects on two separate days (Mar 28 and 31 2017) with each day including repeat eastbound and westbound transects. Both days had similar wind speeds (3–4 m/s), southerly winds (180–200°) and low temperatures (3.5–4.6°C). However, the PBL height was higher on Mar 28 (663 ± 83 m agl) than on Mar 31 (366 ± 51 m agl). The higher boundary layer height required a longer time for plume mixing, $3t_*$ on Mar 28 (32–37 mins) compared to Mar 31 (15–19 mins). In both cases, the slowest calculated time for plume mixing remains shorter than the fastest calculated transport time from the nearest possible source in the facility to the measurements (Tables 3.1-3.2), which indicates sufficient mixing within the PBL for a constant vertical profile of the CH₄ plume. The mean regional wind speed, which is the average within the PBL determined from the meteorological network of surface, tower, and windRASS measurements (Supplement Section A.1), was 3.4 ± 1.0 m/s for Mar 28 and 3.8 ± 0.8 m/s for Mar 31. The calculated emissions rates for Mar 28 are 1.2 ± 0.4 t hr⁻¹ and 1.4 ± 0.5 t hr⁻¹ and the emissions rates for Mar 31 are 0.9 ± 0.4 t hr⁻¹ and 0.6 ± 0.3 t hr⁻¹. The relative uncertainties in the individual measurements are 30–50%; this is from a sensitivity analysis that includes the sum in quadrature of the uncertainty in the background (18–34%), the uncertainty in the mean regional wind speed in the PBL (20–32%) and the PBL height retrieval over the measurement period (13–14%) for each transect. The uncertainty in the wind speed includes uncertainty in the wind direction (10–20%). The four experiments show good reproducibility within the uncertainties and are consistent with the expected methodology uncertainties of 30–50% for mass balance methods (Cambaliza et al., 2014; Gordon et al., 2015). The mean emissions rate of these four experiments for the Suncor open pit mining is 1.0 ± 0.4 t hr⁻¹ where the uncertainty interval is the 1 σ spread in the 4 emission rates.

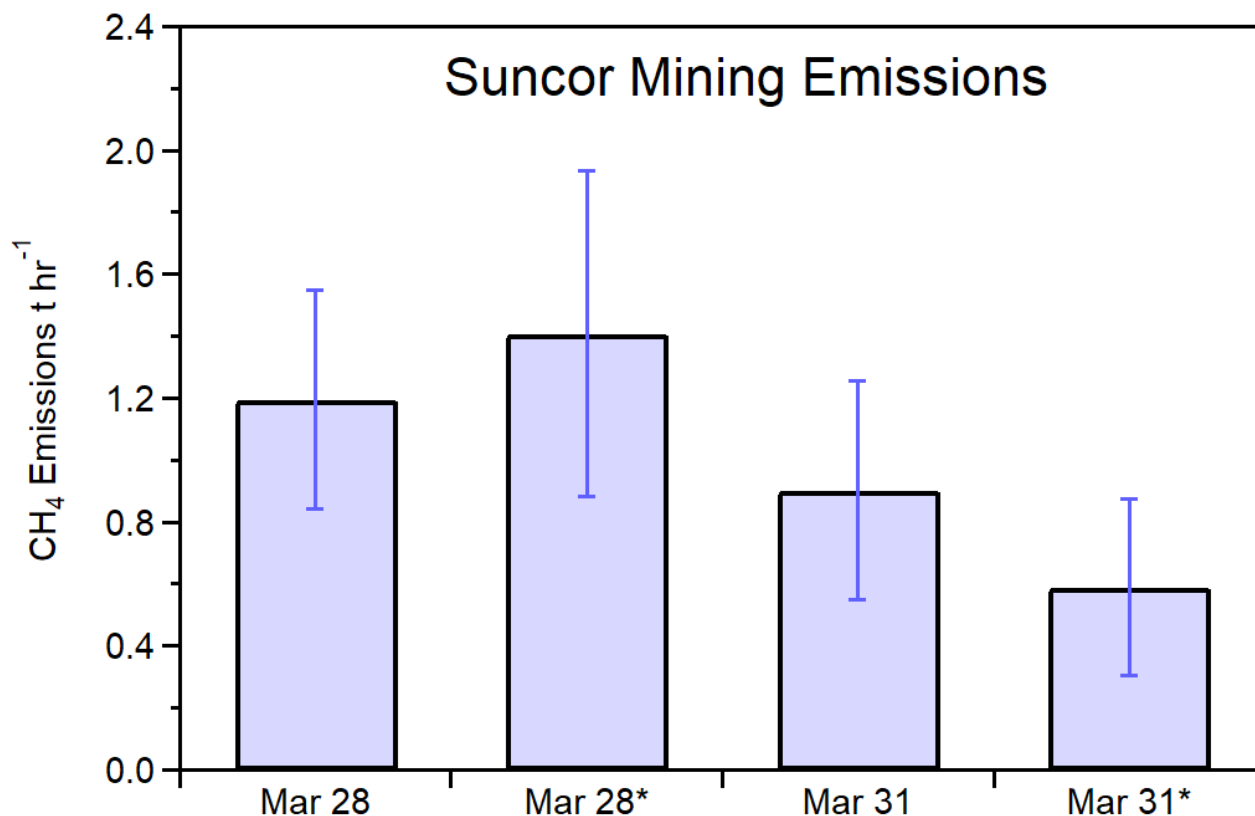


Figure 3.9: Emissions rates for the four repeat transects of Suncor open-pit mining emissions. Error bars are from the sensitivity analysis (Supplement B.1.4) which incorporates uncertainties in the CH₄ measurements and background, the wind speed and direction, and the PBL height retrieval.

3.3.3.4 Treatment of non-ideal transects

Figure 3.10 shows the non-quantitative transect 3 downwind of the CNRL open-pit mining operations. The background was ~2.1 ppm and the maximum mixing ratio from a Gaussian-shaped plume was 2.9 ppm. The enhancement at CNRL is much higher than the enhancement observed from SUN in Figure 3.6 due to the proximity to the source and the lower boundary layer. The nearest source, which is the Horizon open-pit mine, is approximately 3–6 km away from the measurements. The PBL height was low during this time at 252 ± 14 m, with low solar irradiance at 160 ± 9 W m⁻² due to an overcast cloud layer, however the timing of the transect near

noon provided close to the maximum radiation for the day. Table 3.1 shows that the maximum time for complete plume mixing $3t^*$ was 17 minutes, which is within the fastest possible transport time to the open-pit mine at 21 minutes. However, the close margin of these values and the neutral atmospheric conditions (class D) reduces confidence in the assumption of complete plume mixing.

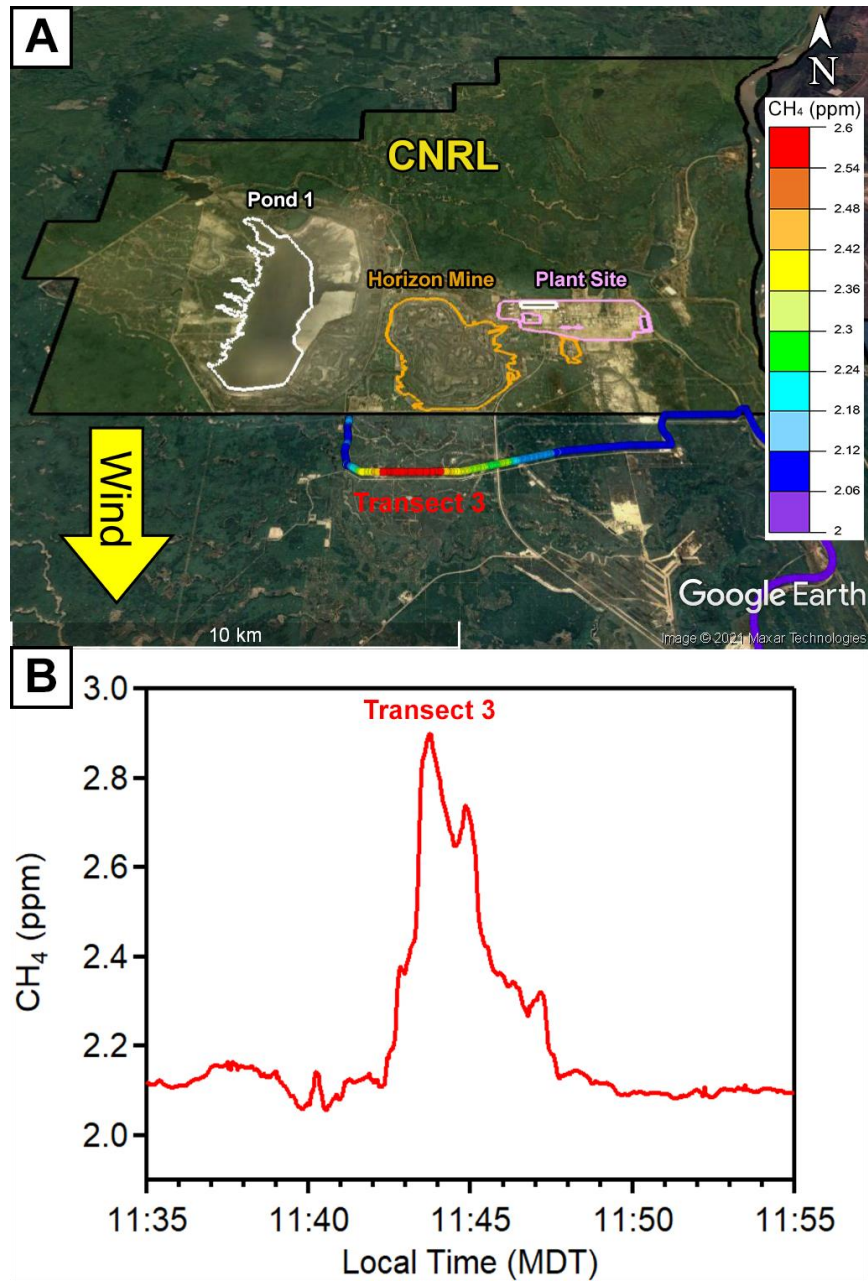


Figure 3.10: Mobile measurements from Mar 30 2017 showing the west-east transect 3 that identified a CH₄ plume from the CNRL facility downwind from open-pit mining. Panel B shows the corresponding time series of CH₄ mixing ratios.

3.3.4 Comparison between top-down and bottom-up estimates

An intensive top-down CH₄ study using aircraft measurements was conducted in Summer 2013 led by Environment and Climate Change Canada (Baray et al., 2018). In that study, CH₄ was tracked using chemical signatures for tailings ponds (VOCs) and open-pit mining (NO_y + black carbon) and emissions were individually quantified per facility and per source. Aircraft mass balance of Suncor open-pit mining in Aug 2013 was $1.5 \pm 0.4 \text{ t hr}^{-1}$ on one day and $1.9 \pm 0.3 \text{ t hr}^{-1}$ on another day. These emissions on average (1.7 ± 0.4) are 70% higher than the average 2017 emissions in this study ($1.0 \pm 0.4 \text{ t hr}^{-1}$). However, we are comparing to a limited number of days of observations (2 days each in 2013 and 2017) and the uncertainty intervals overlap. It is not clear how much of this difference is due to uncertainties in the method – which would be resolved with a larger number of samples – day-to-day variability in the meteorological conditions, a seasonal dependence on emissions, and/or a change in activity factors between 2013 to 2017. For example, in this 2017 study, there is a 0.2 t hr^{-1} difference in repeat measurements for the same day on Mar 28 and a 0.3 t hr^{-1} difference on Mar 31, and the mean difference between the Mar 28 and Mar 31 average emissions rates is 0.55 t hr^{-1} . The mean difference between Aug 2013 aircraft measurement days is 0.4 t hr^{-1} for this same source. These 30-50% uncertainty intervals are typical for mass balance methods (Cambaliza et al., 2014). Hence a signal from a seasonal dependence on emissions, which likely exists, is beneath the noise of the limited samples of mass balance derived emissions. Reductions in the uncertainties, which can be most readily addressed with larger sample sizes, may better characterize finer-scale fluctuations in emissions.

The complex nature of methane emissions in the AOSR have made reconciling divergent top-down and bottom-up emissions estimates challenging. Several studies have taken place in the AOSR area to quantify methane emissions with both bottom-up and top-down approaches which have been compared to industry-reported estimates in the Greenhouse Gas Reporting Program (GHGRP). The GHGRP methane emissions for tailings ponds and open pit mines are derived from flux chamber measurements at the surface according to the protocols described by Alberta Environment and Parks (GOA, 2019). Johnson et al. (2016) showed a control-system approach whereby extracted core samples from undeveloped mine regions were shown to degas CH₄ and

used those samples to develop emissions factors as a function of total mined material or bitumen content to provide an alternate emission estimate from the open pit mining sources. In that study emissions were lower than the GHGRP, however the authors noted that it was unclear whether their emissions factors represented the same emissions that are measured by flux chambers at the mine surface or should be considered as additional emissions. As they elaborated, anecdotal reports suggest that the CH₄ from open-pit mining tends to originate from a small number of locations, with most flux chamber measurements showing near zero fluxes and other locations showing order of magnitude larger emissions. Hence the authors suggest it is more likely that decomposition of the mined material is a different mechanism of emissions from the open pit surface emissions measured at the permeable surface. The Alberta Energy Regulator addresses the heterogeneity of the surface fluxes by setting recommendations for how flux chamber measurements should sample tailings ponds and open pit mines, but studies continue to show discrepancies.

For the summer 2013 aircraft study, the resulting emissions estimates were 48% higher than the GHGRP for the AOSR as a whole and 133% higher than the GHGRP for the Suncor facility. More recently You et al. (2021) used micrometeorological flux methods at SUN Pond 2/3 in summer 2017 and compared their emissions estimates from these tailing ponds to coincident flux chamber measurements. They showed the eddy covariance method emissions were 222% higher than the flux chamber method over the same period of measurements. Extrapolating 5-week 2017 measurements to the entire year resulted in emissions of 6548 t CH₄ yr⁻¹. In this study, our mean estimate for March 2017 Suncor mining is 1.0 t CH₄ hr⁻¹, which corresponds to 8760 t CH₄ yr⁻¹ when extrapolated for all of 2017, with an assumption of a constant temporal profile. Therefore, the sum of these two top-down studies in 2017 for the Suncor facility from: (1) open-mining emissions that we determine using MSMB in this study and (2) tailings ponds emissions in You et al. (2021) using eddy covariance measurements corresponds to 15,338 t CH₄ yr⁻¹, or 1.75 t hr⁻¹. As shown in Figure 3.11, in the GHGRP, the total emissions from Suncor in 2017 were reported to be 5977 kt (0.68 t hr⁻¹); the sum of these two estimates is 157% higher than the GHGRP. Figure 3.11 also shows that in the GHGRP, emissions decreased from 2013 to 2017 by ~63%. Similarly, the difference between top-down measurements in 2013 and 2017 correspond

to a decrease of ~42%. The results may suggest top-down and bottom-up measurements corroborate a similar downtrend in emissions but differ in each year due to some form of bias. Unfortunately, the GHGRP does not report error intervals, so we are unable to determine if these differences can be associated with measurement uncertainties which is highly likely to be an important consideration for the comparison.

Future measurements should aim to reconcile divergent emissions, which can be accomplished by improving both top-down and bottom-up methods (Zavala-Araiza et al., 2015). The continued discrepancy may be due to a combination of factors from a) methodology and accounting of emissions in bottom-up estimates and b) temporal variability and gaps in top-down measurements. A low bias of 64% in the flux chamber method has been discussed in You et al. (2021) for a tailings pond using coincident measurements. If such a low bias demonstrated at one pond in that study is representative of the entire AOSR then it would largely explain the differences shown in Figure 3.11. However, it has been shown in Zhang et al. (2019) that individual flux chamber measurements can either be unrepresentatively high when emissions hotspots overwhelm the instrument or unrepresentatively low since most of the area sources are not uniformly emitting methane. Furthermore, Vaughn et al. (2018) showed that for natural gas production, temporal variability in measurement coverage largely explains the difference between top-down and bottom-up estimates. If tailings ponds and mining emissions are insensitive to environmental conditions, this may result in negligible differences in emissions diurnally and over a month (You et al., 2021). The seasonality of tailings ponds emissions can be further complicated by the unique character of each pond as process-active or reclamation sites (Clark et al., 2021). The fluxes produced by tailings ponds and open pit mines may vary with several environmental (temperature, wind-speed) and activity related factors (mining operations, degassing from fissures, diluent composition and outfalls into tailings ponds, ice melting, etc). Improving emissions estimates on both ends for bottom-up and top-down methods will likely converge upon a more reliable CH₄ budget for the AOSR. Field studies that intercompare between measurement techniques will shed better light on discrepancies and the mechanisms of CH₄ release that influence the pattern of emissions. Ideally, year-round high-density spatial and

temporal field measurements can better characterize these temporal gaps. The cost effective vehicle-based measurements shown in this study can be readily deployed to fit that purpose.

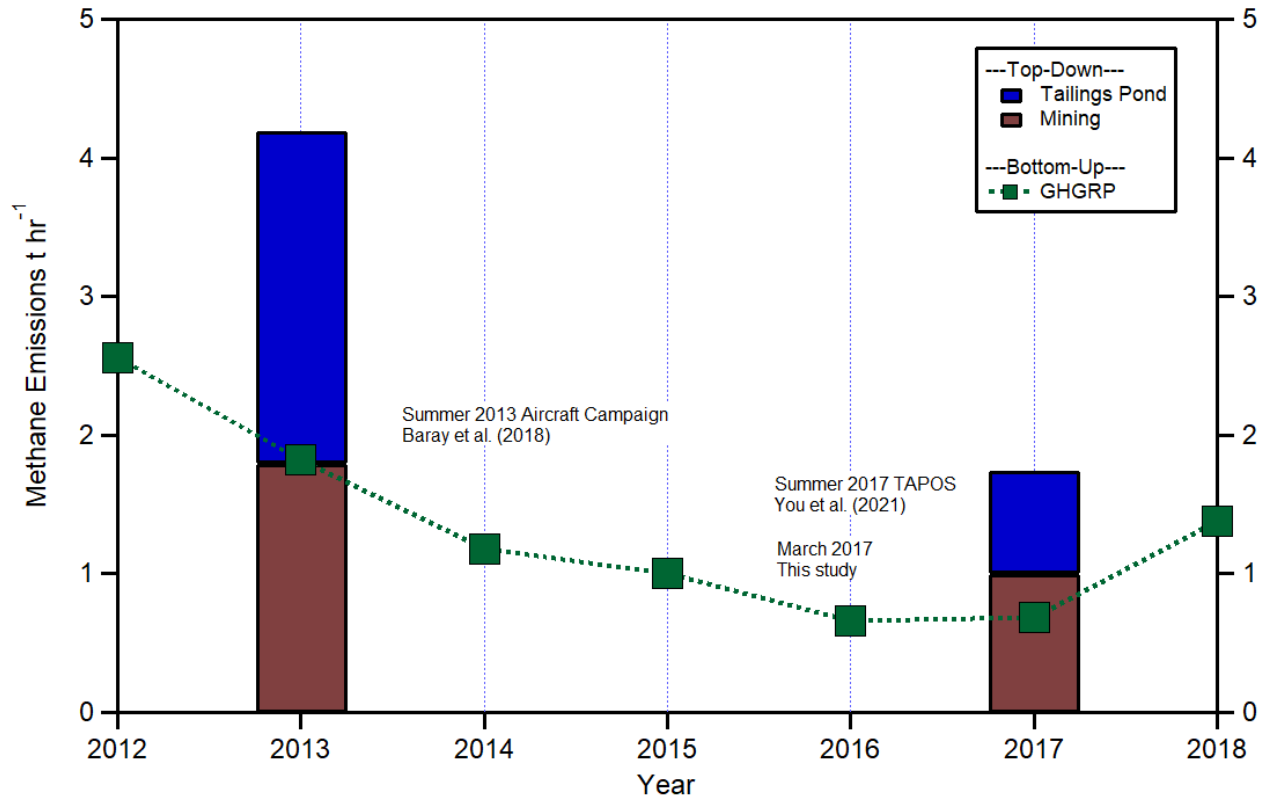


Figure 3.11: Comparison of top-down emission rates (brown and blue bars) to GHGRP (green line and squares) for the Suncor facility. The 2013 tailings ponds and mining emissions rates are from the summer 2013 aircraft campaign (Baray et al., 2018). The 2017 tailings ponds emissions are from the summer 2017 TAPOS eddy covariance measurements (You et al., 2021), and the 2017 open-pit mining emissions are from this study using measurements from March 2017, both upscaled for the year.

3.4 Conclusions

We show mobile surface measurements of CH₄ can be used to survey cold season methane emissions in the AOSR in two different field studies, Fall/Winter 2014 and Spring/Winter 2017 under snow covered conditions. The measurements show that tailings ponds emissions continue to emit large CH₄ plumes, both from Syncrude Mildred Lake Settling Basin (MLSB) and Suncor Pond 2/3 (P23) in both years. Based on previous measurements (Baray et al., 2018) consistent with bottom-up studies (Small et al., 2015), these two tailings ponds sources account for the overwhelming majority (>90%) of pond methane emissions in the AOSR, which this study shows is persistent in the cold season. We repeatedly measured maximum CH₄ mixing ratios exceeding 3.0 ppm on the highways nearing MLSB and P23.

Our measurements also show high CH₄ mixing ratios of 23 ppm in 2014 and 87 ppm in 2017, which in 2017 was visually confirmed to be from venting activity. These localized events were not frequently observed over the two field studies, and we infer that they are not comparable in magnitude to open-pit mining and tailings ponds emissions. However, their existence poses uncertainties for top-down measurements since high emitting events could occur during temporal gaps between measurements.

We used the novel approach of mobile-surface mass-balance (MSMB), which is similar to aircraft mass balance studies that determine emissions rates using single transects. The assumption of a well-mixed plume in the planetary boundary layer is justified here using extensive meteorological measurements in the region and LIDAR backscatter retrievals of the PBL height. We present four repeat transects with optimal conditions downwind of the Suncor open pit mining in 2017 on two different days, and show using HYSPLIT modelling that the plume can be modelled to the Steepbank mine, with unlikely interference from Suncor tailings ponds or upgrader facility emissions. Our estimate for Suncor open pit mining is 1.0 ± 0.4 t CH₄ hr⁻¹ in 2017. When this emissions rate is combined with the Suncor tailings pond emissions rate from You et al. (2021), the resulting sum is a factor of 2.6 higher than the reported emissions in the bottom-up GHG inventory. These results show that there is consistent discrepancy between bottom-up and top-down emissions rates for the AOSR, and further measurements are needed to

produce the most robust budget and mechanistic understanding for these fugitive emissions. Mobile surface campaigns are a cost-effective solution to fill the spatial and temporal observation gaps, as aircraft campaigns are limited in time and surface stations are limited in space. Long-term monitoring of emissions trends provides key data to guide fugitive emissions mitigation policy.

Acknowledgements

The authors thank the Wood Buffalo Environmental Association (WBEA) for meteorological data provision. This project was supported by funding from NSERC CREATE and Environment and Climate Change Canada.

Conflict of interest

The authors declare no conflict of interest.

References

- Ars, S., Vogel, F., Arrowsmith, C., Heerah, S., Knuckey, E., Lavoie, J., Lee, C., Pak, N. M., Phillips, J. L., and Wunch, D.: Investigation of the Spatial Distribution of Methane Sources in the Greater Toronto Area Using Mobile Gas Monitoring Systems, *Environ. Sci. Technol.*, 54, 15671–15679, <https://doi.org/10.1021/acs.est.0c05386>, 2020.
- Baray, S., Darlington, A., Gordon, M., Hayden, K. L., Leithead, A., Li, S.-M., Liu, P. S. K., Mittermeier, R. L., Moussa, S. G., O'Brien, J., Staebler, R., Wolde, M., Worthy, D., and McLaren, R.: Quantification of methane sources in the Athabasca Oil Sands Region of Alberta by aircraft mass balance, *Atmos. Chem. Phys.*, 18, 7361–7378, <https://doi.org/10.5194/acp-18-7361-2018>, 2018.
- Baray, S., Jacob, D. J., Massakkars, J. D., Sheng, J.-X., Sulprizio, M. P., Jones, D. B. A., Bloom, A. A., and McLaren, R.: Estimating 2010–2015 Anthropogenic and Natural Methane Emissions in Canada using ECCO Surface and GOSAT Satellite Observations, *Gases/Atmospheric Modelling/Troposphere/Physics (physical properties and processes)*, <https://doi.org/10.5194/acp-2020-1195>, 2021.
- Cambaliza, M. O. L., Shepson, P. B., Caulton, D. R., Stirm, B., Samarov, D., Gurney, K. R., Turnbull, J., Davis, K. J., Possolo, A., Karion, A., Sweeney, C., Moser, B., Hendricks, A., Lauvaux, T., Mays, K., Whetstone, J., Huang, J., Razlivanov, I., Miles, N. L., and Richardson, S. J.: Assessment of uncertainties of an aircraft-based mass balance approach for quantifying urban greenhouse gas emissions, *Atmos. Chem. Phys.*, 14, 9029–9050, <https://doi.org/10.5194/acp-14-9029-2014>, 2014.
- Clark, M. G., Drewitt, G. B., and Carey, S. K.: Energy and carbon fluxes from an oil sands pit lake, *Science of The Total Environment*, 752, 141966, <https://doi.org/10.1016/j.scitotenv.2020.141966>, 2021.
- Cusworth, D. H., Jacob, D. J., Sheng, J.-X., Benmergui, J., Turner, A. J., Brandman, J., White, L., and Randles, C. A.: Detecting high-emitting methane sources in oil/gas fields using satellite observations, *Atmos. Chem. Phys.*, 18, 16885–16896, <https://doi.org/10.5194/acp-18-16885-2018>, 2018.
- Davis, Z. Y. W., Baray, S., McLinden, C. A., Khanbabakhani, A., Fujs, W., Csukat, C., Debosz, J., and McLaren, R.: Estimation of NO_x and SO₂ emissions from Sarnia, Ontario, using a mobile MAX-DOAS (Multi-AXis Differential Optical Absorption Spectroscopy) and a NO_x analyzer, *Atmos. Chem. Phys.*, 19, 13871–13889, <https://doi.org/10.5194/acp-19-13871-2019>, 2019.
- Gordon, M., Li, S.-M., Staebler, R., Darlington, A., Hayden, K., O'Brien, J., and Wolde, M.: Determining air pollutant emission rates based on mass balance using airborne measurement data over the Alberta oil sands operations, *Atmos. Meas. Tech.*, 8, 3745–3765, <https://doi.org/10.5194/amt-8-3745-2015>, 2015.
- Johnson, M. R., Crosland, B. M., McEwen, J. D., Hager, D. B., Armitage, J. R., Karimi-Golpayegani, M., and Picard, D. J.: Estimating fugitive methane emissions from oil sands mining using extractive core samples, *Atmospheric Environment*, 144, 111–123, <https://doi.org/10.1016/j.atmosenv.2016.08.073>, 2016.
- Karion, A., Sweeney, C., Kort, E. A., Shepson, P. B., Brewer, A., Cambaliza, M., Conley, S. A., Davis, K., Deng, A., Hardesty, M., Herndon, S. C., Lauvaux, T., Lavoie, T., Lyon, D., Newberger, T., Pétron, G., Rella, C., Smith, M., Wolter, S., Yacovitch, T. I., and Tans, P.: Aircraft-Based Estimate of Total Methane Emissions from the Barnett Shale Region, *Environ. Sci. Technol.*, 49, 8124–8131, <https://doi.org/10.1021/acs.est.5b00217>, 2015.

Kong, J. D., Wang, H., Siddique, T., Foght, J., Semple, K., Burkus, Z., and Lewis, M. A.: Second-generation stoichiometric mathematical model to predict methane emissions from oil sands tailings, *Science of The Total Environment*, 694, 133645, <https://doi.org/10.1016/j.scitotenv.2019.133645>, 2019.

Lan, X., Talbot, R., Laine, P., and Torres, A.: Characterizing Fugitive Methane Emissions in the Barnett Shale Area Using a Mobile Laboratory, *Environ. Sci. Technol.*, 49, 8139–8146, <https://doi.org/10.1021/es5063055>, 2015.

Liggio, J., Li, S.-M., Staebler, R. M., Hayden, K., Darlington, A., Mittermeier, R. L., O'Brien, J., McLaren, R., Wolde, M., Worthy, D., and Vogel, F.: Measured Canadian oil sands CO₂ emissions are higher than estimates made using internationally recommended methods, *Nat Commun*, 10, 1863, <https://doi.org/10.1038/s41467-019-09714-9>, 2019.

Maazallahi, H., Fernandez, J. M., Menoud, M., Zavala-Araiza, D., Weller, Z. D., Schwietzke, S., von Fischer, J. C., Denier van der Gon, H., and Röckmann, T.: Methane mapping, emission quantification, and attribution in two European cities: Utrecht (NL) and Hamburg (DE), *Atmos. Chem. Phys.*, 20, 14717–14740, <https://doi.org/10.5194/acp-20-14717-2020>, 2020.

Nambiar, M. K., Robe, F. R., Seguin, A. M., Endsin, M., and Aliabadi, A. A.: Diurnal and Seasonal Variation of Area-Fugitive Methane Advective Flux from an Open-Pit Mining Facility in Northern Canada Using WRF, *Atmosphere*, 11, 1227, <https://doi.org/10.3390/atmos11111227>, 2020.

Peischl, J., Karion, A., Sweeney, C., Kort, E. A., Smith, M. L., Brandt, A. R., Yeskoo, T., Aikin, K. C., Conley, S. A., Gvakharia, A., Trainer, M., Wolter, S., and Ryerson, T. B.: Quantifying atmospheric methane emissions from oil and natural gas production in the Bakken shale region of North Dakota: CH₄ Emissions From the Bakken, *J. Geophys. Res. Atmos.*, 121, 6101–6111, <https://doi.org/10.1002/2015JD024631>, 2016.

Rolph, G., Stein, A., and Stunder, B.: Real-time Environmental Applications and Display sYstem: READY, *Environmental Modelling & Software*, 95, 210–228, <https://doi.org/10.1016/j.envsoft.2017.06.025>, 2017.

Sheng, J.-X., Jacob, D. J., Maasackers, J. D., Sulprizio, M. P., Zavala-Araiza, D., and Hamburg, S. P.: A high-resolution (0.1° × 0.1°) inventory of methane emissions from Canadian and Mexican oil and gas systems, *Atmospheric Environment*, 158, 211–215, <https://doi.org/10.1016/j.atmosenv.2017.02.036>, 2017.

Simpson, I. J., Blake, N. J., Barletta, B., Diskin, G. S., Fuelberg, H. E., Gorham, K., Huey, L. G., Meinardi, S., Rowland, F. S., Vay, S. A., Weinheimer, A. J., Yang, M., and Blake, D. R.: Characterization of trace gases measured over Alberta oil sands mining operations: 76 speciated C₂–C₁₀; volatile organic compounds (VOCs), CO₂, CH₄, CO, NO₂, NO_y, O₃; and SO₂, *Atmos. Chem. Phys.*, 10, 11931–11954, <https://doi.org/10.5194/acp-10-11931-2010>, 2010.

Small, C. C., Cho, S., Hashisho, Z., and Ulrich, A. C.: Emissions from oil sands tailings ponds: Review of tailings pond parameters and emission estimates, 127, 490–501, <https://doi.org/10.1016/j.petrol.2014.11.020>, 2015.

Stein, A. F., Draxler, R. R., Rolph, G. D., Stunder, B. J. B., Cohen, M. D., and Ngan, F.: NOAA's HYSPLIT Atmospheric Transport and Dispersion Modeling System, 96, 2059–2077, <https://doi.org/10.1175/BAMS-D-14-00110.1>, 2015.

Stull, R. B. (Ed.): *An Introduction to Boundary Layer Meteorology*, Springer Netherlands, Dordrecht, <https://doi.org/10.1007/978-94-009-3027-8>, 1988.

Varon, D. J., McKeever, J., Jervis, D., Maasackers, J. D., Pandey, S., Houweling, S., Aben, I., Scarpelli, T., and Jacob, D. J.: Satellite Discovery of Anomalously Large Methane Point Sources From Oil/Gas Production, *Geophys. Res. Lett.*, 46, 13507–13516, <https://doi.org/10.1029/2019GL083798>, 2019.

Vaughn, T. L., Bell, C. S., Pickering, C. K., Schwietzke, S., Heath, G. A., Pétron, G., Zimmerle, D. J., Schnell, R. C., and Nummedal, D.: Temporal variability largely explains top-down/bottom-up difference in methane emission estimates from a natural gas production region, *Proc Natl Acad Sci USA*, 115, 11712–11717, <https://doi.org/10.1073/pnas.1805687115>, 2018.

You, Y., Staebler, R. M., Moussa, S. G., Beck, J., and Mittermeier, R. L.: Methane emissions from an oil sands tailings pond: a quantitative comparison of fluxes derived by different methods, *Atmos. Meas. Tech.*, 14, 1879–1892, <https://doi.org/10.5194/amt-14-1879-2021>, 2021.

Zavala-Araiza, D., Lyon, D. R., Alvarez, R. A., Davis, K. J., Harriss, R., Herndon, S. C., Karion, A., Kort, E. A., Lamb, B. K., Lan, X., Marchese, A. J., Pacala, S. W., Robinson, A. L., Shepson, P. B., Sweeney, C., Talbot, R., Townsend-Small, A., Yacovitch, T. I., Zimmerle, D. J., and Hamburg, S. P.: Reconciling divergent estimates of oil and gas methane emissions, 201522126, <https://doi.org/10.1073/pnas.1522126112>, 2015.

Zhang, L., Cho, S., Hashisho, Z., and Brown, C.: Quantification of fugitive emissions from an oil sands tailings pond by eddy covariance, *Fuel*, 237, 457–464, <https://doi.org/10.1016/j.fuel.2018.09.104>, 2019.

Zhang, Y., Gautam, R., Pandey, S., Omara, M., Maasackers, J. D., Sadavarte, P., Lyon, D., Nesser, H., Sulprizio, M. P., Varon, D. J., Zhang, R., Houweling, S., Zavala-Araiza, D., Alvarez, R. A., Lorente, A., Hamburg, S. P., Aben, I., and Jacob, D. J.: Quantifying methane emissions from the largest oil-producing basin in the United States from space, *Sci. Adv.*, 6, eaaz5120, <https://doi.org/10.1126/sciadv.aaz5120>, 2020.

Chapter 4 Estimating 2010-2015 anthropogenic and natural methane emissions in Canada using ECCC surface and GOSAT satellite observations

Author Contributions

Sabour Baray¹, Daniel J. Jacob², Joannes D. Maasakkers³, Jian-Xiong Sheng⁴, Melissa P. Sulprizio², Dylan B.A. Jones⁵, A. Anthony Bloom⁶, and Robert McLaren¹

1. Centre for Atmospheric Chemistry, York University, Toronto, Canada
2. Harvard University, Cambridge, MA, USA
3. SRON Netherlands Institute for Space Research, Utrecht, The Netherlands
4. Massachusetts Institute of Technology, Cambridge, MA, USA
5. University of Toronto, Toronto, Canada
6. Jet Propulsion Laboratory, California Institute of Technology, Pasadena, CA, USA

SB, DJJ and RM designed the study. SB conducted the simulations and analysis with contributions from JDM, JXS, MPS, and DBAJ. AAB provided WetCHARTS emissions and supporting data. SB and RM wrote the paper with contributions from all authors.

Abstract

Methane emissions in Canada have both anthropogenic and natural sources. Anthropogenic emissions are estimated to be 4.1 Tg a^{-1} from 2010–2015 in the National Inventory Report submitted to the United Nation’s Framework Convention on Climate Change (UNFCCC). Natural emissions, which are mostly due to Boreal wetlands, are the largest methane source in Canada and highly uncertain, on the order of $\sim 20 \text{ Tg a}^{-1}$ in biosphere process models. Aircraft studies over the last several years have provided ‘snapshot’ emissions that conflict with inventory estimates. Here we use surface data from the Environment and Climate Change Canada (ECCC) in situ network and space borne data from the Greenhouse Gases Observing Satellite (GOSAT) to determine 2010–2015 anthropogenic and natural methane emissions in Canada in a Bayesian inverse modelling framework. We use GEOS-Chem to simulate anthropogenic emissions comparable to the National Inventory and wetlands emissions using an ensemble of WetCHARTS v1.0 scenarios in addition to other minor natural sources. We conduct a comparative analysis of the monthly natural emissions and yearly anthropogenic emissions optimized by surface and satellite data independently. Mean 2010–2015 posterior emissions using ECCC surface data are $6.0 \pm 0.4 \text{ Tg a}^{-1}$ for total anthropogenic and $11.6 \pm 1.2 \text{ Tg a}^{-1}$ for total natural emissions. These results agree with our posterior using GOSAT data of $6.5 \pm 0.7 \text{ Tg a}^{-1}$ for total anthropogenic and $11.7 \pm 1.2 \text{ Tg a}^{-1}$ for total natural emissions. The seasonal pattern of posterior natural emissions using either dataset shows a slower to start emissions in the spring and a less intense peak in the summer compared to the mean of WetCHARTS scenarios. We combine ECCC and GOSAT data to characterize limitations towards sectoral and provincial level inversions. We estimate Energy + Agriculture emissions to be $5.1 \pm 1.0 \text{ Tg a}^{-1}$ which is 59% higher than the National inventory. We attribute 39% higher anthropogenic emissions to Western Canada than the prior. Natural emissions are lower across Canada. Inversion results are verified against independent aircraft data and surface data which show better agreement with posterior emissions. This study shows a readjustment of the Canadian methane budget is necessary to better match atmospheric observations with lower natural emissions partially offset by higher anthropogenic emissions.

4.1 Introduction

Methane is a significant anthropogenically-influenced greenhouse gas second to carbon dioxide in terms of its direct radiative forcing (Myhre et al., 2013). The mixing ratio of methane has increased from ~720 to ~1800 ppb since pre-industrial times (Hartmann et al., 2013). Present-day global methane emissions are well known to be $550 \pm 60 \text{ Tg a}^{-1}$ (Prather et al., 2012). However recent trends in atmospheric methane since the 1990s are not well understood (Turner et al., 2019). Anthropogenic methane sources include oil and gas activities, livestock, rice cultivation, coal mines, landfills, and wastewater treatment. Natural methane emissions are dominated by wetlands, but also include seeps, termites and biomass burning (Kirschke et al., 2013). The main sink of methane is oxidation by the hydroxyl radical (OH) resulting in a lifetime of 9.1 ± 0.9 years (Prather et al., 2012). Improving constraints on national methane emissions is a requirement of mitigation policy (Nisbet et al., 2020). Here we use atmospheric methane observations from the Environment and Climate Change Canada (ECCC) surface network and satellite observations from the Greenhouse Gas Observing Satellite (GOSAT) to estimate Canadian methane emissions and disaggregate anthropogenic and natural sources.

In the Government of Canada's submission to the United Nations Framework Convention on Climate Change (UNFCCC), hereafter referred to as the National Inventory, anthropogenic emissions are estimated to be 4.1 Tg a^{-1} in 2015, with 68% of emissions originating from the Western Canadian provinces of Alberta (42%), Saskatchewan (17%) and British Columbia (9%). Sectoral contributions over the entire country are from three categories: Energy (49%), Agriculture (29%) and Waste (22%) (Environment and Climate Change Canada, 2017). Natural emissions, which are mostly due to Boreal wetlands, are highly uncertain, on the order of ~10-30 Tg a^{-1} from biosphere process modelling (Miller et al., 2014; Bloom et al., 2017).

Atmospheric observations provide constraints on methane emissions. Studies constraining anthropogenic and/or natural methane emissions within Canada have included the use of surface in situ measurements (Miller et al., 2016; Atherton et al., 2017; Ishizawa et al., 2019), aircraft campaigns (Johnson et al., 2017; Baray et al., 2018) and satellites (Wecht et al., 2014; Turner et al., 2015; Maasakkers et al., 2021). These observations can determine emissions through mass

balance methods or be used in conjunction with a chemical transport model (CTM). Bayesian inverse modelling constrains prior knowledge of emissions based on the mismatch between modelled and observed concentrations. This requires reliable mapping of “bottom-up” inventory emissions for the “top-down” observational constraints to be useful (Jacob et al., 2016). Inverse modelling has been more challenging for Canada than the United States due to a) the sparsity of surface stations and satellite data (Sheng et al., 2018a), b) a factor of ~10 lower anthropogenic emissions (Maasakkers et al., 2019), c) large spatially-overlapping emissions from Boreal wetlands that are highly uncertain (Miller et al., 2014), and d) model biases in the high-latitudes stratosphere (Patra et al., 2011), compromising the interpretation of observed methane columns.

These observing system challenges have made Canadian methane emissions difficult to quantify. However, studies show a consistent story across different scales and measurement platforms. Miller et al. (2014, 2016) determined that the North American network can successfully constrain Canadian natural emissions and found Boreal wetlands to be lower in 2008 when compared to prior fluxes in the WETCHIMP model. Aircraft campaigns over the Alberta oil and gas sector have found higher emissions than inventories in the Red Deer and Lloydminster regions (Johnson et al., 2017) and unconventional oil extraction in the Athabasca Oil Sands region (Baray et al., 2018). Atherton et al. (2017) conducted ground-based mobile measurements of gas production in British Columbia and determined higher emissions than reported, and Zavala-Araiza et al. (2018) conducted similar ground-based measurements in Alberta to show a profile of super-emitters dominating the fugitive methane profile similar to sites in the United States. Ishiziwa et al. (2019) constrained arctic wetland fluxes to be similar in magnitude to the mean of the WetCHARTS inventory but with better identified seasonal and interannual variability. Satellite inversions over North America using the GEOS-Chem CTM and data from SCIAMACHY (Wecht et al., 2014) or GOSAT (Turner et al., 2015; Maasakkers et al., 2019) consistently require an increase in anthropogenic emissions in Western Canada and a decrease in natural emissions in Boreal Canada to match observations, even with the use of updated Canadian fluxes in Maasakkers et al. (2019) for anthropogenic (Sheng et al., 2017) and wetlands (Bloom et al., 2017) sources. Inverse modelling studies that use both in situ and satellite observations are valuable for intercomparison and for identifying the limits of spatial

and temporal discretization that are possible (Lu et al., 2021; Tunnicliffe et al., 2020). The Tropospheric Monitoring Instrument (TROPOMI) launched in 2017 with a data record beginning in 2018 and is expected to provide significant improvements in emissions monitoring through denser observational coverage at a similar precision to GOSAT (Hu et al., 2018). It is necessary to build a reliable historical record of Canadian methane emissions, as anthropogenic emissions are sensitive to changes in policy and economic activity (Rogelj et al., 2018) and natural emissions in Boreal Canada may be sensitive to climate change (Kirschke et al., 2013).

In this study we use surface observations from the ECCC GHG monitoring network and satellite data from GOSAT to constrain anthropogenic and natural emissions in Canada. We use the GEOS-Chem CTM to simulate 2010–2015 methane concentrations. The model setup includes the use of an improved bottom-up inventory for Canadian oil and gas emissions (Sheng et al., 2017), the WetCHARTS extended ensemble for wetland emissions (Bloom et al., 2017) and EDGAR v4.3.2 for other anthropogenic sources. We perform an ensemble forward model analysis which compares six wetlands scenarios to the ECCC surface observation network to assess the influence of process model configurations on Canadian methane. A series of Bayesian inverse analyses are performed that use ECCC and GOSAT data independently and in a joint surface-satellite system. We constrain monthly natural emissions and yearly total anthropogenic emissions from 2010–2015 using ECCC and GOSAT data independently for comparison to produce aggregated-source emissions estimates. We test the limitations of the ECCC and GOSAT joint observation system towards constraining emissions by inventory sector and according to provincial boundaries. We demonstrate where the observation system succeeds in providing strong constraints on major emissions sources and quantify the information content of the system to understand the limitations for resolving all minor Canadian emissions.

4.2 Data and methods

We use the GEOS-Chem CTM v12-03 (<http://acmg.seas.harvard.edu/geos/>) to simulate methane fields from 2010–2015 on a $2^\circ \times 2.5^\circ$ global grid and compare to surface observations from the ECCC in situ GHG monitoring network and satellite observations from GOSAT within the Canadian domain. We test for bias in the global model representation of background methane

using both surface and aircraft in situ data at Canada's most westerly site, Estevan Point (ESP), using global GOSAT data, and using global NOAA/HIPPO data. The sensitivity of simulated methane in Canada to the use of different wetlands flux parametrization is evaluated by comparing an ensemble of WetCHARTS v1.0 configurations to ECCC surface observations. The WetCHARTS ensemble mean in addition to other GEOS-Chem prior emissions are used in the Bayesian inverse analysis which optimizes Canadian sources using ECCC surface data and GOSAT satellite data independently for comparative analysis. We show the limitations of the observing system towards subnational level discretization by combining ECCC and GOSAT data in a joint-inversion. Here we describe the observations, the model, and the inverse analysis in further detail.

4.2.1 Observations

4.2.1.1 In situ surface observations

We use continuous measurements from eight sites in the ECCC greenhouse gas monitoring network from 2010–2015. Figure 4.1 shows a map of the sites and Table 4.1 provides a descriptive list. The eight sites are Estevan Point, British Columbia (ESP), Lac La Biche, Alberta (LLB), East Trout Lake, Saskatchewan (ETL), Churchill, Manitoba (CHC), Fraserdale, Ontario (FRA), Egbert, Ontario (EGB), Chibougamau, Quebec (CHM) and Sable Island, Nova Scotia (SBL). All sites use Picarro cavity ring-down spectrometers (G1301, G2301 or G2401) measuring dry-air mole fractions of methane with hourly-average precision better than 1 ppb. For model comparison the measurements are averaged over 4h from 12:00 to 16:00 local time, when the planetary boundary layer is well-mixed. The instruments are calibrated against World Meteorological Organization (WMO) certified standard gases. The westernmost site, ESP, measures methane continuously from a 40 m tower at a lighthouse station on the west coast of Vancouver Island. ESP is surrounded by forests to the north, east, and south and the Pacific Ocean to the west. ESP is used to evaluate boundary conditions and model bias in the methane background as it is the least sensitive to Canadian emissions due to prevailing westerly winds. Sites LLB and ETL are the most sensitive to anthropogenic emissions in Western Canada. LLB measures continuously from a 50 m tower located in a region of peatlands and forest ~200 km

NE of Edmonton and ~230 km S of Fort McMurray. ETL measures from a height of 105 m located ~150 km north of Prince Albert surrounded by Boreal forest. The sites in the Hudson Bay Lowlands (HBL) region, CHC and FRA, are the most sensitive to natural wetland emissions as this area produces some of the largest methane fluxes from wetlands in North America. CHC measures continuously from a 60 m tower in a small port town on the western edge of Hudson Bay surrounded by flat tundra. FRA measures from a 40 m tower and is located on the southern perimeter of James Bay surrounded by extensive wetlands coverage. The site CHM in Quebec is also sensitive to natural wetland emissions and is excluded in the inverse analysis to be used to verify the posterior results. CHM is substituted by Chapais, Quebec ~50 km away from 2011 onwards. The remaining Central and Atlantic Canada sites EGB and SBL are sensitive to net outflow from Canadian sources, both natural and urban, and some emissions from the Eastern United States. EGB is in a small rural village ~80 km north of Toronto and measures from a 25 m tower. SBL is on a remote uninhabited island 275 km ESE of Halifax, Nova Scotia and measures from a height of 25 m.

Table 4.1: Descriptive list of ECCC in situ observation sites used in the analysis.

Site Code	Full Name, Province	Latitude	Longitude	Elevation (asl) / Sampling Height (agl) (m)
ESP	Estevan Point, British Columbia	49.4° N	126.5° W	7 / 40
LLB	Lac La Biche, Alberta	55.0° N	112.5° W	548 / 50
ETL	East Trout Lake, Saskatchewan	54.4° N	105.0° W	500 / 105
CHC	Churchill, Manitoba	58.7° N	93.8° W	16 / 60
FRA	Fraserdale, Ontario	49.8° N	81.5° W	210 / 40
EGB	Egbert, Ontario	44.2° N	79.8° W	225 / 25
SBL	Sable Island, Nova Scotia	43.9° N	60.0° W	2 / 25
CHM ^{*†}	Chibougamau, Quebec	49.7° N	74.3° W	383 / 30
CHA ^{*†}	Chapais, Quebec	49.8° N	75.0° W	381 / 30

* Chibougamau, Quebec is replaced by Chapais, Quebec ~50 km away from 2011 onwards, overlapping in Fig.4.1

† Site is used to evaluate the posterior inversion results, and is not used in the inversion itself

4.2.1.2 GOSAT satellite observations

The Greenhouse Gas Observing Satellite (GOSAT) was launched in January 2009 by the Japan Aerospace Exploration Agency (JAXA). GOSAT is in a low-Earth polar sun-synchronous orbit with an equator overpass around 13:00 local time. The TANSO-FTS instrument on-board GOSAT retrieves column-averaged dry air mol fractions of methane using short-wave infrared (SWIR) solar backscatter in the 1.65 μm absorption band (Butz et al., 2011). Observation pixels in the default mode are 10 km in diameter separated by 260 km along the orbit track with repeated observations every 3 days. Target mode observations provide denser spatial coverage over areas of interest. There has been no observed degradation of GOSAT data quality since the beginning of data collection (Kuze et al., 2016). Here we use version 7 of the University of Leicester proxy methane retrieval over land from January 2010 to December 2015 (Parker et al., 2011, 2015; ESA CCI GHG project team, 2018). The single-observation precision of GOSAT XCH₄ data is 13 ppb, and the relative bias is 2 ppb when validated against the Total Column Carbon Observing Network (TCCON; Buchwitz et al., 2015). Figure 4.1 shows the GOSAT observations over Canada used in our analysis within the domain of 45° N–60° N latitude and 50° W–150° W longitude. The observations used have passed all quality assurance flags for a total of 45,936 observations from 2010–2015, or approximately ~7600 observations per year. Our analysis excludes glint data over oceans, and cloudy conditions are accounted for by the quality assurance flags. We avoid using data above 60° N latitude due to higher uncertainty in the satellite retrieval and the model comparison (Maasakkers et al., 2019; Turner et al., 2015).

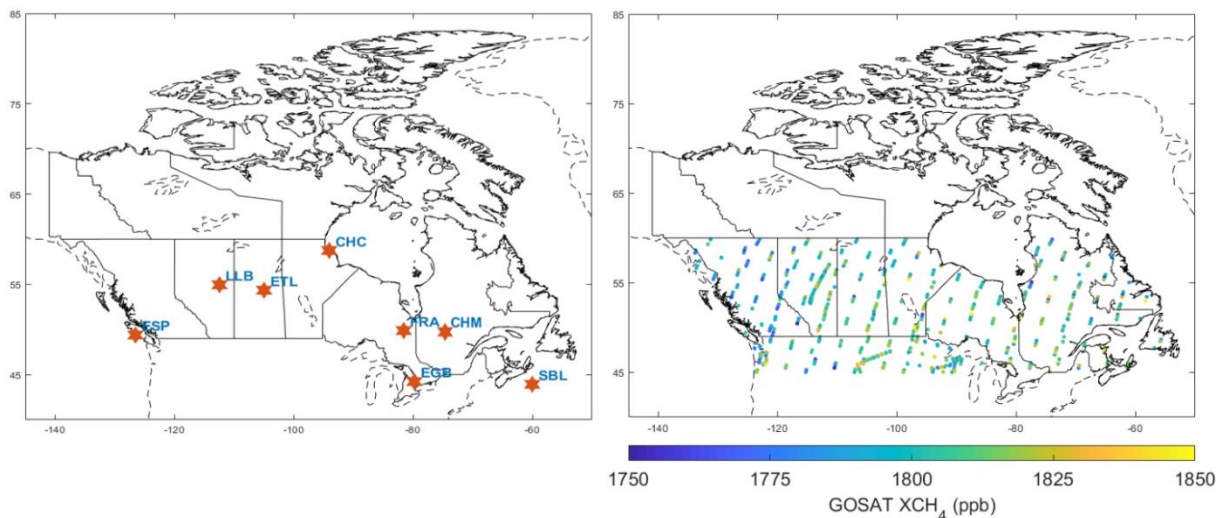


Figure 4.1: ECCCC surface (left) and GOSAT satellite (right) observations used in the inverse analysis. A descriptive list of the ECCCC sites is shown in Table 4.1. GOSAT data shown is from a single year in 2013 and is filtered to the Canadian domain within 45°N–60°N latitude and 50°W–150°W longitude. There are ~600 GOSAT observations per month in this domain with a minimum Nov–Jan (112–248) and maximum Jul–Sep (872–1098), individual months are shown in the Supplement (Fig. C.1).

4.2.2 Forward Model

We use the GEOS-Chem CTM v12-03 at $2^\circ \times 2.5^\circ$ grid resolution driven by 2009–2015 MERRA-2 meteorological fields from the NASA Global Modeling and Assimilation Office (GMAO). Initial conditions from January 2009 are from a previous GOSAT inversion by Turner et al. (2015) which was shown to be unbiased globally when compared to surface and aircraft data. Bottom-up anthropogenic emissions in GEOS-Chem are from the 2013 ICF Canadian oil and gas inventory (Sheng et al., 2017) and the 2012 EDGAR v4.3.2 global inventory for other Canadian and global sources, and the gridded US 2012 EPA Inventory for the United States (Maasackers et al., 2016). For wetlands, six configurations from the 2010–2015 extended ensemble of WetCHARTS (Bloom et al., 2017) are used in the ensemble forward model analysis (Section 4.3.1) and the ensemble mean is used as the prior for the inverse analysis (Sections

4.3.2–4.3.4). Figure 4.2 shows the spatial distribution of the prior methane emissions in Canada from the major anthropogenic and natural sources. The two largest sources are from the ICF oil and gas inventory, (Sheng et al., 2017) and wetland emissions from the ensemble mean of the WetCHARTS inventory (Bloom et al., 2017), with significant emissions from livestock and waste emissions from EDGAR. Oil and gas are 54% of the anthropogenic total and wetlands are 94% of the natural total. The prior emissions estimates in this simulation are summarized in Table 4.2, which organizes emissions by Canadian source categories and are compared to sector attribution in the National Inventory (Environment and Climate Change Canada, 2017). Our totals for Energy, Agriculture and Waste are 2.4, 1.0, and 0.9 Tg a⁻¹ respectively compared to 2.0, 1.2 and 0.9 Tg a⁻¹ in the National Inventory. In the absence of a spatially disaggregated Canadian inventory for methane, we consider these prior estimates reasonably similar for the purpose of comparing our posterior emissions to the National Inventory, however we cannot compare the spatial pattern of emissions which will likely show more discrepancies. Natural emissions are divided into wetlands, which are 14.0 Tg a⁻¹ in the ensemble mean, and other natural sources, which are 0.8 Tg a⁻¹ from biomass burning, seeps, and termites. Each component of other natural emissions has a separate spatially disaggregated inventory as described in Maasackers et al. (2019). Emissions from the United States and the rest of the world are included in the model but not optimized in the inversions. Loss of methane from oxidation due to OH is computed using archived 3-D monthly fields of OH from a previous GEOS-Chem full-chemistry simulation (Wecht et al., 2014).

Table 4.2: Mean 2010–2015 prior estimates of Canadian methane emissions used in GEOS-Chem arranged according to categories in the National Inventory (Environment and Climate Change Canada, 2017).

Category	Source Type ^a	Emissions (Tg a ⁻¹) ^a	Total (Tg a ⁻¹) ^a	Inventory (Tg a ⁻¹) ^b	
Anthropogenic	Energy	Oil	0.52	2.42	2.00
		Gas	1.81		
		Coal	0.09		
	Agriculture	Livestock	1.00	1.00	1.20
	Waste	Landfills	0.66	0.94	0.92
		Wastewater	0.19		
Other Anthropogenic		0.09			
Natural	Wetlands	-	14.0	14.0	-
	Other Natural	Biomass Burning	0.28	0.84	-
		Seeps	0.28		
		Termites	0.28		

^aEmissions inputs for GEOS-Chem. These are shown for the individual source types and summed over the categories Energy, Agriculture and Waste. In Canada, oil and gas are from Sheng et al. (2017), coal, livestock, landfills, wastewater and other anthropogenic are from EDGAR v4.3.2, wetlands are from Bloom et al. (2017). Biomass burning is from QFED (Darmenov and da Silva, 2013) and termite emissions are from Fung et al. (1991). Seeps and other global sources are described in Maasakkers et al. (2019).

^bEmissions from the National Inventory (Environment and Climate Change Canada, 2017) that correspond to the Energy, Agriculture and Waste categories. These are used in the discussion of results but are not included in the inverse model.

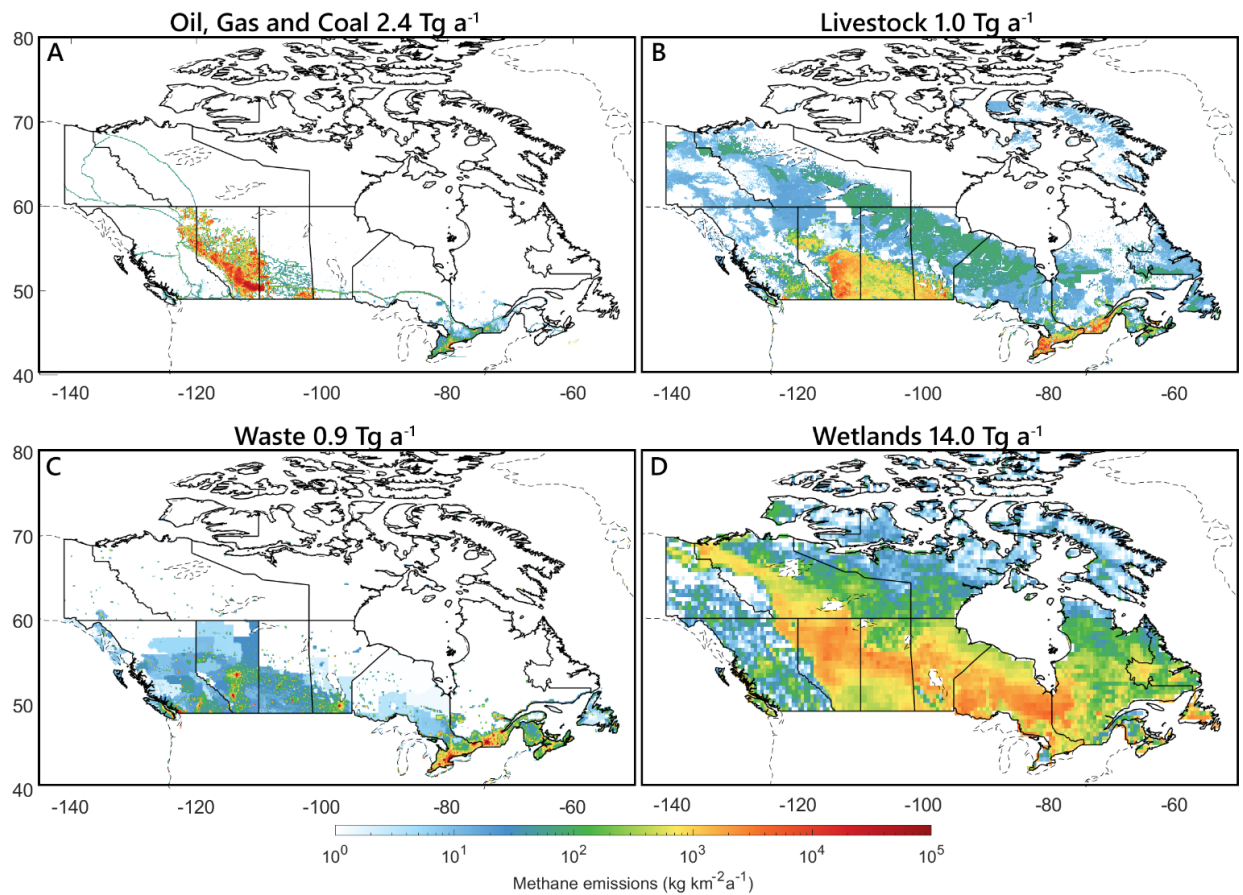


Figure 4.2: Prior estimates of anthropogenic and natural methane emissions. Colour bars are in log scale in units of $\text{kg CH}_4 \text{ km}^{-2} \text{ a}^{-1}$. Most anthropogenic emissions fall under the energy category (A) which are oil and gas in the ICF inventory (Sheng et al., 2017) plus minor emissions from coal in EDGAR 4.3.2. Livestock (B) and waste (C) are from EDGAR. Natural emissions are primarily wetlands from the WetCHARTS inventory (D; Bloom et al., 2017).

4.2.3 Inverse Model Methodology

We optimize emissions in the inverse analysis by minimizing the Bayesian cost function $J(\mathbf{x})$ (Rodgers, 2000).

$$J(\mathbf{x}) = \frac{1}{2} (\mathbf{x} - \mathbf{x}_a)^T \mathbf{S}_a^{-1} (\mathbf{x} - \mathbf{x}_a) + \frac{1}{2} (\mathbf{y} - \mathbf{F}(\mathbf{x}))^T \mathbf{S}_o^{-1} (\mathbf{y} - \mathbf{F}(\mathbf{x})) \quad \{4.1\}$$

Where \mathbf{x} is the vector of emissions being optimized, \mathbf{x}_a is the vector of prior emissions (Table 4.2), $\mathbf{F}(\mathbf{x})$ is the simulation of methane concentrations corresponding to the observation vector \mathbf{y} of ECCC surface and/or GOSAT data. \mathbf{S}_a is the prior error covariance matrix and \mathbf{S}_o is the observational error covariance matrix. The observational error matrix includes both instrument and model transport error. The GEOS-Chem model relating methane concentrations to emissions $\mathbf{F}(\mathbf{x})$ is essentially linear and can be represented by the Jacobian matrix \mathbf{K} such that $\mathbf{F}(\mathbf{x}) = \mathbf{K}\mathbf{x} + \mathbf{b}$, where \mathbf{b} is the model background. The background includes initial conditions from Turner et al. (2015) and methane from global emissions that are held constant in the inversion. Possible bias in the background is evaluated in detail in the Supplement Section C.3 and shown to be minimal. The \mathbf{K} matrix is of m by n size where n is the number of state vector elements being optimized and m is the number of ECCC surface and/or GOSAT observations being used. The \mathbf{K} matrix is constructed using the forward mode of GEOS-Chem and the tagged tracer output for Canadian sources which describes the sensitivity of concentrations to emissions dy/dx in ppb Tg⁻¹.

GEOS-Chem continuously simulates global emissions with a global source-sink imbalance of +13 Tg a⁻¹ in the budget as described in Maasakkers et al. (2019). We show in Section C.3 of the Supplement that this configuration of the model reliably reproduces the global growth rate in atmospheric methane with adjustments only needed for 2014 and 2015 primarily due to differences in tropical wetland emissions (Maasakkers et al., 2019), with reduced transport errors at the 2° × 2.5° resolution (Stanevich et al., 2020). This gives a well-represented background for methane which is tested using global GOSAT and NOAA data, as well as in situ data at Canadian background sites. We improve the model representation of methane using bias

corrections which are discussed in Section C.3 of the Supplement, and we show the consistency of the inversion results without adjustments to the model. A high resolution inversion over North America over the 2010–2015 time-period using the same prior has shown adjustments to US emissions near the Canadian border are also relatively minimal, (Maasakkers et al., 2021), so we treat US emissions as constant. The assumption of constant US emissions is tested in Section C.3.2 of the Supplement by removing ECCC stations near the US border from the inversion, which show consistent results. Hence, we can attribute the model-observation mismatch ($\mathbf{y} - \mathbf{F}(\mathbf{x})$) using observations limited to Canada to Canadian emissions which are optimized in the inversion. In the main text we show three inversions with a different number of state vector elements: a) the monthly inversion ($n = 78$) optimizes monthly natural emissions in Canada and yearly anthropogenic emissions from 2010–2015, b) the sectoral inversion ($n = 5$) optimizes emissions according to the major inventory categories in Table 4.2 individually for each year, and c) the provincial inversion ($n = 16$) optimizes emissions according to subnational boundaries which is also repeated for each year. The monthly inversion provides higher temporal resolution relative to the other approaches in this study to constrain the seasonality of natural emissions, assuming the spatial distribution is correct. The sectoral inversion provides direct constraints on inventory categories, and the provincial inversion provides relatively higher spatial resolution for subnational attribution. Substituting $\mathbf{F}(\mathbf{x}) = \mathbf{K}\mathbf{x}$ in eq. 4.1 and subtracting the background \mathbf{b} , the analytical solution of the cost function $dJ(\mathbf{x})/d\mathbf{x} = 0$ yields the optimal posterior solution $\hat{\mathbf{x}}$ (Rodgers, 2000):

$$\hat{\mathbf{x}} = \mathbf{x}_a + \mathbf{S}_a \mathbf{K}^T (\mathbf{K} \mathbf{S}_a \mathbf{K}^T + \mathbf{S}_o)^{-1} (\mathbf{y} - \mathbf{K} \mathbf{x}_a) \quad \{4.2\}$$

The analytical solution provides closed-form error characterization, such that the posterior error covariance $\hat{\mathbf{S}}$ of the posterior solution $\hat{\mathbf{x}}$ is given by:

$$\hat{\mathbf{S}} = (\mathbf{K}^T \mathbf{S}_o^{-1} \mathbf{K} + \mathbf{S}_a^{-1})^{-1} \quad \{4.3\}$$

The averaging kernel matrix \mathbf{A} is used to evaluate the surface and satellite observing systems and is given by:

$$\mathbf{A} = \mathbf{I}_n - \hat{\mathbf{S}}\mathbf{S}_a^{-1} \quad \{4.4\}$$

where \mathbf{I}_n is the identity matrix of length n corresponding to the number of state vector elements. The averaging kernel matrix \mathbf{A} describes the sensitivity of the posterior solution $\hat{\mathbf{x}}$ to the true state \mathbf{x} ($\mathbf{A} = d\hat{\mathbf{x}}/d\mathbf{x}$). The trace of \mathbf{A} provides the degrees of freedom for signal (DOFS), which is the number of pieces of information of the state vector that is gained from the inversion ($\text{DOFS} \leq n$). The diagonal values of \mathbf{A} provide information on which Canadian state vector elements can be constrained by ECCO surface and GOSAT satellite observations above the noise, and higher DOFS closer to n correspond to better constrained sources in total. As a further diagnostic of the inversion we conduct a singular value decomposition of the prewhitened Jacobian $\check{\mathbf{K}} = \mathbf{S}_o^{-1/2}\mathbf{K}\mathbf{S}_a^{1/2}$ (Rodgers, 2000). The number of singular values greater than one is the effective rank of $\check{\mathbf{K}}$, which shows the independence of the state vector elements and the number of pieces of information above the noise that are resolved in the inversion (Heald et al., 2004). The comparison between this eigenanalysis and the DOFS are discussed in the Supplement Section C.4 and is used to inform the limitations of the observation system.

We construct the prior error covariance matrix \mathbf{S}_a based on aggregated error estimates for source categories and regions. We use 50% error standard deviation for the aggregated anthropogenic emissions which includes the Sheng et al. (2017) oil and gas inventory and other EDGAR sources, 60% for wetland emissions from the Bloom et al. (2017) WetCHARTS inventory and 100% for non-wetlands natural sources. We assume no correlation between state vector elements so that \mathbf{S}_a is diagonal. Anthropogenic emissions have been shown to be spatially uncorrelated (Maasackers et al., 2016) however wetlands show spatial correlation (Bloom et al., 2017). Here we optimize broadly aggregated categories, so our method assumes the spatial pattern of each state vector element is correct, however correlations between state vector

elements in the eigenanalysis are used to assess the limitations of source discretization in the observing systems.

We construct the diagonal observation error matrix \mathbf{S}_o which captures instrument and model error using the relative residual error method (Heald et al., 2004). In this approach the vector of observed-modelled differences $\Delta = y_{\text{GEOS-Chem}} - y_{\text{observations}}$ is calculated and the mean observed-modelled difference $\overline{\Delta} = \overline{y_{\text{GEOS-Chem}} - y_{\text{observations}}}$ is attributed to the emissions that will be optimized. Hence, the standard deviation in the residual error $\Delta' = \Delta - \overline{\Delta}$ represents the observational error and is used as the diagonal elements of \mathbf{S}_o . For our Canadian inversion we find positive model-observation biases in the warmer months (April to September) and negative biases in the colder months (October to March). We calculate the relative residual error for growing and non-growing seasons separately, such that Δ' is partitioned into Δ'_g (April to September) and Δ'_{ng} (October to March) which is then used to calculate the diagonal elements of \mathbf{S}_o . For surface observations the mean observational error is 65 ppb. Since the instrument error is <1 ppb for afternoon mean methane measurements, the observational error is entirely attributed to transport and representation error of surface methane in the model grid pixels. For satellite observations the mean observational error is 16 ppb where the instrument error is 11 ppb, showing most of the observational error is from the instrument rather than the forward model representation of the total column. Column-averaged methane concentrations are less sensitive to surface emissions resulting in the lower model error (Lu et al., 2021).

In summary, the inverse model is designed to suit the objectives of this study, which are to: (1) optimize anthropogenic and natural emissions in Canada at the national-scale and (2) compare the results of inversions using surface and satellite observations, and (3) characterize the limitations of the observing system towards subnational-scale emissions discretization. The spatial and temporal resolution of the inversion is limited by the precision of GOSAT data, the precision of the model representation of surface methane for ECCO data, and the sparse coverage of both systems relative to the smaller magnitude of Canadian emissions. This simplified approach, where Canadian emissions are optimized using only observations in Canada, may be sensitive to errors in the global model that are projected onto the Canadian domain. This is

minimized if errors in the regional representation of methane, which are corrected in the inversion, are much larger than errors in the background from the global model, or if the background methane is corrected using global observations outside of the Canadian domain. We show an analysis of the global model alongside sensitivity tests of the inversions in Section C.3 of the Supplement which produce consistent results. Future studies may deploy a more sophisticated, high resolution inverse model that will match more sophisticated observations, which include an expanded ECCC surface network, as well as satellites with higher density (TROPOMI; Hu et al., 2018) or higher precision (GOSAT-2; Nakajima et al., 2017) observations outside of the years of this analysis.

4.3 Results and discussion

4.3.1 Evaluation of WetCHARTS extended ensemble for wetland emissions in Canada

Wetlands are the largest methane source in Canada with uncertainties in the magnitude, seasonality, and spatial distribution of emissions. Our inverse analysis constrains the magnitude and seasonality of emissions with observations. Ideally, the prior emissions in the model should be the best possible representation of emissions to reduce error in the optimization problem (Jacob et al., 2016). Table 4.2 shows 2010–2015 mean wetland emissions in Canada to be 14.0 Tg a⁻¹ from the mean of the WetCHARTS v1.0 inventory (Bloom et al., 2017). These emissions are more than three times the total of anthropogenic emissions 4.4 Tg a⁻¹. The much larger signal from wetland emissions poses a difficulty for constraining anthropogenic emissions (Miller et al., 2014). In this section, we evaluate our use of the mean of the WetCHARTS v1.0 extended ensemble by running a series of forward model runs using alternate ensemble members in GEOS-Chem and comparing model output to ECCC in situ observations.

The WetCHARTS extended ensemble for 2010–2015 contains an uncertainty dataset of 18 possible global wetlands configurations as described in Bloom et al. (2017). These depend on three processing parameters which are: three CH₄:C temperature-dependent respiration fractions, q_{10} , corresponding to a 10°C change in surface skin temperature ($q_{10} = 1, 2, \text{ or } 3$; where 1 is the highest temperature dependency), two inundation extent models (GLWD vs. GLOBCOVER; where GLWD corresponds to higher inundation in Canada) and three global scaling factors for

global emissions to amount to 124.5, 166 or 207.5 Tg CH₄ yr⁻¹ (3×2×3=18). We find using the scaling factors corresponding to 124.5 and 207.5 Tg CH₄ yr⁻¹ within GEOS-Chem results in an imbalance in the global budget beyond what is observed in our measurements and degrades the representation of background methane, so we limit the extended ensemble to six members which depend on three temperature parameterizations and two inundation scenarios (3×2=6). Figure 4.3 shows the magnitude and spatial distribution of wetland emissions in the six scenarios. The total wetland emissions within Canada show nearly an order of magnitude difference between ensemble members from 3.9 Tg a⁻¹ to 32.4 Tg a⁻¹. Compared to the rest of North America, Boreal Canada shows the largest variability between ensemble members, with the Southeast United States as the second most uncertain (Sheng et al., 2018b).

We use ECCC in situ observations to better constrain the range of wetlands methane emissions in the ensemble members. All six configurations are used in GEOS-Chem to produce a series of forward model runs for a subrange of years between 2013–2015. Figure 4.4 shows GEOS-Chem simulated methane concentrations using the six WetCHARTS configurations and compares them to four ECCC in situ measurement sites in Canada (LLB, ETL, FRA, EGB). This subset of available data is representative of sites sensitive to both anthropogenic and natural emissions. Most of Canadian anthropogenic emissions are from Western Canada (Fig. 4.2), which we use sites LLB and ETL to evaluate (Fig. 4.1), and a significant amount of Canadian natural emissions are from regions surrounding the Hudson’s Bay Lowlands, which we use sites FRA and EGB to evaluate. Methane concentrations from GEOS-Chem show large differences when compared to ECCC observations, ranging from +1050 to –150 ppb. The boundary-condition site ESP (Fig. C.3) showed a mean bias of 5.3 ppb for all of 2010–2015. Since there is no similar mismatch in the global representation of methane, these biases up to 1050 ppb can therefore be attributed to misrepresented local Canadian emissions plus associated transport and representation error. Two types of biases with opposite signs appear from this comparison. The first type is a positive summertime bias where the modelled methane concentrations significantly exceed the observations; this bias is more pronounced in sites FRA (Fig. 4.4-C) and EGB (Fig. 4.4-D), which are in Ontario and sensitive to the Hudson Bay Lowlands. The bias is also visible in the western sites LLB (Fig. 4.4-A) and ETL (Fig. 4.4-B) to a lesser extent. As we use a

smaller magnitude of wetlands methane emissions corresponding to the ensemble members in Figure 4.3 (from 32.4 Tg a⁻¹ to 3.9 Tg a⁻¹), this summertime bias decreases proportionately. Therefore, we can attribute these large positive summertime biases to growing season wetland emissions that are overestimated in the process model configurations. The second type of bias is a year-long negative bias that appears most in site LLB (Fig. 4.4-A) and is magnified with the use of lower-magnitude wetland emissions. This suggests the presence of year-round anthropogenic emissions in Western Canada that are underestimated in the prior, or that winter-time wetland emissions could also be underestimated in WetCHARTS due to the lack of explicit soil water and temperature dependencies. The inverse modelling results in the next section attribute this bias to anthropogenic emissions.

Miller et al. (2016) conducted a study constraining North American Boreal wetland emissions from the WETCHIMP inventory modelled in WRF-STILT by comparing to observations in 2008. Their study included the use of three of the ECCC stations described here (CHM, FRA and ETL). The model comparison to observations in that study showed a similar pattern of modelled methane exceeding observations in the summer and a low bias at ETL. They suggested wetland emissions were overestimated in most model configurations and that the wetlands bias may be masking underestimated anthropogenic emissions. These conclusions are corroborated by the 2013–2015 comparison shown here, we show high wetland emissions configurations in WetCHARTS produce a high bias that exceed measured summertime methane concentrations, and the use of lower wetlands configurations reveal a year-long low bias apparent in Western Canada. Our results suggest the combined use of higher inundation extent and lower temperature dependencies (GLWD and $q_{10} = 3$), or the use of lower inundation extent and higher temperature dependencies (GLOBCOVER and $q_{10} = 1$) best reproduce observations near the mean of the range of emissions, although the ensemble forward model analysis is unable to specify more detailed process model constraints.

The forward model analysis in this section is a direct evaluation of wetlands configurations. This approach allows us *manually* tune wetlands scenarios and diagnose the sensitivity of the modelled-observed differences to the process modelling parameters. The inverse analysis shown subsequently is a statistical optimization that applies scaling factors to emissions based on the

same model-observation differences. The inverse analysis can be viewed analogously as an *automatic* approach. These results show the challenge with optimizing Canadian methane emissions when wetland emissions are largely uncertain. Our approach of optimizing anthropogenic and natural emissions simultaneously in an inversion is useful because attempting to constrain either emissions category, anthropogenic or natural, obfuscates the analysis on the other. We exploit the different pattern of anthropogenic and natural emissions in time and space (Fig. 4.4). Natural emissions peak in the summertime and are concentrated in Boreal Canada, while anthropogenic emissions are persistent year-round and are concentrated in Western Canada (Fig. 4.2). Hence when optimizing the model-observation mismatch in a Bayesian inverse framework, some elements of the observation vector will correspond to high biases from summertime observations in Boreal Canada and some elements will correspond to low biases in Western Canada. As the choice of prior for the inversion we use the mean of the WetCHARTS configurations (14.0 Tg a^{-1}) which corresponds to the middle of the range shown shaded in red in Figure 4.4. The 60% range of uncertainty in the prior error covariance matrix \mathbf{S}_a appropriately excludes the extreme scenarios in Fig. 4.3 and 4.4.

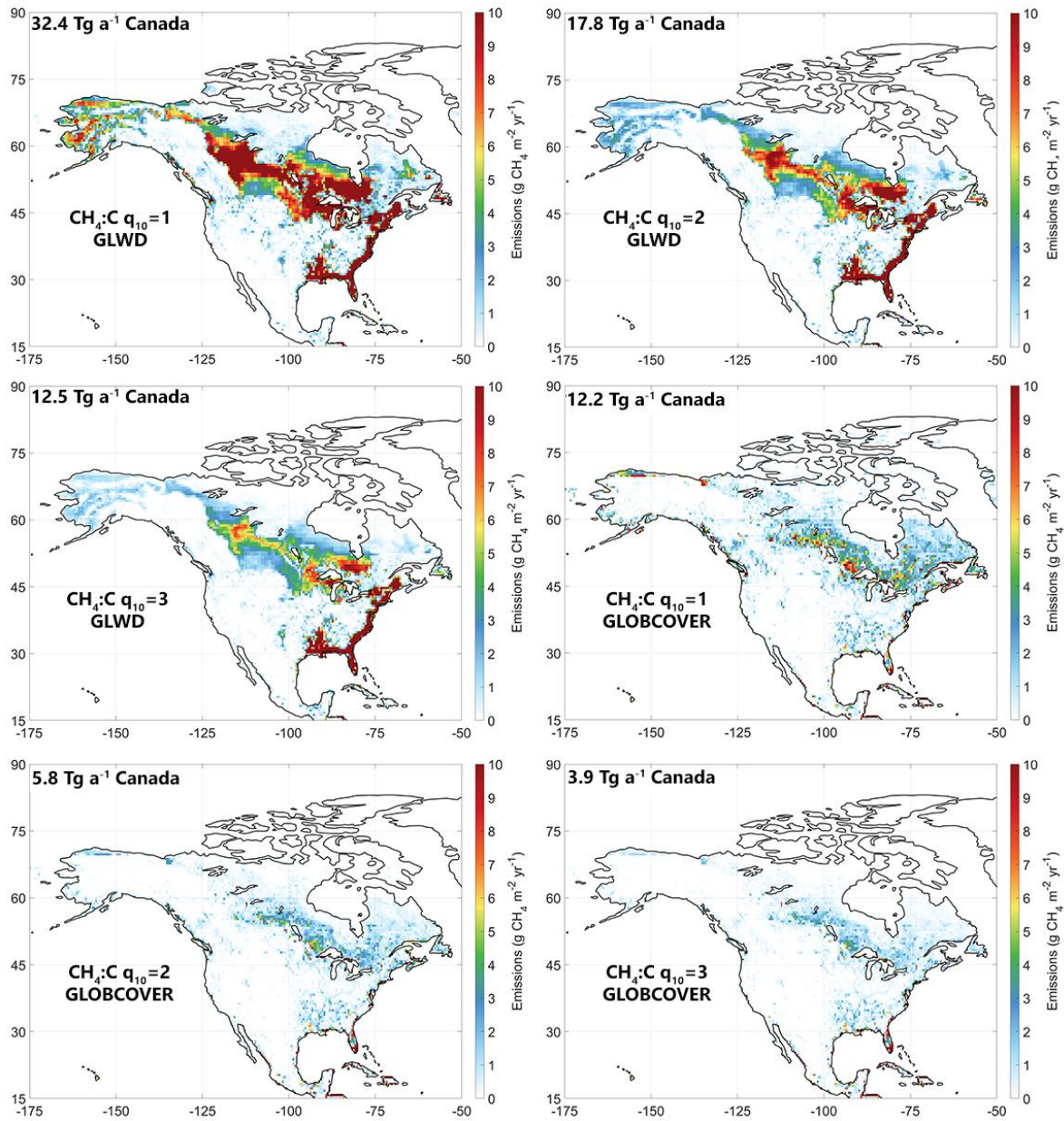


Figure 4.3: Ensemble members from the WetCHARTS v1.0 inventory (Bloom et al., 2017) with totals for wetland methane emissions within Canada for each configuration shown in $\text{Tg CH}_4 \text{ a}^{-1}$. Ensemble members vary according to the use of three $\text{CH}_4:\text{C } q_{10}$ temperature dependencies and two inundation extent scenarios (GLWD vs. GLOBCOVER) for $3 \times 2 = 6$ scenarios.

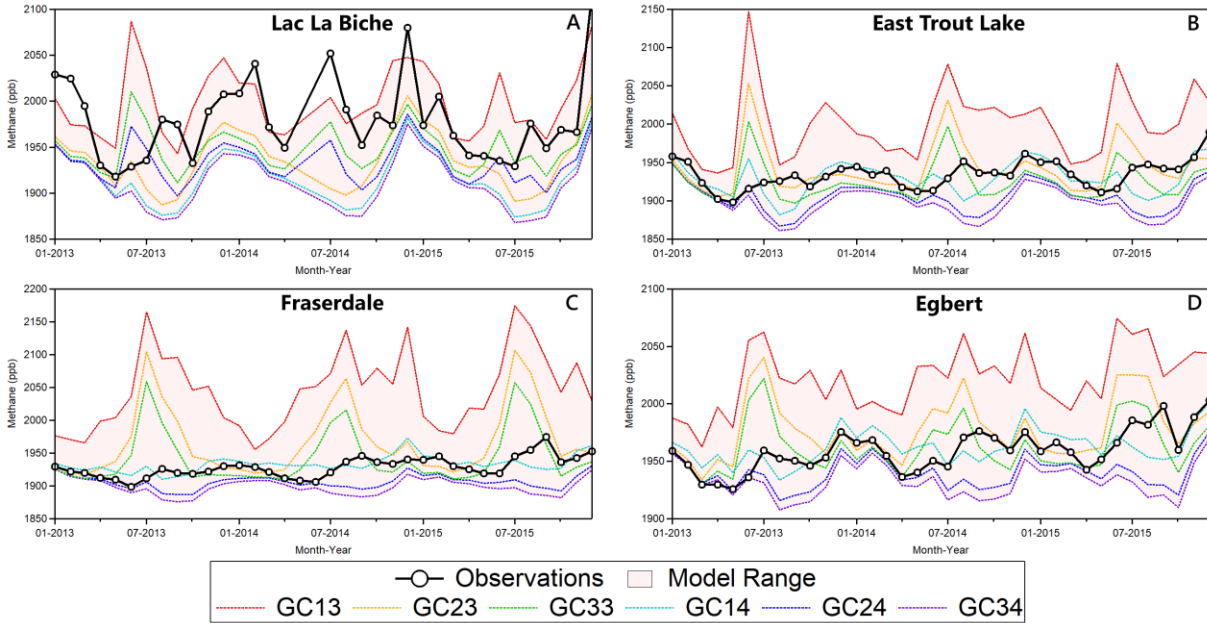


Figure 4.4: Time series of 2013–2015 modelled and observed methane concentrations. Monthly-mean methane from ECCC in situ observations (black) are shown and compared to six GEOS-Chem simulations differing in the use of WetCHARTS ensemble members for wetland emissions, with other emissions corresponding to Table 4.2. The six configurations are labelled GCXY where first digit (X=1,2,3) corresponds to the CH₄:C q₁₀ temperature dependency, which decreases the sensitivity of emissions to temperature with increasing value. The second digit (Y=3,4) corresponds to the model used for inundation extent (3 = GLWD, 4 = GLOBCOVER) where GLOBCOVER produces lower emissions in Canada. Emissions configurations are those shown in Fig. 4.3 in order of magnitude from red to purple lines, with the shaded red showing the range of concentrations. Sites are LLB, Alberta (A), ETL, Saskatchewan (B), FRA, Northern Ontario (C) and EGB, Southern Ontario (D).

4.3.2 Comparative Analysis of Inversions using ECCC in situ and GOSAT Satellite Data

We optimize 2010–2015 emissions in Canada using an $n = 78$ state vector element inversion setup with GOSAT and ECCC data independently. Elements 1–72 of the inversion are monthly total natural emissions (wetlands + other natural) from 2010–2015 and elements 73–78 are yearly total anthropogenic emissions (energy + agriculture + waste) for the same years. These categories correspond to the emissions shown in Table 4.2. We do not optimize emissions according to clustered grid boxes like other satellite inversions using GEOS-Chem (Wecht et al., 2014; Turner et al., 2015; Maasakkers et al., 2019) and instead scale the amplitudes of these two aggregated categories. This approach is a trade-off of time for space, due to the limitations of the observations, giving up finer spatial resolution for finer temporal resolution. This is useful for optimizing Canadian methane emissions since a) anthropogenic emissions are largely concentrated in Western Canada and require less spatial discretization over the entire country and b) natural emissions are the largest source and have an uncertain seasonality – as shown in the previous section – and require finer temporal discretization. The limitations of this method are that natural emissions are very unlikely to be spatially homogenous and vary due to hydrological differences even at the microtopographic level (Bubier et al., 1993). Perfectly resolving Canadian emissions sources in time and space is challenged by the sparsity and precision of the observing system and the model representation of the observations. We show the limitations of the combined ECCC and GOSAT observing system towards resolving subnational emissions in more detail in the subsequent section.

Figure 4.5 (top) shows 2010-2015 posterior emissions using this 78 state vector approach with ECCC in situ data (blue) and GOSAT satellite data (green). Error bars are from the diagonal elements of the posterior error covariance matrix $\hat{\mathbf{S}}$. Posterior anthropogenic emissions averaged over the 6 year period are $6.0 \pm 0.4 \text{ Tg a}^{-1}$ (1σ year-to-year variability) using ECCC data and $6.5 \pm 0.7 \text{ Tg a}^{-1}$ using GOSAT data. Posterior estimates are 36% and 48% higher than the prior of 4.4 Tg a^{-1} for ECCC and GOSAT results, respectively. There does not appear to be a significant year-to-year trend above the noise for the anthropogenic emissions optimized by either dataset. The posterior anthropogenic emissions using ECCC and GOSAT data show agreement with each other in each year but 2011, where the GOSAT derived emissions are statistically higher. The

error from the diagonal of the posterior error covariance matrix $\hat{\mathbf{S}}$ may be overly optimistic, particularly for GOSAT data. This is due to the observational error covariance matrix \mathbf{S}_o being treated as diagonal when realistically there are correlations between GOSAT observations that are difficult to quantify (Heald et al., 2004). Our results for anthropogenic emissions show agreement with top-down aircraft estimates of methane emissions in Alberta that are higher than bottom-up inventories (Johnson et al., 2017; Baray et al., 2018) and previous satellite inverse-modelling studies over North America that upscale emissions in Western Canada (Turner et al., 2015; Maasakkers et al., 2019; Maasakkers et al., 2021; Lu et al., 2021). We show source attribution through a sectoral and subnational scale analysis of anthropogenic emissions in the subsequent section.

Inversion results for monthly natural emissions from 2010–2015 are also shown in Figure 4.5 (bottom). The total of posterior natural emissions averaged over the 6-year period is 11.6 ± 1.2 Tg a⁻¹ using ECCC data and 11.7 ± 1.2 Tg a⁻¹ using GOSAT data. The prior for natural emissions is 14.8 Tg a⁻¹ from the mean of the WetCHARTS extended ensemble (14.0 Tg a⁻¹) plus other natural (biomass burning + termites + seeps = 0.8 Tg a⁻¹). There is some interannual variability in the prior due to higher emissions in 2010 and 2015. Posterior results averaged over the six years are 22% lower than the prior using ECCC data and 21% lower using GOSAT data, with both posterior results showing agreement with each other. These results are within the uncertainty range of the WetCHARTS extended ensemble, and we show the magnitude of emissions from the larger uncertainty dataset (3.9 to 32.4 Tg a⁻¹) can be better constrained with both ECCC and GOSAT observations.

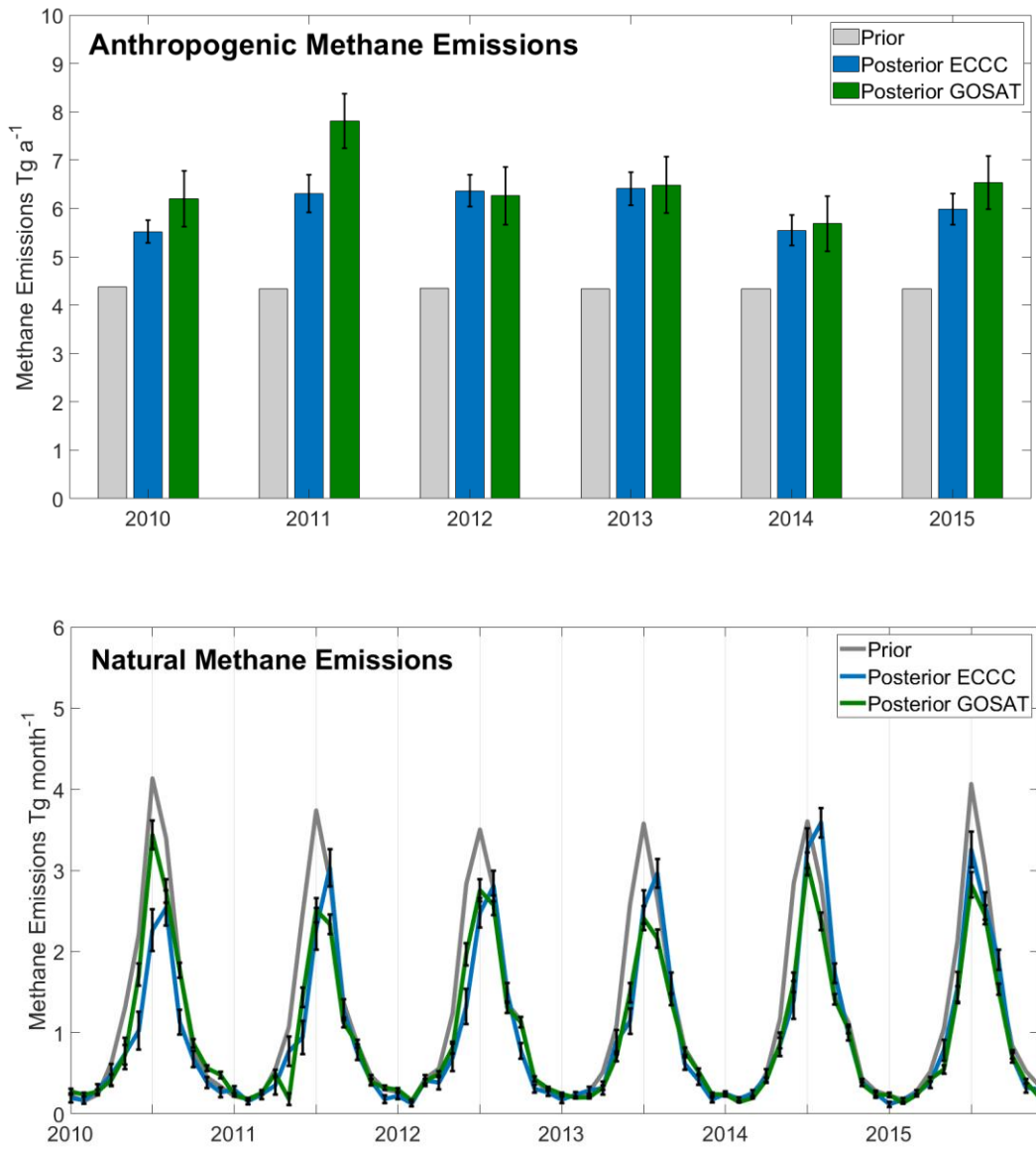


Figure 4.5: Comparative analysis of inversion results optimizing annual total Canadian anthropogenic emissions (top) and monthly total natural emissions (bottom) in an $n = 78$ state-vector element setup. The posterior emissions determined using ECCC in situ (blue) and GOSAT satellite (green) data are compared to the prior (gray). Error bars are from the diagonal elements of the posterior error covariance matrix.

While our results show lower natural emissions in all years, a linear fit to the posterior annual emissions using ECCC data shows a trend of increasing natural emissions at a rate of $\sim 0.56 \text{ Tg a}^{-1}$ per year from 2010–2015. The posterior with GOSAT data does not corroborate this result, the overall emissions trend using GOSAT data is not robust and shows a decreasing trend of $\sim 0.2 \text{ Tg a}^{-1}$ per year. The lack of corroboration of trends between ECCC and GOSAT data may be reflective of the lower overall sensitivity of total column methane to these surface fluxes (Sheng et al., 2017; Lu et al., 2021) or the inability of this inverse system to constrain trends sufficiently. The combined ECCC+GOSAT inversion using this setup is consistent with the results of the individual inversions, it is shown in the Supplement (Fig C.11) while the intercomparison is emphasized here, although we note the combined inversion also does not corroborate this trend. We evaluate the possible influence of errors in the global model on the projection of a trend onto the ECCC inversion in Section C.3.2 of the Supplement. While the mean natural emissions over 2010–2015 show consistent results in the sensitivity tests, the limitations of the observation system, the inversion procedure and the timescale of the analysis limit the interpretation of trends. Poulter et al. (2017) estimated global wetland emissions using biogeochemical process models constrained by inundation and wetlands extent data. They estimated mean annual emissions over all of Boreal North America to be $25.1 \pm 11.3 \text{ Tg a}^{-1}$ in 2000–2006, $26.1 \pm 11.8 \text{ Tg a}^{-1}$ in 2007–2012 and $27.1 \pm 12.5 \text{ Tg a}^{-1}$ which suggests a small increasing trend. Observational constraints over longer timescales are necessary to investigate the possibility of trends in Canadian natural methane emissions. Improvements to the observation network and a better understanding of climate sensitivity in WetCHARTS are necessary to understand how wetlands methane emissions will evolve in future climates.

Figure 4.6 shows the 2010–2015 average seasonal pattern of natural emissions in the prior and posterior results. The seasonality of natural methane emissions in the prior shows a sharp peak in July with a narrow methanogenic growing season. The posterior with ECCC data shows a peak 1-month later in August in most years instead of July, with lower than prior emissions in the spring months before the peak (March to May) and similar emissions to the prior in the autumn months after the peak (September to November). Posterior emissions with GOSAT show a peak in July and corroborates the pattern of slower-to-begin spring emissions and the lower intensity

summer peak seen from the ECCC inversion. The posterior results show the seasonality of emissions is not symmetrical around the temperature peak in July. August emissions are higher than June, September emissions are higher than May, and October emissions are higher than April. This pattern around July is present in the prior emissions from WetCHARTS, however the inversion results constrained by ECCC or GOSAT observations intensify the relative difference between emissions before and after July. Miller et al. (2016) found a similar seasonal pattern of emissions in the Hudson Bay Lowlands using an inverse model constrained by 2007–2008 in situ data. They found a less narrow and less intense peak of summertime emissions with higher autumn over spring emissions. Warwick et al. (2016) used a forward model and isotopic measurements of $\delta^{13}\text{C-CH}_4$ and $\delta\text{D-CH}_4$ from 2005–2009 to show northern wetland emissions should peak in August–September with a later spring kick-off and later autumn decline. This is further corroborated by Arctic methane measurements (Thonat et al., 2017) and high latitude eddy covariance measurements (Peltola et al., 2019; Treat et al., 2018; Zona et al., 2016) that show a larger contribution from the nongrowing season. Our inverse model results using ECCC and GOSAT data both show agreement with slower to start emissions in the spring and a less intense summertime peak for Canadian wetland emissions.

Several mechanisms have been proposed to describe a larger relative contribution from cold season methane emissions. Pickett-Heaps et al. (2011) attributed a delayed spring onset in the HBL to the suppression of emissions by snow cover. The temperature dependency in WetCHARTS is based on surface skin temperature (Bloom et al., 2017), however subsurface soil temperatures may continue to sustain methane emissions while the surface is below freezing. When subsurface soil temperatures are near 0°C , this “zero curtain” period can further continue to release methane for an extended period (Zona et al., 2016). Subsurface soils may remain unfrozen at a depth of 40 cm even until December (Miller et al., 2016). Alternatively, field studies in the 1990’s suggested the seasonality of emissions may be more influenced by hydrology than temperature, with large differences between peatlands sites (Moore et al., 1994). The WetCHARTS extended ensemble inundation extent variable is constrained seasonally by precipitation. While this does not directly constrain water table depth and wetland extent it provides an aggregate constraint on hydrological variability (Bloom et al., 2017). We show the

mean seasonal pattern of both air temperature and precipitation from climatological measurements in subarctic Canada are similarly asymmetrical about the July peak (Fig. C.2 in the Supplement). August is warmer and wetter than June, September is warmer and wetter than May, and October is wetter and warmer than April – with wetness being more persistent into the autumn than air temperature. Our inversion results showing a delayed spring start in the seasonal pattern of natural methane emissions in Canada may suggest a lag in the response of methane emissions to temperature and precipitation. This may be due to lingering subsurface soil temperatures and/or more complex parametrization necessary for hydrology.

The overall agreement between ECCC and GOSAT inversions shows robustness in the results. While the same model, prior emissions and inversion procedure are used for assimilating ECCC and GOSAT data, the two datasets are produced with very different measurement methodologies (in situ vs. remote sensing) and sample different parts of the atmosphere (surface concentrations or the total vertical column). The posterior error intervals shown from \hat{S} reflect assumptions about the treatment of observations and may insufficiently account for correlations, however the comparative analysis provides a useful sensitivity test of the posterior emissions since the datasets reflect different treatment of these assumptions.

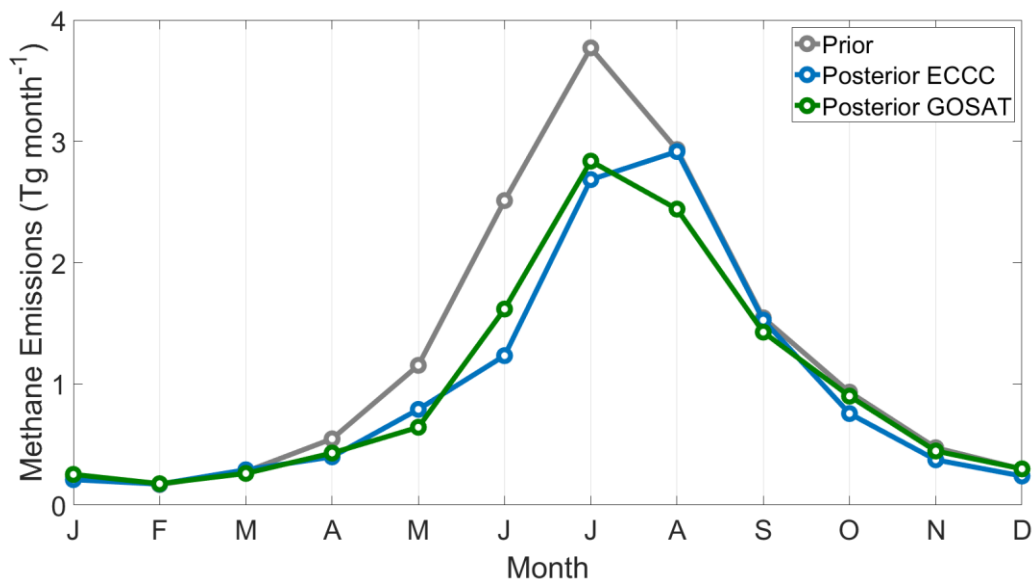


Figure 4.6: Mean 2010–2015 seasonal pattern of natural methane emissions in Tg month^{-1} . The annual total emissions are 14.8 Tg a^{-1} (prior, gray), $11.6 \pm 1.2 \text{ Tg a}^{-1}$ (posterior ECCC, blue) and $11.7 \pm 1.2 \text{ Tg a}^{-1}$ (posterior GOSAT, green). The posterior results are within the uncertainty range provided by the WetCHARTS extended ensemble ($3.9\text{--}32.4 \text{ Tg a}^{-1}$ for Canada).

4.3.3 Joint inversions combining ECCC in situ and GOSAT satellite data

We combine the ECCC and GOSAT datasets in two policy-themed inversions: (1) optimizing emissions according to the sectors in the national inventory ($n = 5$ state vector elements; corresponding to the categories in Table 4.2) and (2) optimizing emissions by provinces split into anthropogenic and natural totals ($n = 16$) and show the results in Figure 4.7. These inversions are under-determined and show the limitations of the ECCC+GOSAT observing system towards constraining emissions in Canada with very small magnitudes. We conduct the inversions for each year from 2010–2015 individually and present the average from these six samples. Since these two policy inversions use a low number of state vector elements, they are vulnerable to both aggregation error and overfitting of the well-constrained state vector elements and do not necessarily benefit from using a larger data vector from all six years. We discuss the diagnostics and information content for these inversions in detail in Section C.4 of the Supplement. The error bars are the 1σ standard deviation of the six yearly results and therefore represent both noise in

the inversion procedure and year-to-year differences in the state (emissions and/or transport). Here we do not apply a weighting factor to either dataset, the observations are treated equivalently for the cost function in eq. (4.1). While there are about 5 times more GOSAT observations than ECCO observations for use in the analysis and the in-situ observations have larger observational error in \mathbf{S}_a (due to model error), the surface measurements are much more sensitive to surface fluxes, which offsets the weight of the larger amount of GOSAT data. As further diagnostics we show the inversions using GOSAT and ECCO individually (Table C.4 and C.5) which show general agreement between the datasets. We also use a singular value decomposition eigenanalysis (Heald et al., 2004) to evaluate the independence of the state vector elements and to demonstrate which sectoral categories and provinces can be reliably constrained above the noise in the system (Fig. C.9 and C.10 in the Supplement).

Figure 4.7 (top) shows the sectoral inversion corresponding to categories in the National Inventory (Table 4.2). The prior emissions with 50% error estimates (60% for wetlands) are 2.4 Tg a^{-1} (Energy), 1.0 Tg a^{-1} (Agriculture), 0.9 Tg a^{-1} (Waste), 14.0 Tg a^{-1} (Wetlands) and 0.8 Tg a^{-1} (Other Natural). The posterior emissions are $3.6 \pm 0.9 \text{ Tg a}^{-1}$ (Energy), $1.5 \pm 0.4 \text{ Tg a}^{-1}$ (Agriculture), $0.8 \pm 0.2 \text{ Tg a}^{-1}$ (Waste), $9.6 \pm 1.1 \text{ Tg a}^{-1}$ (Wetlands), and $1.7 \pm 0.9 \text{ Tg a}^{-1}$ (Other Natural). The degrees of freedom for signal and singular value decomposition (Fig. C.9) show 3–4 independent pieces of information can be retrieved, which are differentiated in the figure by solid and hatched bars. The singular value decomposition shows strong source signals corresponding to wetlands and energy with signal-to-noise ratios of ~ 37 and ~ 5 , respectively. These are the two largest emissions sources in Canada and show the inverse system can successfully disentangle the major anthropogenic and natural contributors. Emissions from waste have a signal-to-noise ratio of ~ 2 and can be constrained despite the low magnitude of emissions. This is likely due to waste emissions being more concentrated in Central Canada and away from the influence of large energy and agriculture emissions in Western Canada. Emissions from other natural sources are at the noise limit and show a moderate correlation with wetlands, which shows that these two sources are not completely independent. Agriculture emissions are below the noise in the system and highly correlated with energy emissions. This is likely due to the high spatial overlap of energy and agriculture emissions in Western Canada. As a result of these

limitations, we present the total of energy and agriculture as $5.1 \pm 1.0 \text{ Tg a}^{-1}$ and the total of wetlands and other natural as $11.3 \pm 1.4 \text{ Tg a}^{-1}$. Our results for total natural and total anthropogenic emissions are consistent with the results from the previous monthly inversion, with the added benefit of identifying which sectors are responsible for the higher anthropogenic emissions at the cost of lower temporal resolution. Waste emissions are 15% lower than the prior and 14% lower than the National Inventory. The total for energy and agriculture is 49% higher than the prior and 59% higher than the total in the inventory. These results show that energy and/or agriculture are the sectors that are responsible for the higher anthropogenic emissions.

Figure 4.7 (bottom) shows the provincial inversion corresponding to the six largest emitting provinces (BC British Columbia, AB Alberta, SK, Saskatchewan, MB Manitoba, ON Ontario, QC Quebec) and two aggregated regions (ATL Atlantic Canada, NOR Northern Territories). These regions are further subdivided into total anthropogenic and total natural methane emissions, with below detection limit anthropogenic emissions from Atlantic Canada and Northern Territories. This inversion especially challenges the limitations of the ECCC+GOSAT observation system, as only about 8 of 16 independent pieces of information are retrieved. This means that half of the posterior provincial emissions are below the noise, and we are unable to constrain province-by-province emissions. The singular value decomposition identifies which regions are well constrained (Fig. C.10). For the anthropogenic emissions AB and ON are strongly constrained. For the natural emissions AB, ON, SK and MB are well constrained. BC shows correlation between its own anthropogenic and natural emissions and cannot be completely disaggregated. As a result, we group elements together in Western Canada (BC + AB + SA + MB) and Central Canada (ON + QC) for interpretation. The total for Western Canada anthropogenic emissions is $4.7 \pm 0.6 \text{ Tg a}^{-1}$ which is 42% higher than the prior of 3.3 Tg a^{-1} . The total for Central Canada is $0.8 \pm 0.2 \text{ Tg a}^{-1}$ which is 11% lower than the prior of 0.9 Tg a^{-1} .

Each of our top-down inversion results show higher total anthropogenic emissions than bottom-up estimates. This is consistent regardless of the observation vector incorporating ECCC data, GOSAT data or ECCC+GOSAT data. The subnational scale emissions are limited in their ability to provide full characterization of minor emissions across Canada but can successfully constrain major emissions for source attribution. The sectoral inversion attributes higher

anthropogenic emissions to energy and/or agriculture and applies a small decrease to waste emissions. The provincial inversion attributes higher anthropogenic emissions to Western Canada and a small decrease to Central Canada. These results suggest that anthropogenic emissions in Canada are underestimated primarily because of higher emissions from Western Canada energy and/or agriculture. This interpretation is consistent with previous satellite inverse modelling studies over North America that apply positive scaling factors to grid box clusters in Western Canada to match observations (Maasakkers et al., 2019; Turner et al., 2015; Wecht et al., 2014). Aircraft studies in Alberta have also shown higher emissions from oil and gas in Alberta than bottom-up estimates (Baray et al., 2018; Johnson et al., 2017). Atherton et al. (2017) estimated higher emissions from natural gas in north-eastern British Columbia using mobile surface in situ measurements (Atherton et al., 2017). Zavala-Araiza et al. (2018) showed a significant amount of methane emissions in Alberta from equipment leaks and venting go unreported due to current reporting requirements and in some regions a small number of sites may be responsible for most methane emissions. Our inverse modelling results from 2010–2015 suggest a consistent presence of under-reported or unreported emissions which require a policy adjustment to reporting practices.

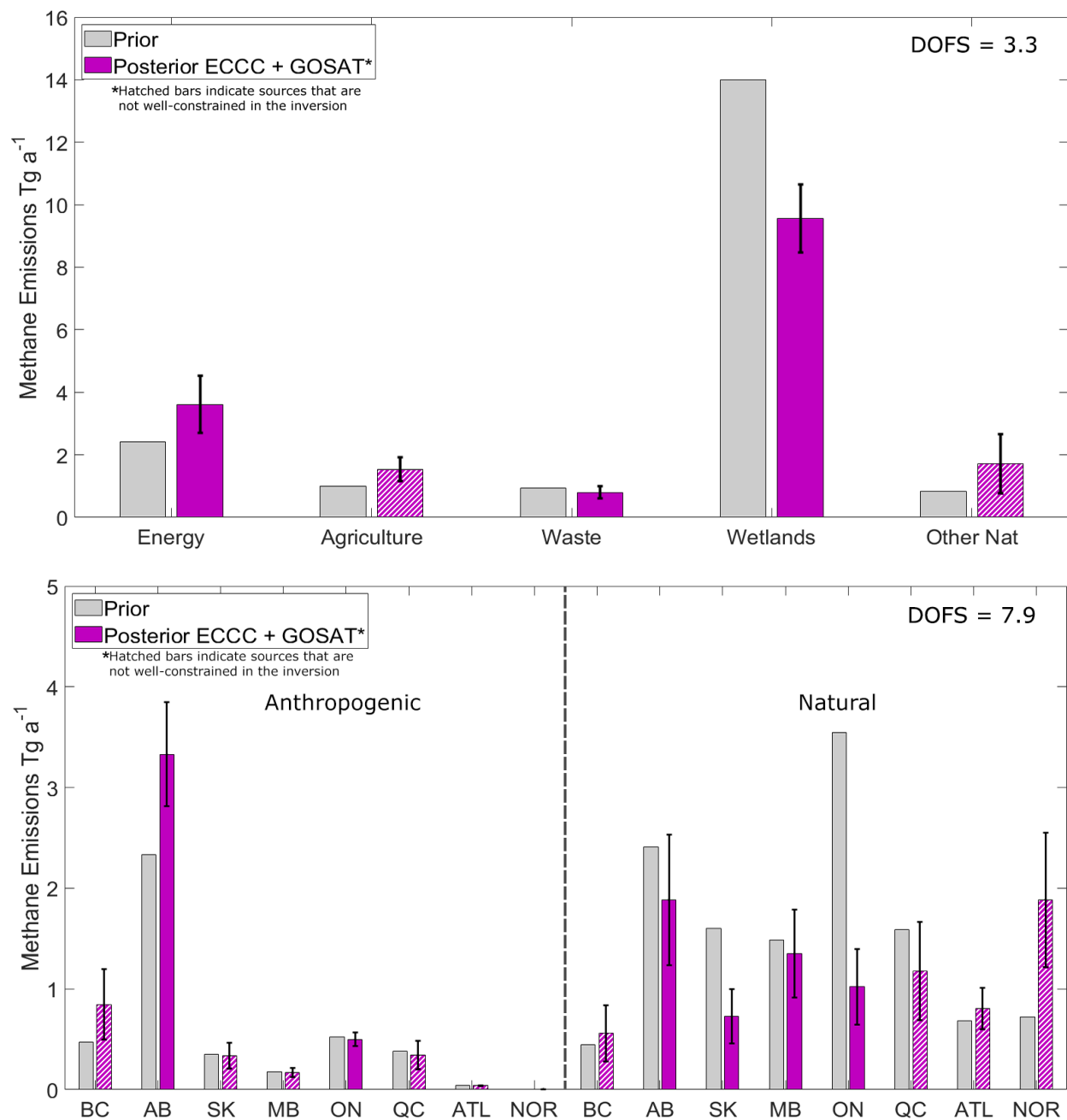


Figure 4.7: Joint-inversions combining 2010–2015 ECCC in situ and GOSAT satellite data showing how the combined observing system remains limited towards resolving all Canadian sources. Inversions are done for each year and we present the six-year average with error bars showing the 1σ standard deviation of the yearly results. Hatched bars indicate sources that are not well-constrained, these are defined as state vector elements with averaging kernel

sensitivities less than 0.8 which are affected by aliasing with other sources (See Supplemental Fig. C.9 and C.10). The top panel shows the sectoral inversion according to the categories in the National Inventory (Energy, Agriculture, Waste) and two natural categories (Wetlands and Other Natural). As an example, the diagnostics in Figure C.9 shows Agriculture emissions are beneath the noise and cannot be distinguished from Energy. The bottom panel shows the subnational regional inversion according to provinces (BC British Columbia, AB Alberta, SK, Saskatchewan, MB Manitoba, ON Ontario, QC Quebec) and aggregated regions (ATL Atlantic Canada, NOR Northern Territories) further subdivided according to total anthropogenic and total natural emissions. The diagnostics in Fig. C.10 show more than half of the regions are at or below the noise. For anthropogenic emissions, the best constraints are on provinces AB and ON. For natural emissions, the best constraints are on AB, SK, MB and ON.

4.3.4 Comparison to independent aircraft and in situ data

We test the robustness of the optimized emissions from each of the three inversions shown (monthly natural, sectoral, and provincial) by comparing to independent measurements not used in the inversions. Prior and posterior simulated methane concentrations are compared to measurements from NOAA ESRL aircraft profiles at East Trout Lake, Saskatchewan (Mund et al., 2017) and ECCC surface measurements in sites Chapais and Chibougamau in Quebec, Canada. The surface data was averaged to daily afternoon means (12:00 to 16:00 local time) in the same manner as the surface measurements used in the inversion. Aircraft data from the NOAA ESRL profiles coincide spatially with the surface measurements at ETL through a joint analysis program with Environment and Climate Change Canada and have occurred on a regular basis approximately once a month from 2005 until present time. Aircraft measurements reach ~7000 m above the surface with samples at multiple altitudes accomplished using a programmable multi-flask system that is further discussed in Mund et al. (2017), however we limit the comparison to the lowest 1 km above ground since higher altitude measurements are mostly background. The aircraft data is not averaged however the flights occur around the same time in the early afternoon.

Figure 4.8 shows the comparison using reduced-major axis (RMA) regressions with the coefficient of determination (R^2), the slope, and the mean-bias shown as metrics to evaluate the agreement. Surface data in CHA, Quebec shows better posterior agreement with observations according to all metrics for each of the three inversions. The R^2 of the prior is 0.36 and improves to a range of 0.44–0.49 for the posterior results, the slope is 1.17 in the prior and improves to a range of 0.92–1.12 and the mean bias (model – observations) is +16.4 ppb in the prior and improves to +13.2 and +5.6 ppb. Since this site in Quebec is particularly sensitive to the Hudson Bay Lowlands, the agreement in all metrics suggests our posterior emissions can better represent wetland emissions in this region. This includes the reduced peak seasonality of natural emissions in the monthly inversion, the reduction of wetland emissions in the sectoral inversion and the reduction of natural emissions primarily in Central Canada in the provincial inversion. Aircraft data in Saskatchewan shows improvement in the R^2 and mean bias metrics but slightly degrades the slope in one case. The R^2 of the prior is 0.14 and improves to a range of 0.20–0.30, the mean bias of the prior is +6.8 ppb and improves to +1.2 and +3.1 ppb. The slope of the prior is 1.15 which slightly degrades to 0.83 in the monthly inversion and improves to a range of 0.88–0.93 in the provincial and sectoral inversions. The high resolution aircraft measurements are more susceptible to representation error at this $2^\circ \times 2.5^\circ$ grid resolution. Furthermore, the time-series comparison to surface data at East Trout Lake (Fig. 4.4) shows overall lower sensitivity to summertime wetland emissions than Fraserdale and Egbert, and lower sensitivity to anthropogenic emissions from Alberta than Lac La Biche. Hence the modelled methane concentrations at the aircraft measurement points are adjusted less by the change in posterior emissions. However, improvement in the R^2 and mean bias metrics show there is still a better representation of the variance in the data which suggests the posterior emissions reduce bias due to peak emission episodes.

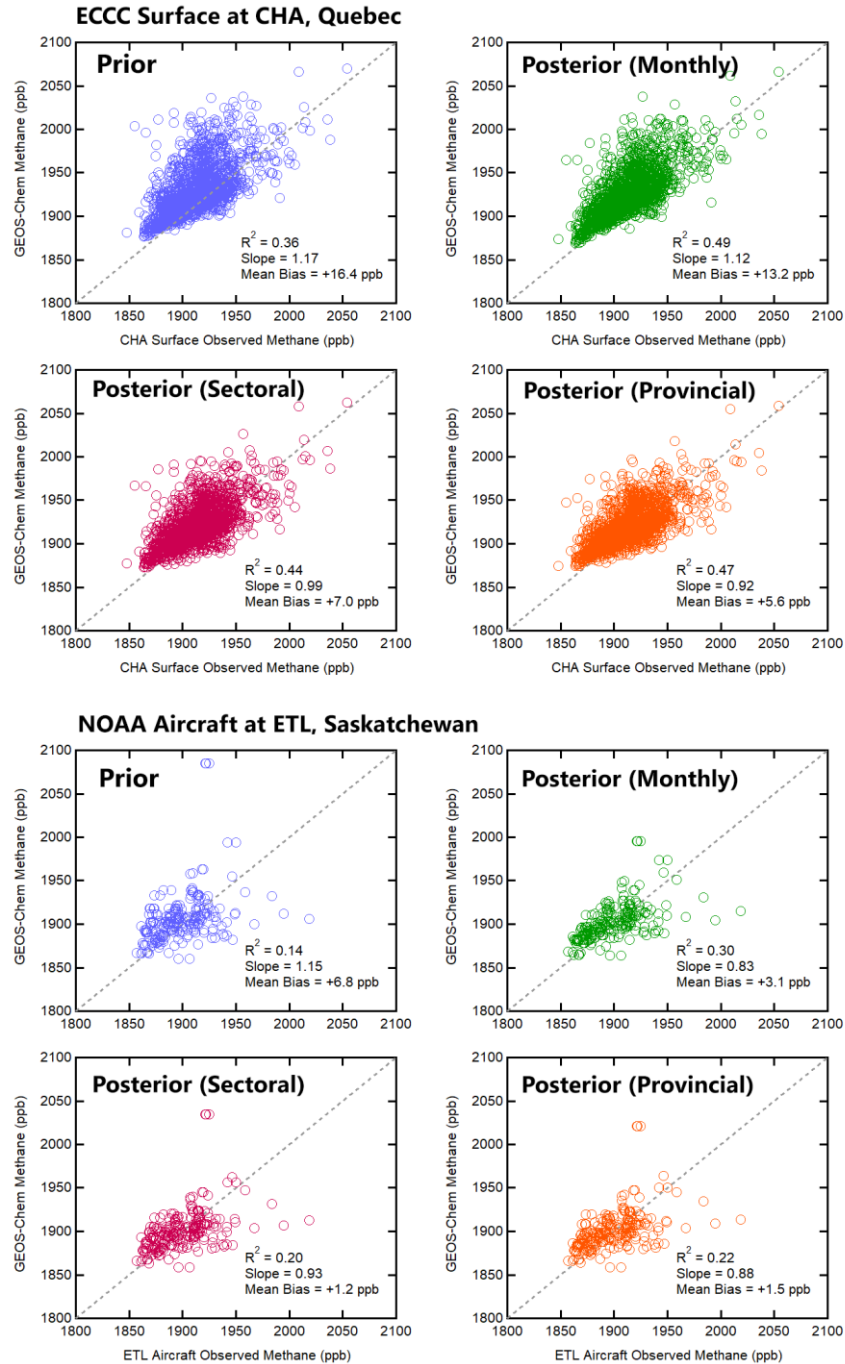


Figure 4.8: Evaluation of inversion results with reduced-major axis (RMA) regressions using independent data. The top four panels show the comparison to ECCC surface observations at Chapais and Chibougamau in Quebec, Canada and the bottom four panels show the comparison to NOAA aircraft profiles at East Trout Lake, Saskatchewan. The agreement of observations

with prior simulated methane concentrations (blue) are compared to posterior concentrations using optimized emissions from the monthly inversion (green), the sectoral inversion (magenta), and the provincial inversion (orange). The coefficient of determination (R^2), slope and mean bias are shown as metrics of agreement.

4.4 Conclusions

We conduct a Bayesian inverse analysis to optimize anthropogenic and natural methane emissions in Canada using 2010–2015 ECCC in situ and GOSAT satellite observations in GEOS-Chem. Methane concentrations are simulated on a $2^\circ \times 2.5^\circ$ grid using recently updated prior emissions inventories for energy and wetland emissions in Canada. Modelled background conditions for the Canadian domain are shown to be unbiased in the comparison to surface in situ data at the western most site in Canada, Estevan point, with agreement within 6 ppb. A forward model analysis shows much larger biases between -100 ppb and $+1050$ ppb at surface sites throughout Canada demonstrating the presence of misrepresented local emissions. We show large positive biases (overestimation of emissions) in the summertime are observed at sites sensitive to wetland emissions, these biases are reduced by using lower magnitude wetland emissions scenarios with lower $\text{CH}_4:\text{C}$ temperature sensitivities or lower inundation extent. We also show the opposite case of negative biases (underestimation of emissions) observed year-round at sites in Western Canada. The forward model analysis is consistent with the results of the inverse analysis that reduce emissions from natural sources and increase emissions from anthropogenic sources to minimize the mismatch between modelled and observed methane.

We show three approaches for using ECCC and GOSAT data towards inverse modelling of Canadian methane emissions. These approaches differ according to the temporal and spatial resolution of the solution. We show: (1) a relatively higher time-resolution inversion that solves for natural emissions each month from 2010–2015 and anthropogenic emissions as yearly totals, (2) a sectoral inversion that solves for emissions according to categories in the National Inventory, (3) a provincial inversion that solves for total anthropogenic and natural emissions at the subnational level. The monthly inversion provides information on the seasonality of natural emissions (which are $\sim 95\%$ wetlands) but does not provide more depth into anthropogenic

emissions beyond yearly scaling. The sectoral inversion provides more information on the categories of anthropogenic emissions that are misrepresented in the prior but without spatial detail. The provincial inversion provides the highest level of spatial discretization but is largely underdetermined due to the limitations of the observing system towards characterizing very low magnitude emissions from smaller contributing provinces.

Inversion results (1) show mean 2010–2015 posterior emissions for total anthropogenic sources in Canada are $6.0 \pm 0.4 \text{ Tg a}^{-1}$ using ECCC data and $6.5 \pm 0.7 \text{ Tg a}^{-1}$ using GOSAT data. Annual mean natural emissions are $11.6 \pm 1.2 \text{ Tg a}^{-1}$ using ECCC data and $11.7 \pm 1.2 \text{ Tg a}^{-1}$ using GOSAT data. Both inverse modelling estimates are higher than the prior for anthropogenic emissions 4.4 Tg a^{-1} and lower than the prior for natural emissions 14.8 Tg a^{-1} . Inversion results using both datasets show a change in the seasonal profile of natural methane emissions where emissions are slower to begin in the spring and show a less intense peak in the summer. The agreement between two datasets assembled with different measurement methodologies that sample different parts of the atmosphere is a robust result that lends weight to our conclusions. Our results corroborate recent studies showing a less-intense and less-narrow summertime peak in North American Boreal wetland emissions with a higher relative contribution from the cold season (Miller et al., 2016; Zona et al., 2016; Warwick et al., 2016; Thonat et al., 2017; Treat et al., 2018; Peltola et al., 2019). These top-down studies using atmospheric observations show biosphere process models can better account for a more complex response to peak surface soil temperatures.

We also conduct combined ECCC+GOSAT inversions that aim to resolve finer resolution emissions corresponding to (2) the sectors of the National Inventory and corresponding to (3) provincial boundaries. These policy-themed inversions challenge the capabilities of the ECCC+GOSAT observation system and show the system is not capable of resolving many minor emissions in Canada. The degrees of freedom for signal for these inversions are 3–4 out of 5 state vector elements for the sectoral inversion and 8 out of 16 for the provincial inversion. The limitation of this inverse approach towards constraining sectoral or regional scale emissions in Canada is due to the low magnitude of these emissions, their overlapping nature in concentrated regions, and the sparsity of data available to distinguish them apart. Grouping correlated sectors

together, we determine $5.1 \pm 1.0 \text{ Tg a}^{-1}$ for energy and agriculture which is 59% higher than the inventory, $0.8 \pm 0.2 \text{ Tg a}^{-1}$ for waste which is 14% lower than the inventory. For provincial emissions, we show Western Canada is $4.7 \pm 0.6 \text{ Tg a}^{-1}$ which is 42% higher than the prior and Central Canada is 0.8 ± 0.2 which is 11% lower. Both regions show lower natural emissions. These results show that the higher anthropogenic emissions in the posterior results can be attributed to energy and/or agriculture primarily in Western Canada where most of Canadian anthropogenic emissions are concentrated. Our results are consistent with other top-down studies that show higher than reported anthropogenic emissions in Western Canada (Wecht et al., 2014; Turner et al., 2015; Atherton et al., 2017; Johnson et al., 2017; Baray et al., 2018; Maasackers et al., 2019). This may be due to oil and gas emissions that are under-reported or unreported due to current reporting requirements (Zavala-Araiza et al., 2018). These top-down studies show a need for policy readjustment in reporting practices for Canadian anthropogenic methane emissions.

This study shows the value of using complementary surface and satellite datasets in an inverse analysis. We emphasize the value of comparative analysis using the datasets independently versus as joint inversions, as minor emissions are too low in magnitude for the observational precision to distinguish finer scale discretization above the noise. The comparative analysis has the added benefit of evaluating the datasets against each other and the assumptions that are specific to using either surface or satellite data. The capabilities for combining and intercomparing datasets is expected to improve, with the successful launch of Copernicus Sentinel-5p satellite (TROPOMI) in 2017 and continued expansions on in situ observation networks. The ability for next generation observations to constrain subnational level emissions in Canada will depend on instrument and model precision, as well as the emissions magnitudes and spatiotemporal overlap of the targets. These technical capabilities should be weighed alongside policy needs for improved methane monitoring.

Competing Interests

The authors declare that they have no conflict of interest.

Data Availability

GEOS-Chem is from <http://acmg.seas.harvard.edu/geos/> which includes links to all gridded prior emissions and meteorological fields used in this analysis. GOSAT satellite data is from the University of Leicester v7 proxy retrieval is available through the Copernicus Climate Change Service <https://climate.copernicus.eu/>. ECCC in situ data is available through the World Data Centre for Greenhouse Gases (WDCGG) <https://gaw.kishou.go.jp/>. NOAA/ESRL aircraft data is from the Global Monitoring Laboratory <https://www.esrl.noaa.gov/gmd/ccgg/aircraft/>.

Acknowledgements

Work at Harvard was supported by the NASA Carbon Monitoring System. We thank the Japanese Aerospace Exploration Agency (JAXA) responsible for the GOSAT instrument, and the University of Leicester for the retrieval algorithm used in this analysis. Doug Worthy and the Climate Research Division at Environment and Climate Change Canada are responsible for the in situ surface measurements and the NOAA/ESRL/GML program is responsible for the Carbon Cycle Greenhouse Gases (CCGG) cooperative air sampling network measurements.

References

- Atherton, E., Risk, D., Fougère, C., Lavoie, M., Marshall, A., Werring, J., Williams, J. P. and Minions, C.: Mobile measurement of methane emissions from natural gas developments in northeastern British Columbia, Canada, *Atmos. Chem. Phys.*, 17(20), 12405–12420, doi:10.5194/acp-17-12405-2017, 2017.
- Baray, S., Darlington, A., Gordon, M., Hayden, K. L., Leithead, A., Li, S.-M., Liu, P. S. K., Mittermeier, R. L., Moussa, S. G., O'Brien, J., Staebler, R., Wolde, M., Worthy, D. and McLaren, R.: Quantification of methane sources in the Athabasca Oil Sands Region of Alberta by aircraft mass balance, *Atmos. Chem. Phys.*, 18(10), 7361–7378, doi:10.5194/acp-18-7361-2018, 2018.
- Bloom, A. A., Bowman, K. W., Lee, M., Turner, A. J., Schroeder, R., Worden, J. R., Weidner, R., McDonald, K. C. and Jacob, D. J.: A global wetland methane emissions and uncertainty dataset for atmospheric chemical transport models (WetCHARTs version 1.0), *Geosci. Model Dev.*, 10(6), 2141–2156, doi:10.5194/gmd-10-2141-2017, 2017.
- Bubier, J. L., Moore, T. R. and Roulet, N. T.: Methane Emissions from Wetlands in the Midboreal Region of Northern Ontario, Canada, *Ecology*, 74(8), 2240–2254, doi:10.2307/1939577, 1993.
- Buchwitz, M., Reuter, M., Schneising, O., Boesch, H., Guerlet, S., Dils, B., Aben, I., Armante, R., Bergamaschi, P., Blumenstock, T., Bovensmann, H., Brunner, D., Buchmann, B., Burrows, J. P., Butz, A., Chédin, A., Chevallier, F., Crevoisier, C. D., Deutscher, N. M., Frankenberg, C., Hase, F., Hasekamp, O. P., Heymann, J., Kaminski, T., Laeng, A., Lichtenberg, G., De Mazière, M., Noël, S., Notholt, J., Orphal, J., Popp, C., Parker, R., Scholze, M., Sussmann, R., Stiller, G. P., Warneke, T., Zehner, C., Bril, A., Crisp, D., Griffith, D. W. T., Kuze, A., O'Dell, C., Oshchepkov, S., Sherlock, V., Suto, H., Wennberg, P., Wunch, D., Yokota, T. and Yoshida, Y.: The Greenhouse Gas Climate Change Initiative (GHG-CCI): Comparison and quality assessment of near-surface-sensitive satellite-derived CO₂ and CH₄ global data sets, *Remote Sensing of Environment*, 162, 344–362, doi:10.1016/j.rse.2013.04.024, 2015.
- Butz, A., Guerlet, S., Hasekamp, O., Schepers, D., Galli, A., Aben, I., Frankenberg, C., Hartmann, J.-M., Tran, H., and Kuze, A.: Toward accurate CO₂ and CH₄ observations from GOSAT, *Geophys. Res. Lett.*, 38, L14812, <https://doi.org/10.1029/2011GL047888>, 2011.
- Darmenov, A. and da Silva, A.: The quick fire emissions dataset (QFED)—documentation of versions 2.1, 2.2 and 2.4, NASA Technical Report Series on Global Modeling and Data Assimilation, NASA TM-2013-104606, 32, 183 pp., 2013.
- Environment and Climate Change Canada: National Inventory Report 1990–2015: Greenhouse Gas Sources and Sinks in Canada, Canada's Submission to the United Nations Framework Convention on Climate Change, Part 3. Available at: http://publications.gc.ca/collections/collection_2018/eccc/En81-4-2015-3-eng.pdf, 2017.
- ESA CCI GHG project team: ESA Greenhouse Gases Climate Change Initiative (GHG_cci): Column-averaged CH₄ from GOSAT generated with the OCPR (UoL-PR) Proxy algorithm (CH₄_GOS_OCPR), v7.0. Centre for Environmental Data Analysis, Available at: <https://catalogue.ceda.ac.uk/uuid/f9154243fd8744bdaf2a59c39033e659>, 2018.
- Fung, I., John, J., Lerner, J., Matthews, E., Prather, M., Steele, L. P. and Fraser, P. J.: Three-dimensional model synthesis of the global methane cycle, *J. Geophys. Res.*, 96(D7), 13033, doi:10.1029/91JD01247, 1991.
- Hartmann, D. L., Tank, A. M. K., Rusticucci, M., Alexander, L. V., Brönnimann, S., Charabi, Y. A. R., Dentener, F. J., Dlugokencky, E. J., Easterling, D. R., Kaplan, A., Soden, B. J., Thorne, P. W., Wild, M.,

and Zhai, P. M.: Observations: atmosphere and surface, in: *Climate Change 2013 the Physical Science Basis: Working Group I Contribution to the Fifth Assessment Report of the Intergovernmental Panel on Climate Change*, Cambridge University Press, 2013.

Heald, C. L., Jacob, D. J., Jones, D. B. A., Palmer, P. I., Logan, J. A., Streets, D. G., Sachse, G. W., Gille, J. C., Hoffman, R. N. and Nehrkorn, T.: Comparative inverse analysis of satellite (MOPITT) and aircraft (TRACE-P) observations to estimate Asian sources of carbon monoxide: COMPARATIVE INVERSE ANALYSIS, *J. Geophys. Res.*, 109(D23), doi:10.1029/2004JD005185, 2004.

Hu, H., Landgraf, J., Detmers, R., Borsdorff, T., Aan de Brugh, J., Aben, I., Butz, A. and Hasekamp, O.: Toward Global Mapping of Methane With TROPOMI: First Results and Intersatellite Comparison to GOSAT, *Geophys. Res. Lett.*, 45(8), 3682–3689, doi:10.1002/2018GL077259, 2018.

Ishizawa, M., Chan, D., Worthy, D., Chan, E., Vogel, F. and Maksyutov, S.: Analysis of atmospheric CH₄ in Canadian Arctic and estimation of the regional CH₄ fluxes, *Atmos. Chem. Phys.*, 19(7), 4637–4658, doi:10.5194/acp-19-4637-2019, 2019.

Jacob, D. J., Turner, A. J., Maasakkers, J. D., Sheng, J., Sun, K., Liu, X., Chance, K., Aben, I., McKeever, J. and Frankenberg, C.: Satellite observations of atmospheric methane and their value for quantifying methane emissions, *Atmos. Chem. Phys.*, 16(22), 14371–14396, doi:10.5194/acp-16-14371-2016, 2016.

Johnson, M. R., Tyner, D. R., Conley, S., Schwietzke, S. and Zavala-Araiza, D.: Comparisons of Airborne Measurements and Inventory Estimates of Methane Emissions in the Alberta Upstream Oil and Gas Sector, *Environ. Sci. Technol.*, 51(21), 13008–13017, doi:10.1021/acs.est.7b03525, 2017.

Kirschke, S., Bousquet, P., Ciais, P., Saunois, M., Canadell, J. G., Dlugokencky, E. J., Bergamaschi, P., Bergmann, D., Blake, D. R., Bruhwiler, L., Cameron-Smith, P., Castaldi, S., Chevallier, F., Feng, L., Fraser, A., Heimann, M., Hodson, E. L., Houweling, S., Josse, B., Fraser, P. J., Krummel, P. B., Lamarque, J.-F., Langenfelds, R. L., Le Quééré, C., Naik, V., O'Doherty, S., Palmer, P. I., Pison, I., Plummer, D., Poulter, B., Prinn, R. G., Rigby, M., Ringeval, B., Santini, M., Schmidt, M., Shindell, D. T., Simpson, I. J., Spahni, R., Steele, L. P., Strode, S. A., Sudo, K., Szopa, S., van der Werf, G. R., Voulgarakis, A., van Weele, M., Weiss, R. F., Williams, J. E. and Zeng, G.: Three decades of global methane sources and sinks, *Nature Geosci.*, 6(10), 813–823, doi:10.1038/ngeo1955, 2013.

Kuze, A., Suto, H., Shiomi, K., Kawakami, S., Tanaka, M., Ueda, Y., Deguchi, A., Yoshida, J., Yamamoto, Y., Kataoka, F., Taylor, T. E., and Buijs, H. L.: Update on GOSAT TANSOFTS performance, operations, and data products after more than 6 years in space, *Atmos. Meas. Tech.*, 9, 2445–2461, <https://doi.org/10.5194/amt-9-2445-2016>, 2016.

Lu, X., Jacob, D. J., Zhang, Y., Maasakkers, J. D., Sulprizio, M. P., Shen, L., Qu, Z., Scarpelli, T. R., Nesser, H., Yantosca, R. M., Sheng, J., Andrews, A., Parker, R. J., Boesch, H., Bloom, A. A., and Ma, S.: Global methane budget and trend, 2010–2017: complementarity of inverse analyses using in situ (GLOBALVIEWplus CH₄ ObsPack) and satellite (GOSAT) observations, *Atmos. Chem. Phys.*, 21, 4637–4657, <https://doi.org/10.5194/acp-21-4637-2021>, 2021.

Maasakkers, J. D., Jacob, D. J., Sulprizio, M. P., Turner, A. J., Weitz, M., Wirth, T., Hight, C., DeFigueiredo, M., Desai, M., Schmeltz, R., Hockstad, L., Bloom, A. A., Bowman, K. W., Jeong, S. and Fischer, M. L.: Gridded National Inventory of U.S. Methane Emissions, *Environ. Sci. Technol.*, 50(23), 13123–13133, doi:10.1021/acs.est.6b02878, 2016.

Maasakkers, J. D., Jacob, D. J., Sulprizio, M. P., Scarpelli, T. R., Nesser, H., Sheng, J.-X., Zhang, Y., Hersher, M., Bloom, A. A., Bowman, K. W., Worden, J. R., Janssens-Maenhout, G. and Parker, R. J.:

Global distribution of methane emissions, emission trends, and OH concentrations and trends inferred from an inversion of GOSAT satellite data for 2010–2015, *Atmos. Chem. Phys.*, 19(11), 7859–7881, doi:10.5194/acp-19-7859-2019, 2019.

Maasakkers, J. D., Jacob, D. J., Sulprizio, M. P., Scarpelli, T. R., Nesser, H., Sheng, J., Zhang, Y., Lu, X., Bloom, A. A., Bowman, K. W., Worden, J. R., and Parker, R. J.: 2010–2015 North American methane emissions, sectoral contributions, and trends: a high-resolution inversion of GOSAT observations of atmospheric methane, *Atmos. Chem. Phys.*, 21, 4339–4356, <https://doi.org/10.5194/acp-21-4339-2021>, 2021.

Miller, S. M., Worthy, D. E. J., Michalak, A. M., Wofsy, S. C., Kort, E. A., Havice, T. C., Andrews, A. E., Dlugokencky, E. J., Kaplan, J. O., Levi, P. J., Tian, H. and Zhang, B.: Observational constraints on the distribution, seasonality, and environmental predictors of North American boreal methane emissions, *Global Biogeochem. Cycles*, 28(2), 146–160, doi:10.1002/2013GB004580, 2014.

Miller, S. M., Commane, R., Melton, J. R., Andrews, A. E., Benmergui, J., Dlugokencky, E. J., Janssens-Maenhout, G., Michalak, A. M., Sweeney, C. and Worthy, D. E. J.: Evaluation of wetland methane emissions across North America using atmospheric data and inverse modeling, *Biogeosciences*, 13(4), 1329–1339, doi:10.5194/bg-13-1329-2016, 2016.

Moore, T. R., Heyes, A. and Roulet, N. T.: Methane emissions from wetlands, southern Hudson Bay lowland, *J. Geophys. Res.*, 99(D1), 1455, doi:10.1029/93JD02457, 1994.

Mund, J., Thoning, K., Tans, P., Sweeny, C., Higgs, J., Wolter, S., Crotwell, A., Neff, D., Dlugokencky, E., Lang, P., Novelli, P., Moglia, E. and Crotwell, M.: Earth System Research Laboratory Carbon Cycle and Greenhouse Gases Group Flask-Air Sample Measurements of CO₂, CH₄, CO, N₂O, H₂, and SF₆ from the Aircraft Program, 1992-Present, , doi:10.7289/V5N58JMF, 2017.

Myhre, G.: Anthropogenic and Natural Radiative Forcing, in *Climate Change 2013: The Physical Science Basis. Contribution of Working Group I to the Fifth Assessment Report of the Intergovernmental Panel on Climate Change.*, 2013.

Nakajima, M., Suto, H., Yotsumoto, K., Shiomi, K., and Hirabayashi, T.: Fourier transform spectrometer on GOSAT and GOSAT-2, in: *International Conference on Space Optics — ICSO 2014, International Conference on Space Optics 2014, Tenerife, Canary Islands, Spain, 2*, <https://doi.org/10.1117/12.2304062>, 2017.

Nisbet, E. G., Fisher, R. E., Lowry, D., France, J. L., Allen, G., Bakkaloglu, S., Broderick, T. J., Cain, M., Coleman, M., Fernandez, J., Forster, G., Griffiths, P. T., Iverach, C. P., Kelly, B. F. J., Manning, M. R., Nisbet-Jones, P. B. R., Pyle, J. A., Townsend-Small, A., al-Shalaan, A., Warwick, N. and Zazzeri, G.: Methane Mitigation: Methods to Reduce Emissions, on the Path to the Paris Agreement, *Rev. Geophys.*, 58(1), doi:10.1029/2019RG000675, 2020.

Parker, R., Boesch, H., Cogan, A., Fraser, A., Feng, L., Palmer, P. I., Messerschmidt, J., Deutscher, N., Griffith, D. W., and Notholt, J.: Methane observations from the Greenhouse Gases Observing SATellite: Comparison to ground-based TCCON data and model calculations, *Geophys. Res. Lett.*, 38, L15807, <https://doi.org/10.1029/2011GL047871>, 2011.

Parker, R. J., Boesch, H., Byckling, K., Webb, A. J., Palmer, P. I., Feng, L., Bergamaschi, P., Chevallier, F., Notholt, J., Deutscher, N., Warneke, T., Hase, F., Sussmann, R., Kawakami, S., Kivi, R., Griffith, D. W. T., and Velasco, V.: Assessing 5 years of GOSAT Proxy XCH₄ data and associated uncertainties, *Atmos. Meas. Tech.*, 8, 4785–4801, <https://doi.org/10.5194/amt-8-4785-2015>, 2015.

- Patra, P. K., Houweling, S., Krol, M., Bousquet, P., Belikov, D., Bergmann, D., Bian, H., Cameron-Smith, P., Chipperfield, M. P., Corbin, K., Fortems-Cheiney, A., Fraser, A., Gloor, E., Hess, P., Ito, A., Kawa, S. R., Law, R. M., Loh, Z., Maksyutov, S., Meng, L., Palmer, P. I., Prinn, R. G., Rigby, M., Saito, R. and Wilson, C.: TransCom model simulations of CH₄ and related species: linking transport, surface flux and chemical loss with CH₄ variability in the troposphere and lower stratosphere, *Atmos. Chem. Phys.*, 11(24), 12813–12837, doi:10.5194/acp-11-12813-2011, 2011.
- Peltola, O., Vesala, T., Gao, Y., Rätty, O., Alekseychik, P., Aurela, M., Chojnicki, B., Desai, A. R., Dolman, A. J., Euskirchen, E. S., Friborg, T., Göckede, M., Helbig, M., Humphreys, E., Jackson, R. B., Jocher, G., Joos, F., Klatt, J., Knox, S. H., Kowalska, N., Kutzbach, L., Lienert, S., Lohila, A., Mammarella, I., Nadeau, D. F., Nilsson, M. B., Oechel, W. C., Peichl, M., Pypker, T., Quinton, W., Rinne, J., Sachs, T., Samson, M., Schmid, H. P., Sonntag, O., Wille, C., Zona, D. and Aalto, T.: Monthly gridded data product of northern wetland methane emissions based on upscaling eddy covariance observations, *Earth Syst. Sci. Data*, 11(3), 1263–1289, doi:10.5194/essd-11-1263-2019, 2019.
- Pickett-Heaps, C. A., Jacob, D. J., Wecht, K. J., Kort, E. A., Wofsy, S. C., Diskin, G. S., Worthy, D. E. J., Kaplan, J. O., Bey, I. and Drevet, J.: Magnitude and seasonality of wetland methane emissions from the Hudson Bay Lowlands (Canada), *Atmos. Chem. Phys.*, 11(8), 3773–3779, doi:10.5194/acp-11-3773-2011, 2011.
- Poulter, B., Bousquet, P., Canadell, J. G., Ciais, P., Pregon, A., Saunio, M., Arora, V. K., Beerling, D. J., Brovkin, V., Jones, C. D., Joos, F., Gedney, N., Ito, A., Kleinen, T., Koven, C. D., McDonald, K., Melton, J. R., Peng, C., Peng, S., Prigent, C., Schroeder, R., Riley, W. J., Saito, M., Spahni, R., Tian, H., Taylor, L., Viovy, N., Wilton, D., Wiltshire, A., Xu, X., Zhang, B., Zhang, Z. and Zhu, Q.: Global wetland contribution to 2000–2012 atmospheric methane growth rate dynamics, *Environ. Res. Lett.*, 12(9), 094013, doi:10.1088/1748-9326/aa8391, 2017.
- Prather, M. J., Holmes, C. D., and Hsu, J.: Reactive greenhouse gas scenarios: Systematic exploration of uncertainties and the role of atmospheric chemistry, *Geophys. Res. Lett.*, 39, L09803, <https://doi.org/10.1029/2012GL051440>, 2012.
- Rodgers, C. D.: *Inverse Methods for Atmospheric Sounding: Theory and Practice*, WORLD SCIENTIFIC., 2000.
- Rogelj, J., Popp, A., Calvin, K. V., Luderer, G., Emmerling, J., Gernaat, D., Fujimori, S., Strefler, J., Hasegawa, T., Marangoni, G., Krey, V., Kriegler, E., Riahi, K., van Vuuren, D. P., Doelman, J., Drouet, L., Edmonds, J., Fricko, O., Harmsen, M., Havlík, P., Humpenöder, F., Stehfest, E. and Tavoni, M.: Scenarios towards limiting global mean temperature increase below 1.5 °C, *Nature Clim Change*, 8(4), 325–332, doi:10.1038/s41558-018-0091-3, 2018.
- Sheng, J.-X., Jacob, D. J., Maasackers, J. D., Sulprizio, M. P., Zavala-Araiza, D. and Hamburg, S. P.: A high-resolution (0.1° × 0.1°) inventory of methane emissions from Canadian and Mexican oil and gas systems, *Atmospheric Environment*, 158, 211–215, doi:10.1016/j.atmosenv.2017.02.036, 2017.
- Sheng, J.-X., Jacob, D. J., Turner, A. J., Maasackers, J. D., Benmergui, J., Bloom, A. A., Arndt, C., Gautam, R., Zavala-Araiza, D., Boesch, H. and Parker, R. J.: 2010–2016 methane trends over Canada, the United States, and Mexico observed by the GOSAT satellite: contributions from different source sectors, *Atmos. Chem. Phys.*, 18(16), 12257–12267, doi:10.5194/acp-18-12257-2018, 2018a.
- Sheng, J.-X., Jacob, D. J., Turner, A. J., Maasackers, J. D., Sulprizio, M. P., Bloom, A. A., Andrews, A. E. and Wunch, D.: High-resolution inversion of methane emissions in the Southeast US using SEAC 4 RS aircraft observations of atmospheric methane: anthropogenic and wetland sources, *Atmos. Chem. Phys.*, 18(9), 6483–6491, doi:10.5194/acp-18-6483-2018, 2018b.

- Stanevich, I., Jones, D. B. A., Strong, K., Parker, R. J., Boesch, H., Wunch, D., Notholt, J., Petri, C., Warneke, T., Sussmann, R., Schneider, M., Hase, F., Kivi, R., Deutscher, N. M., Velazco, V. A., Walker, K. A., and Deng, F.: Characterizing model errors in chemical transport modeling of methane: impact of model resolution in versions v9-02 of GEOS-Chem and v35j of its adjoint model, *Geosci. Model Dev.*, 13, 3839–3862, <https://doi.org/10.5194/gmd-13-3839-2020>, 2020.
- Thonat, T., Saunio, M., Bousquet, P., Pison, I., Tan, Z., Zhuang, Q., Crill, P. M., Thornton, B. F., Bastviken, D., Dlugokencky, E. J., Zimov, N., Laurila, T., Hatakka, J., Hermansen, O. and Worthy, D. E. J.: Detectability of Arctic methane sources at six sites performing continuous atmospheric measurements, *Atmos. Chem. Phys.*, 17(13), 8371–8394, doi:10.5194/acp-17-8371-2017, 2017.
- Treat, C. C., Bloom, A. A. and Marushchak, M. E.: Nongrowing season methane emissions—a significant component of annual emissions across northern ecosystems, *Glob Change Biol*, 24(8), 3331–3343, doi:10.1111/gcb.14137, 2018.
- Tunnicliffe, R. L., Ganesan, A. L., Parker, R. J., Boesch, H., Gedney, N., Poulter, B., Zhang, Z., Lavrič, J. V., Walter, D., Rigby, M., Henne, S., Young, D., and O'Doherty, S.: Quantifying sources of Brazil's CH₄ emissions between 2010 and 2018 from satellite data, *Atmos. Chem. Phys.*, 20, 13041–13067, <https://doi.org/10.5194/acp-20-13041-2020>, 2020. Turner, A. J. and Jacob, D. J.: Balancing aggregation and smoothing errors in inverse models, *Atmos. Chem. Phys.*, 15(12), 7039–7048, doi:10.5194/acp-15-7039-2015, 2015.
- Turner, A. J., Jacob, D. J., Wecht, K. J., Maasakkers, J. D., Lundgren, E., Andrews, A. E., Biraud, S. C., Boesch, H., Bowman, K. W., Deutscher, N. M., Dubey, M. K., Griffith, D. W. T., Hase, F., Kuze, A., Notholt, J., Ohyama, H., Parker, R., Payne, V. H., Sussmann, R., Sweeney, C., Velazco, V. A., Warneke, T., Wennberg, P. O. and Wunch, D.: Estimating global and North American methane emissions with high spatial resolution using GOSAT satellite data, *Atmos. Chem. Phys.*, 15(12), 7049–7069, doi:10.5194/acp-15-7049-2015, 2015.
- Turner, A. J., Frankenberg, C. and Kort, E. A.: Interpreting contemporary trends in atmospheric methane, *Proc Natl Acad Sci USA*, 116(8), 2805–2813, doi:10.1073/pnas.1814297116, 2019.
- Warwick, N. J., Cain, M. L., Fisher, R., France, J. L., Lowry, D., Michel, S. E., Nisbet, E. G., Vaughn, B. H., White, J. W. C., and Pyle, J. A.: Using $\delta^{13}\text{C-CH}_4$ and $\delta\text{D-CH}_4$ to constrain Arctic methane emissions, *Atmos. Chem. Phys.*, 16, 14891–14908, <https://doi.org/10.5194/acp-16-14891-2016>, 2016.
- Wecht, K. J., Jacob, D. J., Frankenberg, C., Jiang, Z. and Blake, D. R.: Mapping of North American methane emissions with high spatial resolution by inversion of SCIAMACHY satellite data: NORTH AMERICA METHANE EMISSION INVERSION, *J. Geophys. Res. Atmos.*, 119(12), 7741–7756, doi:10.1002/2014JD021551, 2014.
- Zavala-Araiza, D., Herndon, S. C., Roscioli, J. R., Yacovitch, T. I., Johnson, M. R., Tyner, D. R., Omara, M. and Knighton, B.: Methane emissions from oil and gas production sites in Alberta, Canada, *Elem Sci Anth*, 6(1), 27, doi:10.1525/elementa.284, 2018.
- Zona, D., Gioli, B., Commane, R., Lindaas, J., Wofsy, S. C., Miller, C. E., Dinardo, S. J., Dengel, S., Sweeney, C., Karion, A., Chang, R. Y.-W., Henderson, J. M., Murphy, P. C., Goodrich, J. P., Moreaux, V., Liljedahl, A., Watts, J. D., Kimball, J. S., Lipson, D. A. and Oechel, W. C.: Cold season emissions dominate the Arctic tundra methane budget, *Proc Natl Acad Sci USA*, 113(1), 40–45, doi:10.1073/pnas.1516017113, 2016.

Chapter 5 Surveying urban methane emissions in the Greater Toronto Area using mobile surface measurements

Abstract

Reducing methane emissions from urban areas is a key part of the international strategy for mitigating greenhouse gas emissions, with major world cities posting ambitious reduction plans. The City of Toronto has a target to reduce 65% of methane emissions by 2030 from a baseline of 1990. Monitoring the efficacy of urban methane mitigation over policy-relevant timescales is challenging to constrain with atmospheric observations due to the precision requirements necessary to observe changes in low emissions magnitudes. Uncertainties on the order of 50% for mass balance methods and inverse modelling are unable to adequately monitor finer temporal and spatial scale variability and require substantial improvements to observation networks. In this study we show cost-effective surveys can be conducted using a Picarro cavity ring-down spectrometer in a moving vehicle to screen the Greater Toronto Area for on-road combustion emissions, natural gas leaks, and to identify major emitters for mitigation targets. We conducted stationary surveys in October 2014 at key highway locations to evaluate mobile combustion sources and verify inventory emissions factors for on-road vehicles. A single-day survey was conducted in May of 2017 to evaluate city infrastructure for natural gas leaks. Results from the ~90 km driving survey show minimal emissions from natural gas leaks in both suburban (York Region) and urban (downtown Toronto) areas when compared to similar studies in Boston and Washington DC. We identify a single super-emitter at the edge of the downtown core likely from wastewater. Our results show natural gas infrastructure can be successfully monitored with this method and large individual sources can be identified which are an attractive target for mitigation policy.

5.1 Introduction

Methane (CH₄) is a significant greenhouse gas next to CO₂ for direct radiative forcing, but with a global warming potential 28–32 times more than CO₂ over a 100 year timescale and 84–90 times more over a 20 year timescale (Myhre et al., 2013). Anthropogenic methane sources include oil and gas activities (extraction, processing, transport, and combustion), livestock, rice cultivation, coal mines, landfills, and wastewater treatment. Natural methane emissions are primarily from wetlands, but also include seeps, termites and biomass burning (Kirschke et al., 2013). Atmospheric methane has a lifetime of 9.1 ± 0.9 years with the major sink being oxidation by the hydroxyl radical (Prather et al., 2012). Significant reductions in anthropogenic methane emissions are a major goal for countries signing the Paris Agreement in 2015, which would result in short-term benefits due to the relatively shorter lifetime of methane compared to CO₂.

In Canada, the national inventory reports total anthropogenic methane emissions to be 4.1 Tg year⁻¹ from the years 2010–2015, of which 2.00 Tg year⁻¹ is from the energy sector, 1.2 Tg year⁻¹ is from the agriculture sector, and 0.92 Tg year⁻¹ is from waste (Environment and Climate Change Canada, 2017). A recent top-down inverse modelling study constraining Canadian emissions using ECCO surface and GOSAT satellite observations reported 2010–2015 anthropogenic emissions to be 6.0–6.5 Tg a⁻¹, with most of the difference attributed to the energy and/or agricultural sector in Western Canada (Baray et al., 2021). Numerous other studies have shown higher methane emissions from Western Canadian oil and gas sources, constrained using observations from aircraft (Baray et al., 2018; Johnson et al., 2017), surface (Baray et al., 2021b; Chan et al., 2020; Atherton et al., 2018) and satellite (Lu et al., 2020; Maasackers et al., 2020; Turner et al., 2015). Conversely, Baray et al. (2021) showed that emissions in Ontario, where the sources are primarily from urban waste, may be lower than the inventory, with denser urban observations necessary to validate this result.

Urban centres account for 37–49% of global greenhouse gas emissions (Seto et al., 2014). Fugitive methane emissions from natural gas distribution pipelines and residential use are a major source of methane in urban areas, especially where the infrastructure is older. Studies have

demonstrated the presence of fugitive methane emissions in Boston (McKain et al., 2015), Washington DC (Jackson et al., 2014), Indianapolis (von Fischer et al., 2017), Los Angeles (Wunch et al., 2016), Toronto (Ars et al., 2020) and other cities (Plant et al., 2019). In this study, mobile vehicle measurements were deployed to measure different urban methane sources in the Greater Toronto Area (GTA). We use a Picarro cavity ring-down spectrometer to measure CH₄, CO₂, CO and H₂O and survey on-road combustion sources from stationary positions in October 2014, which are used to calculate fuel-based emissions factors and compare to the database in the National Inventory (Table 5.1). We deploy mobile measurements to survey natural gas infrastructure in May 2017 and map the geospatial distribution of methane concentrations and compare our results for Toronto to similar studies across North American cities.

Table 5.1: Fuel-based emissions factors for mobile combustion sources in Canada (Environment and Climate Change Canada, 2017)

Vehicle Class and Year	Emissions Factor (Gasoline) g CH₄ L⁻¹ fuel	Emissions Factor (Diesel) g CH₄ L⁻¹ fuel
Light Duty Vehicles		
2004-2012	0.14	0.051
1994-2003	0.23	0.051
Light Duty Trucks		
2004-2012	0.14	0.068
1994-2003	0.24	0.068
Heavy Duty Trucks		
2004-2012	0.068	0.11
1994-2003	0.29	0.14
Motorcycles		
1996-Present	0.77	-
1960-1995	2.3	-
Off Road	2.7	0.15

5.2 Data and Methods

5.2.1 Description of Measurements

Measurements of CH₄, CO₂, CO and H₂O were made using a Picarro G2401-m cavity ring-down spectrometer (CRDS) at an interpolated rate of ~0.5Hz. The instrument was securely mounted inside of a civilian van and operated using two different power sources in the two mentioned field studies: a) in the 2014 study a gas generator for stationary measurements on-road that was placed ~10 metres downwind of the Picarro position, and b) in the 2017 study using auxiliary batteries (Goal Zero Yeti + marine battery) for mobile measurements with a capacity of ~6 hours. The inlet was a reverse facing sample port with a 47 mm teflon filter that was regularly changed. The precision of the instrument is 2–3 ppb and the instrument was calibrated using standard reference gases. A GPS was used to measure position (latitude, longitude) at a rate of 1 Hz that was used to construct the map of CH₄ measurements.

For the 2014 field study, Table 5.1 lists the locations of stationary on-road measurements. For the 2017 study the full spatial map of mobile measurements is shown in the later section. In 2014, the measurement locations were chosen such that the forecasted wind direction would project the highway emissions towards the site. Measurements were mostly focused on the Highway 401 east-west artery highway, which had a total of 17 lanes of east-west and west-east traffic and a vehicle count of approximately ~400 per minute. The secondary location was Highway 400 which is a north-south artery highway with 8 lanes of traffic. For a measure of slowly moving or idling vehicle conditions, the parking garage at York University was selected. For measurements of public transportation diesel vehicles, the bus loop at York University was selected which contains a relatively dense number (~10) of transit vehicles idling and exchanging commuters. These sites allowed for the determination of emissions factors from (a) a typical fleet of highway vehicles, (b) individual public transportation diesel vehicles, and (c) individual gasoline vehicles.

For the 2017 single day study, mobile measurements were used to survey the natural gas infrastructure across York Region (suburban) and the Toronto core (urban) roads. Approximately 6 hours of measurements were taken and ~90 km of road was driven, which included multiple

passes through the downtown core at major east-west roads, as well as a special survey of a super emitter at the junction of Highway DVP and Lakeshore Road near a wastewater facility on Lake Ontario.

Table 5.2: List of on-road measurement locations for the October 2014 field study

Day	Lat, Lon (°)	Location Description	Target Vehicles
Oct 16	43.726, -79.466	Hwy 401 near Allen Road, South Side	Sample of Hwy Fleet (Gasoline and Diesel)
Oct 21	43.726, -79.466	Hwy 401 near Allen Road, South Side	Sample of Hwy Fleet (Gasoline and Diesel)
Oct 22	43.726, -79.466	Hwy 401 near Allen Road, South Side	Sample of Hwy Fleet (Gasoline and Diesel)
Oct 23	43.780, -79.537	Hwy 400 near Hwy 7, between traffic	Sample of Hwy Fleet (Gasoline and Diesel)
Oct 24	43.726, -79.466	Hwy 401 near Allen Road, South Side	Sample of Hwy Fleet (Gasoline and Diesel)
Oct 27	43.771, -79.338	Hwy 404 and Hwy 401, Northeast corner	Sample of Hwy Fleet (Gasoline and Diesel)
Oct 28	43.774, -79.501	York University Public Transit Bus Loop	Public Transit Vehicles (Diesel)
Oct 29	43.773, -79.507	York University Parking Garages	Personal Commuter Vehicles (Gasoline)

5.2.2 Determination of Vehicle Emissions Factors

Fuel-based emissions factors were calculated using atmospheric measurements of CH₄, CO₂ and CO according to equation {5.1}

$$EF = W_c \cdot \frac{M_{CH_4}}{M_C} \cdot \left(\frac{|CH_4|}{|CO_2| + |CO|} \right) \quad \{5.1\}$$

Where EF is the fuel-based emissions factor (in kg of CH₄ / kg of fuel), W_c is the weight content of carbon (estimated at 0.87 kg of carbon per kg of fuel) and M_{CH₄}/M_C are the relative molecular weights of methane and carbon. This calculation assumes that >99% of the carbon content in the fuel is converted into CO₂ and CO (Singer and Harley, 1996). By using the background-elevated concentrations of CH₄/(CO₂ + CO) enhanced by the highway fleet vehicle emissions, an average emissions factor could be calculated. Additionally, emissions factors for individual tailpipe emissions could be calculated from separate experiments. While the highway locations were heavily populated sites, highly-correlated spikes of CO₂, CO and CH₄ could be treated as individual vehicle emissions to build a database of measured emissions factors. To differentiate between background levels and emissions from the target vehicles, the derivatives ΔCH₄/ΔCO₂ and ΔCO/ΔCO₂ from a linear regression of CH₄ vs CO₂ and CO vs CO₂ measurements could be attained to determine background-enhanced concentrations and emissions factors.

5.3 Results and Discussion

5.3.1 Measurements of On-Road Vehicle Methane

Figure 5.1 shows three example time series highway measurements from the study in 2014 on Oct 21, Oct 23 and Oct 29. Two features of the time-series were observed at each of the study locations. These features were 1) a high variability in CO₂ around a median value and 2) usually correlated, intermittent spikes of CH₄ and CO. For example, in Figure 5.1A, the median value of CO₂ was ~470 ppm. The 1σ variance of CO₂ in this timeseries was ± 25 ppm. Since the instrument detection limit is <0.2 ppm for 0.5 Hz measurements of CO₂, this variance is due to

real atmospheric conditions and not to instrument noise. The variance in CO_2 is attributed to the very large volume of vehicles consistently emitting CO_2 while causing physical turbulence in the air. The intermittent spikes in CO and CH_4 are attributed to occasional vehicles measured with either poor emissions controls or possibly unique combustion mechanics (such as natural gas combustion in the case of spikes of CH_4 in the absence of CO). These spikes sometimes showed a correlation between CO and CH_4 but not in every case. For example in Figure 5.1A, just before 5:00 pm the largest spike in CO was observed up to 11 ppm which was correlated with the largest spike in CH_4 up to 2.02 ppm. Immediately after, another enhancement of CH_4 was observed up to 1.96 ppm that did not show the same high correlation with CO. These observations of CO, CO_2 and CH_4 show that the majority of highway vehicles in typical conditions are low emitters of CO and CH_4 with some exceptions. A rough estimate of the vehicle count showed ~400 per minute which is ~48,000 over the two-hour time series. Over this same time, there are approximately ~20 spikes of CH_4 . Hence, our results show that about 1 in 2400 vehicles are unusual emitters of CH_4 or CO. Figure 5.1B shows an alternate highway location in between northbound and southbound lanes with higher traffic congestion. On this day less variance in CO_2 is observed due to the congested flow of vehicles, however intermittent spikes in CO and CH_4 continued to be observed. Figure 5.1C shows an indoor parking garage location at York University. This location had the lowest volume of traffic, as shown by the lowest variance in CO_2 , while maintaining the pattern of periodic CO and CH_4 spikes. At 9:15, a vehicle that initiated a cold start idled near the inlet which caused the highest CO and CH_4 enhancements on this day.

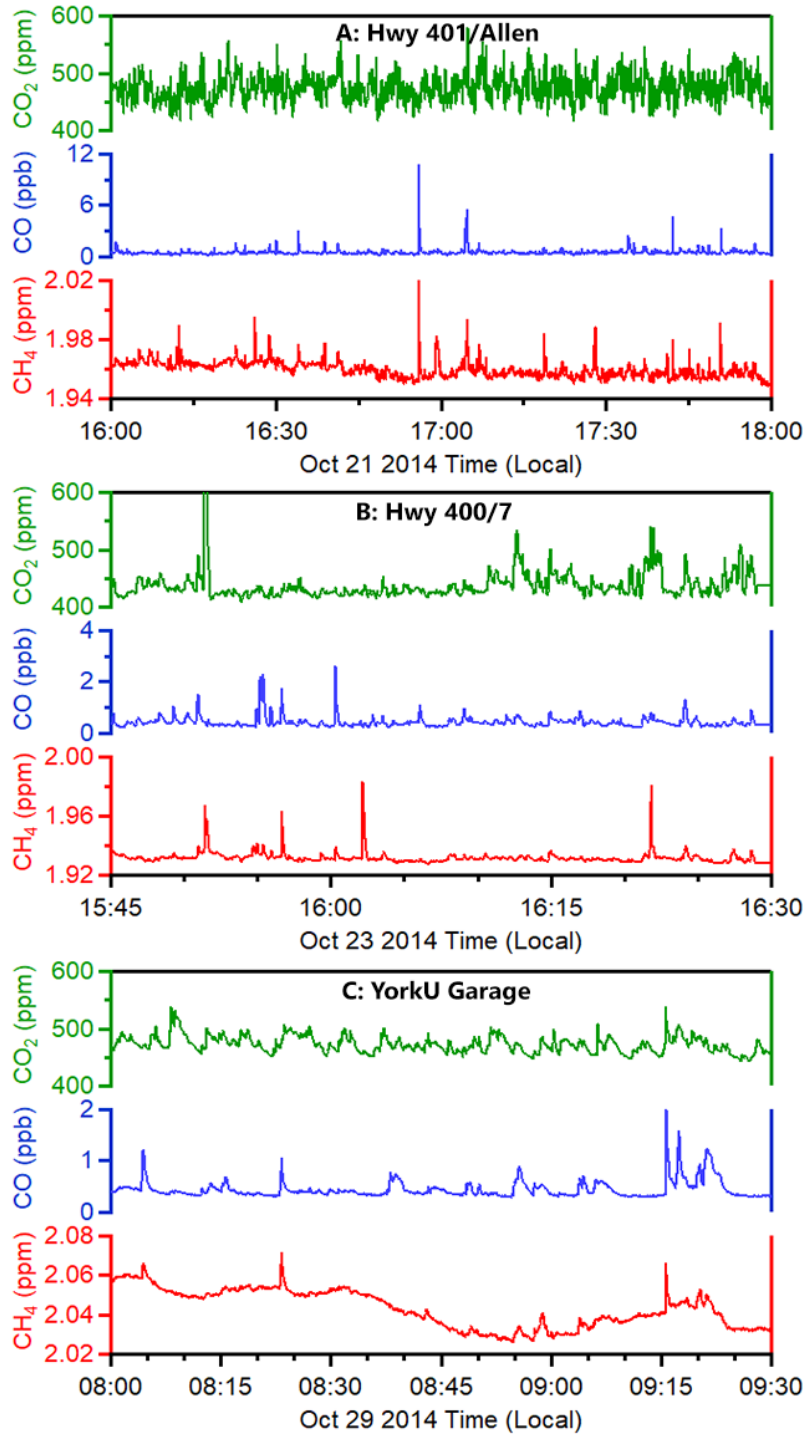


Figure 5.1: Time series plots of CH₄ (red), CO₂ (green) and CO (blue) measurements from three locations in the 2014 study: Highway 401/Allen road on Oct 21 (panel A), Highway 400/7 on Oct 23 (panel B), and the YorkU commuter parking garage on Oct 29 (panel C).

The ratio of CH₄ to CO₂ enhancements can be used to calculate an emissions factor for this typical highway fleet of vehicles. Figure 5.2 shows a correlation plot of CH₄ vs. CO₂ with a linear regression for the time series shown in Figure 5.1A. The slope of the linear regression corresponds to the ratio of $\Delta\text{CH}_4/\Delta\text{CO}_2$, which is $(7.80 \pm 0.4) \times 10^{-5}$. Using eq. {5.1} and simplifying $|\text{CO}_2| + |\text{CO}| \approx |\text{CO}_2|$, this corresponds to an emissions factor of 0.063 ± 0.003 g CH₄ per L of fuel. This result is 48% lower than the 0.12 ± 0.03 g CH₄ L⁻¹ fuel emissions factor recommended by model predictions from Nam et al. (2004). Our results are also 55% lower than the emissions factor for personal vehicles in the National Inventory, which is 0.14 g CH₄ L⁻¹ fuel (Environment and Climate Change Canada, 2014). A possible explanation for these lower values can be due to the presence of diesel trucks on residential highways. Diesel trucks consume significantly more fuel than the average passenger vehicle and have emissions factors as low as 0.068 g CH₄ / L. Furthermore, the inventory emissions factors are based on vehicle models manufactured up until 2012, and do not include newer model vehicles with more efficient emissions control technology. One final reason for the potential discrepancy is that EF's are typically measured with vehicles on dynamometers which includes a variety of conditions, including a "cold" start (during which emissions are higher, as shown in Figure 5.1C), whereas the driving conditions observed on the highway during these measurements was steady speed with vehicles that were obviously "warm".

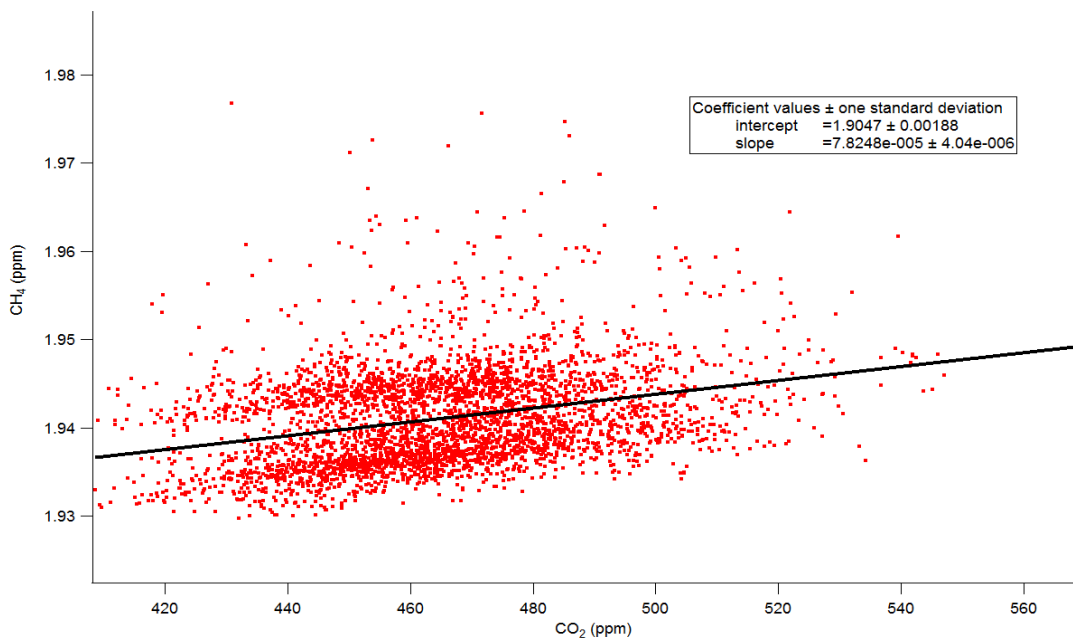


Figure 5.2: Correlation plot of CH₄ vs CO₂ for Oct 21 2014 measurements shown in Figure 5.1A

Figure 5.3 shows an example of tailpipe emissions from a cold start vehicle. This vehicle-initiated operation with an exhaust plume going into the inlet allows for a cold start emissions factor to be calculated. The cold start conditions produced large measurements of CO, up to 23 ppm, CH₄, up to 2.25 ppm, and CO₂ up to 630 ppm. The emissions factor was calculated at 0.85 g CH₄ L⁻¹ fuel, which is a factor of 13.5 times higher than the previously measured highway fleet average, and a factor of 6.1 times higher than the emissions factor for gasoline combustion in the National Inventory. This result suggests that inefficient vehicle combustion can vary significantly more in methane emissions than the average of a typical vehicle, which is consistent with the periodic spikes that were observed in the highway time series. Table 5.3 shows results from experiments where different types of individual vehicle tailpipe emissions were sampled. The emissions factors for gasoline vehicles vary from 0.22 – 0.94 g CH₄ L⁻¹ fuel, with cold start vehicles generally producing the highest methane emissions factors. The lowest emissions factor of 0.057 g CH₄ L⁻¹ was measured from an idling tow truck, which was powered by diesel fuel combustion resulting in a lower emissions factor. These results show that on-road vehicle emissions factors are highly variable between different types of fuel combustion and operation

conditions. This poses a challenge for bottom-up engineering budgets to produce typical emissions factors, which can be constrained with atmospheric measurements. In general, these real-world emissions factors confirm that CH₄ emissions from mobile combustion are low, and possibly lower than published bottom-up dynamometer tests. This shows that on-road transportation is a very minor source of CH₄ in Canada, accounting for less than 1% of the national budget.

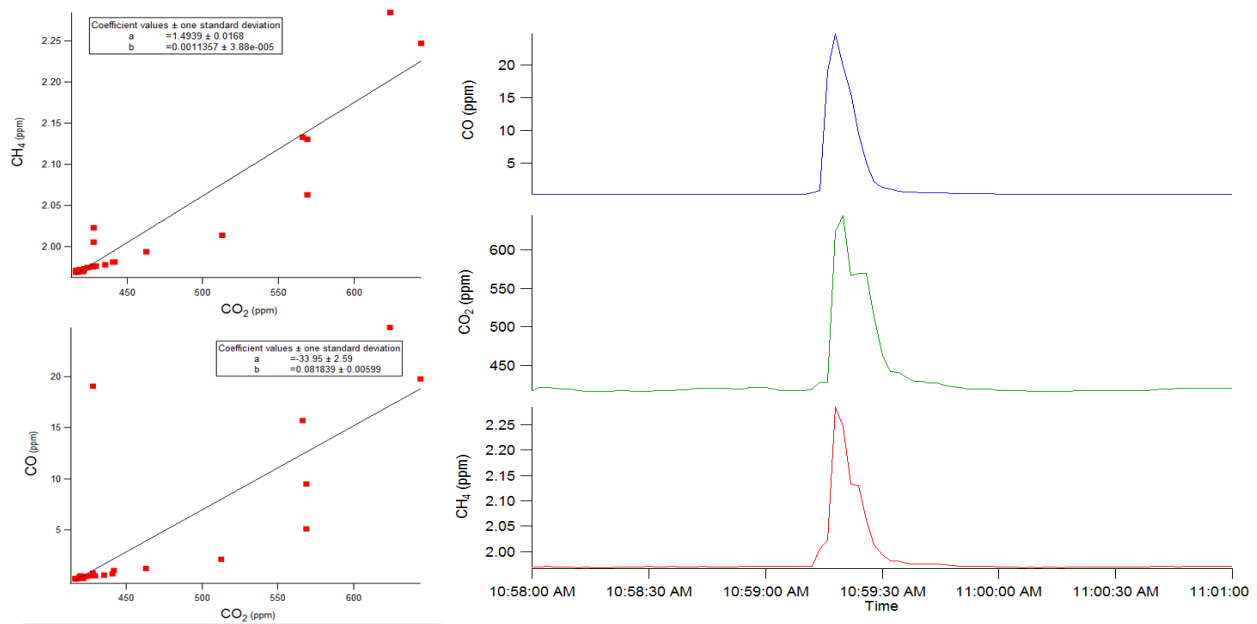


Figure 5.3: Tailpipe emissions from a cold start vehicle observed on Oct 27. Time series of CO, CO₂ and CH₄ for the small 1-minute period of enhancement (right). Correlation plots of CH₄ vs. CO₂ (top left) and CO vs. CO₂ (bottom left).

Table 5.3: Tailpipe emissions factors from individual vehicle experiments

Measured Vehicle	Emissions Factor (g CH₄ / L of fuel)	National Inventory Report^a (g CH₄ / L of fuel)
Cold Start: Light-Duty Gasoline Vehicle	0.85	0.14
Cold Start: Light-Duty Gasoline Truck	0.83	0.14
Idling: Diesel Tow Truck	0.057	0.068 – 0.11
Driving: Light-Duty Gasoline Truck	0.34	0.14
Idling: 2004 Impala (LDGV)	0.33	0.14
Idling: 2014 Caravan (LDGT)	0.038	<0.14
Driving: Light-Duty Gasoline Vehicle	0.22	0.14
Driving: Light-Duty Gasoline Truck	0.94	0.14
Operating: Gasoline Generator	1.72	2.7

^a Environment and Climate Change Canada National Inventory Report (2014)

5.3.2 Mobile Survey of GTA Methane

Methane was measured using a mobile vehicle setup in May of 2017 to survey the Greater Toronto Area for methane leaks, normally caused by ageing natural gas infrastructure. Figure 5.4 shows the Google Earth map of measurements with methane concentrations shown in color, and Figure 5.5 shows the time series for the same measurements. The vehicle route began in York Region (suburban north GTA) around Yonge Street and Major Mackenzie, with measurements continuing down Yonge Street to Lake Ontario (downtown urban Toronto). This was followed by six east–west and west–east cross-transects at the major downtown Toronto roads, where infrastructure was expected to be the oldest. The driving route was completed by driving northbound and returning to the York University campus (northwest GTA). The results show that a much lower number of methane leaks are observable in Toronto when compared to similar studies in other cities in the United States. Table 5.4 summarizes the comparison of methane leaks from this study to other studies led by the Environmental Defense Fund (von Fischer et al., 2017). We defined a leak consistent with the EDF methodology as >10% of the background, where the background is defined as a 2-minute moving average of the measurements. On this

day, the background average was 1.96 ± 0.01 ppm with a small decrease over the course of the day, hence an increase in methane up to 2.156 ppm (+196 ppb) qualifies as a methane leak according to this definition. In this one day of measurements, we observed this threshold four times over the entire study, therefore we measured approximately 1 leak per 23 kilometers of road driven, or 4–5 leaks when normalized to 100 km of road driven. Ars et al. (2021) reported a leak rate of 4–22 leaks per 100 km of road driven in the GTA using 77 mobile surveys from May 2018 to August 2019, which is consistent with our single survey. This leak rate in the GTA is at the lower end of the range of leaks observed in other cities, compared to 1 leak per 0.4 km in Washington, DC (Jackson et al., 2014), and 1 leak per 320 km in Indianapolis, IN (Environmental Defense Fund, 2015). Additionally, our measurements show a “hotspot” at the intersection of the DVP and Lake Shore (southeast of the map, on Lake Ontario), which is a hotspot also confirmed by Ars et al. (2020), where measurements as high as 6 ppm of CH₄ were observed. This data was not included in the leak calculation as it was a significant methane source that was clearly distinct. This hotspot was also observed in the GTA-wide study by Ars et al. (2020) which they attributed to a wastewater facility.

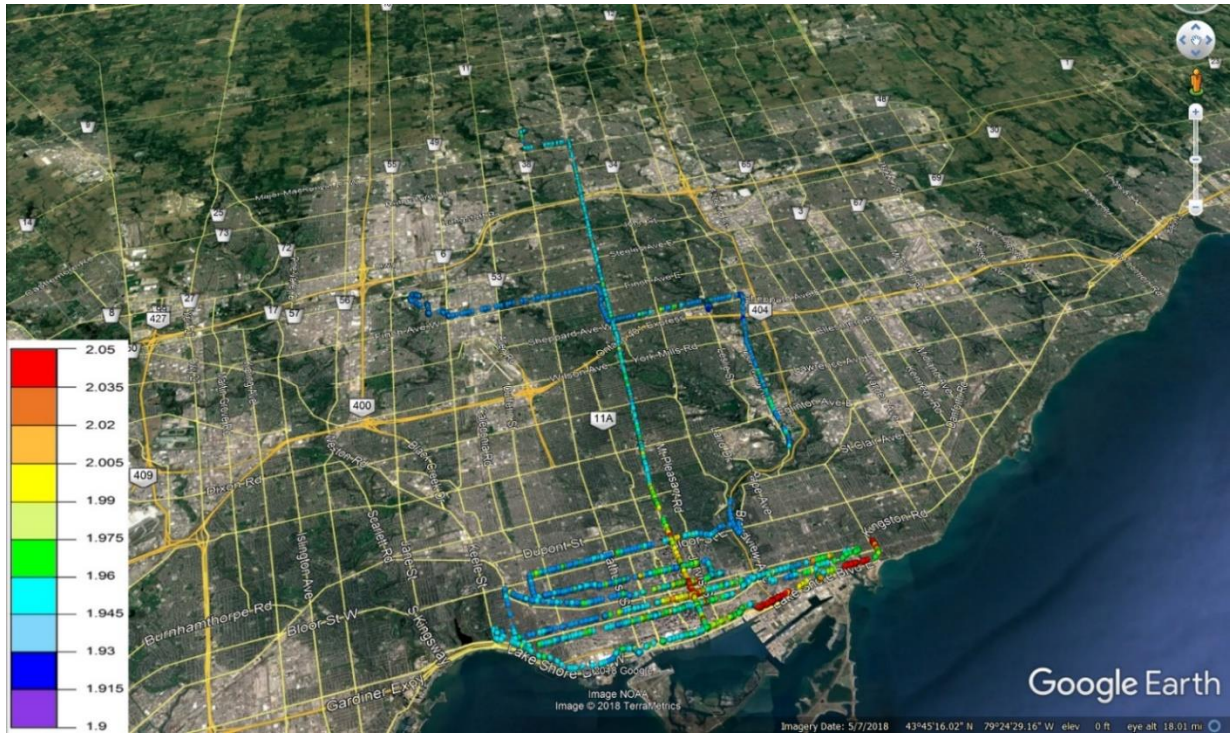


Figure 5.4: Mobile survey of GTA methane leaks conducted on May 18 2017. Approximately 90 kilometers of road was driven between 10:30 am to 4:30 pm local time (EDT)

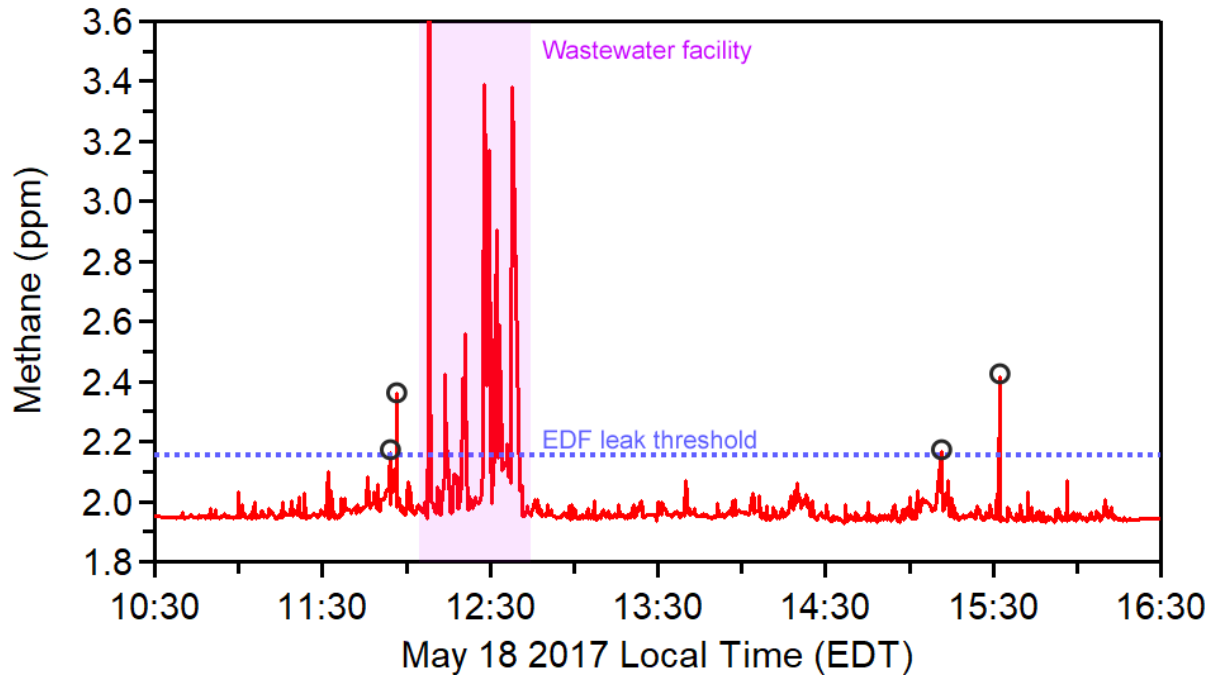


Figure 5.5: Timeseries of methane measurements May 18 2017 from 10:30 am to 4:30 pm local time (EDT) corresponding to Figure 5.4. The EDF leak threshold (blue line) is defined as 10% higher than the background, and the black circles show the four measured leaks above this requirement. Measurements of the wastewater facility are highlighted in purple and not included in the leak calculations.

Table 5.4: Comparison of natural gas leaks as a function of road driven in different North American urban centers

City	Leaks per Kilometer	Reference (Months of Measurements)
Boston, MA	1 per 1.6 km	EDF, 2013 (Mar–Jun)
Boston, MA	1 per 0.37 km	Philips et al. 2013 (Aug–Oct 2011)
Burlington, VT	1 per 16 km	EDF, 2014 (Oct)
Chicago, IL	1 per 4.8 km	EDF, 2014 (Sep–Dec)
Dallas, TX	1 per 3.2 km	EDF, 2015 (Jan–Feb)
Indianapolis, IN	1 per 320 km	EDF, 2013 (Jun)
Jacksonville, FL	1 per 15 km	EDF, 2015 (Feb–Jun)
Los Angeles, CA	1 per 6–10 km	EDF, 2015 (Aug–May)
Mesa, AZ	1 per 97 km	EDF, 2016 (Mar–Apr)
Pittsburgh, PA	1 per 3.2 km	EDF, 2015 (Jun–Nov)
Staten Island, NY	1 per 1.6 km	EDF, 2014 (Jan–Apr)
Syracuse NY	1 per 3.2 km	EDF, 2014 (Apr–Aug)
Washington, DC	1 per 0.4 km	Jackson et al., 2014 (Jan–Feb 2013)
Toronto, ON	1 per 23 km	This Study (May 2017)

5.4 Conclusions

This study demonstrates a methodology to study methane in an urban setting using vehicle-based cavity-ring down spectroscopy measurements. In October of 2014 stationary vehicle measurements were used at highway roads to determine fuel-based emissions factors for combustion sources. The results showed that most vehicles are average emitters of CH₄ and CO, with the average fleet emissions factor determined to be 0.063 ± 0.003 g CH₄ per L of fuel. This value is 55% lower than the emissions factor for personal vehicles in the National Inventory, which we attribute as likely being due to two factors: the presence of diesel vehicles on the highway that combust fuel at a higher temperature and pressure, resulting in more efficient conversion to CO₂, and with lower CH₄ emissions, and due to the warm steady driving conditions of gasoline vehicles on the highway that do not have a cold start component to their emissions. Separately in cases where individual vehicles could be isolated in a garage, in a bus loop or roadside, we show examples of individual vehicles with emissions factors much higher

than the highway average, up to 0.94 g CH₄ per L of fuel, often due to inefficient cold start conditions. These results show that some transportation vehicles are still unusually large emitters, which is expected to be reduced with time due to improved emissions controls for newer model vehicles.

In May of 2017, mobile vehicle measurements were used across major roads in the GTA to quantify the presence of methane leaks from natural gas. Measurements were taken in both suburban (York Region) and downtown (Toronto core) locations, with the average of the 1-day study showing 1 leak per 23 km of road driven. When compared to other studies in North America using the same metric, Toronto is on the lower range of methane leaks, which we attribute to the newer and better maintained infrastructure in the city. We also show measurements of a high methane emitting wastewater facility on Lake Ontario, where we measured methane up to 6 ppm. Our results from a single survey of leaks in 2017 for the GTA is consistent with the range reported by Ars et al. (2020) for 77 surveys conducted between 2018 to 2019 in the same city. These results show that while some cities may have better infrastructure overall with less natural gas pipeline leakage, the presence of super-emitters from landfills or waste facilities may account for a significant fraction of the city's methane budget. As shown in other studies, these super-emitters can be measured using surface, aircraft and satellite observations, and the mobile vehicle measurements we show can be the most cost-effective method for an initial survey.

References

- Ars, S., Vogel, F., Arrowsmith, C., Heerah, S., Knuckey, E., Lavoie, J., Lee, C., Pak, N. M., Phillips, J. L., and Wunch, D.: Investigation of the Spatial Distribution of Methane Sources in the Greater Toronto Area Using Mobile Gas Monitoring Systems, *Environ. Sci. Technol.*, acs.est.0c05386, <https://doi.org/10.1021/acs.est.0c05386>, 2020.
- Atherton, E., Risk, D., Fougère, C., Lavoie, M., Marshall, A., Werring, J., Williams, J. P., and Minions, C.: Mobile measurement of methane emissions from natural gas developments in northeastern British Columbia, Canada, *Atmos. Chem. Phys.*, 17, 12405–12420, <https://doi.org/10.5194/acp-17-12405-2017>, 2017.
- Baray, S., Darlington, A., Gordon, M., Hayden, K. L., Leithead, A., Li, S.-M., Liu, P. S. K., Mittermeier, R. L., Moussa, S. G., O’brien, J., Staebler, R., Wolde, M., Worthy, D., and McLaren, R.: Quantification of methane sources in the Athabasca Oil Sands Region of Alberta by aircraft mass balance, *Atmos. Chem. Phys.*, 18, 7361–7378, <https://doi.org/10.5194/acp-18-7361-2018>, 2018.
- Baray, S., Jacob, D. J., Massakkars, J. D., Sheng, J.-X., Sulprizio, M. P., Jones, D. B. A., Bloom, A. A., and McLaren, R.: Estimating 2010–2015 Anthropogenic and Natural Methane Emissions in Canada using ECCO Surface and GOSAT Satellite Observations, *Gases/Atmospheric Modelling/Troposphere/Physics (physical properties and processes)*, <https://doi.org/10.5194/acp-2020-1195>, 2021.
- Cambaliza, M. O. L., Shepson, P. B., Bogner, J., Caulton, D. R., Stirm, B., Sweeney, C., Montzka, S. A., Gurney, K. R., Spokas, K., Salmon, O. E., Lavoie, T. N., Hendricks, A., Mays, K., Turnbull, J., Miller, B. R., Lauvaux, T., Davis, K., Karion, A., Moser, B., Miller, C., Obermeyer, C., Whetstone, J., Prasad, K., Miles, N., and Richardson, S.: Quantification and source apportionment of the methane emission flux from the city of Indianapolis, *Elem. Sci. Anth.*, 3, 000037, <https://doi.org/10.12952/journal.elementa.000037>, 2015.
- Chan, E., Worthy, D. E. J., Chan, D., Ishizawa, M., Moran, M. D., Delcloo, A., and Vogel, F.: Eight-Year Estimates of Methane Emissions from Oil and Gas Operations in Western Canada Are Nearly Twice Those Reported in Inventories, *Environ. Sci. Technol.*, 54, 14899–14909, <https://doi.org/10.1021/acs.est.0c04117>, 2020.
- von Fischer, J. C., Cooley, D., Chamberlain, S., Gaylord, A., Griebenow, C. J., Hamburg, S. P., Salo, J., Schumacher, R., Theobald, D., and Ham, J.: Rapid, Vehicle-Based Identification of Location and Magnitude of Urban Natural Gas Pipeline Leaks, *Environ. Sci. Technol.*, 51, 4091–4099, <https://doi.org/10.1021/acs.est.6b06095>, 2017.
- Jackson, R. B., Down, A., Phillips, N. G., Ackley, R. C., Cook, C. W., Plata, D. L., and Zhao, K.: Natural Gas Pipeline Leaks Across Washington, DC, *Environ. Sci. Technol.*, 48, 2051–2058, <https://doi.org/10.1021/es404474x>, 2014.
- Johnson, M. R., Tyner, D. R., Conley, S., Schwietzke, S., and Zavala-Araiza, D.: Comparisons of Airborne Measurements and Inventory Estimates of Methane Emissions in the Alberta Upstream Oil and Gas Sector, *Environ. Sci. Technol.*, 51, 13008–13017, <https://doi.org/10.1021/acs.est.7b03525>, 2017.
- Kirschke, S., Bousquet, P., Ciais, P., Saunois, M., Canadell, J. G., Dlugokencky, E. J., Bergamaschi, P., Bergmann, D., Blake, D. R., Bruhwiler, L., Cameron-Smith, P., Castaldi, S., Chevallier, F., Feng, L., Fraser, A., Heimann, M., Hodson, E. L., Houweling, S., Josse, B., Fraser, P. J., Krummel, P. B., Lamarque, J.-F., Langenfelds, R. L., Le Quééré, C., Naik, V., O’Doherty, S., Palmer, P. I., Pison, I., Plummer, D., Poulter, B., Prinn, R. G., Rigby, M., Ringeval, B., Santini, M., Schmidt, M., Shindell, D. T.,

- Simpson, I. J., Spahni, R., Steele, L. P., Strode, S. A., Sudo, K., Szopa, S., van der Werf, G. R., Voulgarakis, A., van Weele, M., Weiss, R. F., Williams, J. E., and Zeng, G.: Three decades of global methane sources and sinks, *Nature Geosci*, 6, 813–823, <https://doi.org/10.1038/ngeo1955>, 2013.
- Lu, X., Jacob, D. J., Zhang, Y., Maasackers, J. D., Sulprizio, M. P., Shen, L., Qu, Z., Scarpelli, T. R., Nesser, H., Yantosca, R. M., Sheng, J., Andrews, A., Parker, R. J., Boech, H., Bloom, A. A., and Ma, S.: Global methane budget and trend, 2010–2017: complementarity of inverse analyses using in situ (GLOBALVIEWplus CH₄; ObsPack) and satellite (GOSAT) observations, *Gases/Atmospheric Modelling/Troposphere/Physics* (physical properties and processes), <https://doi.org/10.5194/acp-2020-775>, 2020.
- Maasackers, J. D., Jacob, D. J., Sulprizio, M. P., Scarpelli, T. R., Nesser, H., Sheng, J., Zhang, Y., Lu, X., Bloom, A. A., Bowman, K. W., Worden, J. R., and Parker, R. J.: 2010–2015 North American methane emissions, sectoral contributions, and trends: a high-resolution inversion of GOSAT satellite observations of atmospheric methane, *Gases/Remote Sensing/Troposphere/Chemistry* (chemical composition and reactions), <https://doi.org/10.5194/acp-2020-915>, 2020.
- Maazallahi, H., Fernandez, J. M., Menoud, M., Zavala-Araiza, D., Weller, Z. D., Schwietzke, S., von Fischer, J. C., Denier van der Gon, H., and Röckmann, T.: Methane mapping, emission quantification, and attribution in two European cities: Utrecht (NL) and Hamburg (DE), *Atmos. Chem. Phys.*, 20, 14717–14740, <https://doi.org/10.5194/acp-20-14717-2020>, 2020.
- McKain, K., Down, A., Raciti, S. M., Budney, J., Hutyra, L. R., Floerchinger, C., Herndon, S. C., Nehrkorn, T., Zahniser, M. S., Jackson, R. B., Phillips, N., and Wofsy, S. C.: Methane emissions from natural gas infrastructure and use in the urban region of Boston, Massachusetts, *Proc Natl Acad Sci USA*, 112, 1941–1946, <https://doi.org/10.1073/pnas.1416261112>, 2015.
- Pandey, S., Gautam, R., Houweling, S., van der Gon, H. D., Sadavarte, P., Borsdorff, T., Hasekamp, O., Landgraf, J., Tol, P., van Kempen, T., Hoogeveen, R., van Hees, R., Hamburg, S. P., Maasackers, J. D., and Aben, I.: Satellite observations reveal extreme methane leakage from a natural gas well blowout, *Proc Natl Acad Sci USA*, 116, 26376–26381, <https://doi.org/10.1073/pnas.1908712116>, 2019.
- Peischl, J., Ryerson, T. B., Brioude, J., Aikin, K. C., Andrews, A. E., Atlas, E., Blake, D., Daube, B. C., de Gouw, J. A., Dlugokencky, E., Frost, G. J., Gentner, D. R., Gilman, J. B., Goldstein, A. H., Harley, R. A., Holloway, J. S., Kofler, J., Kuster, W. C., Lang, P. M., Novelli, P. C., Santoni, G. W., Trainer, M., Wofsy, S. C., and Parrish, D. D.: Quantifying sources of methane using light alkanes in the Los Angeles basin, California: SOURCES OF METHANE IN L.A., *J. Geophys. Res. Atmos.*, 118, 4974–4990, <https://doi.org/10.1002/jgrd.50413>, 2013.
- Plant, G., Kort, E. A., Floerchinger, C., Gvakharia, A., Vimont, I., and Sweeney, C.: Large Fugitive Methane Emissions From Urban Centers Along the U.S. East Coast, *Geophys. Res. Lett.*, 46, 8500–8507, <https://doi.org/10.1029/2019GL082635>, 2019.
- Prather, M. J., Holmes, C. D., and Hsu, J.: Reactive greenhouse gas scenarios: Systematic exploration of uncertainties and the role of atmospheric chemistry: ATMOSPHERIC CHEMISTRY AND GREENHOUSE GASES, *Geophys. Res. Lett.*, 39, n/a-n/a, <https://doi.org/10.1029/2012GL051440>, 2012.
- Turner, A. J., Jacob, D. J., Wecht, K. J., Maasackers, J. D., Lundgren, E., Andrews, A. E., Biraud, S. C., Boesch, H., Bowman, K. W., Deutscher, N. M., Dubey, M. K., Griffith, D. W. T., Hase, F., Kuze, A., Notholt, J., Ohyama, H., Parker, R., Payne, V. H., Sussmann, R., Sweeney, C., Velasco, V. A., Warneke, T., Wennberg, P. O., and Wunch, D.: Estimating global and North American methane emissions with high spatial resolution using GOSAT satellite data, *Atmos. Chem. Phys.*, 15, 7049–7069, <https://doi.org/10.5194/acp-15-7049-2015>, 2015.

Vaughn, T. L., Bell, C. S., Pickering, C. K., Schwietzke, S., Heath, G. A., Pétron, G., Zimmerle, D. J., Schnell, R. C., and Nummedal, D.: Temporal variability largely explains top-down/bottom-up difference in methane emission estimates from a natural gas production region, *Proc Natl Acad Sci USA*, 115, 11712–11717, <https://doi.org/10.1073/pnas.1805687115>, 2018.

Weller, Z. D., Yang, D. K., and von Fischer, J. C.: An open source algorithm to detect natural gas leaks from mobile methane survey data, *PLoS ONE*, 14, e0212287, <https://doi.org/10.1371/journal.pone.0212287>, 2019.

Wunch, D., Toon, G. C., Hedelius, J. K., Vizenor, N., Roehl, C. M., Saad, K. M., Blavier, J.-F. L., Blake, D. R., and Wennberg, P. O.: Quantifying the loss of processed natural gas within California’s South Coast Air Basin using long-term measurements of ethane and methane, *Atmos. Chem. Phys.*, 16, 14091–14105, <https://doi.org/10.5194/acp-16-14091-2016>, 2016.

Chapter 6 Conclusions

The research objective of this dissertation was to use atmospheric measurements to better understand CH₄ emissions in Canada. The studies shown include the use of surface, aircraft and satellite observations in combination with a variety of experimental and modelling techniques. The results provide key insights into the magnitudes and patterns of anthropogenic and natural CH₄ sources in Canada. In addition, the studies evaluate the limitations of the various approaches and measurement platforms and provide guidance on future improvements.

Aircraft measurements in the AOSR during an intensive campaign in the summer of 2013 showed that the major sources of CH₄ in the region were fugitive in nature, due to tailings ponds and open-pit mining, with some emissions from facility plant sites. It was demonstrated that an array of instrumentation simultaneously measuring many chemical species could be used to trace the sources of CH₄ plumes to one of the three major categories. For tailings ponds, concurrent BTEX plumes were reliable indicators for emissions from MLSB and Pond 2/3. NO_y and rBC were used to identify CH₄ plumes from open pit mining due to the concentrated presence of heavy hauler diesel trucks. SO₂ and NO_y plumes at higher altitudes were used to track facility plumes from upgrader stacks, which were shown to contain high methane from the CNRL facility. These chemical fingerprints were combined with a screen-based mass balance approach to quantify horizontal advective fluxes from CH₄ plumes. The results of 7 aircraft flights determined total emissions rates of $8.8 \pm 0.9 \text{ t hr}^{-1}$ from tailings ponds (45% of the AOSR total), $9.8 \pm 0.9 \text{ t hr}^{-1}$ from open pit mining (50%), and $1.0 \pm 0.3 \text{ t hr}^{-1}$ from facility plant sites (5%). These results were consistent with the results from a box-based mass balance approach, which was a more exhaustive quantification of horizontal and vertical fluxes within the flight path surrounding a facility. In total, the AOSR emissions from aircraft mass balance was determined to be $19.6 \pm 1.1 \text{ t CH}_4 \text{ hr}^{-1}$ or $0.17 \pm 0.1 \text{ Tg CH}_4 \text{ yr}^{-1}$ when scaled up assuming seasonally constant emissions. These results are 48% higher than the GHGRP, which shows a discrepancy between bottom-up inventories and top-down emissions.

Cold-season CH₄ measurements using surface in-situ measurements in a mobile vehicle were deployed in the Fall/Winter of 2014 and the Winter/Spring of 2017 to address the limited

temporal coverage of aircraft measurements and provide insight into the seasonal behavior of fugitive emissions. Aircraft campaigns are highly resource intensive field studies, and simpler-to-deploy vehicle measurements provided additional sampling of seasonal variation. The measurements showed consistently high CH₄ plumes in both 2014 and 2017 from tailings ponds MLSB and Pond 2/3 exceeding 3 ppm. Similarly, CH₄ plumes downwind of open-pit mining were observed in both 2014 and 2017 between 2–3 ppm. Occasional, geographically narrow CH₄ measurements of 23 ppm in 2014 and 87 ppm in 2017 showed the presence of leaking or venting activity that was not previously captured by aircraft measurements. Due to the infrequency of these high CH₄ measurements, it was inferred for the 2014 and 2017 dataset that they were not comparable in magnitude to tailings pond and open-pit mining emissions. However, the confirmed existence of high leaking or venting events poses a challenge for top-down measurements since super-emitter events could be missed by the temporal gap in field studies. Transects downwind of sources perpendicular to plume transport direction were conducted for mass-balance quantification, and these transects were filtered for optimal conditions such that surface measurements were sufficiently representative of the PBL. This MSMB approach was able to quantify SUN open-pit mining emissions to be $1.0 \pm 0.4 \text{ t hr}^{-1}$, which shows an overlap with the uncertainty intervals with aircraft mass-balance quantification of the same source in the summer of 2013. These results suggest that tailings ponds and open pit mining emissions persist in the cold season; any seasonal dependence on emissions magnitudes, which is likely to exist, is within the uncertainties of mass balance methods. Constraining these fugitive emissions sources with higher precision using similar mass balance methods requires larger sample sizes for the reduction of uncertainties.

Anthropogenic and natural CH₄ emissions at the national scale across Canada were estimated for 2010–2015 using a surface in-situ network from ECCC and satellite observations from GOSAT in a Bayesian inverse modelling approach. The forward model GEOS-Chem was equipped with state-of-the-science emissions inventories for the oil and gas sector in Western Canada and for an ensemble of wetlands emissions scenarios and process-models from the WetCHARTS inventory. The mean 2010–2015 emissions for anthropogenic and natural emissions in the prior was 4.4 Tg a^{-1} and 14.8 Tg a^{-1} , respectively. An ensemble forward model

analysis was conducted which included 6 key WetCHARTS scenarios. The comparison to in-situ observations showed large positive biases in the summer (+1050 ppb), indicating an overestimation of emissions, at in-situ stations sensitive to Boreal Canada wetlands emissions, and year-round negative biases (−100 ppb), indicating an underestimation of emissions, at in-situ stations in sensitive to energy and agriculture emissions in Western Canada. Three inversions were performed, which defined different state vectors of emissions to be optimized: (1) an inversion which optimized monthly natural emissions and anthropogenic emissions on a yearly basis, (2) an inversion which optimized emissions according to sectoral categories in the National Inventory, and (3) an inversion which optimized anthropogenic and natural emissions on the provincial scale. The three inversion results were consistent in showing higher anthropogenic emissions and lower natural emissions in the posterior and were consistent when optimizing emissions separately with in-situ and satellite data. From the monthly inversion, mean 2010–2015 posterior emissions using ECCC surface data are $6.0 \pm 0.4 \text{ Tg a}^{-1}$ for total anthropogenic and $11.6 \pm 1.2 \text{ Tg a}^{-1}$ for total natural emissions, in agreement with the posterior using GOSAT data of $6.5 \pm 0.7 \text{ Tg a}^{-1}$ for total anthropogenic and $11.7 \pm 1.2 \text{ Tg a}^{-1}$ for total natural emissions. The seasonal pattern of natural emissions in the posterior showed slower-to-begin emissions in the spring and a less intense peak for summertime emissions, which indicate temperature and inundation dependencies that need to be better understood in process models. Emissions from the Energy + Agriculture sector in the posterior were $5.1 \pm 1.0 \text{ Tg a}^{-1}$, which is 59% higher than the National Inventory. From the provincial inversion, 39% higher anthropogenic emissions were attributed to Western Canada than the prior. The results from this study show a readjustment of the Canadian CH₄ budget is necessary to better match atmospheric observations with lower natural emissions partially offset by higher anthropogenic emissions. Additionally, the results from the sectoral and provincial inversions show that the ECCC + GOSAT combined observing system is inadequate for completely constraining subnational scale emissions, as finer scale emissions from most provinces could not be resolved above the noise in the system. Improvements to the observing system using an expanded in-situ network and next-generation satellites, such as TROPOMI and GOSAT-2, may better address these limitations in the years following this analysis.

A cost-effective urban field study completed in 2014 and 2017 using CRDS observations in a mobile vehicle was able to survey CH₄ emissions from mobile combustion sources and from natural gas infrastructure in the Greater Toronto Area. On-road emissions factors for vehicles were verified to be low contributors to the urban CH₄ budget, however numerous super-emitting vehicles were observed that emitted high CH₄ and CO. These high CH₄ + CO measurements indicated the presence of poorly maintained vehicles with aging equipment resulting in incomplete combustion of fuel into CO₂ or failing catalytic converters and emissions controls. The average fleet emissions factor was determined to be 0.063 ± 0.003 g CH₄ per L of fuel, which is 55% lower than the emissions factor for personal vehicles in the National Inventory. However this is perhaps not surprising as the emissions were measured from vehicles on highways during steady state driving conditions without starts and stops. In the 2017 field study, ~90 km of road was driven to survey the presence of leaking natural gas infrastructure. The average of the 1-day study showed 1 leak per 23 km of road driven, which is low when compared to other studies in North America. The 2017 study also showed the presence of a high emitting urban wastewater facility on Lake Ontario, with maximum CH₄ in the plume observed to be 6 ppm. The results from the urban studies show that cities with better maintained infrastructure can reduce CH₄ emissions from natural gas leakage, however super-emitters from landfills or waste facilities may account for a substantial fraction of the city CH₄ budget, which can be better characterized with observations.

The studies presented in this dissertation show the value of atmospheric observations towards improving characterization of CH₄ emissions in Canada. Aircraft observations provide dense local coverage, and when combined with measurements of tracer species, emissions can be determined at the facility and sub-facility source level. The primary limitation of aircraft studies is temporal coverage, since they provide ‘snapshot’ emissions in time which may change over seasons and years. A solution to this limitation is the use of comparable mobile surface measurements, which are less resource intensive. These surface measurements, when combined with a network of meteorological measurements and plume modelling, can also determine emissions at the sub-facility source level using a mass-balance approach. However, the limitation of this approach is the dependence on the assumption of a well-mixed plume in the PBL, which

excludes many observations from the analysis. Satellite observations have improved substantially in the last decade, with increasing observation coverage and precision. When combined with a global chemical transport model such as GEOS-Chem, emissions can be determined on the national and subnational scale in an inverse analysis, successfully disentangling anthropogenic and natural sources. Satellite inverse modelling in Canada is generally limited by errors in the retrieval and model transport biases in the high latitude domain which compromise interpretation of the XCH₄ column. In addition, background-enhanced signal from surface emissions in the column-average observed from space is weaker than signal that could be measured by local in-situ observations; hence detectable emissions are limited by source magnitudes relative to instrument precision, which are not a major consideration for CRDS instruments. However, the daily, global coverage of satellite observations is extraordinarily valuable to address the temporal and spatial gaps in field studies, and these capabilities are rapidly improving. For example, the TROPOMI instrument launched in 2017 provided ~64 million XCH₄ observations in 2019, this is factor of 274x higher than the ~0.23 million XCH₄ observations provided by GOSAT in 2013.

The scientific community will continue to accomplish improvements to atmospheric observations and these measurements will continue to be used to better constrain emissions at the sub-facility to global scale. In the near future, it is easily foreseeable that this will reduce uncertainties in the Earth's CH₄ cycle, resulting in more precise source-attribution of the global growth rate and decadal trends in atmospheric CH₄. Optimistically, this knowledge will be used by policymakers to competently target CH₄ reductions, resulting in a trend of decreasing atmospheric CH₄ before the half century and reducing its impact on radiative forcing. How this knowledge will be used towards climate policy is outside of the jurisdiction of science, although scientists outside of their jurisdiction may yet have much to contribute on this subject.

Appendices

Appendix A: Supplement to Quantification of methane sources in the Athabasca Oil Sands Region of Alberta by aircraft mass balance

A.1 Assessment of Uncertainties

Tables A.1-6 show the results of the sensitivity analysis to estimate contributions to total uncertainty. Parameters contributing to uncertainties depend on the mass balance method used and the screen-based (Eq. 2.1) or the box-approach (Eq. 2.2). Minor uncertainties that contribute to both methods are errors in the CH₄ mixing ratio measurement and wind measurements. CH₄ measurement errors from the instrument are <1%. Measurements of trace species from other instruments were used qualitatively to deduce plume origins, thus they do not contribute to total uncertainties. In a previous study, a Monte Carlo simulation was used to demonstrate the wind measurements contribute <1% to the change in uncertainties (Gordon et al., 2016). A significant source of uncertainty for both mass balance methods is the extrapolation of CH₄ mixing ratios to the surface for ground-level plumes. Surface extrapolation uncertainties are highly variable with flight, consistent with the literature. Cambaliza et al. (2014) found surface extrapolation uncertainties to be 4, 9 and 16% for three different mass balance flights downwind of Indianapolis to determine CH₄ fluxes, and Gordon et al., 2016 found this to be 15% and 26% for two Oil Sands flights for the CNRL facility. The uncertainty depends on the range of surface mixing ratios resulting from fitting varying extrapolation methods. We derive a range of possible emissions rates by comparing results from constant, linear and half-Gaussian extrapolations to the surface. CH₄ measurements at Fort McKay are used as constraints on surface mixing ratios when flight paths are directly overhead (Aug 16 Flight 4A, SML and SUN). Half-gaussian extrapolations are used where fits are above constraints ($r^2 > 0.40$). Future studies can further minimize these uncertainties with simultaneous ground-level mixing ratio measurements.

Additional uncertainties specific to the box-approach (Eq. 2.2) are assessed according to the methodology described in Gordon et al., 2016. Contributing factors are: (1) the uncertainty in the box-top height (affecting the E_{CH} and E_{CV} terms), estimated by reducing the box height by 100 m, (2) changes in air mass density within the volume of the box (affecting E_{CM}), estimated using the minimum and maximum of pressure and temperature ratios derived from surrounding meteorological stations, (3) inclusion of the estimated vertical turbulence term (E_{CVT}), and (4) uncertainty in the mean CH_4 mixing ratio at the box-top (affecting E_{CV}) determined from the 95% confidence interval ($2\sigma/\sqrt{n}$) of interpolated measurements. These terms are recalculated according to the range of possible input parameters in order to derive resulting uncertainties in the emissions rates. Screen-approach specific uncertainties (Eq. 2.1) are mostly due to the variability in the background mixing ratio $[CH_4]_B$, determined using the outer edges of the screen away from plume sources (screen flights) and upwind measurements (box flights). For each flight measurements from multiple background regions ($>1\text{km}$) occurring closely in time are used as possible inputs, which are identified clearly due to the high CH_4 mixing ratios observed from plumes. Other sources of uncertainty are the vertical extent of the screen (upper bound, z) and the horizontal boundaries (s_1 - s_2) of individually characterized plumes. These plume boundaries are expanded and contracted to derive a range of possible integrals.

Uncertainties for each mass balance flight are added in quadrature to derive a range of possible emissions rates. Estimates for the same source category within a facility, as well as total estimates for the same facility, are treated as independent estimates and combined using an error-weighted mean ($1/\sigma^2$).

A.2 Meteorological Conditions

Tables A.1-6 (bottom) present various flight details and meteorology. Flights used are those with a high number of aircraft transects (≥ 6) that show full characterization of plume vertical extent. Boundary layer heights are determined using visual inspection of dew point temperature alongside LIDAR backscatter reports from ground-site AMS13 during flight times. Ground temperature and wind direction measurements are based on ground-site data at AMS13 over the course of the day. Wind speeds shown are from interpolated screens $\pm 1\sigma$.

Table A.1-6: Top: Sensitivity analysis displaying uncertainty contributions shown in percent change from the best-estimate emissions rate, added in quadrature for totals. Uncertainties in individual plumes are noted with superscripts for tailings ponds (t), mines (m) and facility/other (f). Screen estimates using an overlapping subset of downwind measurements from a box flight of the same day are shown with an asterisk (*). Middle: List of emissions rates for source categories and facility totals in tonnes CH₄ per hour (tonnes hr⁻¹). Bottom: Various aircraft flight details and meteorological parameters.

Table A.1: Syncrude Mildred Lake (SML)

	Aug 14 Box	Aug 14 Screen A*	Aug 14 Screen B	Aug 16 Screen A
Measurement Error (%)	1	1	1	1
Wind Error (%)	1	1	1	1
Surface Extrapolation (%)	4	11	3	28
Box				
Box-top Height (%)	15			
Density Change (%)	11			
Vertical Turbulence (%)	2			
Box-Top Mixing Ratio (%)	4			
Screen				
Background Mixing Ratio (%)		13	19	8
Screen-Top Height (%)		6	6	1
Plume Separation (%)		6 ^t , 11 ^m	5 ^t , 12 ^m	5 ^t , 8 ^m
Total Uncertainty Facility (%)	20	19	21	30
Total Uncertainty Plumes (%)		20 ^t , 22 ^m	21 ^t , 24 ^m	30 ^t , 31 ^m
Emissions Rate Ponds (tonnes hr ⁻¹)		6.38 ± 1.23	5.83 ± 1.22	8.63 ± 2.59
Emissions Rate Mines (tonnes hr ⁻¹)		2.71 ± 0.60	2.67 ± 0.64	3.07 ± 0.95
Emissions Rate Facility/Other (tonnes hr ⁻¹)				
Emissions Rate Total (tonnes hr⁻¹)	7.68 ± 1.54	9.10 ± 1.73	8.50 ± 1.79	11.82 ± 3.55
Aircraft Transect Count	6	6	8	9
Boundary Layer Height (m agl)	360-400	360-400	400-600	350-400
Temperature (°C)	20.8 ± 6.0	20.8 ± 6.0	20.8 ± 6.0	19.5 ± 3.8
Wind Speed (m/s)	3.1 ± 2.5	3.1 ± 2.5	5.1 ± 1.6	2.8 ± 0.8
Daily Mean Wind Direction (°)	220 ± 37	220 ± 37	220 ± 37	225 ± 57

Table A.2: Suncor Energy OSG (SUN)

	Aug 16 Screen A	Aug 29 Box	Aug 29 Screen*
Measurement Error (%)	1	1	1
Wind Error (%)	1	1	1
Surface Extrapolation (%)	4	14	4
Box-top Height (%)		1	
Density Change (%)		17	
Vertical Turbulence (%)		2	
Box-Top Mixing Ratio (%)		5	
Background Mixing Ratio (%)	23		2
Screen-Top Height (%)	1		9
Plume Separation (%)	12 ^t , 1 ^m		9 ^t , 9 ^m
Total Uncertainty Facility (%)	24	23	11
Total Uncertainty Plumes (%)	27 ^t , 24 ^m		14 ^t , 14 ^m
Emissions Rate Ponds (tonnes hr ⁻¹)	3.16 ± 0.85		2.30 ± 0.32
Emissions Rate Mines (tonnes hr ⁻¹)	1.53 ± 0.37		1.88 ± 0.26
Emissions Rate Facility/Other (tonnes hr ⁻¹)			
Emissions Rate Total (tonnes hr⁻¹)	4.69 ± 1.13	3.96 ± 0.91	4.18 ± 0.42
Aircraft Transect Count	9	7	7
Boundary Layer Height (m agl)	350-400	400-500	400-500
Temperature (°C)	19.5 ± 3.8	15.2 ± 2.4	15.2 ± 2.4
Wind Speed (m/s)	2.8 ± 0.8	1.8 ± 1.3	1.8 ± 1.3
Daily Mean Wind Direction (°)	225 ± 57	26 ± 40	26 ± 40

Table A.3: Canadian National Resources Limited Horizon (CNRL)

	Aug 20 Box	Aug 20 Screen*	Sep 02 Box	Sep 02 Screen*
Measurement Error (%)	1	1	1	1
Wind Error (%)	1	1	1	1
Surface Extrapolation (%)	22	26	12	11
Box-top Height (%)	1		18	
Density Change (%)	5		6	
Vertical Turbulence (%)	2		7	
Box-Top Mixing Ratio (%)	3		8	
Background Mixing Ratio (%)		16		25
Screen-Top Height (%)		5		2
Plume Separation (%)				6 ^m , 12 ^f
Total Uncertainty Facility (%)	23	31	25	28
Total Uncertainty Plumes (%)				29 ^m , 30 ^f
Emissions Rate Ponds (tonnes hr ⁻¹)				
Emissions Rate Mines (tonnes hr ⁻¹)				2.56 ± 0.74
Emissions Rate Facility/Other (tonnes hr ⁻¹)				0.98 ± 0.29
Emissions Rate Total (tonnes hr⁻¹)	3.65 ± 0.84	3.67 ± 1.14	3.53 ± 0.88	3.54 ± 1.00
Aircraft Transect Count	12	12	10	10
Boundary Layer Height (m agl)	700-900	700-900	600-1000	600-1000
Temperature (°C)	16.3 ± 4.3	16.3 ± 4.3	12.7 ± 5.1	12.7 ± 5.1
Wind Speed (m/s)	2.4 ± 1.9	2.4 ± 1.9	5.9 ± 2.8	5.9 ± 2.8
Daily Mean Wind Direction (°)	262 ± 35	262 ± 35	338 ± 59	338 ± 59

Table A.4: Shell Albian and Jackpine (SAJ)

	Aug 21 Box	Aug 21 Screen*	Sep 06 Box	Sep 06 Screen*
Measurement Error (%)	1	1	1	1
Wind Error (%)	1	1	1	1
Surface Extrapolation (%)	5	7	12	7
Box-top Height (%)	8		5	
Box Density Change (%)	10		16	
Box Vertical Turbulence (%)	5		2	
Box-Top Mixing Ratio (%)	9		7	
Screen Background Mixing Ratio (%)		27		17
Screen Screen-Top Height (%)		10		5
Screen Plume Separation (%)				
Total Uncertainty Facility (%)	18	30	22	20
Total Uncertainty Plumes (%)				
Emissions Rate Ponds (tonnes hr ⁻¹)				
Emissions Rate Mines (tonnes hr ⁻¹)		1.44 ± 0.43		1.18 ± 0.24
Emissions Rate Facility/Other (tonnes hr ⁻¹)				
Emissions Rate Total (tonnes hr⁻¹)	1.60 ± 0.29	1.44 ± 0.43	1.25 ± 0.28	1.18 ± 0.24
Aircraft Transect Count	10	10	10	10
Boundary Layer Height (m agl)	1200-1500	1200-1500	900-1200	900-1200
Temperature (°C)	16.5 ± 3.6	16.5 ± 3.6	14.8 ± 6.2	14.8 ± 6.2
Wind Speed (m/s)	1.3 ± 0.8	1.3 ± 0.8	4.3 ± 0.9	4.3 ± 0.9
Daily Mean Wind Direction (°)	258 ± 50	258 ± 50	7 ± 50	7 ± 50

Table A.5: Syncrude Aurora (SAU)

	Aug 29 Box	Aug 29 Screen*	Sep 06 Screen*
Measurement Error (%)	1	1	1
Wind Error (%)	1	1	1
Surface Extrapolation (%)	10	14	6
Box-top Height (%)	4		
Box Density Change (%)	9		
Box Vertical Turbulence (%)	2		
Box-Top Mixing Ratio (%)	3		
Screen Background Mixing Ratio (%)		11	13
Screen Screen-Top Height (%)		4	13
Screen Plume Separation (%)			
Total Uncertainty Facility (%)	15	19	20
Total Uncertainty Plumes (%)			
Emissions Rate Ponds (tonnes hr ⁻¹)			
Emissions Rate Mines (tonnes hr ⁻¹)		1.29 ± 0.25	1.56 ± 0.31
Emissions Rate Facility/Other (tonnes hr ⁻¹)			
Emissions Rate Total (tonnes hr⁻¹)	1.70 ± 0.26	1.29 ± 0.25	1.56 ± 0.31
Aircraft Transect Count	3	3	10
Boundary Layer Height (m agl)	400-500	400-500	900-1200
Temperature (°C)	15.2 ± 2.4	15.2 ± 2.4	14.8 ± 6.2
Wind Speed (m/s)	2.3 ± 0.7	2.3 ± 0.7	4.3 ± 0.9
Daily Mean Wind Direction (°)	26 ± 40	26 ± 40	7 ± 50

Table A.6: Total Oil Sands Screen

		Aug 16 Screen B
	Measurement Error (%)	1
	Wind Error (%)	1
	Surface Extrapolation (%)	3
Box	Box-top Height (%)	
	Density Change (%)	
	Vertical Turbulence (%)	
	Box-Top Mixing Ratio (%)	
	Background Mixing Ratio (%)	14
Screen	Screen-Top Height (%)	5
	Plume Separation (%)	
	Total Uncertainty Facility (%)	16
	Total Uncertainty Plumes (%)	
	Emissions Rate Ponds (tonnes hr ⁻¹)	
	Emissions Rate Mines (tonnes hr ⁻¹)	
	Emissions Rate Facility/Other (tonnes hr ⁻¹)	
	Emissions Rate Total (tonnes hr⁻¹)	23.6± 3.8
	Aircraft Transect Count	10
	Boundary Layer Height (m agl)	400-450
	Temperature (°C)	19.5 ± 3.8
	Wind Speed (m/s)	2.8 ± 1.0
	Daily Mean Wind Direction (°)	225 ± 57

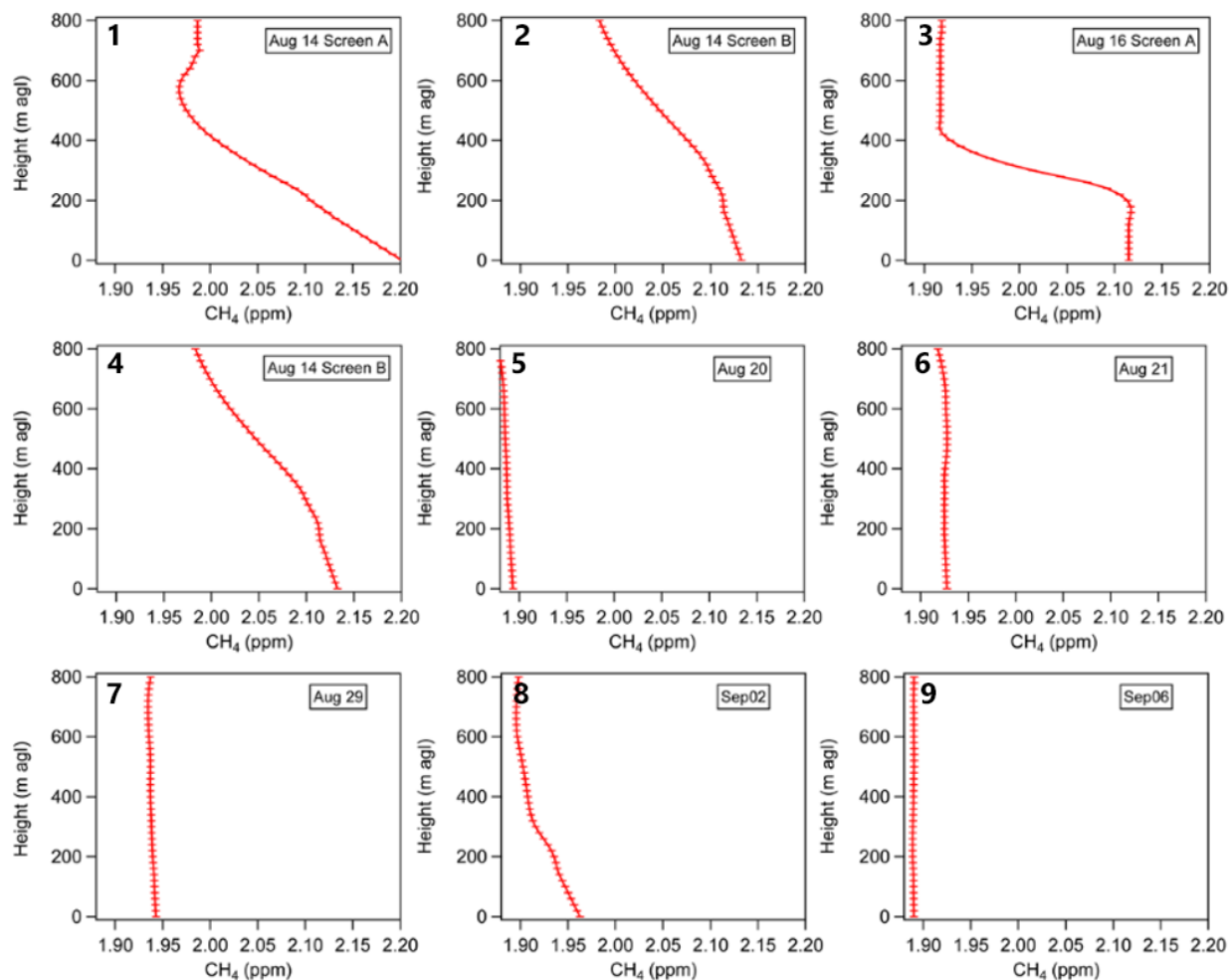


Figure A.1: Background profiles, $[\text{CH}_4]_{\text{B}}(z)$, were selected from regions of the interpolated screens away from plume sources, corresponding to 2-20km spatial lengths depending on the flight paths. Error bars are the 1σ variability within the 2-20km spatial regions of background air. Background CH_4 for the vertical regions 150-200m above ground to the surface are estimated based on extrapolations (constant or linear) from the lowest transects to the surface and included in the uncertainty analysis. The lowest 5 aircraft transects usually converged to a constant value (Box 3,5,6,7,9 left to right) or showed a small linear enhancement (Box 2,4,8) which provided best fits to the surface.

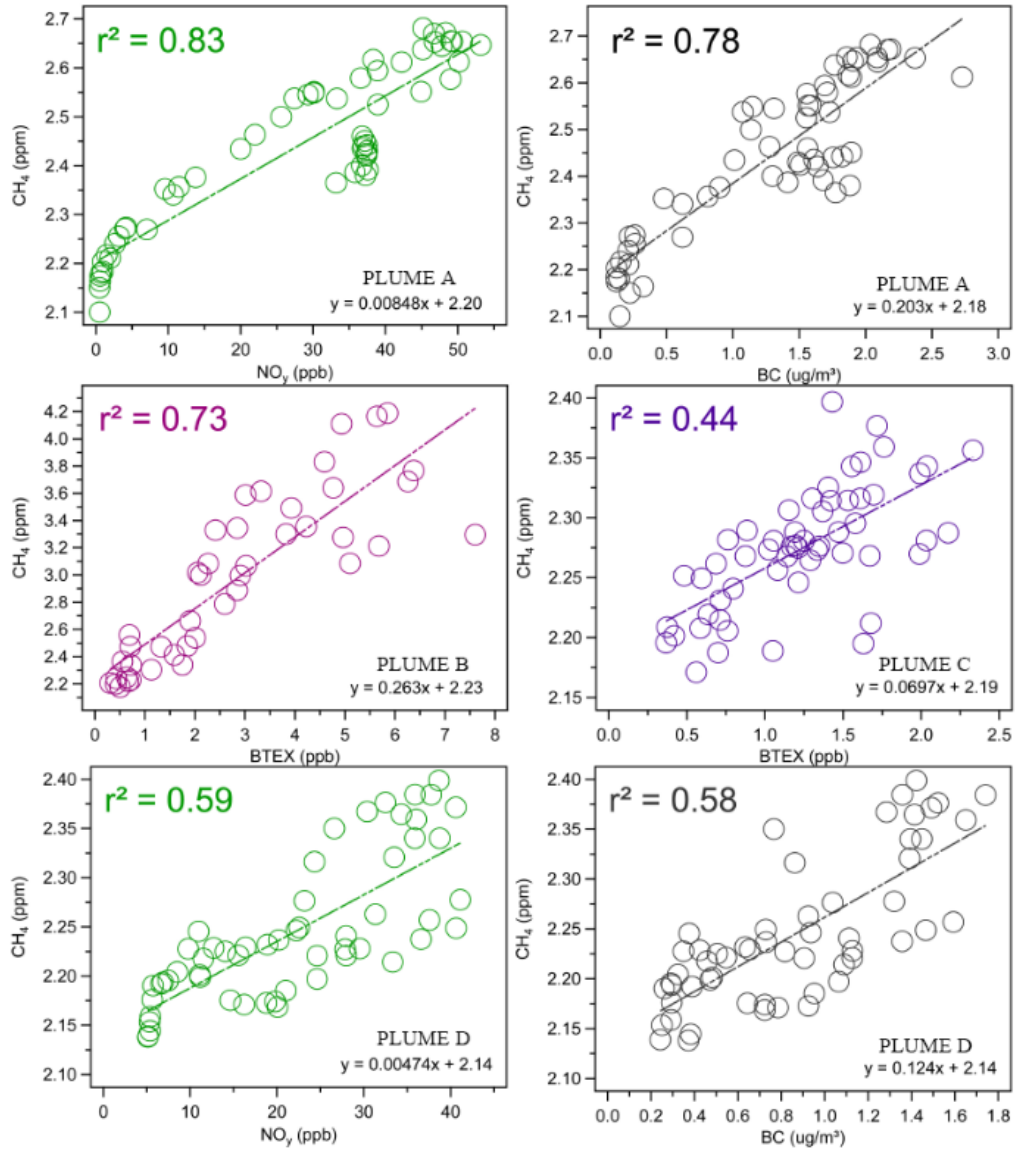


Figure A.2: Correlation Plots for Plumes A-D corresponding to Figure 2.2 (SML Mine, SML Tailings Pond, SUN Tailings Pond, SUN Mine). CH₄ is well correlated with tracer species NO_y, BC and BTEX for the various sources. Linear coefficients of determination (r^2) are in the range of 0.44-0.83. The lowest r^2 values are from the CH₄ vs BTEX plot for Plume C and the CH₄ vs NO_y and CH₄ vs BC plots for Plume D. These two sources correspond to lower emissions and mixing ratios of both CH₄ and the 5 associated species. In the context of our results, this analysis confirms the correlation of CH₄ with various species as shown in Figure 2.2 which are used to spatially define plume boundaries.

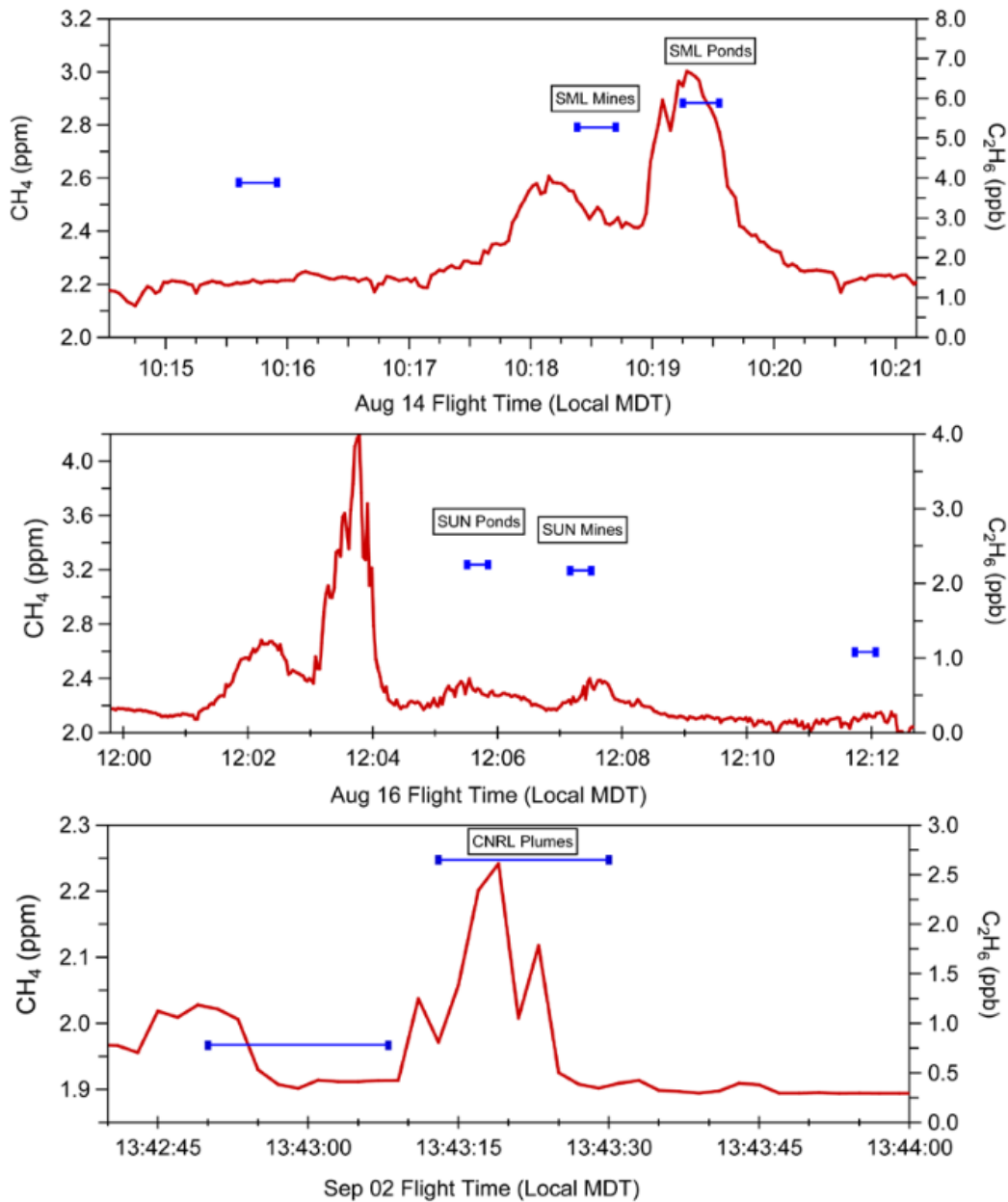


Figure A.3: Time series plots of methane (red line) and discrete canisters samples analyzed for ethane (blue lines) corresponding to the same plumes used in Table 2.1 for the ethane/methane ratio calculations. These are a small subset of the canisters that were sampled over the aircraft campaign. These example plumes attempt to isolate known sources from the three facilities and support the conclusion that there were not any significant sources of ethane in the AOSR, in agreement with Simpson et al., 2010.

Appendix B: Supplement to Cold season methane emissions estimated in the Athabasca Oil Sands Region of Alberta using mobile surface measurements

B.1 Analysis of winds

B.1.1 Description of meteorological measurements

Meteorological measurements at selected WBEA and ECCC monitoring stations (Table B.1, Figure B.1) were combined to determine a regionally representative vertical profile (Figures B.2-3). Measurements of horizontal and vertical winds were available at multiple heights above altitude, including up to 310m from the windRASS at AMS1 and 2000m from the SODAR at AMS17. Wind measurements along the vehicle transects during stationary periods were available from the anemometer mounted on the vehicle, which were used to independently verify WBEA wind speeds.

To calculate the average wind vector within the PBL (Tables B.2-3) for the March 28th and 31st plumes, the wind data from the measurement stations, excluding AMS17 SODAR, were vector averaged over the estimated transport time period for each plume. The AMS17 measurements were excluded because the wind-speeds were significantly higher at this location compared to the other stations (Figures B.2-3), likely due to the location of AMS17's SODAR at a relatively higher elevation (Table B.1). Hence, this data is not considered representative of the plume transport behaviour.

Figures B.2-3 show average vertical profiles of wind-speed and wind-direction determined by vector averaging wind measurements at the same altitudes above sea level (a.s.l.) in 10 m altitude bins rather than altitude above local surface level. In the figures the profiles are shown relative to the altitudes at the location of the peak CH₄ (344 m for March 28th and 355 m for March 31st). This method was based on the greater strength of correlation between wind data from AMS1 and AMS5 stations for the same altitudes a.s.l. compared to the same altitudes above local surface level for March 2017 (Tables B.4-5). For the wind-speed correlations, the slopes of the linear regression were close to 1.0 using comparable altitudes a.s.l. versus 1.4-2.0 for altitudes above local surface (Table B.2). These results suggest that the wind streamlines likely become flatter at altitudes sufficiently above the surface (e.g., >40 m) but follow the ground close to the surface.

Note that in the Athabasca Oil Sands Region, complex wind flow is possible due to the presence of the Athabasca River valley (Gordon et al., 2018). A time-series comparison of wind-speeds and wind-directions at comparable altitudes a.s.l. during the estimated time of transport for the March 28th and 31st plumes are shown in Figures B.4-7. The wind-speeds and wind-directions were relatively constant and consistent between the different locations for the March 28th and 31st estimated time of the plumes' transport (Table 3.1).

Note that while the windRASS can measure up to ~550 m above local surface level, the data retrievals become noisy for speeds >5 m/s such that many datapoints are missing >310 m for the study days. Therefore, only WindRass data 40-310 m above the local surface were used in the calculations. The vertical profile of wind speed >310 m was extrapolated for each transect by fitting a power-law function to the average vertical profile (Fig. B.2-3), see section B.1.3 in the supplement for more details on modelling wind profiles using a power-law function. The errors of the power law equations were estimated using the RMSE of the modelled values (Table B.2). The average wind-speed used in the emission calculation (Eq 4.1) for the March 28th and 31st plumes was determined by vertically averaging the combined averaged measured and power-law extrapolated profiles within the PBL height. The average wind-directions in the PBL were determined by vertically averaging the vertical profile of averaged measurements between 0 and 310 m (Table B.3). The profiles were not extrapolated above 310 m because wind-direction appeared relatively constant with altitude above the near-surface for all transects (Figures B.2-3).

Table B.1: Locations, elevation, and altitudes of measurements of the wind measurement stations from WBEA. *NA = instrument type is not known.

Meteorological Measurement Station	Altitude Above Sea Level (m)	Latitude (°), Longitude (°)	Altitudes of Measurement above Local Surface (m)	Instrument	Time Resolution (mins.)
AMS5 (Mannix)	332	56.968, -111.482	20, 45, 75, 90	Ultrasonic Anemometer	5
AMS3 (Lower Camp Met Tower)	238	57.032, -111.506	20, 45, 100, 167	NA	5
AMS1 (Bertha Ganter)	267	57.189, -111.641	40, ..., 310 [10 m intervals]	WindRass	15
AMS17 (Wapasu)	490	57.259, -111.039	100, ..., 2000 [100 m intervals]	SODAR	60
JP104	335	57.119, -111.425	2, 16, 21, 29	NA	60

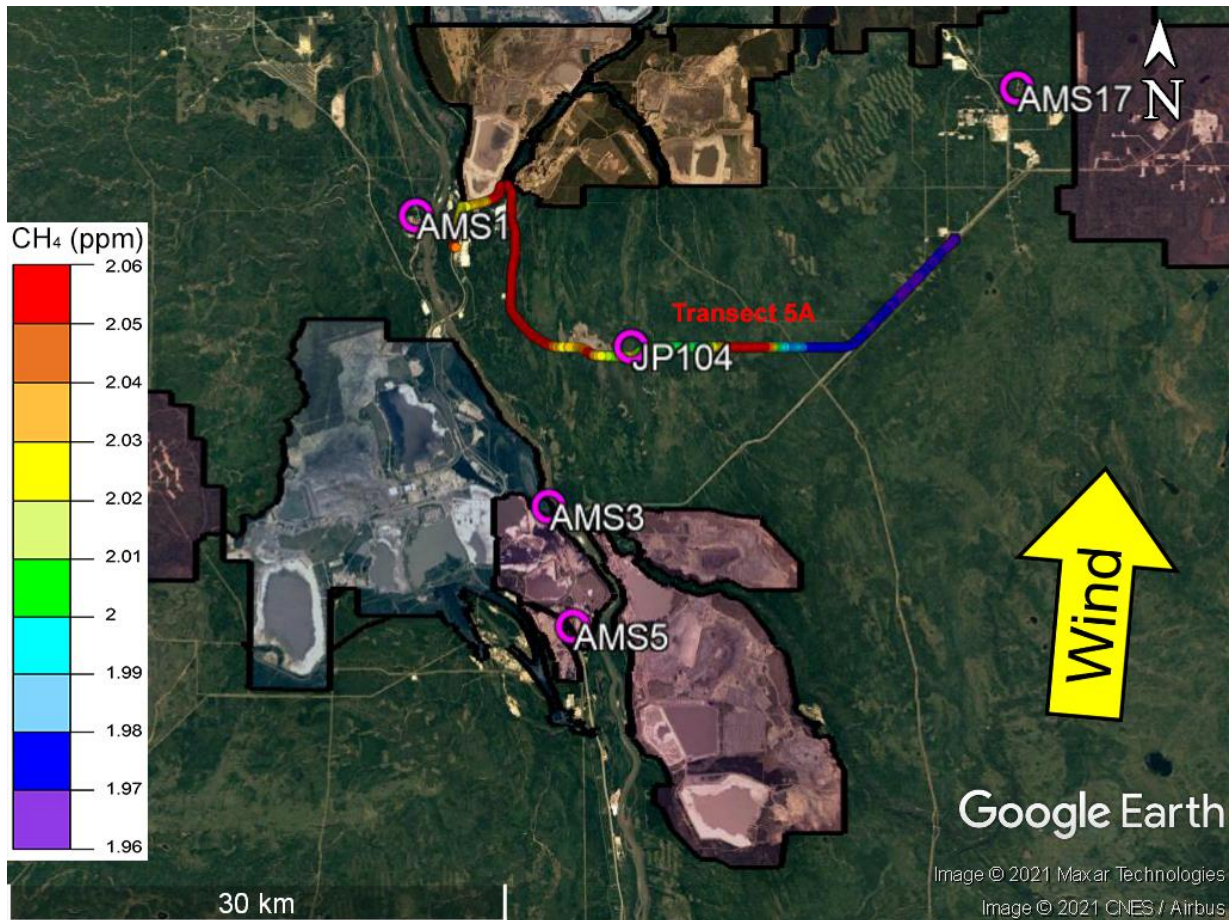


Figure B.1: Locations of meteorological measurement instruments and example of transect 1 from March 31st.

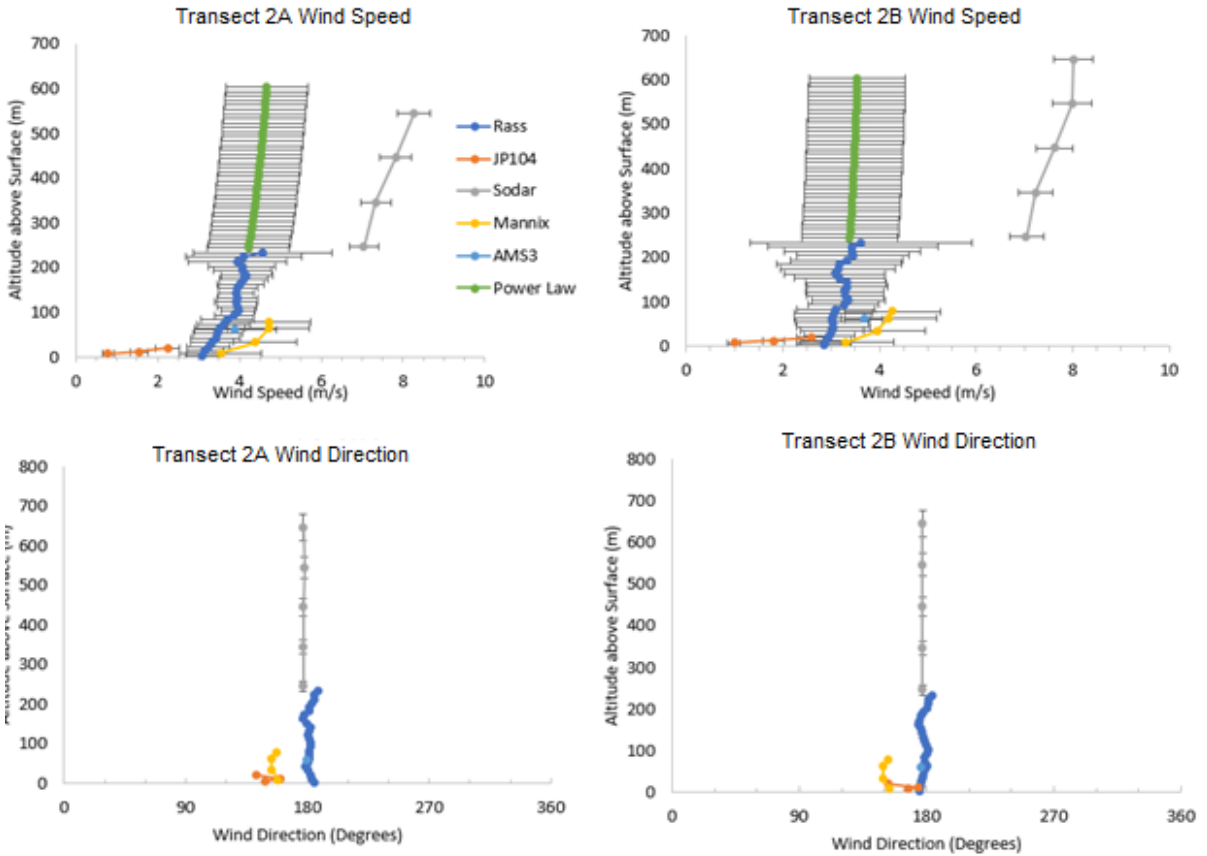


Figure B.2: Vertical profiles of wind-speed (top) and wind-direction (bottom) for the transects on March 28th.

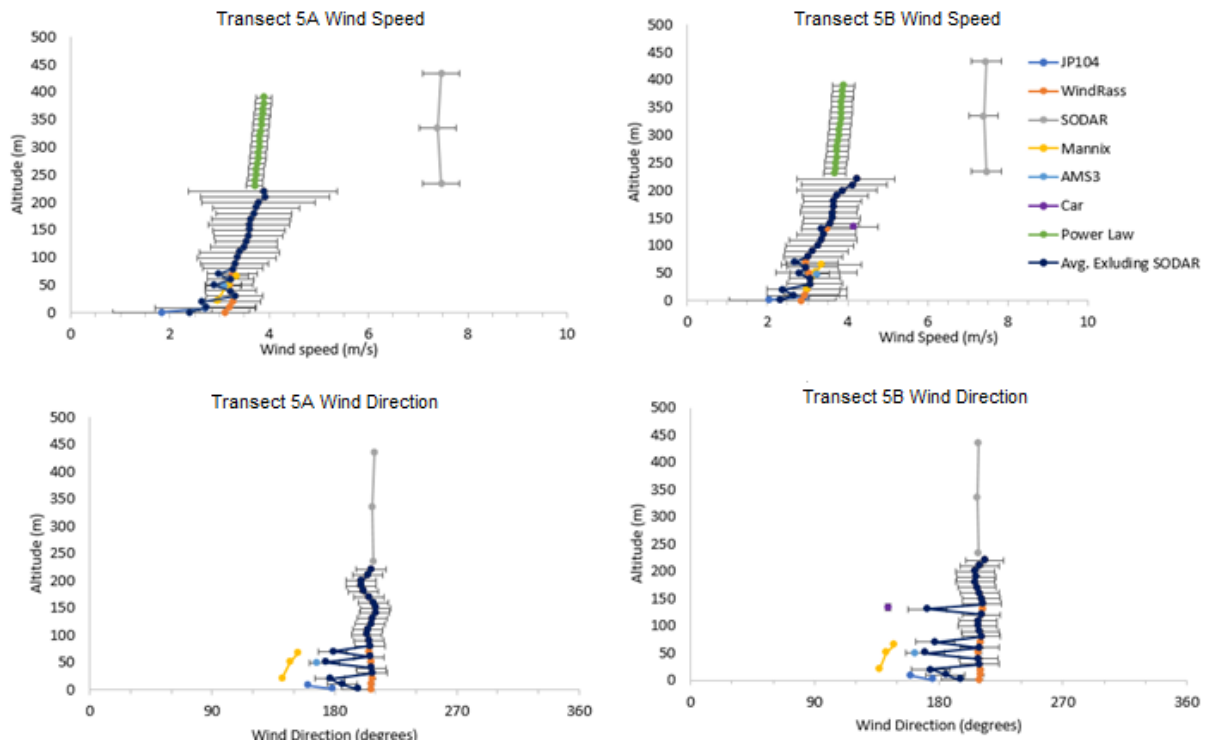


Figure B.3: Vertical profiles of wind-speed (top) and -direction (bottom) for transects on March 31st.

Table B.2 Transect average of wind-speed within the PBL for Mar 28 and Mar 31 2017 plumes. Instrumental uncertainty is the manufacturer reported uncertainty of the WindRass instrument (Table B.1). Interpolation uncertainty is the root-mean square error of the power-law fit to the vertical profile of wind-speed from 0–310 m (Fig. B.5).

Transect	Average Wind-Speed (m/s)	Standard Deviation (m/s)	Instrumental Uncertainty (m/s)	Interpolation Uncertainty (m/s)	Total Uncertainty (m/s)
2A	4.2	0.4	0.5	0.3	0.7
2B	3.4	0.2	0.5	0.2	0.6
5A	3.6	0.3	0.5	0.16	0.6
5B	3.6	0.4	0.5	0.26	0.7

Table B.3 Transect average of wind-direction from measurements 0–310 m above surface level for Mar 28 and Mar 31 2017 plumes. Instrumental uncertainty is the manufacturer reported uncertainty of the WindRass instrument (Table B.1).

Transect	Average Wind-Direction (Degrees)	Standard Deviation (Degrees)	Instrumental Uncertainty (Degrees)	Total Uncertainty (Degrees)
2A	179	6	2	6
2B	176	6	2	6
5A	200	10.9	1.5	11.0
5B	201	14.5	1.5	14.6

B.1.2 Comparison of vertical profiles of wind data using absolute or relative altitudes

This section shows an analysis of wind data from different meteorological stations comparing the consistency of observations when using absolute altitude above sea level and relative altitude above the surface. There is a considerable effect of topography on meteorology in the region, as Table B.1 shows the altitudes above sea level between different stations ranges from 238 m (AMS3) to 490 m (AMS17). The differences in wind speeds are most apparent when comparing to AMS17 SODAR (Figure B.2-3), which is higher than the other stations due to the highest elevation. For example, Table B.4 shows linear regression statistics in the comparison between AMS5 and the WindRass at AMS1. The R^2 and slope both improve when using absolute altitude above sea level for the vertical grid of measurements as opposed to comparing the measurements according to their relative height above the ground. The results from this section show that a grid of absolute altitudes above sea level improve comparisons between stations. Figures B.4-7 show this result visually for the transect days showing the consistency of measurements at different relative heights above the ground, but similar absolute altitudes above sea level.

Table B.4 Linear Regression Statistics for correlation between Mannix and WindRass wind-speeds at comparable altitudes above the local surface and above sea-level for March 2017. Note that N=2800, the 5-minute Mannix data was vector averaged into the 15-minute time intervals of the WindRass data, the Mannix data was the y-data and that the y-intercept was set to zero.

Mannix Altitude	Same Altitude Above Local Surface			Same Absolute Altitude Above Sea Level		
	WindRass Altitude	R^2	Slope	WindRass Altitude	R^2	Slope
20	NA	NA	NA	90	0.43	0.91
45	40	-0.10	2.2	110	0.50	1.1
75	70	0.48	1.4	140	0.52	1.0
90	90	0.48	1.4	160	0.48	1.1

Table B.5 Circular regression statistics for correlation between Mannix and WindRass Wind-Directions at comparable altitudes above the local surface and above sea-level for March 2017. Note that N=2800, the 5-minute Mannix data was vector averaged into the 15-minute time intervals of the WindRass data, and the Mannix data was the y-data. The statistics were calculated using the Circular Statistics Toolbox in MATLAB (Berens, 2009).

Mannix Altitude	Same Relative Altitude Above Local Surface			Same Absolute Altitude Above Sea Level		
	WindRass Altitude	R ²	p-value	WindRass Altitude	R ²	p-value
20	NA	NA	NA	90	0.56	0.0
45	40	0.43	0	110	0.65	0.0
75	70	0.50	0	140	0.71	0.0
90	90	0.55	0	160	0.71	0.0

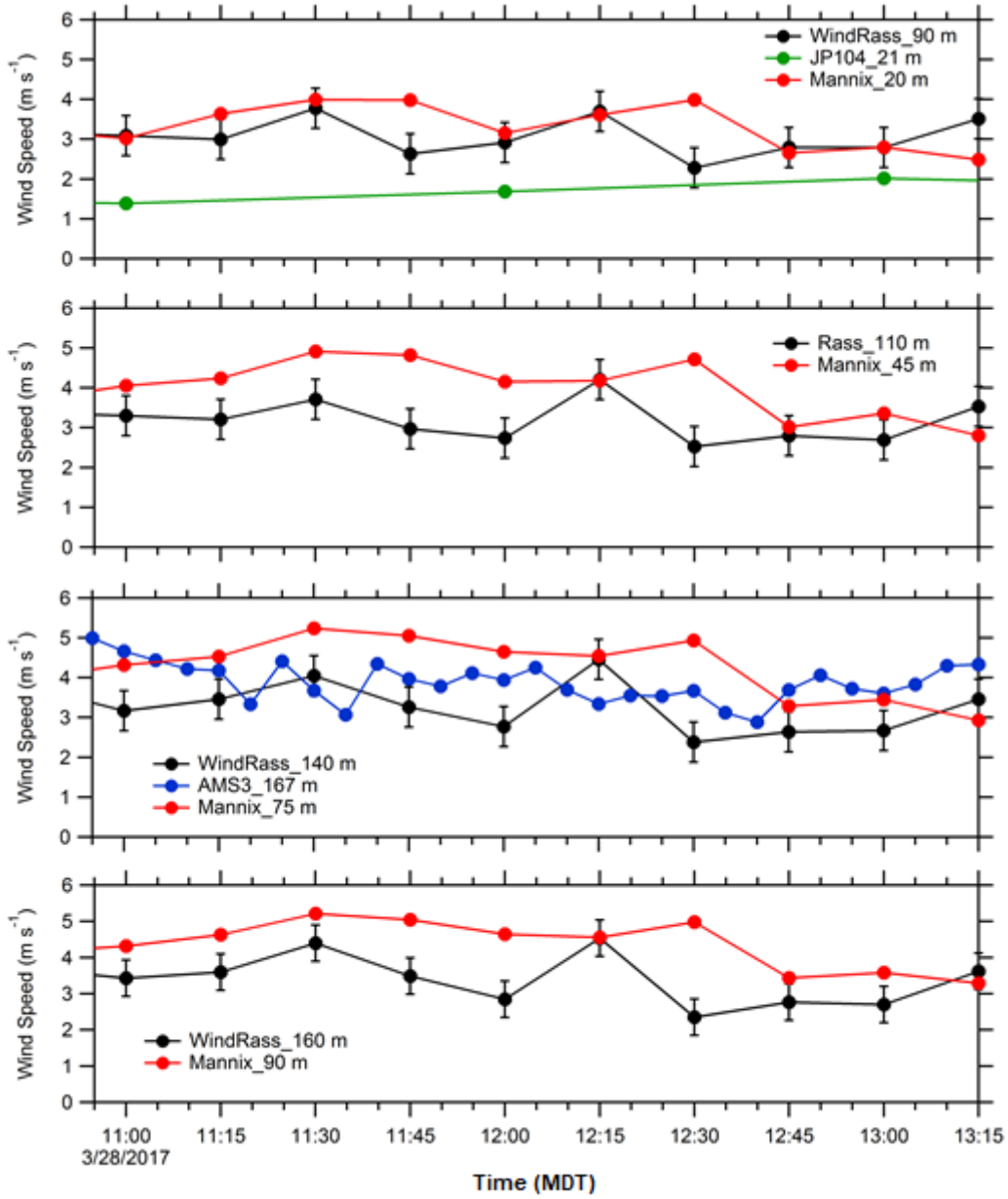


Figure B.4: Comparison of March 28th wind-speeds from different measurement locations. The altitudes in the plot legends for each location refer to altitude above surface level at the measurement location.

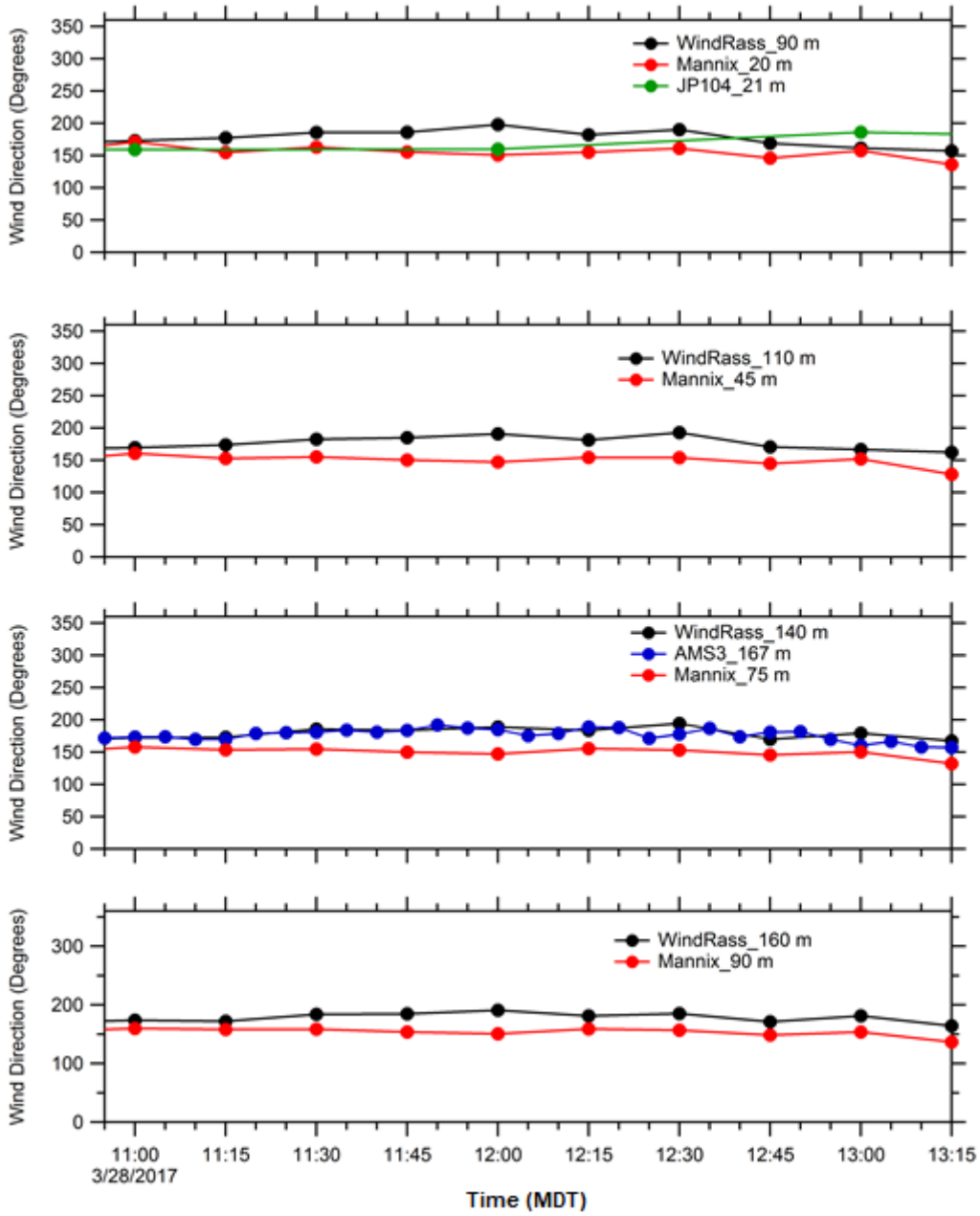


Figure B.5: Comparison of March 28th wind-directions from different measurement locations. The altitudes in the plot legends for each location refer to altitude above surface level at the measurement location.

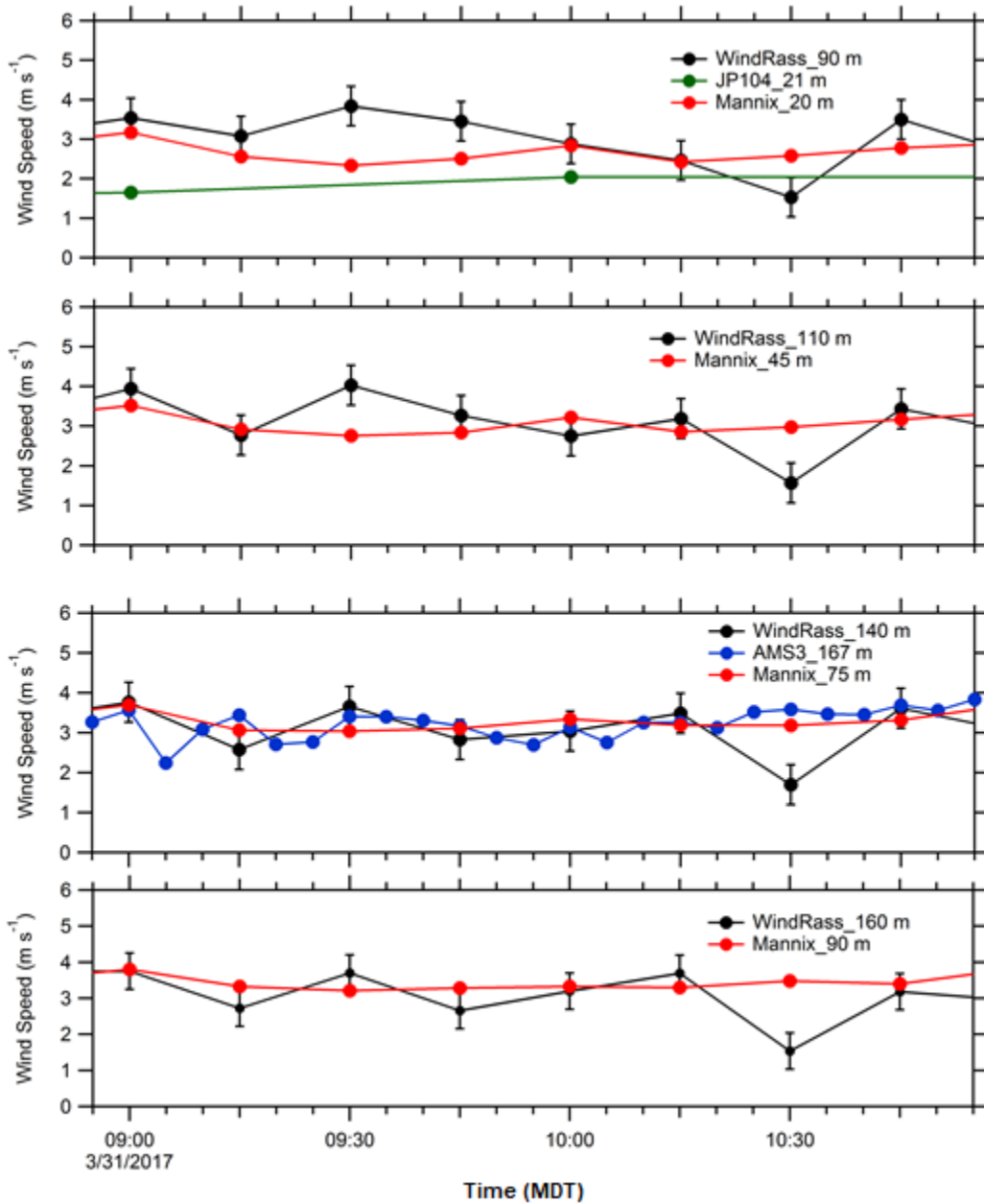


Figure B.6: Comparison of March 31st wind-speeds from different measurement locations. The altitudes in the plot legends for each location refer to altitude above surface level at the measurement location.

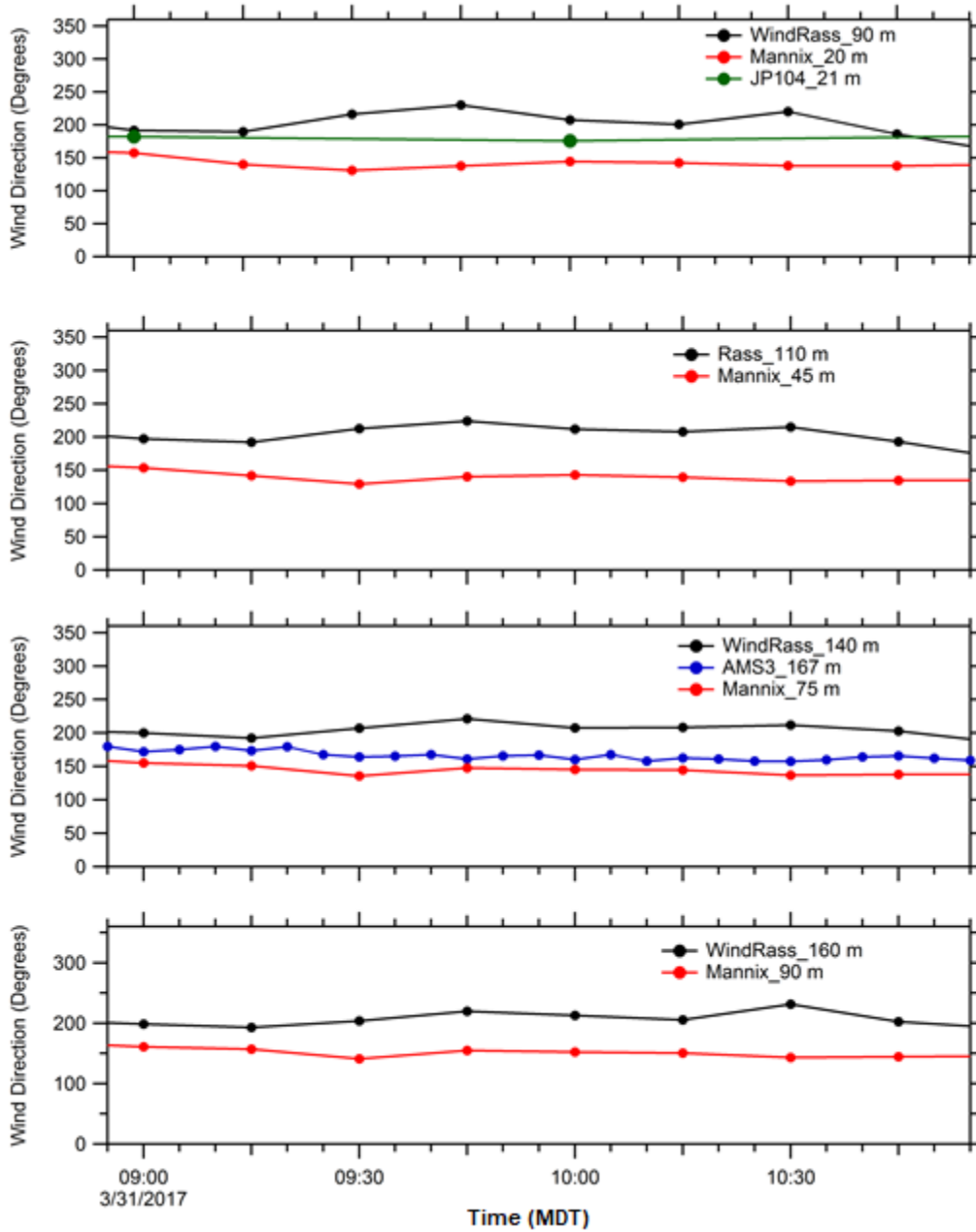


Figure B.7: Comparison of March 31st wind-directions from different measurement locations. The altitudes in the plot legends for each location refer to altitude above surface level at the measurement location.

B.1.3 The power-law model of vertical profiles of wind speed

The power-law (P-L) function can be used to model vertical profiles of wind-speed with height z , $U_{PL}(z)$ (Kikumoto et al., 2017)

$$U_{PL}(z) = U_n \left(\frac{z}{z_n} \right)^p \quad \{B.1\}$$

$U_{PL}(z)$ depends on the reference height (z_n), the wind-speed at height z_n (U_n), and the power-law index (p). The terrain roughness and atmospheric stability determines the value of p (Table B.4) (Kikumoto et al., 2017). In this study, U_n is the average of the wind speeds measured closest to 10 m above surface level and $p=0.10$ based on rural terrain and a slightly unstable atmosphere.

Table B.6 Power-Law Exponents (PLI) for Urban and Rural Wind Profiles (EPA, 2000)

Stability Class	Definition	Urban PLI	Rural PLI
A	Very Unstable	0.15	0.07
B	Unstable	0.15	0.07
C	Slightly Unstable	0.2	0.10
D	Neutral	0.25	0.15
E	Slightly Stable	0.3	0.35
F	Stable	0.3	0.55

Note that the P-L model of wind-speeds is not necessarily applicable to all atmospheric conditions since it was originally designed for neutral atmospheric stability and high wind-speeds (see Kikumoto et al. (2017) for more details). The conditions were slightly unstable for the plume transport period (Table 3.1) and the average wind-speed profiles were generally well fit by a power-law function (Figures B.2-3). The vertical profile of wind-speed predicted using the PLI in Table B.4 and the average 10 m wind-speed is shown in orange in Figure B.8. This modelled profile is consistent with the fitted profile and lends confidence to the use of the power-law function to extrapolate the wind-speed profiles above 310 m since the z_{PBL} were ~400 and 600 m for March 31st and 28th, respectively (Table 3.1).

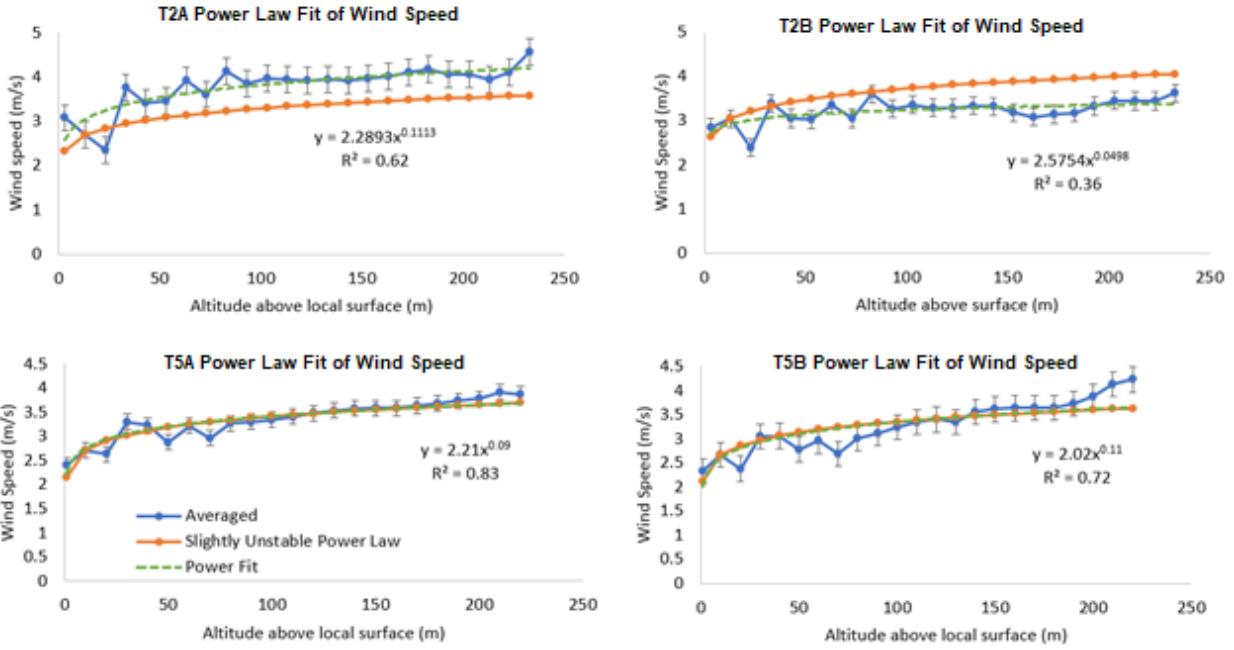


Figure B.8: Power law fits of average vertical profiles of wind-speed from 0-310 m above local surface level and predicted profiles using the 10 m wind-speed and the PLI for rural conditions and slightly unstable conditions in Table B.4 for March 28th (top) and March 31st (bottom).

B.2 Sensitivity analysis of mass balance emissions rate calculations

The sensitivity analysis with respect to key parameters in the mass balance eq. 4.1 is shown in Table B.5. The total uncertainty for the method is within 30–50%, and depends on uncertainties in the CH₄ background, the mean regional wind speed and the PBL height. Measurement uncertainty for the Picarro instrument is less than 1%.

Table B.7 Sensitivity analysis for the four experimental transects on Mar 28 2017 and Mar 31 2017

	Mar 27 T2A W to E	Mar 27 T2B E to W	Mar 31 T5A W to E	Mar 31 5B E to W
Methane Measurement (%)	<1	<1	<1	<1
Methane Background (%)	18	29	30	34
Mean Regional Wind Speed ^a (%)	20	21	22	32
PBL Height (%)	13	13	14	14
Total Uncertainty (%)	30	37	39	48
Total Uncertainty (tonnes hr ⁻¹)	0.35	0.52	0.35	0.28
Emissions Rate (tonnes hr ⁻¹)	1.2 ± 0.4	1.4 ± 0.5	0.9 ± 0.4	0.6 ± 0.3

^a Includes uncertainty in the wind direction

Supplement references

Berens, P.: CircStat: A MATLAB Toolbox for Circular Statistics, *J. Stat. Softw.*, 31(10), <http://www.jstatsoft.org/v31/i10> , 2009.

EPA: Meteorological Monitoring Guidance for Regulatory Modeling Applications, United States Environmental Protection Agency- Office of Air Quality Planning and Standards. [online] Available from: <https://www3.epa.gov/scram001/guidance/met/mmgrma.pdf>, 2000.

Kikumoto, H., Ooka, R., Sugawara, H. and Lim, J.: Observational study of power-law approximation of wind profiles within an urban boundary layer for various wind conditions, *J. Wind Eng. Ind. Aerodyn.*, 164, 13–21, doi:10.1016/j.jweia.2017.02.003, 2017.

Appendix C: Supplement to Estimating 2010-2015 anthropogenic and natural methane emissions in Canada using ECCC surface and GOSAT satellite observations

C.1 Monthly GOSAT Data in the Canadian Domain

Figure C.1 shows the GOSAT data available per month using 2013 as an example year, this corresponds to the data coverage shown in Fig. 4.1 of the main text but highlights the variability in satellite observational coverage over a single year. GOSAT data shown passes all quality assurance flags and includes our domain filter to land data that is within 50°W to 150°W longitude and 45°N to 60°N latitude. The minimum in December observations ($n=112$) and neighbouring months is due to less solar radiation in the winter resulting in less retrievals. Fewer observations cause the inversion to favour the prior state of emissions. There are less methane emissions from Canadian wetlands in the coldest months of the winter, and the comparison between the prior, the posterior using GOSAT data, and the posterior using ECCC data shows very small differences in emissions estimates for these coldest months.

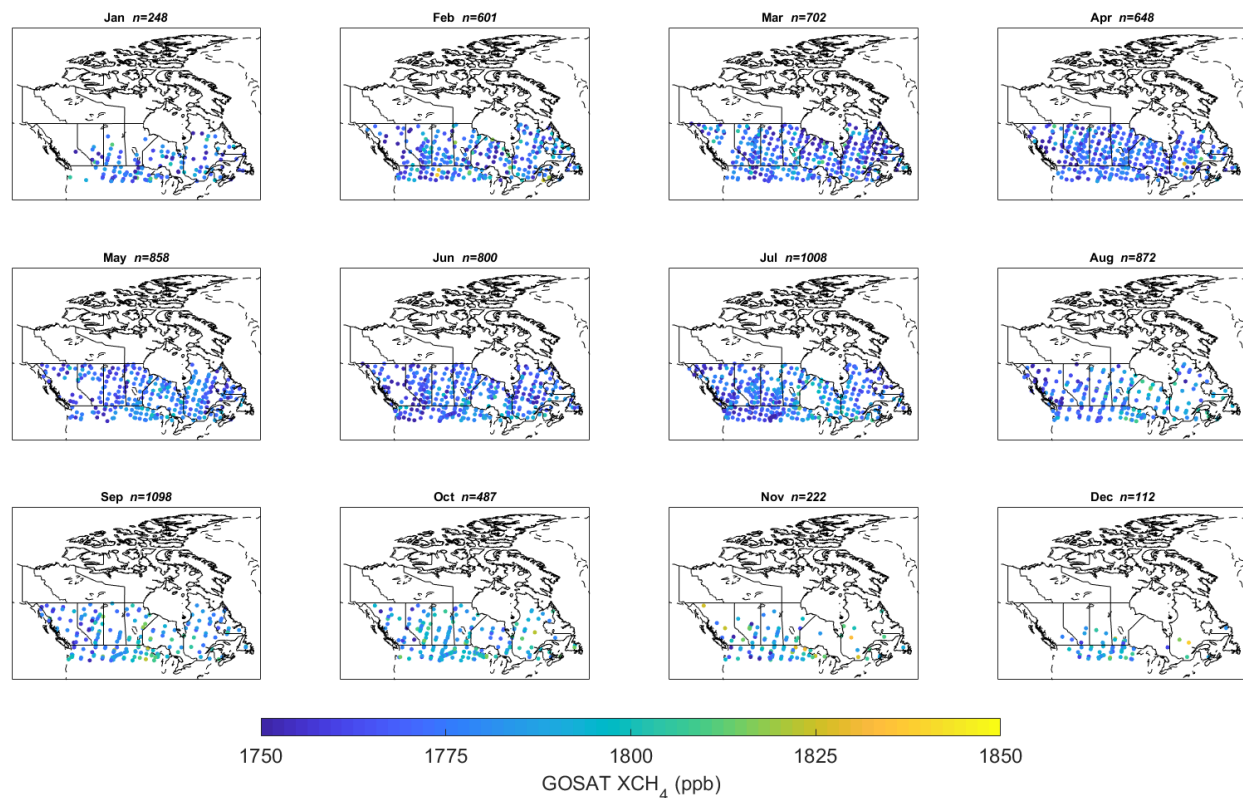


Figure C.1: GOSAT observations per month in the year 2013 corresponding to Fig. 4.1 in the main text ($n=7656$ observations for the entire year). Observations are filtered to land data that is within 50°W to 150°W longitude and 45°N to 60°N latitude.

C.2 Sensitivity of Seasonal Emissions to Climatological Data

We select four climatological stations shown in Table C.1 to sample temperature and precipitation data from 2010–2015 in the four provinces where wetland emissions are concentrated (Alberta, Saskatchewan, Manitoba, and Ontario). These stations are not exhaustive and are chosen for their proximity to the stations shown in Table C.1. Station measurements are quality-controlled from the National Climate Data Archive from Environment and Climate Change Canada (Hutchinson et al., 2009).

Table C.1 Climatological sites used for air temperature and total precipitation measurements for the seasonality comparison.

Site Name, Province	Latitude	Longitude
Lac La Biche Climate, Alberta	54.8° N	112.0° W
La Ronge, Saskatchewan	55.1° N	105.3° W
Churchill Climate, Manitoba	58.7° N	94.1° W
Moosonee, Ontario	51.3° N	80.6° W

Figure C.2 shows the mean 2010–2015 seasonal pattern of natural methane emissions constrained by ECCC and GOSAT data corresponding to Fig. 4.6 in the main text. These emissions are compared to monthly mean air temperature and precipitation averaged over the four climatological stations in Table C.1. We consider air temperature a reasonable proxy for the surface skin temperature that is used in WetCHARTS. Surface skin temperature is itself a proxy for soil temperatures deeper beneath the surface where methane is produced (Miller et al., 2016). Hence both metrics may be lagging indicators for the peak of methane emissions. Both air temperature and precipitation show peaks in July which correspond well with the maxima of methane emissions in the prior from WetCHARTS. Methane emissions in the prior begin to accelerate from March to April, however for both months air temperature is below freezing. It is not likely that soil temperatures and subsurface soil temperatures would be above freezing in these months. Air temperature crosses from below 0° to above freezing one month later from April to May, which corresponds to where the posterior ECCC and GOSAT emissions begin to accelerate. Total precipitation shows the highest acceleration one month later from May to June. As the peak in July is passed, late-summer and autumn air temperatures are higher than the months opposite of the peak (August is warmer than June, September is warmer than May, October is warmer than April). This pattern is corroborated by the precipitation measurements. Air temperatures go below freezing from October to November. As shown by Zona et al. (2016), “zero-curtain” emissions may continue even when the soil is at freezing temperatures. This mechanism may be more likely to occur in the months after the peak if subsurface soils are slower to thaw in the spring and slower to freeze in the autumn. These simple climatological measurements and the described mechanisms suggested in other studies corroborate our posterior

results of lower spring methane emissions and lower peak methane emissions in the summer. Our results suggest process models may benefit from better parameterization of possible lagging effects from air temperature and precipitation for Boreal Canada methane emissions.

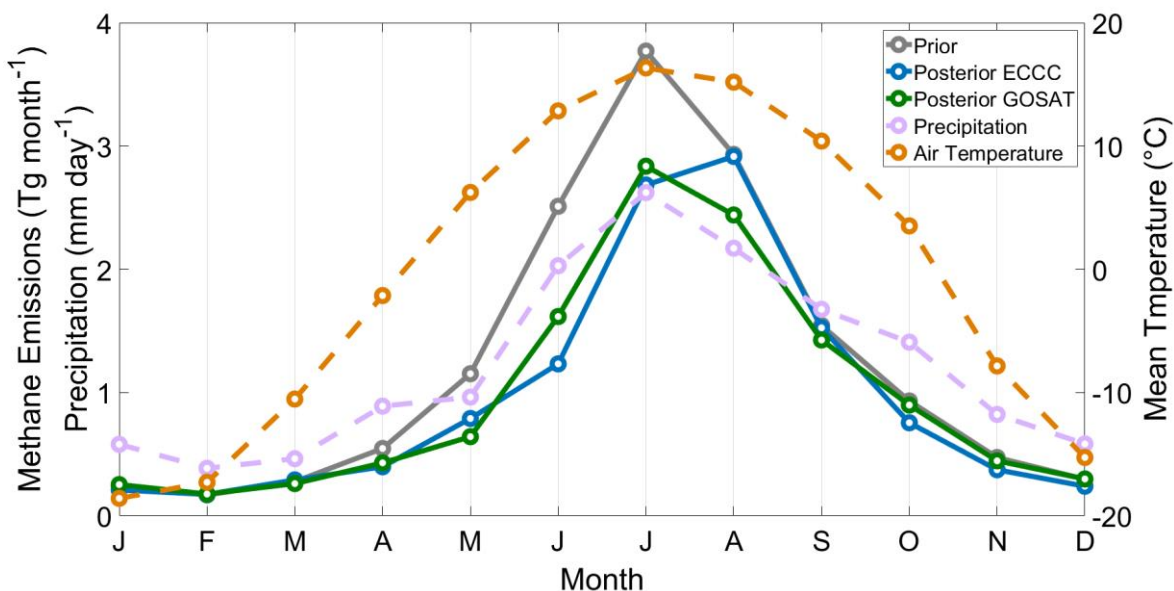


Figure C.2: Mean seasonal pattern of 2010-2015 methane emissions from the prior (gray), posterior constrained with ECCC data (blue), posterior constrained with GOSAT data (green). This is compared to the seasonal pattern of monthly mean air temperature (orange, right axis) and precipitation (pink, left axis) from station measurements listed in Table C.1. Both air temperature and precipitation show an asymmetry about the July peak, with higher temperature and precipitation in the fall months than the spring.

C.3 Evaluation of bias in the global model

In this section we test the GEOS-Chem representation of background methane for both surface ECCC data and column GOSAT data using global and/or boundary condition observations. We show the model representation of methane can be improved using surface and

column bias corrections which are presented as the base case in the main text. We test the sensitivity of the posterior emissions to the use of these bias corrections and show the inversions produce consistent results.

C.3.1 Evaluation of the ECCC surface data background and bias corrections

The left panel of Figure C.3 shows the comparison of monthly mean GEOS-Chem surface methane concentrations and methane measured at the ECCC station ESP from 2009 to 2015. ESP is located at the west coast of Vancouver Island (Fig. 4.1); this site is used as an evaluation of background methane and tests the bias in the global model as it is the least sensitive to Canadian emissions due to westerly prevailing winds. The model reliably reproduces surface observations at this station and the growth rate in background methane due to the source-sink imbalance of $+13 \text{ Tg a}^{-1}$ in the model global budget (Maasakkers et al., 2019) with a small mean model-observation bias of $+5.3 \text{ ppb}$. The right panel of Figure C.3 shows the comparison of modelled methane to NOAA aircraft profiles at the same site. Aircraft profiles occur approximately once a month continuously over the study period. The data is not averaged here and is directly compared to GEOS-Chem simulated grid boxes at the pressure level of the measurement. The reduced mean axis (RMA) regression shows a slope of 0.86 and a coefficient of regression $r^2 = 0.67$ which shows a reasonable model representation of the measurements. These statistics are consistent with previous inversions using GEOS-Chem that showed relatively unbiased conditions against NOAA surface stations globally (Turner et al., 2015; Maasakkers et al., 2019). A high resolution inversion over North America over the same 2010–2015 time-period using the same prior have shown adjustments to US emissions near the Canadian border are relatively minimal (Maasakkers et al., 2021), so we treat US emissions as constant in the inversion. The acceptable reproducibility of background methane at this site allows us to attribute much larger differences observed at other sites, up to a maximum of $\sim 1000 \text{ ppb}$ in the summer (Figure 4.4), to Canadian emissions which are optimized using Canadian observations while holding other global emissions constant.

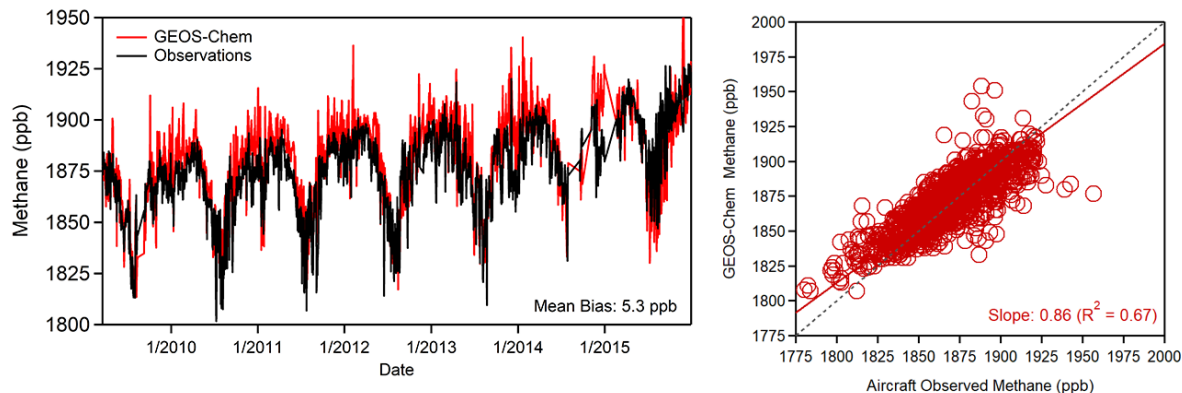


Figure C.3: Time-series comparison (left) from 2009–2015 of surface GEOS-Chem simulated methane (red) and measured in situ methane (black) at site ESP off the west coast of British Columbia. Comparison to NOAA aircraft profiles (right) from 2009–2015 at the same site using a reduced major axis (RMA) regression along with the 1:1 line (black).

While the mean model bias of +5.3 ppb in Figure C.3 shows a net over-estimation in the model, the later years 2014 and 2015 show a model underestimation primarily due to underestimated tropical emissions (Maasakkers et al., 2019). This positive-to-negative difference in the model background can project errors onto the trend of ECCC-constrained emissions. This is addressed by removing the annual-mean background bias at the Canadian boundary conditions from the observation vector. We use the westmost boundary condition site ESP and a second northernmost background site at Alert, Nunavut (ALT) to diagnose errors in the methane background and show the annual mean model-observation differences in Table C.2. The average of these two sites is used to adjust the model for the base-case ECCC inversion in the main text. In Section C.3.2 of the Supplement, we test the sensitivity of the posterior emissions to the use of these various background corrections and show consistent results, with the background-adjusted inversion showing slightly more agreement with the GOSAT inversion.

Table C.2 Mean annual model-measurement differences at background sites ESP and ALT.

Year	Mean Model–Measurement Difference (ppb)		
	ESP ^a	ALT ^b	Average ^c
2010	+5.0	+8.8	+6.9
2011	+5.8	+8.5	+7.2
2012	+3.6	+5.9	+4.8
2013	+2.6	+10.5	+6.6
2014	+2.1	+11.3	+6.7
2015	−6.9	−4.7	−5.8

^aSite ESP is located at 49.38°N, 126.54°W, and is the westernmost boundary condition for Canada.

^bSite ALT is located at 82.45°N, 62.51°W, and is the northernmost boundary condition for Canada.

^cThe average is used in the base-case ECCC inversions shown in the main text. The three alternatives: adjustments using ESP, ALT and no background adjustments are shown as sensitivity tests in the Supplement.

C.3.2 Sensitivity tests of ECCC-constrained emissions

Figure C.4 shows the sensitivity tests comparing the ECCC inversions with an unadjusted model to the two background-adjusted ECCC inversions using either the mean yearly bias from ESP or ALT. The three inversions are consistent with each other within their error intervals, but the adjusted ECCC inversions show improved agreement with the GOSAT results. For anthropogenic sources, the mean yearly emissions are $6.0 \pm 0.4 \text{ Tg a}^{-1}$ in the unadjusted ECCC inversion, $6.1 \pm 0.4 \text{ Tg a}^{-1}$ with the ESP-adjusted ECCC inversion, and $6.0 \pm 0.4 \text{ Tg a}^{-1}$ with the ALT-adjusted inversion. For natural sources, the mean yearly emissions are $10.5 \pm 1.9 \text{ Tg a}^{-1}$ in the unadjusted ECCC inversion, $12.0 \pm 1.4 \text{ Tg a}^{-1}$ in the ESP-adjusted ECCC inversion, and $11.0 \pm 1.2 \text{ Tg a}^{-1}$ in the ALT-adjusted ECCC inversion. The background-adjusted inversions show higher natural emissions in the years 2010–2014 compared to the unadjusted case, and lower natural emissions in 2015 due to the negative background bias that is removed. The background-adjusted inversions show better agreement with the GOSAT mean yearly natural emissions of $11.7 \pm 1.2 \text{ Tg a}^{-1}$. In addition, the trend in natural emissions over this time period is reduced by 40–45% from 1.0 Tg a^{-1} in the unadjusted inversion to $0.55\text{--}0.60 \text{ Tg a}^{-1}$ in the adjusted inversions. These results show that the background error does not largely affect the average 2010–2015 results regarding the overall increase in anthropogenic emissions and decrease in

natural emissions. Correcting for the model background minimizes the projection of underestimated tropical emissions onto the Canadian fluxes in the later years, which improves the consistency with the GOSAT inversion and significantly reduces the presence of a large trend that was not corroborated by GOSAT.

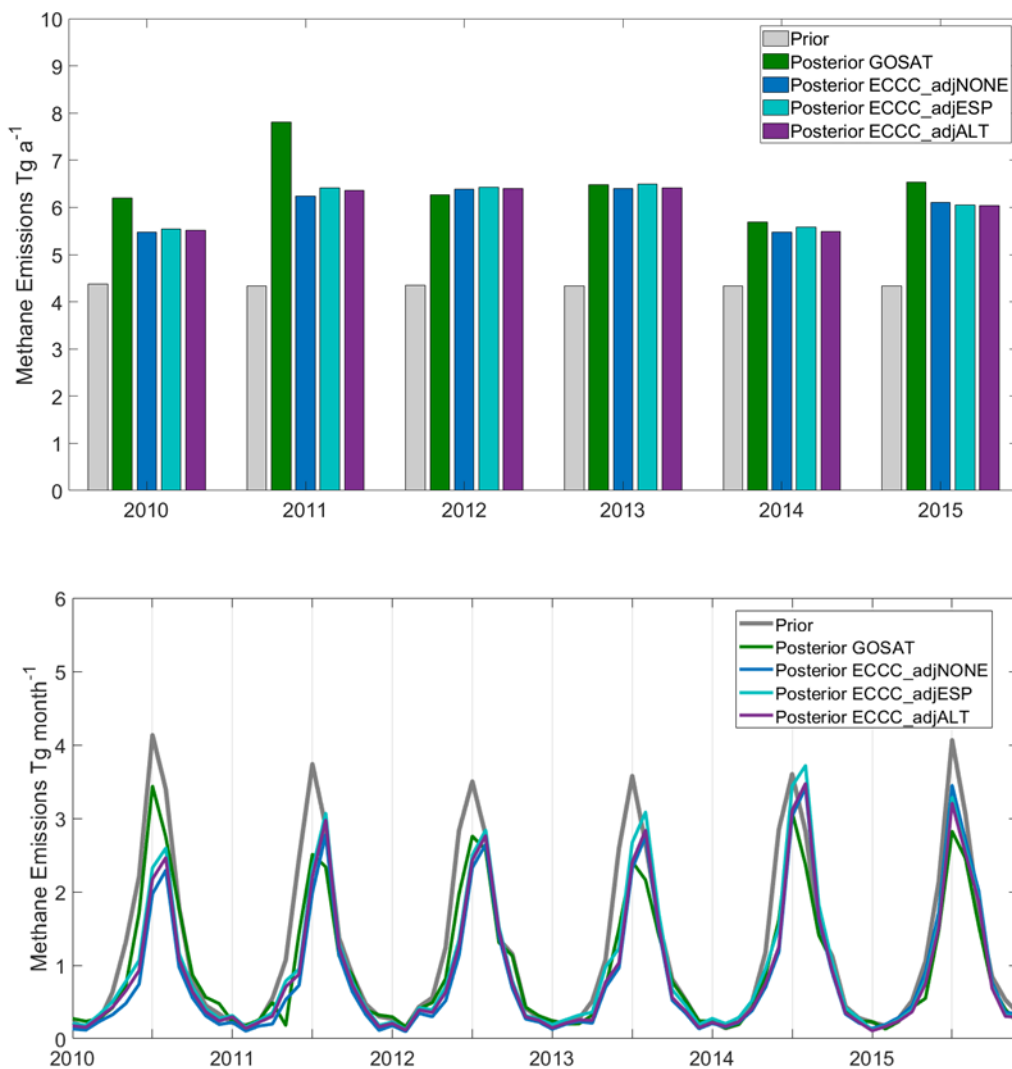


Figure C.4: Sensitivity analysis of inversion results depending on the use of model background correction for surface pixels. Referred to as the monthly inversion, this approach optimizes annual total Canadian anthropogenic emissions (top) and monthly total natural emissions

(bottom) in an $n = 78$ state-vector element setup. The prior emissions (gray) are compared to the posterior results using GOSAT (green), and the posterior using ECCC data with an unadjusted background (blue), ECCC data using a background adjusted according to the yearly difference at ESP (teal) and ALT (purple) from Table C.2.

To address the possibility of US emissions influencing the posterior results near the Canadian border, we show a sensitivity test where the two stations most influenced by cross-border transport, Egbert (EGB) and Sable Island (SBL) are removed from the ECCC inversion. Figure C.5 shows posterior-ECCC emissions where EGB and SBL (at latitudes of 44.2°N and 43.9°N , respectively) are removed (note in this case, the background is left un-adjusted to avoid overlap in the issues). The mean of anthropogenic emissions in the inversion without these stations is $6.4 \pm 0.6 \text{ Tg a}^{-1}$, and the mean of natural emissions is $10.9 \pm 1.5 \text{ Tg a}^{-1}$. These results are similar to the posterior from the unadjusted ECCC inversion ($6.0 \pm 0.4 \text{ Tg a}^{-1}$ anthropogenic, $10.5 \pm 1.9 \text{ Tg a}^{-1}$ natural) and the GOSAT inversion ($6.5 \pm 0.7 \text{ Tg a}^{-1}$ anthropogenic, $11.7 \pm 1.2 \text{ Tg a}^{-1}$ natural). This sensitivity test shows that the US signal does not substantially affect the results from the optimization of large biases observed by Canadian observations due to Canadian emissions.

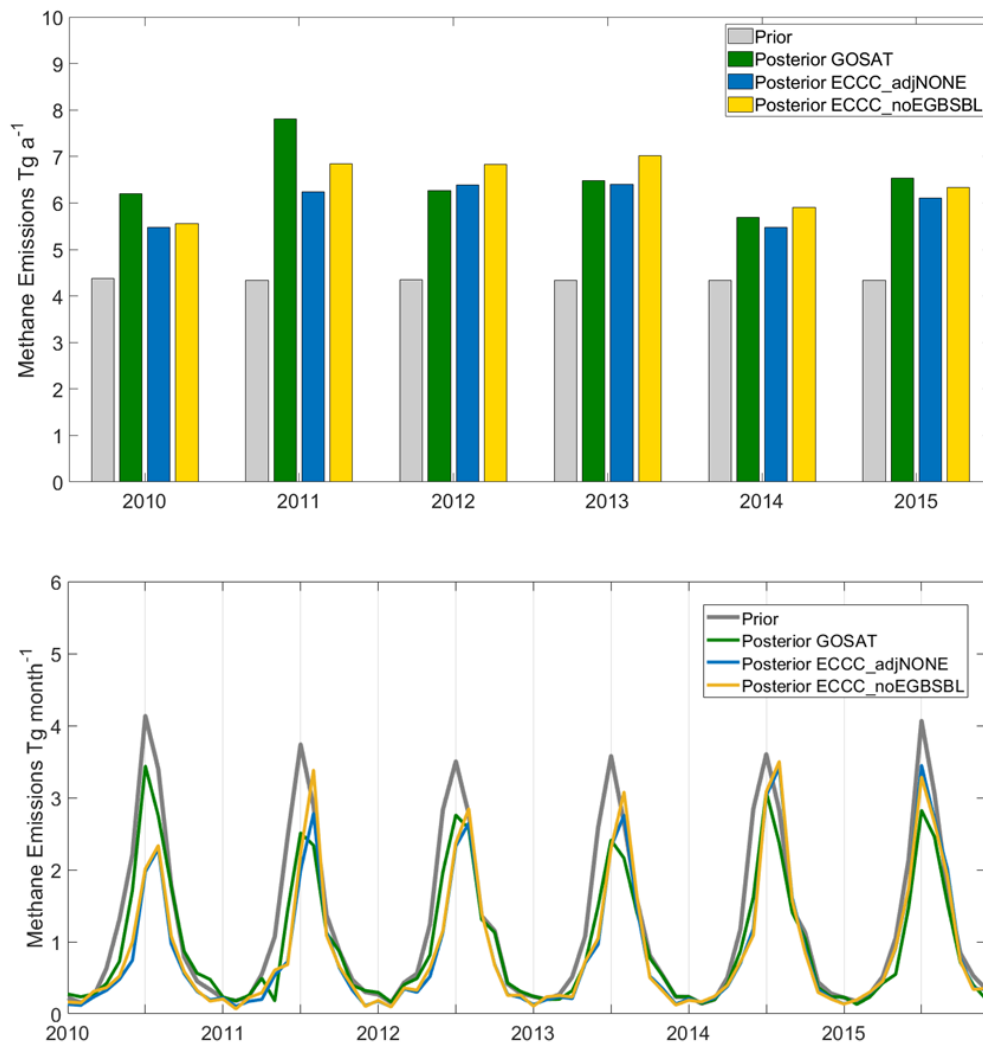


Figure C.5: Sensitivity analysis of inversion results depending on the inclusion of sites EGB and SBL which are sensitive to cross-border transport from the United States. Similar to Fig. C.4, the monthly inversion optimizes annual total Canadian anthropogenic emissions (top) and monthly total natural emissions (bottom) in an $n = 78$ state-vector element setup. The prior emissions (gray) are compared to the posterior results using GOSAT (green), and the posterior using ECCC data including all sites (blue) and ECCC data excluding EGB and SBL (yellow).

C.3.3 Evaluation of Global GOSAT Data and Bias Corrections

The GEOS-Chem simulation of column averaged methane shows three global biases previously discussed in the literature: (1) a latitude-dependent bias, (2) a seasonal bias and (3) a background change for 2014 and 2015 due to differences in the global source-sink imbalance in these two years (Turner et al., 2015; Saad et al., 2018; Maasakkers et al., 2019; Stanevich et al., 2020). We apply these corrections to the simulated column of methane on a global basis to produce an unbiased background for our target Canadian domain (45° N to 60°N, 50° W to 150° W). The latitude-dependent bias (1) is likely due to excessive polar stratospheric transport (Stanevich et al., 2020). We correct for this bias by fitting the model-GOSAT difference for global 2° × 2.5° grid cells according to a second-order polynomial as shown in Figure C.6:

$$\xi = (2.2\theta^2 - 34\theta) \times 10^{-3} - 2.7 \quad \text{\{C.1\}}$$

where ξ is the resulting bias correction in ppb and θ is latitude in degrees. The correction in this work for the latitude bins of our target domain (45° N to 60° N) is between 0.3 to 2.9 ppb. This correction is lower than what has been shown previously (Turner et al., 2015; Maasakkers et al., 2019) and we attribute this improvement to our use of a 2°x2.5° gridded simulation instead of a 4°x4.5° as recommended by Stanevich et al. (2020) to reduce transport errors. A seasonally oscillating bias (2) remains after this correction. The seasonal bias has an amplitude of ± 4 ppb with repeating maxima in June and minima in December. It is not clear whether this seasonal bias is due to emissions and/or transport errors. In our base case we remove the seasonal bias on a monthly basis following Maasakkers et al. (2019) and show a sensitivity test without the correction for our inversion of monthly natural emissions in Canada (Supplement C.3.4). Inversion results using GOSAT data with and without bias corrections in the model simulation of total column methane do not show major differences (Fig. C.7). These scenarios all show agreement with the posterior emissions adjustments determined using unadjusted ECCC in situ data – which is a useful benchmark since modelled methane at the surface is not subject to any bias corrections. The background change (3) that appears in the simulated methane column from

2014 onwards is corrected for in Maasakkers et al. (2019) by optimizing emissions, emissions trends and trends in OH using a global inversion. In that work correction factors do not appear over Canada and the United States that would significantly influence the global change in atmospheric methane, and the main adjustment in 2014 and 2015 were to tropical wetland emissions and OH. Here we treat this as a background change and apply a uniform correction to the simulated column since emissions outside of Canada and changes in OH are treated as fixed in our Canada-focused inversion. The background change (3) is 5 ppb in 2014 and 10 ppb in 2015. The right panel of Figure C.6 shows the latitude dependent bias correction and the left panel shows the resulting global time-series of GEOS-Chem total column methane from 2010–2015 after corrections are applied. The global GEOS-Chem – GOSAT differences in the methane column can be limited globally to within 10 ppb without including the seasonal bias correction, and within 5 ppb with its inclusion. This shows a steady background in methane for the entire time period from 2010–2015 so global emissions do not affect the optimization of Canadian emissions. While biases within 10 ppb have been treated as acceptable for methane inversions (Buchwitz et al., 2015), we evaluate our GOSAT inversion results against inversions with independent ECCO in situ measurements that do not require any bias corrections in the model to produce more robust emissions estimates.

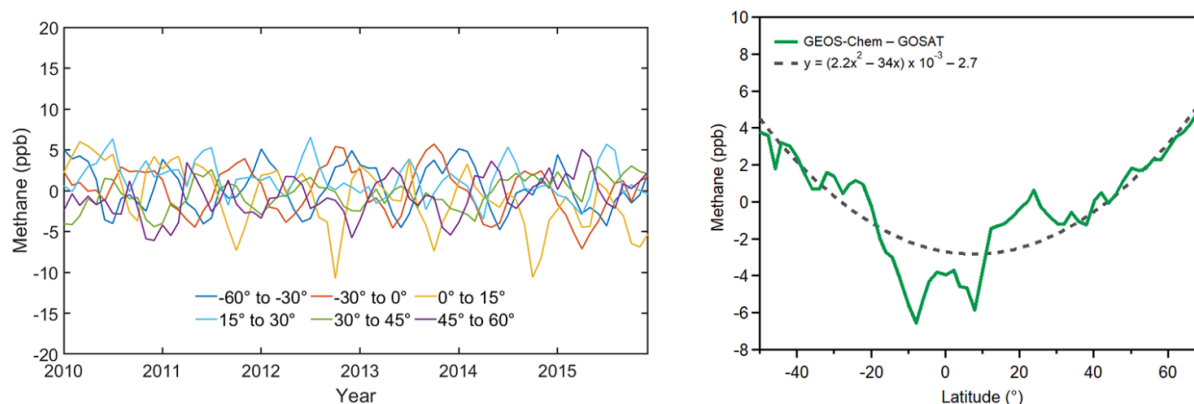


Figure C.6: Time series (left) from 2010–2015 of the difference between GEOS-Chem simulated total column methane and GOSAT observations after applying bias corrections, showing a consistent global background for methane. Data used in the inversion for Canada is from 45° N to 60° N (purple line) and shows acceptable differences within 5 ppb over the entire global latitude band. To produce the left figure, the latitude-dependent bias (right) is shown with the polynomial correction that is applied (gray dash) that is within a magnitude of 0.3 to 2.9 ppb for the same latitude.

C.3.4 Sensitivity tests of GOSAT-constrained emissions

We test the sensitivity of the posterior GOSAT-constrained methane emissions in our analysis to the use of latitude-dependent and seasonal bias corrections in the GEOS-Chem simulated total column of methane. The latitude-dependent bias correction has a magnitude less than 3.5 ppb for our domain of interest (45 to 60°N). On a global basis the seasonal bias correction has an amplitude of ± 4 ppb with a maximum in June and a minimum in December. Figure C.7 shows the sensitivity of posterior monthly emissions to these bias corrections using 2013 as an example. We show four versions of the posterior methane emissions using GOSAT data: GOSAT11 (green) is the base case which applies the latitude-dependent bias correction and the seasonal bias correction, GOSAT10 (purple) applies the latitude-dependent bias correction and does not apply the seasonal correction, GOSAT01 (orange) does not apply the latitude-dependent bias

correction and applies the seasonal correction, and GOSAT00 (light blue) uses neither bias correction. The range of emissions from all four examples is 9.7 – 10.7 Tg a⁻¹, which are all consistent with the unadjusted ECCC emissions of 10.0 Tg a⁻¹ and lower than the prior emissions of 14.3 Tg a⁻¹. Not applying the latitude-dependent bias correction results in a decrease in the resulting emissions and maintains the same seasonal pattern. Not applying the seasonal bias correction results in a change in the temporal distribution of emissions that better matches the August peak in the posterior with ECCC data. Emissions are lower than the base case in the spring and higher than the base case in autumn. This change enhances the autumn-shift in emissions that has been described in Section 4.3.2 of the main text. While this may be more consistent with our interpretations, it is not clear whether the difference is due to emissions or transport biases. Stanevich et al. (2020) showed that the latitude dependent bias is most likely due to excessive polar stratospheric transport at high latitudes. If the seasonal bias is indeed due to mischaracterized natural emissions, it is not clear why the bias would be equally large in December (–4 ppb) as June (+4 ppb) on a global basis. The magnitude of natural emissions in December is much lower than June and emissions mischaracterization would not itself produce an equally large bias as the largely overestimated summertime emissions. Our analysis with ECCC data shows most of the adjustments to wetlands are in the peak of summer with some extension into the autumn. These results show that the bias corrections produce minor differences in the magnitude and seasonal pattern of emissions.

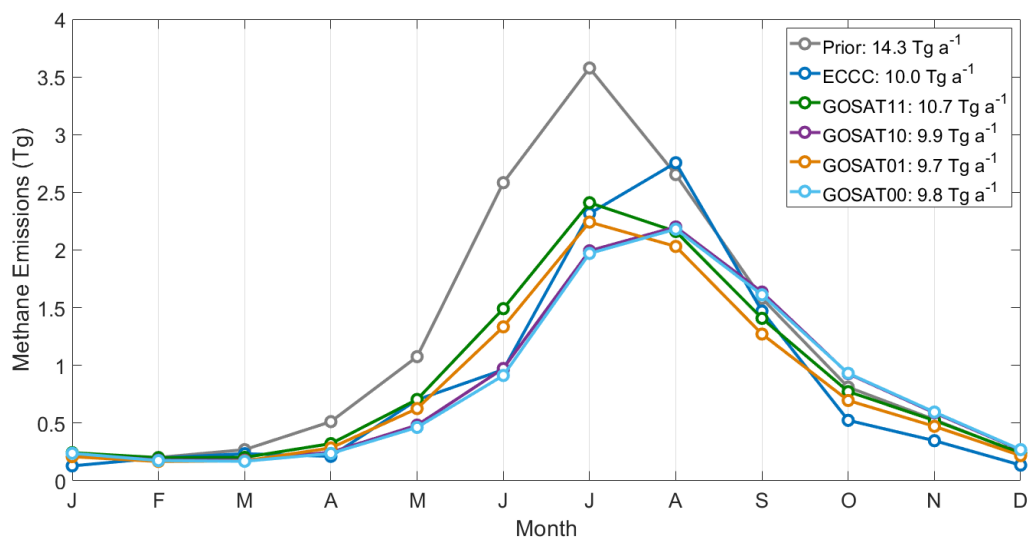


Figure C.7: Sensitivity of 2013 posterior GOSAT constrained methane emissions to bias corrections used in the GEOS-Chem simulated total column of methane. For comparison, the prior in 2013 (gray) and the posterior in 2013 constrained by ECCC data (unadjusted, blue) are shown. The digits in the GOSAT label represent the binary use of bias corrections (1 = applied, 0 = not applied). The first digit corresponds to the use of the latitude bias correction, the second digit corresponds to the use of the monthly bias correction, hence GOSAT11 is the base case that applies both bias corrections and GOSAT00 is the case with no bias corrections applied.

C.3.5 Evaluation of the prior and posterior fluxes using global observations outside of the Canadian domain

The inverse model design in this study uses a simplified approach, where Canadian emissions are optimized using only observations in Canada. The results from this approach may be sensitive to errors in the global model projected onto the Canadian domain if errors in the global model are sufficiently large relative to the local biases in Canada (Figure 4.4 in the main text) and the observational error used in the inversion procedure (16 ppb for GOSAT, 65 ppb for ECCC). Figure C.8 shows an independent evaluation of the prior global model and the posterior in this study to 2010–2015 background observations from the NOAA cooperative flask sampling network (<https://gml.noaa.gov/ccgg/flask.html>) outside of the Canadian domain. We use a simple

version of the posterior where Canadian anthropogenic emissions are scaled up by 37% to 6.0 Tg a⁻¹ and natural emissions are scaled down by 24% to 11.2 Tg a⁻¹. This captures the central results of the monthly, sectoral, and provincial inversions in the main text and avoids a large number of model comparisons. The analysis shows that the prior model reasonably reproduces the methane background, and the posterior from adjusted Canadian emissions does not degrade this result. In the reduced-major axis regression, the prior r^2 coefficients are in the range of 0.77–0.92 and the prior slopes are in the range of 0.94–0.97 across the three surface, ship, and aircraft datasets. In the posterior, the r^2 is in the range of 0.76–0.91 and the slope is in the range of 0.93–0.96. The posterior reflects a decrease of 2.0 Tg a⁻¹ in the global budget due to a net decrease in Canadian emissions, which is shown in the improvements to the mean bias comparisons. This decrease in emissions slightly improves the global model agreement with independent data in the years 2010–2013 (since the model overestimates emissions) and slightly degrades the agreement in 2014–2015 (since the model underestimates tropical emissions), which is understandable considering only Canadian emissions are adjusted and the global model is not optimized. A net decrease in Canadian emissions is consistent with previous global inversion studies using GEOS-Chem (Turner et al., 2015; Maasakkers et al., 2019). The results from the Canada-focused inversion with subnational details in this study show that the net-decrease in Canadian natural emissions masks an increase in anthropogenic emissions in Western Canada which should be considered in global inverse studies.

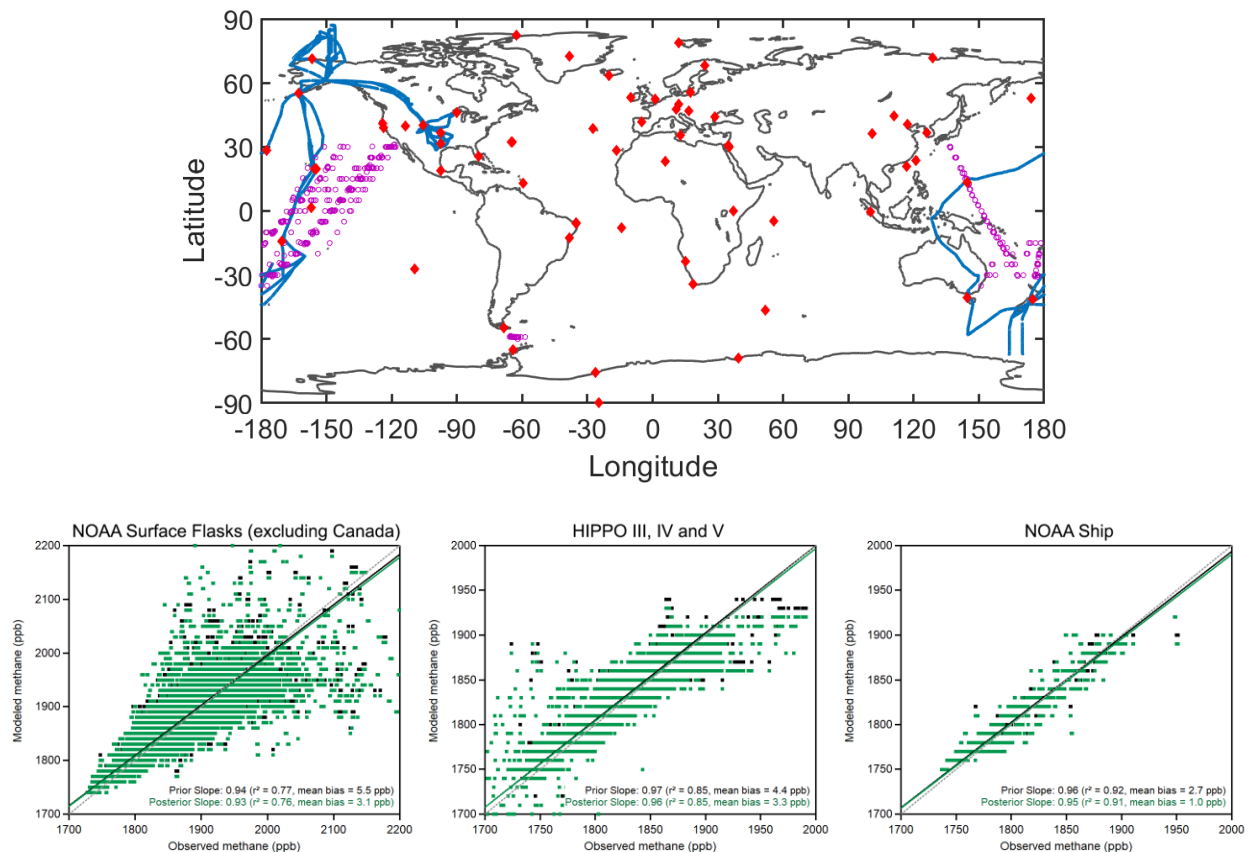


Figure C.8: Model comparison to independent NOAA observations globally from 2010–2015. The top panel shows data used in the global model comparison. Red diamonds indicate NOAA surface flasks, purple circles indicate NOAA ship data, and blue lines indicate HIPPO III, IV and V aircraft data. Comparison of the prior and posterior emissions in GEOS-Chem is shown using a reduced-major axis regression against NOAA Surface flasks (bottom-left), HIPPO III, IV and V aircraft data (bottom-middle), and NOAA Ship data (bottom-right).

C.4 Diagnostics of Sectoral and Provincial Inversions

In this analysis we first evaluate the correlations and/or independence of the state vector elements from the posterior error covariance matrix $\hat{\mathbf{S}}$ as follows (Heald et al., 2004):

$$r_{ij} = \frac{\hat{s}_{ij}}{\sqrt{\hat{s}_{ii}} \sqrt{\hat{s}_{jj}}} \quad \{\text{C.2}\}$$

The error-normalized posterior correlation matrix \mathbf{r} provides information on the independence of the state vector elements. This is corroborated by the averaging kernel matrix \mathbf{A} which shows which state vector elements contain independent pieces of information, with the trace of \mathbf{A} providing the total degrees of freedom for signal for the inversion. To further evaluate the signal-to-noise ratio of the observation-constrained state vector elements and their independence from each other we use an eigenanalysis. The Jacobian matrix \mathbf{K} is normalized about the observational and prior error covariance matrices as follows (Rodgers, 2000):

$$\check{\mathbf{K}} = \mathbf{S}_o^{-1/2} \mathbf{K} \mathbf{S}_a^{1/2} \quad \{\text{C.3}\}$$

The singular value decomposition of $\check{\mathbf{K}}$ gives its rank which is the number of singular values greater than one. The singular values also correspond to the signal-to-noise ratio of state vector elements and hence quantify the strength of the observational constraints on individual emissions categories.

Figure C.9 shows this series of diagnostics for the sectoral (5 state vector element) inversion and Figure C.10 shows the same analysis for the provincial (16 state vector element) inversion. Figure C.9 (top left) shows the error-normalized correlation matrix for the sectoral inversion. The most important result is that the primary source of natural emissions, wetlands, is not correlated with the primary source of anthropogenic emissions, energy. Within the anthropogenic category however, we see that energy is strongly correlated with agriculture, showing that these

two elements cannot be distinguished by the observation system. For natural emissions, other natural sources are weakly correlated with wetlands and are not completely independent. Emissions from waste are shown to be slightly more independent and can be distinguished from the other sources. The averaging kernel matrix corroborates this result, and shows the three independent pieces of information are energy, wetlands and waste, with partial information content from other natural sources and a lack of information on agriculture. The singular values show strong constraints on wetlands with a signal-to-noise ratio of 37.3, and strong constraints on energy with a signal-to-noise ratio of 5.2. Waste sources are 2.2, other natural are 1.2 and agriculture is below the noise at 0.4. These diagnostics demonstrate that a joint ECCC in situ and GOSAT satellite inversion system can successfully provide constraints on and distinguish the three major categories of methane emissions in Canada: wetlands, energy and waste. Emissions from agriculture cannot be distinguished in this system and should be aggregated with energy, this is likely because of the strong spatial overlap between these emissions in Western Canada and the lower signal from lower magnitude agriculture emissions. Emissions from other natural sources (biomass burning, seeps, and termites) also are at the noise and should be aggregated with wetlands. This is because minor natural sources are much lower in magnitude (0.8 Tg a^{-1} out of 14.8 Tg a^{-1}) and also show spatial overlap with wetlands.

Figure C.10 shows the diagnostics on the provincial (16 state vector element) inversion. This choice of state vector elements challenges the observing system and results in a largely underdetermined solution. These diagnostics allow us to identify where the limitations of the ECCC + GOSAT observing system are. The posterior error correlation matrix r shows the provincial emissions are somewhat correlated a) between anthropogenic/natural emissions of the same province and b) with neighboring provinces in the same category of emissions. For example, AB anthropogenic emissions show a small inverse correlation with AB natural emissions. AB anthropogenic emissions also show a small correlation with the anthropogenic emissions of nearby provinces BC and SK. For the natural emissions, natural emissions within a province in most cases extend correlations into the provinces to the east and west. These correlations are not as large as the case of Energy and Agriculture emissions in Fig. C.9, and show a more moderate influence of nearby provinces on the optimized emissions. The primary

limitation of the provincial inversion is the inability to distinguish provinces with a very small magnitude of emissions. This is shown in the averaging kernel matrix, which has a degrees of freedom for signal of 7.9 out of 16 elements. The 6 regions that are best constrained are AB anthropogenic, ON anthropogenic, AB natural, SK natural, MB natural, and ON natural, with partial constraints on BC anthropogenic, SK anthropogenic, QC anthropogenic, BC natural, QC natural and NOR natural. The singular vectors corroborate this result and show that there are 8 regions that are above the noise and 8 that are at or below the noise. The best constraints on anthropogenic emissions are in Alberta, with a signal to noise ratio as good as 15.1 (solid blue line), followed by Ontario (2.5-2.8).

These diagnostics show that the ECCC+GOSAT observing system for Canada is limited in its ability to characterize agricultural emissions, and somewhat limited in its ability to characterize non-wetlands natural emissions. Hence we present Energy+Agriculture and Wetlands+Other Natural together for our conclusions. More precise and more dense measurements at a finer scale would better disaggregate these sources, although the use of the precise in situ data is primarily limited by the model error (Section 4.2.3 of the main text). In the provincial inversion, the observing system provides good constraints on anthropogenic emissions from AB and ON and is capable of distinguishing these emissions from natural sources in the same province. However, anthropogenic sources from other provinces with much lower emissions cannot be distinguished. Natural emissions can be characterized from the provinces that are most responsible for wetland emissions (AB, SK, MB, ON), however the observing system struggles in Atlantic and Northern Canada where the surface and satellite observations we use are limited. The emissions adjustments to state vector elements beneath the noise are due to aliasing with other sources and compensation effects due to interprovincial transport. We limit our conclusions to simple interpretations, we use the limited provincial inversion for spatial attribution to show higher posterior anthropogenic emissions are primarily from the total in Western Canada (BC+AB+SK+MB), and not emissions in Central Canada (ON+QC).

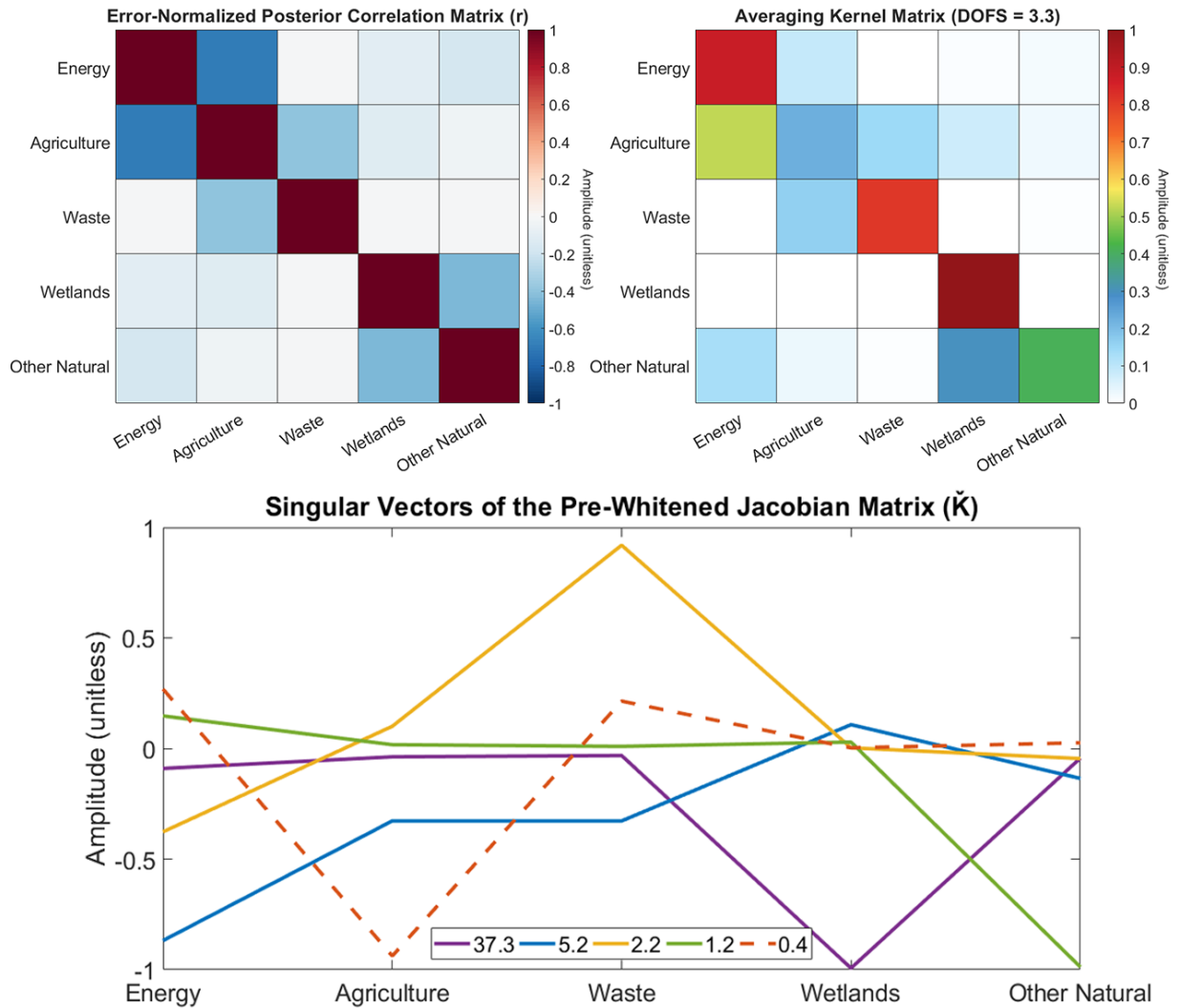


Figure C.9: Diagnostics of the sectoral inversion used to evaluate the independence and information content of the 5 state vector elements. The error-normalized posterior correlation matrix (top left) shows the correlations between elements. The averaging kernel matrix (top right) shows where the independent pieces of information are (DOFS = 3.3). The singular vector decomposition of the pre-whitened jacobian (bottom) quantifies the signal-to-noise ratio of the significant elements – these are the singular values listed above one (4 in total). The singular vector below noise (agriculture) is shown as a dashed line.

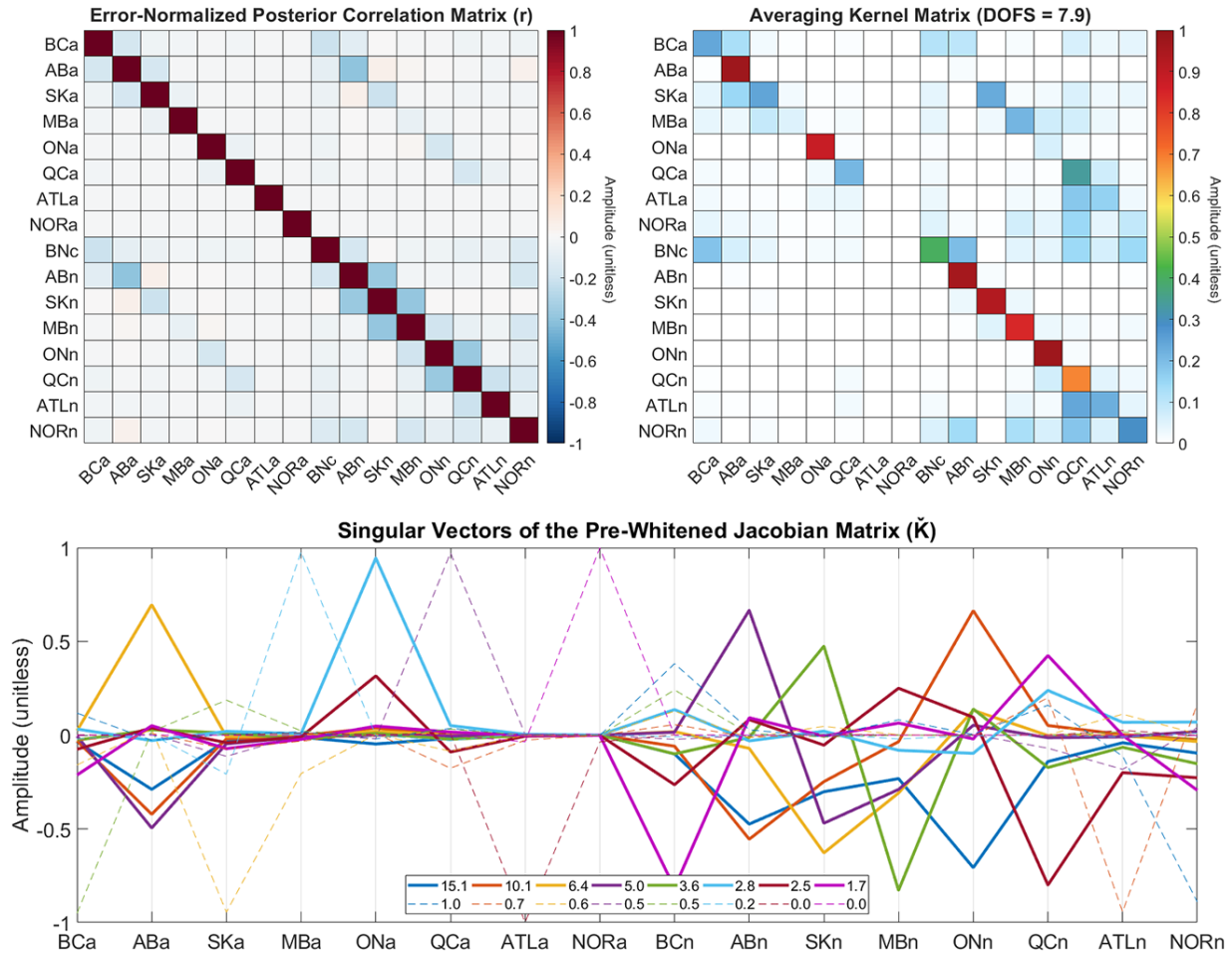


Figure C.10: Similar to Fig. C.9 for the 16 state vector provincial inversion. The DOFS from the averaging kernel matrix are 7.9, which are consistent with the number of singular values greater than unity in the pre-whitened jacobian matrix (8 in total). In the bottom panel, the singular vectors below the noise (corresponding to singular values less than one) are shown as light-dashed lines, these show which emissions are not constrained by observations.

A possible solution to improving the resolution of the solution is to combine all six years of data to constrain finer scale emissions for the sectoral and provincial inversions. In the presented approach inversions were completed on a yearly basis for six years to produce an average result for 2010–2015. We used the year to year variance as a representation of noise in the system and real yearly variability in the state (due to emissions and/or transport). In principle using more years of data provides a better signal to noise ratio. However, due to the way our state vector elements are defined in the sectoral and provincial inversions, the inverse approach is sensitive to aggregation error and overfitting the fewer number of well-defined state vector elements. Overfitting can be diagnosed using the reduced chi-squared metric:

$$\chi_v^2 = \frac{\chi^2}{v} \cong \frac{\sum \frac{(y-Kx)^2}{S_o}}{m} \quad \{C.4\}$$

Where χ_v^2 is the chi-square per degree of freedom v . Here, the χ^2 is equal to the ratio of the square of the innovation, S_o is the diagonal element of the observational error covariance matrix corresponding to the same observation, m is the number of rows of the observation vector and n is the number of state vector elements. A value of χ_v^2 less than one indicates overfitting. We calculate a value of 0.65 for the total vector containing ECCC and GOSAT data which shows evidence of overfitting. Hence using a larger amount of data for the same number of state vector elements would exasperate the issue.

We further test the improvement from combining 6 years of data against independent measurements. To evaluate the differences between using a repeated 1-year approach and a 6-year approach we use independent observations from NOAA ETL aircraft measurements and ECCC CHA in situ surface measurements. Table C.3 lists the metrics of agreement that were in Figure 4.8 and compares them to the results using all 6 years of data simultaneously, using inversions with no model background corrections for the ECCC observation vector. For the sectoral inversion, using 6 years of data provides a small improvement in the slope (0.96 vs. 0.91), no improvement in the R^2 (0.20) and degrades the mean bias (+4.3 ppb vs. +0.4 ppb) when

comparing to NOAA ETL. Similarly with ECCC CHA data, using 6 years of data for the sectoral inversion provides an improvement in the slope (1.01 vs. 0.98), a slightly worse R^2 (0.43 vs. 0.44) and largely degrades the mean bias comparison (+10.6 ppb vs. +5.9 ppb). For the provincial inversion evaluation at NOAA ETL, using 6 years of data slightly degrades the slope (0.83 vs. 0.86), gives an improvement in the R^2 (0.27 vs. 0.22), and degrades the mean bias (+3.2 ppb vs. +0.5 ppb). The same comparison at ECCC CHA degrades agreement in the slope (0.87 vs. 0.91), improves the R^2 (0.51 vs. 0.47), and improves the mean bias (+4.1 ppb vs. +4.9 ppb). These results show that using 6 years of data for the subnational inversions does not improve agreement against independent data and in many cases degrades the mean bias. The inversion converges on a solution within our defined prior error matrix \mathbf{S}_0 with only one year of data. These tests show that using one year of data at a time and calculating the average and variance of the repeated results is reasonable considering the limits of the observation system towards resolve low magnitude emissions.

Table C.3 Sensitivity test against independent observations

		NOAA Aircraft Observations ETL			ECCC Surface Observations CHA		
		Slope	R ²	Mean Bias (ppb)	Slope	R ²	Mean Bias (ppb)
Sectoral	Prior	1.15	0.14	+6.8	1.17	0.36	+16.4
	Posterior (1 yr)	0.91	0.20	+0.4	0.98	0.44	+5.9
	Posterior (6 yr)	0.96	0.20	+4.3	1.01	0.43	+10.6
Provincial	Posterior (1 yr)	0.86	0.22	+0.5	0.91	0.47	+4.9
	Posterior (6 yr)	0.83	0.27	+3.2	0.87	0.51	+4.1

We show a comparison of emissions estimates and methods to derive errors for the sectoral inversion in Table C.4 and for the provincial inversion in Table C.5. The tables compare two error estimates to three sensitivity tests. They show the error estimates from the diagonal elements of the posterior error covariance matrix $\hat{\mathbf{S}}$ and compares to the 1σ variance in the repeated yearly inversions. In both the sectoral and the provincial inversions, the error estimates from the diagonal elements of $\hat{\mathbf{S}}$ often show a more optimistic estimate of the uncertainties. This is likely due to spatial and temporal correlations in the daily-mean ECCC in situ observations and correlations in the GOSAT data that are difficult to quantify in the absence of a full OSSE study. We compare the 1σ variance from repeated yearly inversions from 2010–2015 to the relative change in posterior emissions from using only ECCC data, only GOSAT data, and using 6 years of ECCC+GOSAT data simultaneously. The 1σ yearly variance captures these differences except for state vector elements that were shown to be below the noise and highly correlated with other emissions in Figure C.9 and C.10. The lack of improvement against the comparison to independent data in Table C.3 suggests that this may be suggestive of overfitting. We consider the agreement between the independent use of ECCC and GOSAT data to be a reliable sensitivity test to check the robustness of our results.

Table C.4 Sensitivity analysis of the Sectoral (5 state vector) inversion. The error estimates from the posterior error covariance matrix are compared to the yearly variance and the change in emissions using alternative observation vectors.

	Prior (Tg a ⁻¹)	Posterior (Tg a ⁻¹)	Posterior \hat{S} Relative Error (%)	1 σ Yearly Variance Relative Error (%)	ECCC- only (% change)	GOS- only (% change)	6-year (% change)
Energy	2.4	3.6	±11	±25	+9	-6	-24
Agriculture	1.0	1.5	±28	±25	-1	-19	+64
Waste	0.9	0.8	±25	±25	-8	+50	-29
Wetlands	14.0	9.6	±4	±11	+3	+3	+2
Other	0.8	1.7	±20	±55	-31	-9	+69
Natural							

Table C.5 Sensitivity analysis of the Provincial (16 state vector) inversion. As per S4 error estimates from the posterior error covariance matrix are compared to the yearly variance and the change in emissions using alternative observation vectors.

	Prior (Tg a ⁻¹)	Posterior (Tg a ⁻¹)	Posterior Ŝ Relative Error (%)	1σ Yearly Variance Relative Error (%)	ECCC- only (%) change)	GOS- only (%) change)	6-year (% change)
BCA	0.5	0.8	±24	±41	-20	-11	+115
ABA	2.3	3.3	±5	±16	-6	+2	-2
SKA	0.3	0.3	±44	±37	+18	-1	+6
MBA	0.2	0.2	±50	±25	+2	+6	+22
ONA	0.5	0.5	±17	±14	-4	+11	+2
QCA	0.4	0.3	±51	±40	-4	+19	+14
ATLA	0.0	0.0	±51	±4	+1	+3	-8
NORA	0.0	0.0	±50	±1	0	0	+1
BCN	0.4	0.6	±32	±50	+2	+5	-76
ABN	2.4	1.9	±14	±34	+67	-29	-25
SKN	1.6	0.7	±28	±37	+7	-7	-4
MBN	1.5	1.4	±22	±32	+27	-6	-11
ONN	3.5	1.0	±32	±37	+12	-3	-13
QCN	1.6	1.2	±40	±41	+9	34	-51
ATLN	0.7	0.8	±39	±26	-29	+21	+48
NORN	0.7	1.9	±15	±35	-41	-2	+72

C.5 Combined ECCC+GOSAT Monthly Inversion

Figure C.11 shows the monthly inversion comparing the results from the ECCC-only inversion, the GOSAT-only inversion and the combined ECCC+GOSAT inversion. The mean 2010–2015 anthropogenic emissions in the combined inversion is 6.0 ± 0.4 Tg a⁻¹. The mean 2010–2015 total natural emissions in the combined inversion is 12.0 ± 0.9 Tg a⁻¹. The combined inversion agrees with the ECCC and GOSAT results and appears to follow the seasonality of natural emissions in the GOSAT-only inversion more closely. Combining the two datasets does not appear to improve the results of the individual inversions, hence the intercomparison between the ECCC-only and GOSAT-only inversions adds more value as a consistency test of the posterior results.

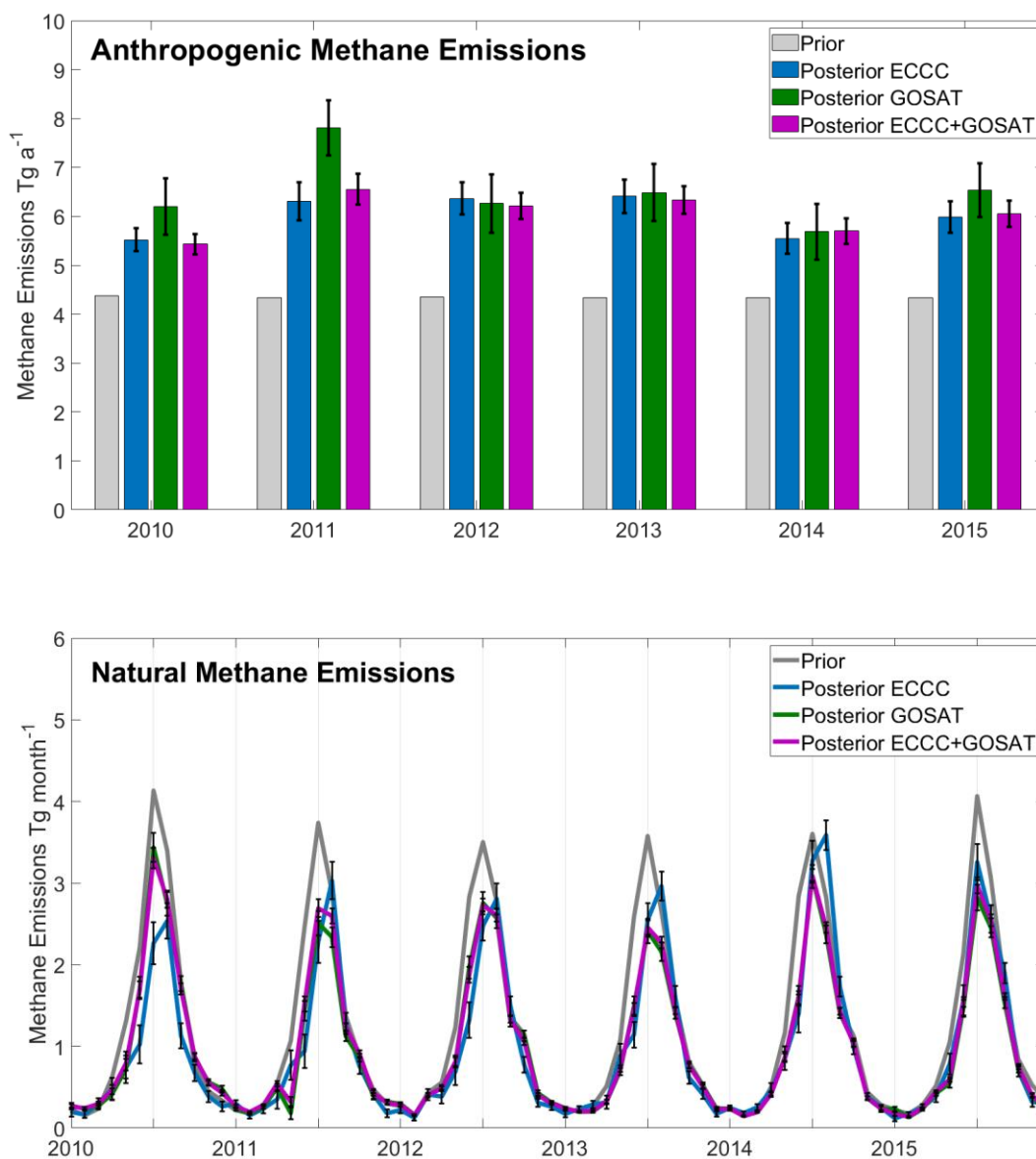


Figure C.11: Sensitivity analysis of the results from the monthly inversion including a comparison to the combined ECCC+GOSAT inversion. Following Fig. 4.4 in the main text, the monthly inversion optimizes annual total Canadian anthropogenic emissions (top) and monthly total natural emissions (bottom) in an $n = 78$ state-vector element setup. The prior emissions (gray) are compared to the posterior results using GOSAT (green), and the posterior combining both ECCC and GOSAT data (purple).

Supplement References

- Buchwitz, M., Reuter, M., Schneising, O., Boesch, H., Guerlet, S., Dils, B., Aben, I., Armante, R., Bergamaschi, P., Blumenstock, T., Bovensmann, H., Brunner, D., Buchmann, B., Burrows, J. P., Butz, A., Chédin, A., Chevallier, F., Crevoisier, C. D., Deutscher, N. M., Frankenberg, C., Hase, F., Hasekamp, O. P., Heymann, J., Kaminski, T., Laeng, A., Lichtenberg, G., De Mazière, M., Noël, S., Notholt, J., Orphal, J., Popp, C., Parker, R., Scholze, M., Sussmann, R., Stiller, G. P., Warneke, T., Zehner, C., Bril, A., Crisp, D., Griffith, D. W. T., Kuze, A., O'Dell, C., Oshchepkov, S., Sherlock, V., Suto, H., Wennberg, P., Wunch, D., Yokota, T. and Yoshida, Y.: The Greenhouse Gas Climate Change Initiative (GHG-CCI): Comparison and quality assessment of near-surface-sensitive satellite-derived CO₂ and CH₄ global data sets, *Remote Sensing of Environment*, 162, 344–362, doi:10.1016/j.rse.2013.04.024, 2015.
- Heald, C. L., Jacob, D. J., Jones, D. B. A., Palmer, P. I., Logan, J. A., Streets, D. G., Sachse, G. W., Gille, J. C., Hoffman, R. N. and Nehr Korn, T.: Comparative inverse analysis of satellite (MOPITT) and aircraft (TRACE-P) observations to estimate Asian sources of carbon monoxide: COMPARATIVE INVERSE ANALYSIS, *J. Geophys. Res.*, 109(D23), doi:10.1029/2004JD005185, 2004.
- Hutchinson, M. F., McKenney, D. W., Lawrence, K., Pedlar, J. H., Hopkinson, R. F., Milewska, E. and Papadopol, P.: Development and Testing of Canada-Wide Interpolated Spatial Models of Daily Minimum–Maximum Temperature and Precipitation for 1961–2003, *Journal of Applied Meteorology and Climatology*, 48(4), 725–741, doi:10.1175/2008JAMC1979.1, 2009.
- Maasackers, J. D., Jacob, D. J., Sulprizio, M. P., Scarpelli, T. R., Nesser, H., Sheng, J.-X., Zhang, Y., Hersher, M., Bloom, A. A., Bowman, K. W., Worden, J. R., Janssens-Maenhout, G. and Parker, R. J.: Global distribution of methane emissions, emission trends, and OH concentrations and trends inferred from an inversion of GOSAT satellite data for 2010–2015, *Atmos. Chem. Phys.*, 19(11), 7859–7881, doi:10.5194/acp-19-7859-2019, 2019.
- Maasackers, J. D., Jacob, D. J., Sulprizio, M. P., Scarpelli, T. R., Nesser, H., Sheng, J., Zhang, Y., Lu, X., Bloom, A. A., Bowman, K. W., Worden, J. R., and Parker, R. J.: 2010–2015 North American methane emissions, sectoral contributions, and trends: a high-resolution inversion of GOSAT observations of atmospheric methane, *Atmos. Chem. Phys.*, 21, 4339–4356, <https://doi.org/10.5194/acp-21-4339-2021>, 2021.
- Miller, S. M., Commane, R., Melton, J. R., Andrews, A. E., Benmergui, J., Dlugokencky, E. J., Janssens-Maenhout, G., Michalak, A. M., Sweeney, C. and Worthy, D. E. J.: Evaluation of wetland methane emissions across North America using atmospheric data and inverse modeling, *Biogeosciences*, 13(4), 1329–1339, doi:10.5194/bg-13-1329-2016, 2016.
- Saad, K. M., Wunch, D., Deutscher, N. M., Griffith, D. W. T., Hase, F., De Mazière, M., Notholt, J., Pollard, D. F., Roehl, C. M., Schneider, M., Sussmann, R., Warneke, T., and Wennberg, P. O.: Seasonal variability of stratospheric methane: implications for constraining tropospheric methane budgets using total column observations, *Atmos. Chem. Phys.*, 16, 14003–14024, <https://doi.org/10.5194/acp-16-14003-2016>, 2016.
- Stanevich, I., Jones, D. B. A., Strong, K., Parker, R. J., Boesch, H., Wunch, D., Notholt, J., Petri, C., Warneke, T., Sussmann, R., Schneider, M., Hase, F., Kivi, R., Deutscher, N. M., Velasco, V. A., Walker, K. A., and Deng, F.: Characterizing model errors in chemical transport modeling of methane: impact of model resolution in versions v9-02 of GEOS-Chem and v35j of its adjoint model, *Geosci. Model Dev.*, 13, 3839–3862, <https://doi.org/10.5194/gmd-13-3839-2020>, 2020.

Turner, A. J., Jacob, D. J., Wecht, K. J., Maasakkers, J. D., Lundgren, E., Andrews, A. E., Biraud, S. C., Boesch, H., Bowman, K. W., Deutscher, N. M., Dubey, M. K., Griffith, D. W. T., Hase, F., Kuze, A., Notholt, J., Ohyama, H., Parker, R., Payne, V. H., Sussmann, R., Sweeney, C., Velazco, V. A., Warneke, T., Wennberg, P. O. and Wunch, D.: Estimating global and North American methane emissions with high spatial resolution using GOSAT satellite data, *Atmos. Chem. Phys.*, 15(12), 7049–7069, doi:10.5194/acp-15-7049-2015, 2015.

Zona, D., Gioli, B., Commane, R., Lindaas, J., Wofsy, S. C., Miller, C. E., Dinardo, S. J., Dengel, S., Sweeney, C., Karion, A., Chang, R. Y.-W., Henderson, J. M., Murphy, P. C., Goodrich, J. P., Moreaux, V., Liljedahl, A., Watts, J. D., Kimball, J. S., Lipson, D. A. and Oechel, W. C.: Cold season emissions dominate the Arctic tundra methane budget, *Proc Natl Acad Sci USA*, 113(1), 40–45, doi:10.1073/pnas.1516017113, 2016.